Radar remote sensing of rain and melting precipitation in high mountains (French Alps)

Anil Kumar Khanal

▶ To cite this version:

Anil Kumar Khanal. Radar remote sensing of rain and melting precipitation in high mountains (French Alps). Environmental Engineering. Université Grenoble Alpes [2020-..], 2022. English. NNT : 2022GRALU035 . tel-04064653

THÈSE

Pour obtenir le grade de

DOCTEUR DE L'UNIVERSITÉ GRENOBLE ALPES

École doctorale : STEP - Sciences de la Terre de lEnvironnement et des Planètes
Spécialité : Océan, Atmosphère, Hydrologie
Unité de recherche : Institut des Géosciences de lEnvironnement

Apport de la télédétection radar pour l'estimation des précipitations liquides, solides et en fusion dans les hautes montagnes (Alpes Françaises)

Radar remote sensing of rain and melting precipitation in high mountains (French Alps)

Présentée par :

Anil Kumar KHANAL

Direction de thèse :

Guy DELRIEU DIRECTEUR DE RECHERCHE EMERITE, Université Grenoble Alpes	Directeur de thèse

Rapporteurs :

Alexis BERNE
PROFESSEUR ASSOCIE, Ecole Polytechnique Fédérale de Lausanne
Marielle GOSSET
CHARGE DE RECHERCHE HDR, IRD délégation Occitanie

Thèse soutenue publiquement le **20 décembre 2022**, devant le jury composé de :

Guy DELRIEU DIRECTEUR DE RECHERCHE EMERITE, CNRS délégation Alpes	Directeur de thèse
Alexis BERNE PROFESSEUR ASSOCIE, Ecole Polytechnique Fédérale de Lausanne	Rapporteur
Marielle GOSSET CHARGE DE RECHERCHE HDR, IRD délégation Occitanie	Rapporteure
Remko UIJLENHOET PROFESSEUR, Technische Universiteit Delft	Examinateur
Anne-Catherine FAVRE PROFESSEUR DES UNIVERSITES, Université Grenoble Alpes	Présidente

Invités :

Nan YU
DOCTEUR EN SCIENCES, Centre de Météorologie Radar (MÉTÉO-FRANCE)

"Radar sees through the fog - - the reality of things at a distance that the human eyes cannot see."

(wordplay on)
Corrie Ten Brown

Abstract

High frequency (X-band) radars provide the necessary resolution to capture the spatial-temporal variability of precipitation in mountainous terrain. A mountain-top radar with 360° visibility can detect incoming systems from long range and captures the fine-scale dynamics of convective systems over a large area. A valley-based radar can capture local (due to beam blockage) but detailed thermodynamic phase change (in melting layer) of falling hydrometeors in stratiform systems. The melting layer (ML) often occurs below mountain-top altitudes in winter. The attenuation is significant in medium-heavy precipitation and in the ML at X-band, and needs to be corrected for quantitative precipitation estimation (QPE) applications. Radar positioning dilemma, attenuation and poor understanding of melting layer, among others, make QPE in complex terrain challenging.

A unique observation system has been deployed in the French Alps (Grenoble), since 2016, composed of two polarimetric X-band radars, *MOUC* atop Mt. Moucherotte at 1913 m asl and *XPORT* at UGA campus in the valley at 220m asl. Two radar systems 11 km apart with an altitude gradient of 1700 m, offers a unique opportunity to simultaneously identify the ML from valley based radars, and study the propagation of electromagnetic waves within the ML using the low-elevation scans of mountain-top radar. A K-band micro rain radar (MRR) and a disdrometer (DSD) at UGA site along with 10 rain gauge stations at scattered around Grenoble complete the RadAlp experiment setup.

An algorithm for ML identification is developed using valley-based radar systems: it uses the quasi vertical profiles of XPORT polarimetric measurements (horizontal and vertical reflectivity, differential reflectivity, cross-polar correlation coefficient), and the MRR vertical profiles of apparent falling velocity spectra and reflectivity. The algorithm produces time series of the altitudes and values of peaks and inflection points of the different radar observables. A literature review links the micro-physical processes at play during the melting process with the available polarimetric and Doppler signatures. A study of climatology of polarimetric indicators of the melting layer helps to characterize the melting layer during the stratiform precipitation event.

Potential to exploit the dual-polarimetric capability in attenuation correction of X-band weather radar in presence of ML is explored by studying the relationship between differential phase shift (Φ_{dp}) and path integrated attenuation (PIA) at different stages of melting. Mountain reference technique provides direct measurements of PIA at low elevation angles of MOUC radar. Φ_{dp} is independent of attenuation, absolute radar calibration errors and ground clutter, and provides a robust way to correct attenuation. It is however obtained from noisy range profiles. A Φ_{dp} regularization algorithm is developed: it exploits the cumulative nature of Φ_{dp} and removes noise using the iterative maximum-allowed step size approach. PIA-Φ_{dp} relationship at X-band within the ML is established.

Dual-polarimetric capabilities of the radar is further exploited to recover multi-moment characteristics of drop/particle size distributions of precipitation aimed at optimizing the recovery of parameters to improve the attenuation correction algorithms at X-band. Different formulations of attenuation correction are revisited to develop a computational model. A sensitivity analysis approach with a cost function helps to optimize the parameters. The comparison of rainfall rates with the rain-gauge provides the validation of QPE improvement.

Keywords: high mountains, weather radar, dual-polarimetric, X-band, precipitation, melting layer, path integrated attenuation, differential phase shift, mountain reference technique, attenuation correction, quantitative precipitation estimation

Acknowledgements

I want to thank Prof. Guy Delrieu for his supervision and for providing me an opportunity to enter the field of Radar Meteorology through this PhD. I have always been fascinated by clouds and precipitation in its various forms, and I am happy to be able to understand them to some extent. I am indebted to the HMCIS team, especially Brice Boudevillain and Claudio Duran Alarcon for their help through out the project. My special thanks goes to Radar Team (DS0) at Meteo France, Toulouse. The friends and colleagues at IGE made my time at IGE very enjoyable and enriching. Last but not the least I want to thank the partners of the project RMC, CHAPI and EDF/DTG.

Contents

List of Figures

List of Tables

List of Abbreviations

RADAR	**RA**dio **D**etection **A**nd **R**anging
EM	**E**lectro**m**agnetic
FM-CW	**F**requency-**M**odulated **C**ontinuous-**W**ave
QPE	**Q**uantitative **P**recipitation **E**stimation
PIA	**P**ath **I**ntegrated **A**ttenuation
ML	**M**elting **L**ayer
BB	**B**right **B**and
MTO	**M**e**t**e**o**rological Station
MRR	**M**icro **R**ain **R**adar
XPORT	**X**band **Port**able radar
MOUC	Radar at Mt **Mouc**herotte
PPI	**P**lan **P**osition **I**ndicator
RHI	**R**ange **H**eight **I**ndicator
DSD	**D**rop **S**ize **D**istribution
PSD	**P**article **S**ize **D**istribution
asl	**a**bove **s**ea **l**evel
aka	**a**lso **k**nown **a**s

Physical Constants

Speed of Light	c_0	$= 2.997\,924\,58 \times 10^{8}\,\mathrm{m\,s^{-1}}$
Dielectric constant of Water	$\lvert K\rvert^2_{water}$	$= 0.93$
Dielectric constant of Solid Ice	$\lvert K\rvert^2_{ice}$	$= 0.176$

List of Symbols

r	Range (distance to the target)	m
Z	Reflectivity	dBZ
Z_h	Horizontal reflectivity	dBZ
Z_v	Vertical reflectivity	dBZ
Z_{dr}	Differential reflectivity	dB
ρ_{hv}	Co-polar cross correlation coefficient	[-]
W	Apparent fall velocity (average Doppler velocity)	$\mathrm{m\,s^{-1}}$
Ψ_{dp}	Measured total differential phase shift	$^\circ$
Φ_{dp}	Total differential phase on propagation	$^\circ$
δ_{hv}	Backscatter differential phase shift	$^\circ$
K_{dp}	Specific differential phase	$^\circ\,\mathrm{km^{-1}}$
AF	Attenuation factor [0-1]	[-]
PIA	Path integrated attenuation	dB
A	Specific attenuation	$\mathrm{dB\,km^{-1}}$

Chapter 1

General Introduction

In meteorology, precipitation is a product of the condensation of atmospheric water vapor that falls under gravity from clouds. Its main forms are drizzle, rain, sleet, snow, ice pellets, graupel and hail. When a portion of the atmosphere becomes saturated with water vapor (reaching 100% relative humidity), the water condenses and "precipitates". Cooling of the atmosphere and the addition of water vapor, often in tandem, result in the saturation of air. Moisture is lifted, due to evaporation, or forced to rise over a layer of sub-freezing air at the surface. Provided there is necessary and sufficient atmospheric moisture content, the moisture within the rising air will condense into clouds, namely nimbostratus and cumulonimbus if significant precipitation is involved. Eventually, the cloud droplets will grow large enough to form raindrops and descend toward the Earth where they will freeze on contact with exposed objects. The ice-crystal mechanism is dominant in continental cold-cloud processes. Heterogeneous nucleation (between -5 and -15°)C, the formation of ice crystals from the collection and freezing of liquid water molecules onto foreign particles like dust and aerosols, accelerates the freezing of drops. These particles grow by processes like vapor deposition, aggregation and riming. These frozen hydrometeors melt as they descend below the $0^{\circ}C$ layer of the atmosphere to produce liquid rain. In mountainous areas, heavy precipitation is possible where up-slope flow is maximized within windward sides of the terrain at elevation. Warm and dry Foehn wind can form on the leeward side due to adiabatic compression heating; it can result in desert climates. Approximately 505,000 cubic kilometres of water falls as precipitation each year; 398,000 cubic kilometres of it over the oceans and 107,000 cubic kilometres over land. Given the Earth's surface area, that means the globally averaged annual precipitation is 990 millimetres, but over land it is only 715 millimetres (*The Water Cycle*). Climate classification systems such as the Köppen climate classification system use average annual rainfall to help differentiate between differing climate regimes. Precipitation is a major component of the water cycle, and is responsible for depositing the fresh water on the planet. Despite being one of the most observed and recorded climate parameter, accurate estimation of precipitation in complex topography is one of the most challenging fields in meteorology. This manuscript focuses on the study of precipitation using ground based remote sensing techniques in the French Alps.

The manuscript is divided into eight chapters. First chapter serves as a general introduction to the study, and introduces characteristics of precipitation and different approaches of precipitation measurement in complex terrain in the midlatitudes. This chapter is divided into four sections. The first section of the chapter aims to inform readers of the importance of accurate precipitation measurements in the mountainous areas. Second section addresses the main challenges to accurately measure precipitation in these areas and the role of weather radars. A short introduction on the development and the state of ground based radar remote sensing in the French Alps is presented as well. Third section describes the study area considered in this study, i.e. a valley in the French Alps (Grenoble) and climatological factors affecting the precipitation regime in the study area. Fourth section discusses the fundamentals of radar remote sensing.

Second chapter describes the RadAlp experiment. It discusses instrument set-up and available datasets within the scope of the study. It builds on to establish the scientific questions that this study aims to answer.

Third is the study of melting layer of the precipitation. It elaborates on the radar observation of the melting layer, its detection, microphysics and climatology.

The fourth chapter elaborates the application of mountain reference technique to measure path integrated attenuation.Fifth chapter introduces differential phase shift (Φ_{dp}) and discusses the Φ_{dp} regularization algorithm. The relationship between PIA and Φ_{dp} at different stages of melting is investigated in chapter six.

The seventh chapter revisits the attenuation correction formulations and uses optimized parameters to improve the QPE of MOUC radar. It exploits the dual-polarimetric capabilities to recover multi-moment characteristics of drop size distribution. Comparison of rainfall rates from corrected reflectivity and polarimetric technique with the raingauges in the scan volume validates the improvements.

The last (eighth) chapter discusses the important findings of this study, its success in achieving the scientific goals discussed in the second chapter, and finally concludes the manuscript with the future perspective of the study and its findings.

1.1 Precipitation in High Mountains

Precipitation is a key meteorological variable and a primary recharge mechanism of inland fresh water reserves like glaciers, lakes, aquifers and rivers. Freshwater is a vital natural resource for sustenance of most life forms on land. Apart from supporting life, precipitation, in its many forms, is important to human sustainability in managing various agricultural, industrial and household activities. Precipitation is often associated with extreme natural phenomena like flood, landslides, storms and droughts which have detrimental socio-economic impacts on local and regional scale, and at times on human health and lives as well. Precipitation characteristics such as intensity, duration, frequency, number of/between rainy days are governed by climatic factors at the regional and continental scales. Climatic factors are often associated with cyclic patterns, and precipitation with seasonality (Sohoulande Djebou and Singh 2016). It is well documented that precipitation is greatly affected by climate change; it introduces non-cyclic anomalies to precipitation pattern and makes occurrence of extreme event less predictable. For example, 1°C temperature increase due to global warming increases water holding capacity of the atmosphere by $\sim$ 7%, and this increase in moisture in the atmosphere increases the chances of extreme (heavy) precipitation events even in areas where overall precipitation is decreasing (Trenberth 2008). Hence, sufficiently accurate observation and estimation of precipitation has an important theoretical and practical significance.

Mountainous regions, defined as areas above 1000 m asl, cover roughly 27% of the total land surface (Ives et al. 1997; Viviroli et al. 2007). Mountains uplift the air masses, subsequent cooling results in release of humidity in the form of precipitation (solid/liquid). While liquid precipitation runs off the slopes instantly to feed aquifers, rivers and lakes downstream, the solid precipitation often melts slowly and trickles over time, acting as a temporary water reserve in the forms of snowpacks, glaciers and permafrosts. Mountains are considered the “water towers” of the world; functioning as watersheds and reservoirs, they supply almost half of the world population with freshwater for drinking, domestic and commercial use. Rivers originating from Hindu Kush belt in the Himalayas alone provide for 1.3 billion people downstream. In arid and semi-arid regions with high vulnerability for seasonal and regional water shortages, mountains contribute 80 to 100% of the total runoff of river basins. The high precipitation rates, steep topography, low evaporation rates owing to low net radiation, frequent snow cover and low vegetation coverage (both seasonal and spatial) often results in higher discharge rates in the mountains. Rocky mountains feed the Colorado river which sustains 40 million people in semi-arid western United States with annual economic value of almost $1.3 trillion.

Agricultural and industrial prosperity of Peru, and 100% of the water demand of its capital Lima is sustained by the water resources off the slopes the Andes. Mt Kenya alone in East Africa supplies freshwater to 7 million people (Mountain Partnership 2014). In Europe, most major cities are built around navigable rivers, which often are fed by mountainous basins.

The orography of the high mountain region has a huge impact on flow patterns of air masses, which dramatically alters the spatio-temporal distribution of precipitation (Rotunno and Houze 2007). The rapid change in the elevation profile within a short distance plays a significant role in spatial variations on precipitation phase (solid/liquid). While the lakes, glaciers and snowpacks in the mountains act as very important freshwater reserves, quick runoff response due to steep slopes and limited vegetation makes the Alpine region, especially the valley dwellers, vulnerable to natural disasters. Estimation of atmospheric precipitation (solid/liquid), often characterized by high seasonal and spatial variability, is of paramount importance in a mountainous region for the assessment and management of snow and water resources for drinking water, hydropower production, agriculture and tourism (De Jong et al. 2008). One of the most critical applications is the prediction of natural hazards associated with intense precipitation and melting of snowpacks i.e. inundations, floods, flash floods and gravitational movements, which requires a high-resolution observation (spatial resolution $\leq 1\ km^2$ and temporal resolution $\leq$ 1hr) (Delrieu et al. 2014).

1.2 QPE in the Mountainous Terrain

Quantitative precipitation estimation (QPE) refers to the estimation of precipitation amounts at a location or over an area with a certain temporal resolution. Manual/automatic field observations (raingauge network, disdrometers), weather radar and satellite observations are most common data sources to map the estimated precipitation amounts and types over an area for a given time span. Raingauges provide direct real-time observation, compared to other alternatives, but the point data is unable to capture the spatial temporal variability of the rainfall regime at finer scales. Having a network of raingauges helps map the precipitation distribution over a domain, but the density of data points still remains a major limitation on coverage and resolution (Jewell and Gaussiat 2015). Most dense raingauge networks are concentrated on urban areas while mountainous areas have sparse population and lack weather stations. Additionally, the space dynamics of precipitation varies rapidly in complex terrain because of the topography, hence limiting the application and effectiveness of traditional raingauge networks.

QPEs from atmospheric models, i.e. numerical weather prediction (NWP) models, are limited by the model's horizontal resolution, deficiencies in the microphysical parameterization schemes, and insufficient understanding of precipitation processes. Mountainous terrain poses challenge to NWP models mainly due to not sufficient resolution of the underlying topography, but also due to physical parameterizations based on assumptions for horizontally homogeneous and flat terrain (Goger et al. 2016).

Advances in remote sensing techniques provide promising tools in tackling the problems related to localized measurements. Ground and satellite based remote sensing techniques have proved to be invaluable, especially in remote areas with scarce distribution observation stations. Precipitation products from satellite platforms are observed using mainly infrared(IR) mounted on geostationary earth orbiting (GEO) satellites and passive microwave sensors (PMW) mounted on low earth orbiting (LEO) satellites (Nguyen et al. 2018; Hong et al. 2019). GEO satellites provide precipitation estimates at high temporal resolution (images every 5–30 min in multiple spectral bands), but their spectral coverage is limited to visible and IR wavelengths; IR-based estimates rely heavily on the cloud top temperature, a variable indirectly related to surface precipitation. As not every cold cloud is a precipitating one and warmer cloud formations too contribute to precipitation, at short temporal scale and specific precipitation type it can lead to erroneous estimates (Bartsotas et al. 2018). Most IR algorithms use fixed brightness temperature thresholds to discriminate between raining and non-raining clouds and the thresholds are usually too cold for the warm orographic clouds, resulting in underestimation of rainfall (Dinku et al. 2011). On the other hand, LEO satellites provide PMW information about the hydrometeors, emissions of rain droplets or scattering from ice particles present in the precipitating system, directly relevant to surface precipitation rates. LEO satellites provide significantly less temporal coverage compared to the geostationary herd, as the available passing strips do not necessarily fill the desired frame and often have long revisiting periods. The rainfall signal for overland PMW rainfall retrievals comes mainly from ice scattering at the upper parts of convective clouds; as orographic rain may not produce much ice aloft, it might result in underestimation of surface rain. Similarly, rain retrieval in mountainous areas using PMW comes from cold surfaces and ice-covers on mountaintops, which could be misidentified as rain. Active microwave sensors (like Ku-band radar on TRMM satellite, W-band radar on CloudSat, Ku-/Ka- band radar on GPM core observatory) can provide the more accurate estimation of rainfall and snowfall but these spaceborne radars also have limitations of long revisiting periods.

1.2.1 Ground radar-based QPE

Ground based weather radars provide high spatiotemporal resolution and coverage of the precipitation field, which makes them one of the best operational tool for precipitation estimation, but radar QPE at ground is riddled with uncertainties. Well illustrated in the literature (e.g. Brandes and Ikeda 2004; Zawadzki et al. 2005), the errors include among others the presence of ground clutter and anomalous propagation, partial or total beam blockage by obstacles, partial beam filling, beam overshooting, attenuation, spatio-temporal variation in the drop size distribution (causing a varying reflectivity rainrate Z–R relationship) and variation in vertical structure of precipitation resulting from microphysical processes and thermodynamic phase transformations of hydrometeors (Klaassen 1988; Bellon et al. 1997; Bringi et al. 2003; Ryzhkov et al. 2005; Kumjian 2013).

QPE with radar remote sensing in a complex terrain such as the Alps is made challenging by the topography and the space-time structure and dynamics of precipitation systems. Radar coverage of the mountain regions brings the following dilemma. On the one hand, installing a radar at the top of a mountain allows a 360° panoramic view and therefore the ability to detect precipitation systems over a long range at the regional scale. This is particularly relevant for localized and heavy convective systems in warm seasons. But the precipitation is likely to undergo significant change in between detection and arrival at ground level, including a phase change when the $0°C$ isotherm is located at the level of or lower than the radar elevation. Such situations are likely to be frequent during cold periods, with a strong impact on QPE quality at ground level. On the other hand, installing a radar at the bottom of the valley provides high resolution and quality data required for vulnerable and densely populated Alpine valleys, but the QPEs are limited at the latter due to beam blockage by surrounding mountains. The use of radar remote sensing in mountainous areas represents an emerging potential in making the quantitative precipitation estimation as accurate as possible and by best characterizing the uncertainty associated with remote sensing.

1.2.2 Alpine Context

MeteoSwiss has a long-standing experience in operating its C-band radar network in the Alps (Joss and Lee 1995; Germann et al. 2006, 2022) and at coping with the associated altitude dilemma. In addition to physically-based radar data processing aimed at determining vertical profiles of reflectivity and at taking benefit of polarimetry, sophisticated radar-raingauge merging techniques and echo tracking techniques, as well as numerical prediction models outputs (Sideris et al. 2014;

Foresti et al. 2018) are implemented to better understand and quantify the complexity of precipitation distribution in such a rugged environment. More recently, Météo-France has chosen to complement the coverage of its operational radar network ARAMIS (for Application Radar à la Météorologie Infra-Synoptique) in the Alps by means of X-Band polarimetric and Doppler radars. A first set of three radars was installed in Southern Alps within the RHyTMME project (Risques Hydrométéorologiques en Territoires de Montagnes et Méditerranéens) in the period 2008-2013 at Montagne de Maurel (1770 m above sea level, asl), Mont Colombis (1740 m asl) and Vars Mayt (2400 m asl) (Westrelin et al. 2012). This effort has been continued in 2014-2015 with the installation of an additional X-band radar system (MOUC radar, hereinafter) on top of Mount Moucherotte (1913 m) that dominates the valley of Grenoble, the biggest city in the French Alps with about 500,000 inhabitants. The choice of the X-Band frequency is challenging due to its sensitivity to attenuation (Delrieu et al. 2000). In the past, the IGE radar team has proposed the so-called Mountain Reference Technique (MRT) (Delrieu et al. 1997; Serrar et al. 2000; Bouilloud et al. 2009) to take advantage of this drawback for both correcting for attenuation and performing a self-calibration of the radar. The idea was to estimate path-integrated attenuations (PIA) in some specific directions from the decrease of mountain returns during rainy periods. Such PIA estimates were then used as constraints for backward or forward attenuation correction algorithms (Marzoug and Amayenc 1994) with optimization of an effective radar calibration aerror, given a drop size distribution (DSD) parameterization. The development of polarimetric radar techniques (Bringi and Chandrasekar 2001; Ryzhkov et al. 2005) has allowed a scientific breakthrough for quantitative precipitation estimation (QPE) at X-band by exploiting the relationship which exists between the specific differential phase on propagation (in $^\circ\, km^{-1}$) and the specific attenuation ($dB\, km^{-1}$). Similarly to the MRT, the differential propagation phase $\Phi_{dp}(r2) - \Phi_{dp}(r1)$ over a given path $(r1, r2)$ can be used to estimate $PIA(r1, r2)$, which can be used to constrain a backward attenuation correction algorithm and allow a self calibration of the radar and/or an adjustment of the DSD parameterization (Testud et al. 2000; Ryzhkov et al. 2014). Two major advantages of the polarimetric technique over the MRT can be formulated:

1. the availability of PIA constraints for any direction with significant precipitation
2. the subsequent possibility to use a backward attenuation correction algorithm, which is known to be much stable while the forward formulation is essentially unstable

Accounting for their respective potential in different rain regimes (moderate to heavy), some combined algorithms making use of various polarimetric observables (reflectivity, differential reflectivity and specific differential phase) have also been proposed for the X-Band frequency (Matrosov et al. 2002, 2005; Koffi et al. 2014). Although the polarimetric QPE methodology is now quite well established and validated for rainy precipitation (Anagnostou et al. 2004; Matrosov et al. 2005; Diss et al. 2009), Yu et al. 2018 point out in their first performance assessment of the RHyTMME radar network:

1. the need to better understand and quantify attenuation effects in the ML
2. the importance of non-uniform beam filling (NUBF) effects at medium to long ranges in such a high-mountain context
3. the stronger impact of radome attenuation at X-band compared to S- or C-Band

1.3 Study Area: Grenoble

Grenoble is a Y-shaped alluvial valley in south-eastern France (Alps) with a mean altitude of about 220 m asl surrounded by three mountain ranges: Chartreuse (culminating at 2083 m asl) to the north, Belledonne (2977 m) to the south-east and Vercors (2307 m) to the west. The valley is embedded in highly complex Alpine topography, where the core of the city is located at the confluence of deep and steep-side valleys, on the basin of rivers Isere and Drac. Grenoble Alpes Métropole, the urban area comprising of 49 municipalities in and around the valley, is home to around 500,000 inhabitants. Figure 1.1 shows the location and the topography.

FIGURE 1.1: Location and topography of Grenoble and its surroundings

The Isère River basin (Fig 1.2), about 12000 km^2 at the Rhône confluence, hosts 132 dams, 120 hydropower plants, about 400 water intakes and many kilometers of penstocks, contributing to the gross installed hydropower capacity of 7.6 GW in the French Alps (total of 22 GW in France) as of 2016 (Claude et al. 2016). The flow regime of the whole Isère river system is strongly influenced by snowmelt and rain induced runoff, stored in large reservoirs during wintertime and springtime, then released as per demand. Apart from the hydropower production, water resource in Grenoble supports large swaths of agricultural farms and industries.

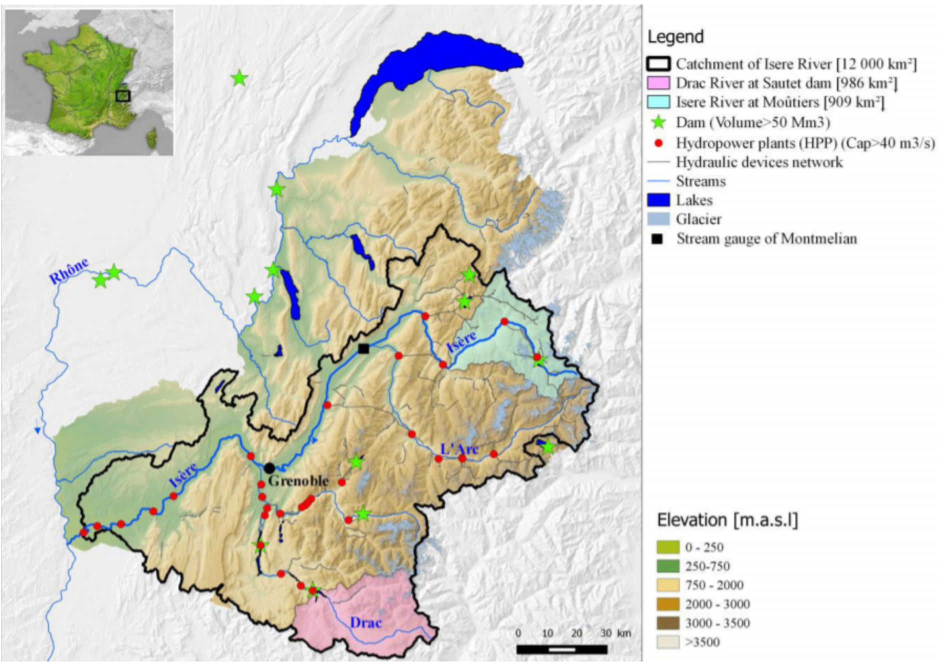

FIGURE 1.2: Isère Catchment (Claude et al. 2016)

1.3.1 Climatology

Orographic effect due to uneven terrain, especially from the Southern branch dictates the air mass flow dynamics in the valley. Grenoble's climate is classified as warm and temperate. There is great deal of rainfall in Grenoble even in the driest month. Grenoble valley receives around 900-1000 mm of rain every year.

The climate is considered to be temperate oceanic climate i.e. *Cfb* according to Köppen-Geiger climate classification.
Cfb: Temperate oceanic climate; coldest month averaging above 0 °C (32 °F) (or -3°C (27 °F)), all months with average temperatures below 22 °C (71.6 °F), and at least four months averaging above 10 °C (50 °F). No significant precipitation difference between seasons (neither above mentioned set of conditions fulfilled).

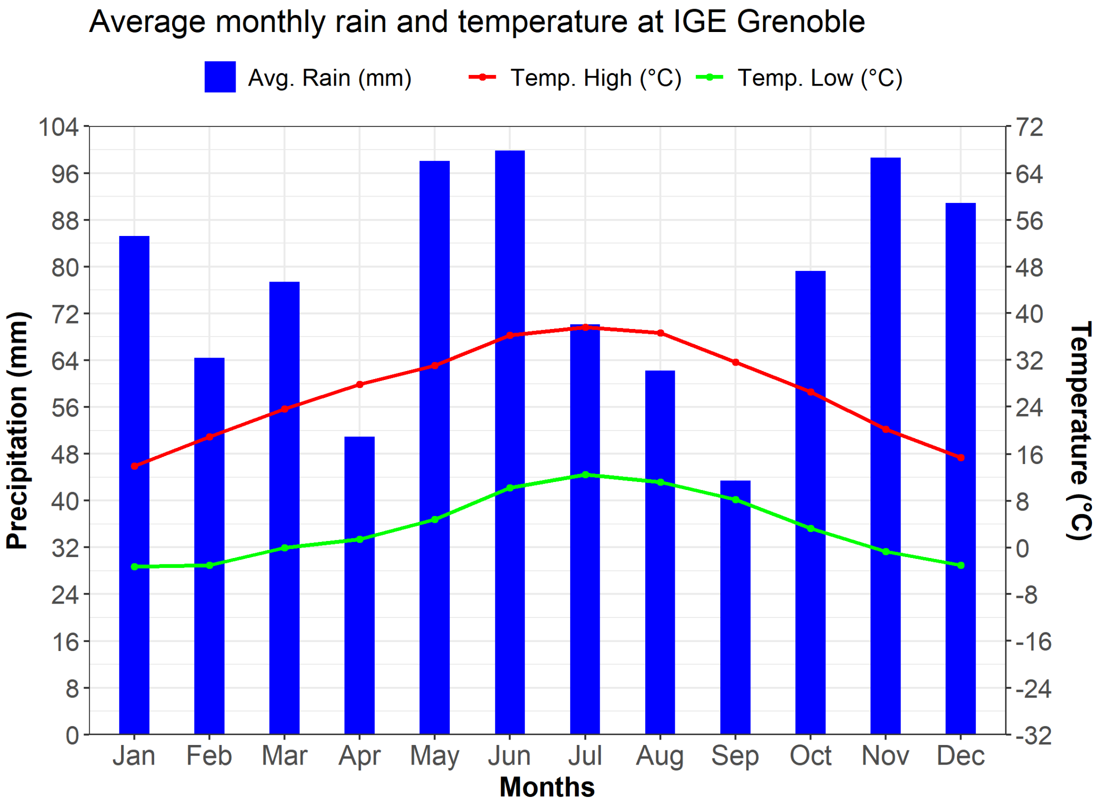

FIGURE 1.3: Monthly average rain and temperatures recorded at MTO station at IGE Grenoble (220 m asl). Recorded between 2014 - 2020. Boxplots show the average monthly rainfall. Line plots show averages of highest (red) and lowest (green) recorded temperatures on each month.

Furthermore Électricité de France (EDF) classifies storms into 8 weather types and 4 general circulation types. Table 1.1 shows the classification of EDF weather patterns.

TABLE 1.1: EDF precipitation/storm classification

Weather Type	**Name**	**Wind Direction**	**General Circulation**
WP1	Altantic wave	NW	Oceanic
WP2	Steady oceanic	W	Oceanic
WP3	South-West circulation	SW	Oceanic
WP4	South circulation	SSE	Mediterranean
WP5	North-East circulation	Continental	
WP6	East return	E	Mediterranean
WP7	Central depression	SSW	Mediterranean
WP8	Anticyclone	-	Anticyclonic

Analysis of rainfall data in the Isere river catchment from 1948-2019 as per EDF weather types and circulation patterns are presented in fig 1.4 (Sodemann and Zubler

2009; Blanchet et al. 2021). The steady oceanic circulation is most dominant(37%) closely followed by anticyclonic conditions(29%) and southern circulation (Mediterranean, 25%). Continental circulation (9%) is a rather rare situation. Regarding the seasonality of these general circulation patterns (Figure 1.4), we can see that anticyclonic weather mirrors the temperature cycle with a peak in July-August, when it is the dominant circulation. Continental circulations are marginal and make a rather stable share. Mediterranean circulation peaks in May and again in October, while Oceanic circulations are seen more in December-January with a small secondary maximum in August.

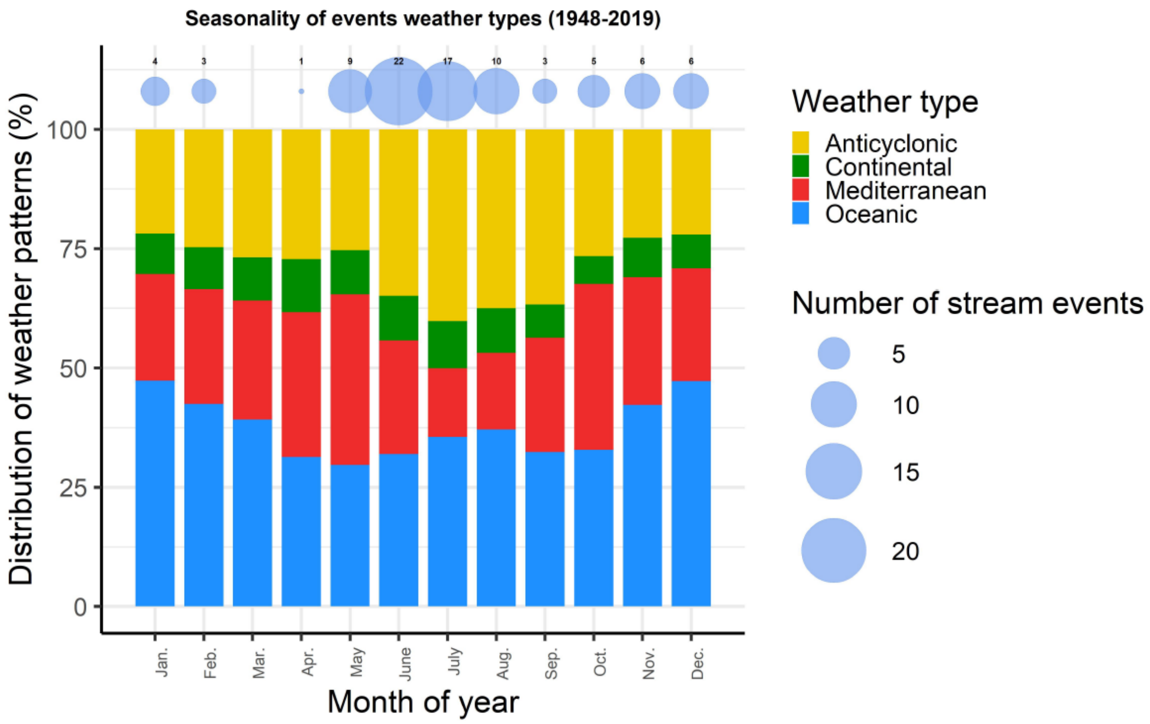

FIGURE 1.4: Shares of weather types by month. Stream events refers to storm events that produced significant discharge to be characterized as flood/extreme event.

1.4 Basics of radar remote sensing

1.4.1 Background

Radar stands for **Ra**dio **D**etection **A**nd **R**anging. From detecting aircraft / flying objects to observing weather fronts / storms, RADAR has broad military, aviation and meteorological applications. The fundamental principles underlying all radars was first observed in 1886 by the German physicist Heinrich Hertz. He found that electromagnetic waves could be reflected from various objects, and even focused into beams by appropriate reflectors. In 1904, a German engineer Hulsmeyer, proposed methods of using electromagnetic waves to help ships with obstacle detection and navigation. Dr. Hoyt and his associates in the US Naval Research Laboratory, in 1922, while experimenting with relatively high frequency radio communications from one side of river to another, discovered a significant loss of reception as ships passed between the transmitter and receiver. This led them to conclude that presence of enemy ships could be detected using radio waves. Leading up to World War II, extensive research in both continuous wave and pulsed radio signals continued. By 1930 continuous waves had practical use in detecting enemies ships and aircrafts. Continuous waves detected targets in short ranges; in 1934 Army Signal corps suggested the possible use of pulsed energy to observe targets at longer ranges. In 1935, Robert Watson-Watt proposed similar system in UK and was successful in producing a functioning equipment. By 1941, with the development of the cavity magnetron, a high-power transmitting tube, and its implementation in radar, UK had advanced significantly in radar technology and established a land radar network.

During WWII, it was realized that precipitation presented targets (noise) on radar displays, and prevented full utilization of radar systems for the intended military use. Radar observation of precipitation fields provided military meteorological officials with new tools to increase the accuracy of short-term forecast, and proved to have a significant value in military operations. Marshal and Palmer in 1948 correlated a given radar reflectivity with the rainfall rate (Z-R relationship) (Marshall and Palmer 1948). As a secretive technology, radar did not see much civilian meteorological applications at that time. Post war, scientists and technicians in the field of meteorology gradually understood the use and limitations of these military oriented radars in weather-detection and slowly incorporated modification to suit them to meteorological requirements. Since 1960s the use of radars have been widespread, development of Doppler and polarimetric capabilities have enabled meteorologist to study the 3D structure of precipitating systems.

Weather radars transmit pulses of electromagnetic energy into the atmosphere, which travel as an EM wave, and receive energy reflected by the particles in the atmosphere (scatterers). Reflectivity ($/eta$) of a pulse volume is a measure of the efficiency of the radar targets in intercepting and returning the transmitted radio energy. It depends upon the number, size, shape, aspect, and dielectric properties of the target. The reflectivity factor (Z) is directly proportional to reflectivity and is often referred to as radar reflectivity. The basic operation principle of weather radars is illustrated in Fig 1.5. During the 1970s, weather radars were standardized and organized into networks. Introduction of Doppler capabilities by Doviak et al. (1979), provided radars the ability to track relative velocities (Doppler velocity (V) and Doppler spectrum width W) of the particles in addition to position and intensity. Between 1980s and 2000s, most developed countries established their own weather radar networks. In the United States, construction of 10 cm wavelength Doppler radar network called NEXRAD or WSR-88D (160 radars currently) stated in 1988. Canada national radar network was installed between 1985 and 2004, Dopplerized in 1993. France (ARAMIS network) and other European countries switched to Doppler networks by early 2000s. Droplets of falling liquid water tend to have a larger horizontal axis due to the drag coefficient of air, causing the water molecule dipole to be oriented in that direction. Conventionally, radar beams were polarized horizontally in order to receive the maximal signal reflection. The radar moments discussed so far relate to horizontal polarization (Z_h, V_h and W_h).

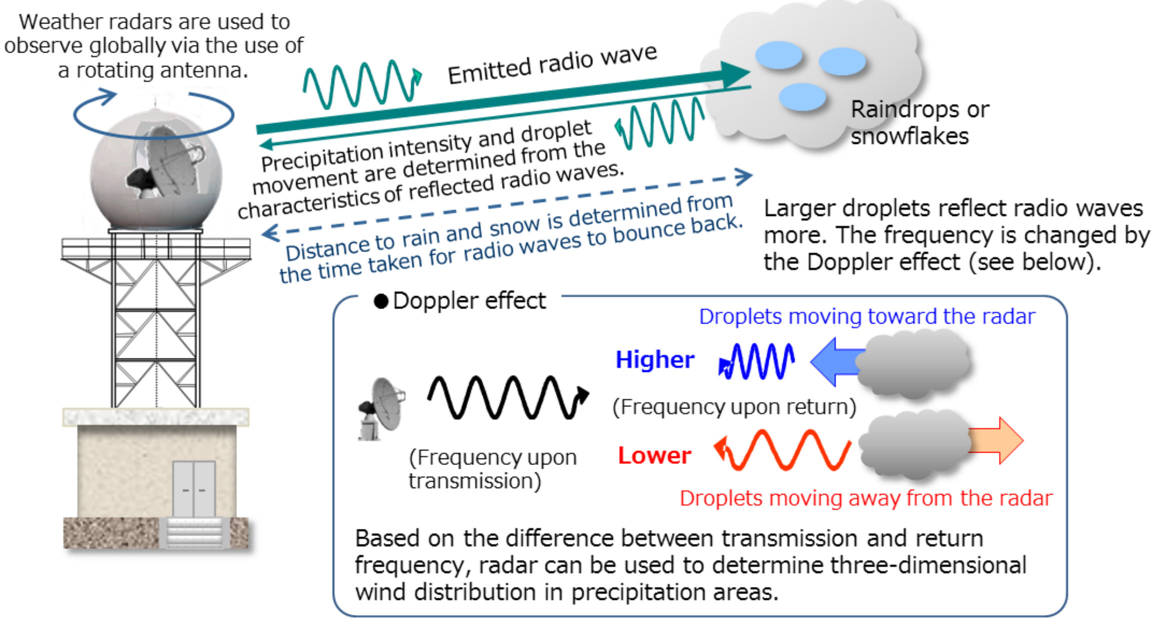

FIGURE 1.5: Overview of Weather radar Observation
source: Japan Meteorological Agency

After 2000, dual-polarization technology was integrated in the operational radars (Doviak and Zrnić 1993; Bringi and Chandrasekar 2001). Dual-polarimetric radars transmit and receive at two polarization (horizontal and vertical with respect to ground) simultaneously. In addition to the former three moments in vertical polarization (Z_v, V_v and W_v), one can gain important insights into the microphysical properties of hydrometeors by comparing the amplitudes and phases of signals returned at two polarization (Kumjian 2013). Polarimetric radar observations are discussed in more detail in section 1.4.4. The existing radar networks are being upgraded with dual-polarimetric capabilities in the last decade.

TABLE 1.2: Frequency bands in electromagnetic spectrum

IEEE Standard 521-1984		
Band	Nominal frequency	Nominal Wavelength
HF	3-30 MHz	100-10 m
VHF	30-300 MHz	10-1 m
UHF	0.3-3 GHz	1-0.1 m
L	1-2 GHz	30-15 cm
S	2-4 GHz	15-8 cm
C	4-8 GHz	8-4 cm
X	**8-12 GHz**	**4-2.5 cm**
Ku	12-18 GHz	2.5-1.7 cm
K	**18-27 GHz**	**1.7-1.2 cm**
Ka	27-40 GHz	1.2-0.75 cm
W	40-75 GHz	4.0-2.73 mm
G	75-110 GHz	2.73-0.1 mm

Most radars operate between 400 MHz to 36 GHz. Characteristics of different frequency bands are listed in Table 1.2. The theoretical principles of radars are the same at any frequency; however, the technical implementation is widely different. The best frequency to use for a radar depends upon its application. The interaction of the EM radiation with the atmosphere (i.e. the type of targets) varies with the frequency. Lower frequencies are sensitive to the composition of the atmosphere (like water vapor and molecular oxygen) whereas higher frequencies attenuate significantly in presence of larger hydrometeors. The choice of frequency involves tradeoffs among different factors like physical size, transmitted power, antenna beamwidth and attenuation. The dimension hardware, in general, is proportional to wavelength. At higher frequencies wavelengths are shorter, radars can be housed in smaller packages and mounted in mobile platforms. The choice of frequency indirectly influences the magnitude of transmitted power because of its impact on hardware size. Level of power a radar transmitter can handle is determined by the voltage gradient and ability to dissipate heat. Low frequency radars (large wavelength) with bulky hardware can transmit more average power. The narrower the beam, greater is the transmitted power that is concentrated in a particular direction at a given time, and the finer the angular resolution. The width of radar's antenna beam is directly proportional to the ratio of wavelength to the width of antenna. At low frequencies, large antennas are used to achieve acceptably narrow beams. Radio waves passing through atmosphere are attenuated by absorption and scattering. While the absorption is mainly due to oxygen and water vapour, scattering results from hydrometeors. Both absorption and scattering increases with frequency.

Depending on the application, weather radars are commonly operated in four different frequency band.

- S-band radars: [Frequency:2-4 GHz, Wavelength:8-15 cm] Because of the wavelength and frequency, S-band radar signal is not significantly attenuated. This makes them useful for near and far range weather observation. It requires a large antenna dish and has high transmitted power. They are deployed mostly in tropical and temperate climate areas, e.g. where hurricanes, tornadoes, large hail and monsoon/heavy rain are common. The NEXRAD network in the United States is composed of 160 S-band radars.

- C-band: [Frequency: 4-8 GHz, Wavelength: 4-8 cm] GHz. Because of the wavelength and frequency, the dish size does not need to be very large. The signal is more easily attenuated, so this type of radar is best used for short range weather observation. The frequency allows C-band radars to create a smaller beam width using a smaller dish. C-band radars also do not require as much power as S-band radar. They are deployed in climates where attenuation by intervening heavy rain or hail is supposed to be a minor issue. European radar network is mainly composed of C-band radars, except in the Mediterranean and mountainous regions in France.

- X-band: [Frequency: 8-12 GHz, Wavelength: 2.5-4 cm] Because of the smaller wavelength, the X-band radar is more sensitive and can detect smaller particles. These radars are used for studies on cloud development because they can detect the tiny water particles and also used to detect light precipitation such as snow. X-band radars also attenuate very easily, so they are used for only short range weather observation. They are deployed mainly in shorter-range hydrological and meteorological applications such as urban and mountain valley hydrology. Most major airplanes are equipped with X-band radar to pick up turbulence and other weather phenomenon.

- K-band: [Frequency: 18-27 GHz, Wavelength: 1.2-1.7 cm] The range of frequencies in the center of the K-band is absorbed by water vapor in the atmosphere due to its resonance peak at 22.24 GHz, 1.35 cm. Therefore these frequencies experience high atmospheric attenuation and cannot be used for long distance applications. Micro rain radar (MRR), a portable, low-cost, low-power, frequency modulated continuous wave (FM–CW) vertically pointing K-band Doppler radar is often used to study the microphysics of precipitation and snowfall measurements. In spaceborne plotforms, due to limitation of liftoff size and required power, high frequency radars are preferred. K_a and K_u band radars are used in Global Precipitation Mission (GPM).

The French national radar network operated by Météo France consists of 20 C-band radars, 5 S-band radars and 6 X-band radars (+2 at Paris and Nice airports). The data from various individual radars in the mainland France are transmitted to a concentrator in Toulouse which develops mosaics of precipitation zones and their accumulation every 5 minutes. Under the Operation Program on the Exchange of Weather Radar Information (OPERA) project, 30 European countries with more than 200 operational radars, mainly C- but some X- and S-bands, Pan-European radar composites are produced every 15 minutes (Saltikoff et al. 2019).

1.4.2 Basic Radar Terms

It seems beneficial to introduce readers to some basic radar terms, before discussing the theory and operating principles of weather radars in next sub-section.

- **Frequency (f)**
  Frequency refers to the number of completed wave cycles per second. Radar frequency is expressed in units of Hertz (Hz).

- **Wavelength (λ)**
  Wavelength is distance from wavecrest to wavecrest (or trough to trough) along an electromagnetic wave's direction of travel is called wavelength. Unit of wavelength is generally centimetre.

- **Phase (δ)**
  Phase of an electromagnetic wave is essentially the fraction of a full wavelength a particular point is from some reference point measured in radians or degrees.

- **Bandwidth (BW)**

  Bandwidth is the frequency difference between the upper and lower frequencies of electromagnetic radiation. It is expressed in units of Hertz (Hz).

- **Pulse width (τ)**

  Pulse width is the time interval between the leading edge and trailing edge of a pulse at a point where the amplitude is 50% of the peak value. It is expressed in units of microseconds.

- **PRF and PRT**

  Pulse repetition frequency is the number of peak power pulses transmitted per second. Pulse repetition time is the time interval between two peak pulses.

- **Beamwidth (θ)**

  beamwidth is the angle between the half-power (3 dB) points of the main lobe, of the antenna diagram, when referenced to the peak effective radiated power of the main lobe. Unit is degree.

1.4.3 Weather radar equation

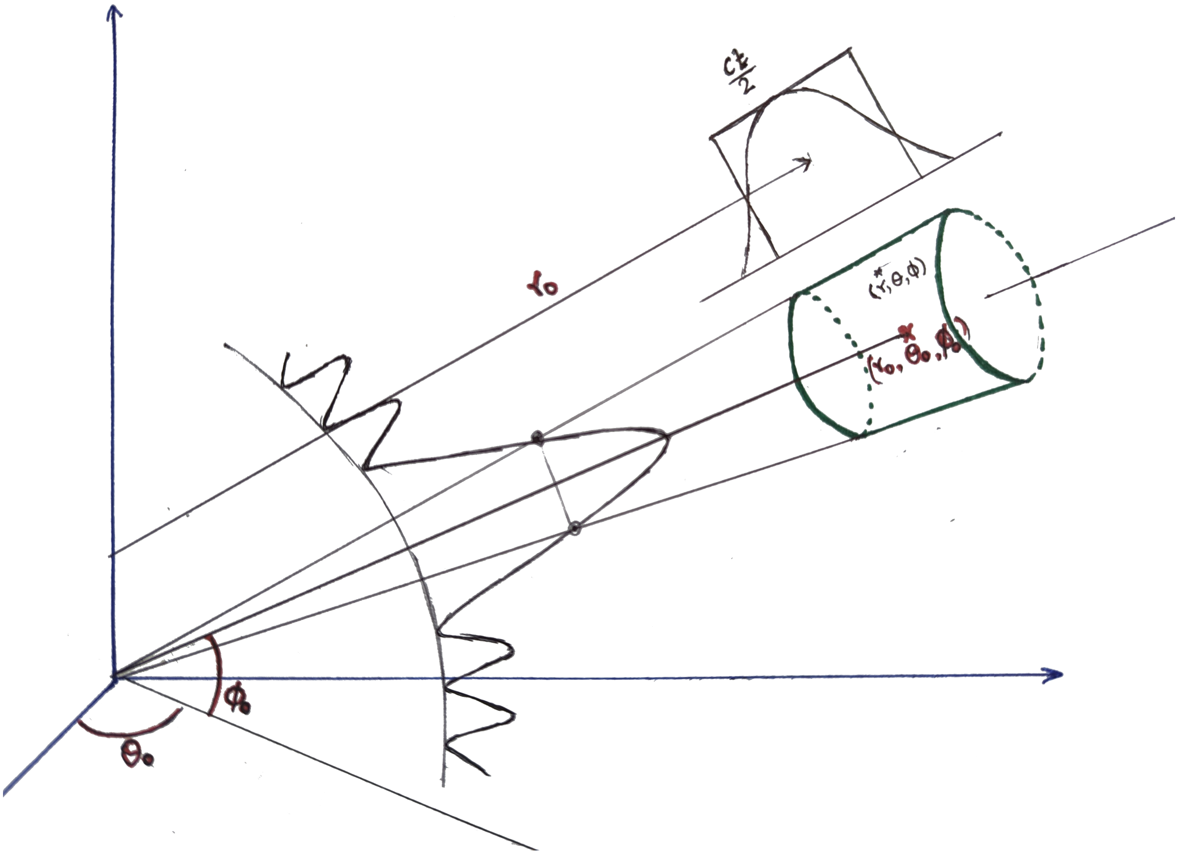

FIGURE 1.6: Pulse Volume of a weather radar in polar coordinates.

The fundamental equation in radar meteorology is called the weather radar equation. It expresses the backscattered power from a meteorological target centered at a point ($r_0,\ \theta_0,\ \phi_0$ as a function of radar and target characteristics (Doviak and Zrnić 1993).

$$P_r(r_0, \theta_0, \phi_0) = \frac{P_t\ \lambda^2}{(4\pi)^3} \iiint_V \frac{I(r,\theta,\phi)\ W_0(r,\theta,\phi)\ \eta(r,\theta,\phi)}{r^4} dV \tag{1.1}$$

where,
η: total effective backscattering surface of hydrometeors / unit volume
W_0: product of the angular and radial weighing functions
I: interception factor due to obstacles (screening) and intervening gases and precipitation (attenuation) between radar and target
P_t: transmitted power
λ: wavelength

This formulation emphasizes on the convolution of the backscattered power by hydrometeors with the weighing functions on one hand and the importance of the propagation effects (screening, attenuation) on other.

The resoultion volume can be expressed as

$$dV = r^2\ dr\ sin\theta\ d\theta\ d\phi \tag{1.2}$$

The resolution volume is defined by cutoff levels of the weighing functions. The product of the weighing functions can be expressed as

$$W_0(r,\theta,\phi) = G^2\ f^4(\theta - \theta_0,\ \phi - \phi_0)|W(r_0, r)|^2 \tag{1.3}$$

where,
G: antenna gain
f: antenna diagram
W: range weighting function

The integral of range weighting function gives the pulse width

$$\int_0^\infty |W(s)|^2\, ds \approx \frac{c\tau}{2} \tag{1.4}$$

where,
c: celerity of light
τ: pulse length

The interception factor between radar and resolution volume can be expressed as

$$I(r,\theta,\phi) = S(r,\theta,\phi)\; AF(r,\theta,\phi) \tag{1.5}$$

where,
S: Screening
AF: Attenuation factor
The screening by mountains can be estimated using digitalized terrain models (Delrieu et al. 1995).

The attenuation factor is given by

$$AF(r,\theta,\phi) = exp(-0.46 \int_0^r A(s)ds) \tag{1.6}$$

where,
A: specific attenuation

The total hydrometeor's backscattering surface can be expressed as

$$\eta(r,\theta,\phi) = \int_0^\infty \sigma_b(D)\; N(D)\; d(D) \tag{1.7}$$

where,
σ_b: back scattering cross section of hydrometeor of diameter D
N: drop size distribution within the unit volume (typically 1 m^3)

Most formulations of the weather radar equation, consider the scattering processes to occur in the Rayleigh regime, i.e. with raindrop diameter smaller compared to the wavelength. All dipoles in the drop oscillate with same phase and the backscattering surface σ is proportional to

$$\sigma = \frac{D^6 \pi^5 |K|^2}{\lambda^4} \tag{1.8}$$

where,
D : drop diameter $[m]$
λ : wavelength $[m]$
$|K|^2$: Dielectric constant [water 0.93, solid ice 0.176]

For liquid rain drops,

$$\sigma_n = \frac{\pi^5}{\lambda^4}\; |K_w|^2\; D^6 \tag{1.9}$$

where,
$|K_w|^2$: dielectric constant of water

The dielectric constant of water is given by

$$K_w = \frac{m^2 - 1}{m^2 + 2} \tag{1.10}$$

where,
m: complex radiative index of water

Radar Reflectivity (η)

The sum of all backscattering cross-sections per unit volume is referred to as radar reflectivity. In other words,

$$\sum_i \sigma_i = \eta \tag{1.11}$$

Using equation 1.8, equation 1.11 can be expressed as:

$$\eta = \sum_i \sigma_i = \frac{\pi^5 |K|^2}{\lambda^4} \sum_i D_i^6 \tag{1.12}$$

Radar Reflectivity Factor (Z)

The radar reflectivity factor is defined as:

$$Z = \int_0^\infty N(D)\ D^6\ dD \tag{1.13}$$

From equation 1.9 and equation 1.13

$$\eta = \frac{\pi^6}{\lambda^4}\ |K_w|^2\ Z \tag{1.14}$$

If η is assumed to be homogenous within the resolution volume and AF independent of θ and ϕ ; i.e. attenuation only along the radial beam path

$$P_r(r_0) = \frac{P_t\ \lambda^4\ G^2}{(4\pi)^3} \int_0^\infty |W(s)|^2 ds \int_0^{2\pi} \int_0^\pi f^4(\theta,\phi)\ sin\theta\ d\theta\ d\phi\ \frac{\eta(r_0)\ AF(r_0)}{r_0^2} \tag{1.15}$$

The antenna diagram can be approximated by

$$\int_0^{2\pi} \int_0^\pi f^4(\theta,\phi)\ sin\theta\ d\theta\ d\phi \approx \frac{\pi\ \theta_{3dB}^2}{8\ ln2} \tag{1.16}$$

where,θ_{3dB} is the 3 dB beamwidth

Substituting eq 1.4, eq 1.16 and replacing reflectivity by reflectivity factor in eq 1.15, we obtain:

$$P_r(r_0) = \frac{P_t\,\lambda^2\,G^2}{(4\,\pi)^3}\,\frac{c\tau}{2}\,\frac{\pi\,\theta_{3dB}^2}{8\,ln2}\,\frac{\pi^5}{\lambda^4}\,|K_w|^2\,\frac{Z(r_0)AF(r_0)}{r_0^2}$$

or,

$$P_r(r_0) = \frac{P_t\,G^2\,c\,\tau\,\pi^3\,\theta_{3dB}^3\,|K_W|^2}{1024\,ln2\,\lambda^2}\,\frac{Z(r_0)\,AF(r_0)}{r_0^2} \tag{1.17}$$

where, the first part is a constant, known as radar constant (C).

$$P_r(r_0) = C\,\frac{Z(r_0)\,AF(r_0)}{r_0^2} \tag{1.18}$$

We use in the following derivations, the concept of "measured reflectivity" defined as:

$$Z_m(r) = Z(r)\;AF(r)\;dC \tag{1.19}$$

where, dC represents a possible radar calibration error i.e. a faulty estimation of the radar constant C.

By taking all the "known" constants together, a radar constant (C) can be defined such that equation 1.18 can be simplified into:

$$P_r(r) = \frac{C}{r^2} Z_m(r) \tag{1.20}$$

The units of radar reflectivity **Z** on equation 1.18 is $mm^6\;m^{-3}$. Here on-wards, Z will be simply referred to as radar reflectivity.

Instead of using linear units [mm^6m^{-3}] the radar reflectivity is often expressed in logarithmic units –decibels [dBZ]

$$dBZ = 10\;log_{10}\,\frac{Z}{Z_0} \tag{1.21}$$

with

$$Z_0 = 1\;mm^6\;m^{-3}$$

Range of the target:

Assuming the wave travels at speed of light (c), range of a target can be calculated as:

$$r = c\frac{\Delta t}{2} \tag{1.22}$$

Δt : *elapsed time interval between emission and reception pulse*

1.4.4 Polarimetry

Conventional (single-polarization and non-coherent) radars operate by transmitting pulses of electromagnetic (EM) radiation and "listening" for echoes returned from various atmospheric targets i.e. scatterers. The energy propagates through the atmosphere as an EM wave with the electric field vector oscillating in the horizontal plane parallel to the ground; therefore, these waves are said to be horizontally polarized. When a horizontally polarized wave illuminates a particle in the atmosphere, the particle behaves as a tiny antenna, emitting radiation in all directions, with the amplitude of this "scattered" energy related to the size, shape, and orientation of the target, as well as its physical composition (e.g., liquid or ice). The particle's physical composition affects scattering through the complex refractive index or complex relative permitivity , which can be thought of as how “reflective” a particle is to EM radiation. Consider a spherical hydrometeor that is small compared to the radar wavelength. When the particle is illuminated by a horizontally polarized radar wave, the particle behaves like a horizontal dipole antenna that becomes excited and scatters energy having horizontal polarization, whereas it behaves like a vertical dipole antenna and scatters energy with vertical polarization when excited by a vertically polarized radar wave (Kumjian 2013). Dual-polarization radars exploit this fact by transmitting radiation with horizontal polarization and vertical polarization simultaneously (Bringi and Chandrasekar 2001; Fabry 2015). By comparing the signals received from returns (amplitude and phase) at each polarization, one can glean information about the size, shape, orientation and microphysical properties of targets within the radar sampling volume.

Scattering Matrix

Assuming, orthogonal polarization of waves in horizontal and vertical plane, when a horizontally polarized wave is incident upon an anisotropic (shape, dipole moment) target, the backscattering wave can have contribution in both horizontal (h) and vertical(v) polarization. Same principle applies for the vertically polarized wave. As the incident electromagnetic waves can be described by horizontal and vertical components, the backscattering properties of the target can be completely described by scattering matrix, S,

$$\begin{bmatrix} E_h^s \\ E_v^s \end{bmatrix} = \begin{bmatrix} S_{hh} & S_{hv} \\ S_{vh} & S_{vv} \end{bmatrix} \begin{bmatrix} E_h^i \\ E_v^i \end{bmatrix} \tag{1.23}$$

where,
i refers to incident wave
s refers to scattered wave

Scattering matrix describes the transformation of the electric field of incident wave to the electric field of the scattered wave. The strength and polarization of the scattered wave for arbitrary polarization of the incident wave can be computed, as any incident wave can be expressed in the $[E_h^i, E_v^i]$ basis set. The four elements of the scattering matrix are complex, can be obtained from the magnitudes and phase measured by the four channels of a polarimetric radar. Bringi and Chandrasekar (2001) and Fabry (2015) elaborate the scattering matrix in detail.

Reflectivity (Zh and Zv)

$$\begin{aligned} Z_h &= \frac{4\lambda^4}{\pi^4}|K_w|^2 < |S_{hh}|^2 > \\ Z_v &= \frac{4\lambda^4}{\pi^4}|K_w|^2 < |S_{vv}|^2 > \end{aligned} \tag{1.24}$$

$< S_{vv} >$ and $< S_{hh} >$ are the copolar elements of the backscattering matrix averaged over an ensemble of scatterers for the h and v polarizations.

Reflectivity is a measure of amount of energy backscattered by the target. Reflectivity factors at horizontal Z_h and vertical Zv polarisation are the dual-polar equivalents of reflectivity (Z [dBZ]). Reflectivity is defined as a measure of the fraction of radiation reflected by a given surface; expressed as a ratio of the radiant energy reflected to the total amount of energy incident upon that surface. The radar reflectivity factor (Z) of precipitation is dependent on the number and size of reflectors (hydrometeors) in a pulse volume. Z_h and Zv depend on the particle size distribution, the incident wavelength, temperature (through σ) and dielectric properties of the hydrometeors.

Differential Reflectivity (Z_{dr})

$$Z_{dr} = 10\, log_{10} \frac{< |S_{hh}|^2 >}{< |S_{vv}|^2 >} \tag{1.25}$$

$< S_{vv} >$ and $< S_{hh} >$ are the copolar elements of the backscattering matrix averaged over an ensemble of scatterers for the h and v polarizations.

The differential reflectivity (Z_{dr}) is the logarithmic (if expressed in dB) ratio of the reflectivity factors at H and V polarizations, and therefore is a measure of the reflectivity-weighted axis ratio (or shape) of the targets. Thus, for spherical targets that return equal power at h and v polarizations, Z_{dr} is 0 dB. Z_{dr} is usually independent of concentration and tends to be influenced by largest particles. Z_{dr} is sensitive to particle shape and size distribution. Even irregularly shaped hydrometeors can produce low Z_{dr} at high elevation angles as all drops look symmetrical when illuminated from below. Z_{dr} also is affected by the physical composition and/or density of particles. For a particle of a given size and shape, Z_{dr} is enhanced as the complex refractive index increases. The dielectric constant of water is five times greater than that of ice. Thus, the Z_{dr} of an oblate water drop is larger than the Z_{dr} of an ice pellet of the same size and shape, which in turn is larger than the Z_{dr} of a lower-density ice particle (e.g., graupel or snow aggregate) of the same size and shape. Because it is a ratio of the reflectivities at *h* and *v* polarizations, Z_{dr} is independent of particle concentration and is not affected by absolute miscalibration of the radar transmitter or receiver. It is, however, affected by the difference in the H and V channels, and therefore can be biased.

Co-polar cross-correlation coefficient (ρ_{hv})

Co-polar cross-correlation coefficient (ρ_{hv}) measures the consistency of the *h* and *v* returned power and phase for each pulse. This "cross correlation" looks at how the power and phase of one channel compares to the other channel. If the consistency is high, changes with one channel are similar to changes with the other.

$$\rho_{hv} = \frac{< S_{vv} S_{hh}^* >}{\sqrt{< |S_{hh}|^2 >< |S_{vv}|^2 >}} \tag{1.26}$$

$< S_{vv} >$ and $< S_{hh} >$ are the copolar elements of the backscattering matrix averaged over an ensemble of scatterers for the h and v polarizations; the asterisk indicates the complex conjugate. ρ_{hv} has many applications, including hydrometeor classification, ground clutter and melting-layer identification, interpretation of microphysics and the retrieval of drop size distribution.

ρ_{hv} is a measure of the diversity of how each scatterer in the sampling volume contributes to the overall *h* and *v* polarization signals. This diversity includes any physical characteristic of the scatterers that affects the returned signal amplitude and phase. Thus, when there exists a large variety in the types, shapes, and orientations of particles within the radar sampling volume, ρ_{hv} is decreased. Note that a diversity of sizes does not affect ρ_{hv} unless the shape of the particles varies across the size spectrum. In addition to reduced values with increased diversity of the physical characteristics of particles, ρ_{hv} can be significantly reduced in the presence of non-Rayleigh scatterers, owing to variability in the backscattered differential phase within the sampling volume. Imperfections in the radar hardware can produce reductions in ρ_{hv} as well. In contrast, more uniform scatterers tend to produce ρ_{hv} near 1.0. Spherical particles of any size will produce ρ_{hv} = 1.0 because they each contribute identically to the signals at H and V polarizations. ρ_{hv} varies between 0 and 1, for liquid and solid precipitation it is generally in between $[0.97 - 1]$, and it drops significantly in the region of melting layer.

Differential Phase Shift (Φ_{dp})

EM radiation acquires additional phase shift travelling through precipitation than through air. In anisotropic medium, like oblate raindrops, the amount of phase shift is different between h and v polarizations. Φ_{dp} is proportional to the number concentration of particles and tends to increase with increasing particle size. It is immune to attenuation, partial beam blockage, ground clutter and radar miscalibration. It is cumulative along the path. For these reasons, it is an attractive variable to use for attenuation correction and quantitative precipitation estimation.

Specific differential phase shift (K_{dp}) is half the range derivative of Φ_{dp}. It gives the differential phase shift per unit distance (usually expressed in degrees per km) along the radial direction. It is useful for locating regions of heavy precipitation. K_{dp} is hard to measure in low precipitation and in presence of non-uniform beam filling (Ryzhkov and Zrnic 1998) and in presence of non-Reyleigh scatterers like melting snow-aggregate and large hail.

Φ_{dp} varies (almost proportionally in rain) with the measure of the difference in 2-way attenuation for horizontal and vertical pulses in a pulse volume because both are propagation parameters and depend on the forward functions of the scattering matrix.

Doppler velocity Spectra and Apparent Fall Velocity (V)

A polarimetric capable radar can measure the phase shift of a received wave compared to transmitted wave. The phenomenon of Doppler shift can be used to calculate the radial velocities of targets. Doppler Spectrum $S(v)$ is the power-weighted distribution of radial velocities within the resolution volume. $S(v)$ represents the power returned to the radar by scatterers with radial velocity between v and $v + \Delta v$. In terms of microphysical parameters:

$$S(v) = \frac{\lambda^4}{\pi^5 |Kw|^2} \int_{v}^{v+\Delta v} v \sigma_h^b(v) dv \tag{1.27}$$

$\sigma_h^b(v)$: average horizontal backscattering coefficient of all scatters with radial velocity (v)

The average radial velocity (V) is the first moment of the normalized Doppler spectrum (divided by total reflectivity) and **spectral width(W)** is the square root of second moment.

$$V = \frac{\int \eta(v) v dv}{\int \eta(v) dv} \tag{1.28}$$

$$W^2 = \frac{\int \eta(v)(v - V)^2 dv}{\int \eta(v) dv} \tag{1.29}$$

v : *Doppler Velocity [ms^{-1}]*

$\eta(v)$: *spectral reflectivity [sm^{-2}]*

Spectrum width is a measure of dispersion of velocities within the radar sample volume.

1.4.5 DSD formulation and polarimetric variables

The (rain) drop size distribution (DSD) is defined as the number density of raindrops per unit size range and per unit volume. It plays a key role in the microphysics and dynamics of raindrops while falling in the atmosphere. Thus, DSD measurements provide important insights into the atmospheric processes of the precipitation volume. Some instruments (like disdrometer) provide a direct measurement of DSD by detecting individual drops with optical light illumination, whereas other measurements (e.g. using radar) are indirect. A generalized DSD formulation with a dimensionless probability density function g(x) is formulated as (Yu et al. 2014):

$$N(D) = \frac{N_t}{D_c} g(\frac{D}{Dc}) \;\; , mm^{-1} m^{-3} \tag{1.30}$$

where,

N_t: total concentration in m^{-3}

D_c: characteristic diameter in mm

Let's denote

$$x = \frac{D}{D_c} \tag{1.31}$$

such that, g(x) is the probability distribution function i.e. $\int_0^\infty g(x)dx = 1$. Some of the candidate models for PDF $g(x)$ are:

exponential:

$$g(x, \lambda) = \lambda \; exp(-\lambda x) \tag{1.32}$$

gamma:

$$g(x, \lambda, m) = \frac{\lambda^{m+1}}{\Gamma^{m+1}}\, x^{m}\, exp(-\lambda x) \tag{1.33}$$

generalized gamma:

$$g(x, \lambda, m, c) = \frac{c\lambda^{c(m+1)}}{\Gamma^{m+1}}\, x^{c(m+1)-1}\, exp(-(\lambda x)^{c}) \tag{1.34}$$

All the radar observable and variables of interest are assumed to be proportional to DSD moments. The k^{th} moment of DSD (M_K) can be written as:

$$M_k = \int_0^\infty N(D)\, D^k\, dD \tag{1.35}$$

Liquid water content, rainfall intensity and reflectivity are considered to be proportional to moment orders 3, 3.67 and 6 of the DSD, respectively in the Rayleigh scattering regime.

1.4.6 Attenuation

Attenuation is the weakening of a radar signal amplitude as the beam travels because of some of the energy being lost to scattering (direction other than receiver) and absorption by hydrometeors and other particles in the atmosphere. The radar beam encounters more and more of these particles as it moves further away from the transmitter. So, storms close to the radar are better sampled than storms far from the radar site. The enhanced reflectivity of the melting layer of precipitation, usually known as the bright band in radar meteorology, results in increased scattering and greater signal extinction (absorption). The bright band may thus contribute a significant portion of the total attenuation (Bellon et al. 1997).

At high frequencies (above 5GHz), the melting snowflakes significantly attenuate the radar signal. This effect is stronger at lower elevation angles, as the distance through the melting layer is the largest. Attenuation is problematic since it leads to a bias in the reflectivity over increasing ranges from the radar. Whereas, in the liquid phase attenuation is well known and can be corrected, in the melting layer it remains poorly known and estimations in the literature sometimes vary over two orders of magnitude (Wolfensberger et al. 2016).

An additional phenomenon is attenuation due to the formation of a water film on the radome when it rains at the radar site, the so-called radome attenuation, known to be severe at X-band (Frasier et al. 2013; Delrieu et al. 2022). We consider both on-site and along path attenuation with the following forulation.

$$\begin{aligned} AF(r) &= AF(r_0)\, AF(r_0, r) \\ &= AF(r_0)\, exp(-0.46 \int_{r_0}^{r} A(s)\, ds.) \end{aligned} \tag{1.36}$$

or equivalently, two-way path integrated attenuation (PIA [dB]) is formulated as:

$$\begin{aligned} PIA(r) &= PIA(r_0) + PIA(r_0, r) \\ &= PIA_0 + 2 \int_{0}^{r} A(s) ds \end{aligned} \tag{1.37}$$

where,
A: Specific attenuation [$dB\, km^{-1}$]
r_0: is the range where the radar measurement starts to be exploitable.

The path integrated attenuation (PIA) is related to the attenuation factor through:

$$PIA = -10 log(AF) \tag{1.38}$$

$$\begin{aligned} AF(r_0, r) &= 10^{-\frac{PIA}{10}} \\ &= exp(-0.46 \int_{r_0}^{r} A(s) ds \end{aligned} \tag{1.39}$$

PIA_0[dB] is called on-site attenuation when it accounts for both the radome attenuation and the along path attenuation in the $[0, r_0]$ range.

The difference between the attenuation of the horizontal signal (A_h) and vertical (A_v) is called differential attenuation (A_{dr}).

1.4.7 Estimation of rainfall from the radar measurables

Conventional

The value of radar QPE is computed through a nonlinear empirical relationship between radar reflectivity (Z) and precipitation rate (R),

$$Z = aR^b \tag{1.40}$$

where a and b are two parameters to be determined.

A simple R(Z) relationship can be obtained statistically over a climatic timescale and then applied to the quantitative estimate of precipitation. The coefficients a and b vary significantly on different regions and precipitation regimes, and they are significantly affected by the characteristics of raindrop-sized spectra. Therefore, the parameters a and b in the R(Z) relationship are affected by synoptic weather situations, the phase of hydrometeors, geography, and so on, and thus vary with time and space. Therefore, a fixed R(Z) relationship may not be accurate for a rainfall event with different intensities.

Marshall-Palmer relationship is one of the most commonly used R(Z) formulation. The R(Z) relationship developed by Marshall and Palmer 1948 is consistent with an exponential drop-size distribution.

$$Z = 200R^{1.6} \tag{1.41}$$

where,
Z [mm6 m-3] is the reflectivity factor
R [mm h-1] is the rainfall rate.

Polarimetic QPE

The relationship between the radar observables, reflectivity $Z[dBZ]$, differential reflectivity (Z_{dr}), specific attenuation $A[dB\,km^{-1}]$, specific differential phase shift (K_{dp}) and variable of interest in QPE, rainfall intensity $R[mm\,h^{-1}]$ are of interest. Based on many trials in the literature, power-law type R(Z,Z_{dr}), $R(K_{dp})$, and R(A) relationships are defined.

One example can be R(A) relationship:

$$R = a_{RA}A^{b_{RA}} \tag{1.42}$$

This chapter introduces the basic concepts of radar meteorology and the formulation of different radar observables. We will delve into to concepts of melting layer, microphysics of a precipitating volume, attenuation correction and QPE in the next sections.

Chapter 2

The RadAlp Experiment

2.1 Introduction

The RadAlp experiment aims at developing advanced methods for rainfall and snowfall estimation using weather radar remote sensing techniques in high mountain regions for improved water resource assessment and hydrological risk mitigation. A unique observation system has been deployed since 2016 in the Grenoble region of France. It is composed of an X-band radar operated by Météo-France on top of the Moucherotte mountain (1901 m a.s.l.; hereinafter MOUC radar). In the Grenoble valley (220 m a.s.l.), IGE operates a research X-band radar called XPORT and in situ sensors (weather station, raingauge and disdrometer). This unique setup of two radar systems just 11 km apart with an altitudinal gradient of 1700 m, should enable us to deal with the radar positioning dilemma and issues associated with the choice of the X-band operating frequency. Figure 2.1 shows the setup of the instrument cluster.

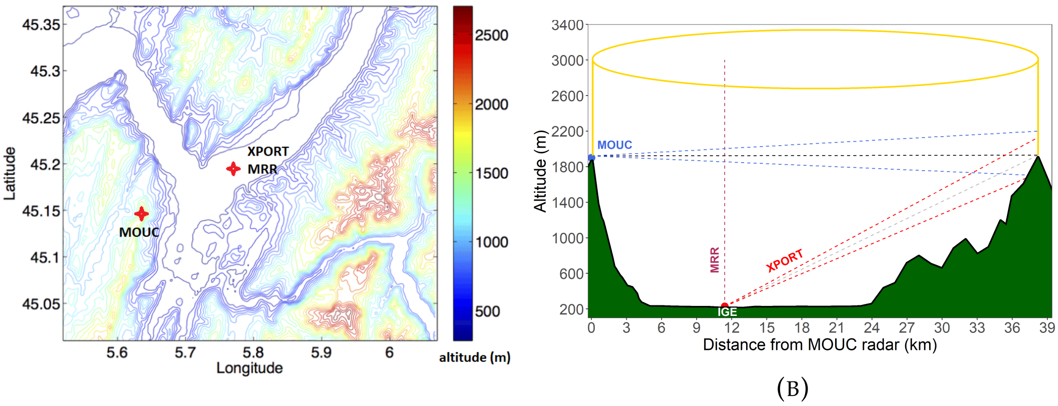

(A)

(B)

FIGURE 2.1: RadAlp Experiment: Instrument Setup. (a) The topographical map of Grenoble along with the positions of two radar systems. (b) A cross-section of the scan volume passing through XPORT and MOUC radars.

In this chapter, we list all the instruments available in the RadAlp setup and look into their characteristics in Section 2.2.1. The relevant dataset utilized from the available instruments is discussed in Section 2.2.2. The scientific objective of the RadAlp experiment is presented in 2.3, followed by the scientific objectives of the PhD in Section 2.4.

2.2 Instruments and dataset

2.2.1 Instruments

The IGE experimental site includes the following devices:

(i) IGE XPORT research radar (Koffi et al. 2014): X-band, dual polarized, volumetric scanning strategy, Table 2.1

(ii) Micro rain radar (MRR): K-Band, FMCW (Löffler-Mang et al. 1999), Table 2.2

(iii) Disdrometer (DSD)

(iv) Meteorological station (MTO) including pressure, temperature, humidity, wind and rainfall intensity measurements

Meteo France operates an X-band, dual polarized, volume scanning radar at the top of Mt Moucherotte. Table 2.1 shows the characteristics of two X-band radars (XPORT, MOUC), and Table 2.2 shows the characteristics of K-band micro rain radar (MRR). Apart from the instrument clusters at IGE, 7 additional raingauges and 2 disdrometers were installed in 2019 over a transect XPORT radar and La Croix de Chamrousse at different altitudes for QPE validation proposes.

TABLE 2.1: Characteristics of XPORT and MOUC radars

Parameter	**units**	**XPORT radar**	**MOUC radar**
Longitude	decimal degree	5.762327	5.639237
Latitude	decimal degree	45.194150	45.147736
Altitude (ground)	m asl	213	1901
Altitude (feedhorn)	m asl	228	1917
Frequency	GHz	9.400	9.420
Antenna diameter	m	1.8	1.8
$3 - dB$ beamwidth	°	1.37	1.28
Antenna gain	dB	42	42
Radome	[-]	no	yes
Peak power (each polarization)	kW	25	30
Radial bin size	m	33	240
Receiver dynamic range	dB	>90	>90
Minimum detectable signal	dBm	-112	-114
Volume scanning period	min	∼6	5
Volume Scanning Protocol (PPI elevation angles)	°	3.5, 7.5, 15, 25, 45, 90	0, 0.6, 1.2, 2, 3, 4, 8, 14
Measured parameters	$Z_h, Z_v, Z_{dr}, \rho_{HV}, \Phi_{dp}, v_r$		

TABLE 2.2: Characteristics of MRR-2 radar

Parameter	**Units**	**Value**
Frequency	GHz	24
Radar type		FMCW
Transmit power	W	0.05
Receiver		Single
Power consumption	W	25
No. of gates		31
Range resolution	m	10 -200
Range resolution in this study	m	100
Resulting measuring range	m	3000
Antenna Diameter	m	0.6
Beamwidth (2-way, 6dB)	degree	1.5
No. of spectral bins		64
Spectral resolution	ms^{-1}	0.19

FMCW stands for frequency modulated continuous wave i.e system transmits continuous wave at a certain frequency.

2.2.2 Dataset

MTO station

The IGE weather station provides continuous surface temperature and rainfall accumulation at 10 minute intervals. The database has continuous data available from 2014 till date. The rainfall data is used to identify the significant rainfall events for further analysis in the study and to calibrate remote sensing equipment. This dataset is used in the analysis of the melting layer in Chapter 3.

AROME model

AROME is a non-hydrostatic numerical weather prediction (NWP) model built and run by Meteo-France.
- used mainly for the operation of XPORT radar on alert.
- contains information on vertical profiles of different meteorological indicators of the atmosphere
- $O°C$ isotherm altitudes available once a day, used in chapter 3
- although very informative, the spatial resolution is not good enough (2.5 km*2.5km) to capture the variability in precipitation fields

XPORT radar

XPORT is a research radar, maintained and operated by IGE. It is operational in Grenoble valley since 2016. The radar observables provided by XPORT are horizontal and vertical reflectivity (Z_h and Z_v), differential reflectivity(Z_{dr}), co-polar cross-correlation coefficient (ρ_{HV}) and total differential phase shift Φ_{dp}. Originally the volume scanning time of the XPORT radar was 6 minutes. The scanning protocol was changed in Sept 2020 to match MOUC radar time resolution of 5 minutes. With the beamwidth of 1.37° and radial bin size of 33 m, XPORT provides high-resolution observation. Beam blockage by surrounding mountains restricts the use of XPORT data; elevation angle $\geq 15°$ are mostly clutter-free. The output is in the NC file format. 25° elevation angle PPI scans are used in Chapter 3 to identify and characterize the melting layer in winter stratiform events above Grenoble.

MRR radar

The vertically pointing K-band micro rain radar is also maintained and operated by the IGE. It is a continuous scanning radar. Radar observables (reflectivity, Doppler spectra and fall velocity) are averaged and recorded every 1 minute. There are only 31 range bins available, which forces us to make a trade-off between range and spatial resolution. We operate it at 100 m bin size, i.e. detection range of 3100 m. It is taken away for different summer campaigns, so MRR data on some events are missing. As reflectivity in K-band is heavily attenuated, Doppler spectra and fall velocities are the main variables of interest. Due to low density of dry snowflakes, the velocity data can be folded in snow due updrafts, a MK12 dealiasing algorithm (Maahn and Kollias 2012) is applied to raw data; it produces the NC type files. It is used to identify and characterize ML in absence of XPORT data, i.e. when the XPORT radar is taken to the field is down for maintenance.

MOUC radar

Polarimetric volume scanning X-band operational radar connected to the French national radar network (ARAMIS) and operated by Météo France. It has time resolution of 5 minutes, beam width of 1.28° at 3 dB, and range bins of 240 m. The 0° elevation angle PPI scan from MOUC radar is the main dataset from Chapter 4 on-wards.

Disdrometer (PARSIVEL 2)

Disdrometer provides the drop size distribution at ground level. There are 4 disdrometers in the RadAlp setup, at IGE, GREENER and 2 newly installed on the XPORT Chamrousse transect. Hydrometeor classification scheme are available for disdrometers at IGE and GREENER. The raw DSD measurements have a time resolution of 1 min. They are binned into 32 diameter classes with increasing sizes from 0.125 mm up to 6 mm. The volumetric concentration spectra as well as the DSD parameters are computed with a 5-min resolution (matching the time resolution of MOUC). The data is processed using CANTMAT version 1.2 (based on T-matrix formulation (Mishchenko et al. 2004)) to calculate DSD moments related to polarimetric radar observables / variables.

2.3 Scientific Objectives of RadAlp experiment

Despite recent development and advancement in active/passive precipitation observation and measurement techniques, QPE over complex terrain still remains a challenging topic. The RadAlp experiment aims to contribute toward the understanding of the precipitation processes in the French Alps and their radar signatures. While the X-band radar provides the necessary resolution to quantify fine-scale processes, attenuation remains the major limitation on radar QPE applications. The EM propagation in the melting layer of precipitation is still poorly understood; ML causes significant attenuation at X-band.

The main goals of the RadAlp experiment are:

- Better cope with the altitude dilemma:
  To quantify the dilemma of the altitude positioning for the Mont Moucherotte radar (MOUC radar hereafter), Figure 2.2 displays the altitudes and vertical extents of the ML as a function of the cumulative rain amounts in the Grenoble valley, for all the precipitation events surpassing a cumulative amount of 5 mm during the years 2016 to 2017. For this preliminary study, the ML top altitudes were approximated by the 0°C isotherm altitudes predicted by the Météo-France Numerical Weather Prediction Model (NWP) model *AROME* at 12:00 UTC. The ML widths were derived from the statistics presented hereinafter (chapter 3) and the rain total amounts were derived from raingauge measurements made at IGE, down in the Grenoble valley. The ML altitude intervals are coloured as a function of their position with respect to the detection layer of the MOUC radar at 0°-elevation angle, up to a range of 20 km (above: red; within: blue; below: green). From this analysis, one can keep in mind that for a rainfall threshold of 5 mm/day, the ML is below (within, resp.) the MOUC detection domain for 26.8 % (36.1 % respectively) of the cases, i.e. a total of about 63% of problematic cases in terms of possible influence of the vertical structure of precipitation on QPE. Interestingly, these figures do not vary too much as a function of the rain threshold, e.g. for a threshold of 20 mm/day, we observe 26.9% (34.9% resp.) of green (blue respectively) cases, i.e. a total 61.5% of potentially problematic cases.

- Better cope with attenuation at X-band frequency Delrieu et al. (1997), Yu et al. (2018), Delrieu et al. (2020), and Delrieu et al. (2022)

- Improve the QPE in high mountain

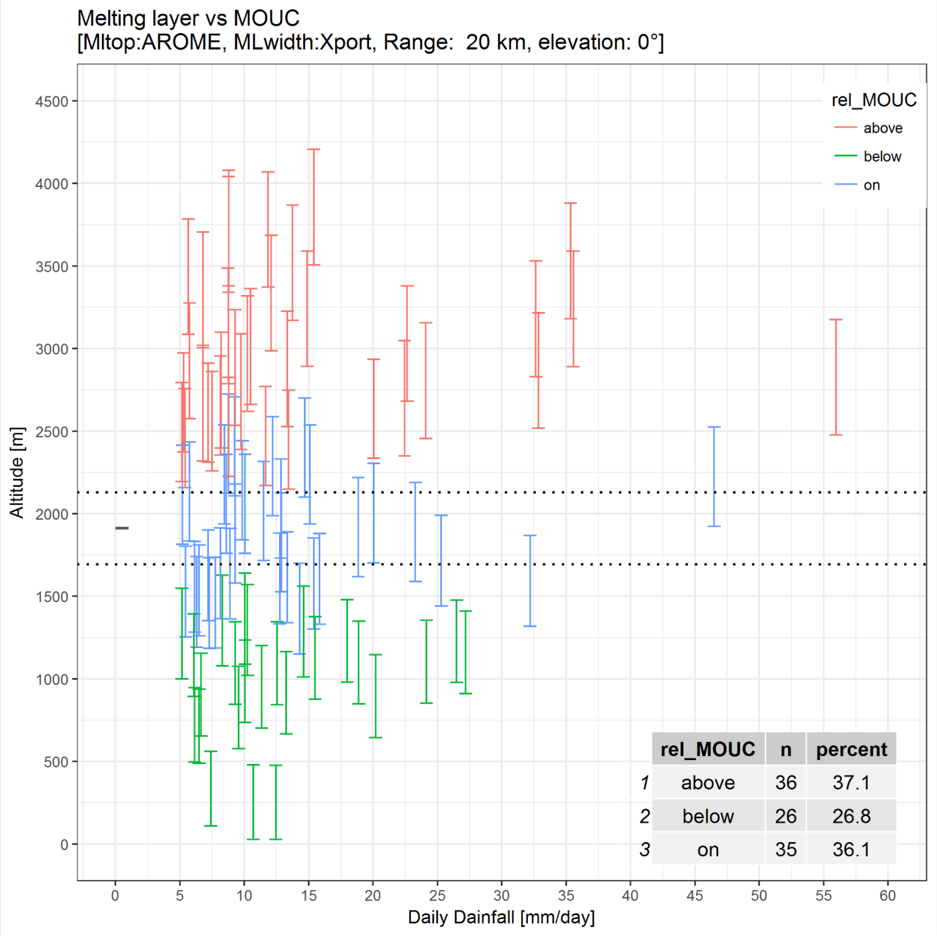

	rel_MOUC	n	percent
1	above	36	37.1
2	below	26	26.8
3	on	35	36.1

FIGURE 2.2: Altitude of ML wrt PPI-0° beam of MOUC radar (1913 m asl). Horizontal dotted black lines show the extent of 0° elevation angle beam at the range of 20 km. All the rain events in 2016 and 2017 are considered. ML top is given by the NWP-AROME.

2.4 Scientific Objectives of the PhD

This manuscript focuses on the melting layer of precipitation. The valley-based radars are used to identify and characterize the ML and mountain top radar observes the propagation effects at stages of ML. For this purpose, we consider the quasi-vertical profiles (QVP) of polarimetric variables (Ryzhkov et al. 2016) recorded with the XPORT radar and vertical profiles of Doppler spectra recorded with a co-located vertically pointing K-Band radar. We will assume attenuation and beam broadening effects to be of limited importance for such close-range / high-elevation angle measurements in predominantly stratiform precipitation with low intensity. The attenuation problem, more precisely the relationship between the total differential phase and path-integrated attenuation in convective rainfall and in the melting layer is formulated in Delrieu et al. 2020.

- Study and characterize spatio-temporal variation and climatology of Melting layer in the stratiform events, most of which occur on cold months i.e. ML is closer to / lower than highest peaks. The valley based XPORT radar is capable of high resolution observations. The study of Quasi-vertical profiles of rain using XPORT helps to understand the micro-physics of snow-melt and local variability on melting layer. The automated ML detection algorithm, applied on XPORT and MRR, helps to identify the events / instances when ML are below or at 0° elevation beam of the operational MOUC radar. Chapter 3 helps to better understand the ML (radar signature and processes).

- Study of Φ_{dp} vs PIA (MRT): Φ_{dp} is very noisy so it was not used in the past studies (at IGE). First goal is to have a robust filtering algorithm, so that this polarimetric variable can be exploited in future studies, specially related to attenuation correction. Second goal is to develop polarimetric method to enable backward attenuation correction algorithm (more stable), by exploiting the relationships between A-K_{dp}. (Chapter 4-6)

- Formulation and Optimization of attenuation correction algorithms: to have robust attenuation correction algorithm based on polarimetry to aid in reliable QPE estimates. (chapter 7)

Chapter 3

Melting Layer of Precipitation

3.1 Introduction

In midlatitude rainfall is mostly initiated through the ice formation process followed by melting, and it falls as rain. The ice particles fall towards the Earth, as they cross the 0° C temperature level they absorb the latent heat of fusion from the atmosphere and melt. The cooling of the atmosphere due to melting particles in a moderate stratiform precipitation can produce isothermal layers (Wexler et al. 1954; Willis and Heymsfield 1989). The formation of isothermal layers can lead to a separation of the dynamics above and below the melting layer and to the formation of a phase transition layer in between. The layer of atmosphere where hydrometeors go through phase transition is a region of discontinuity of the radar measurement properties (Szyrmer and Zawadzki 1999). Often in stratiform conditions, when the transition takes place at well defined height, it appears as a layer of enhanced reflectivity, aka "bright-band", to a centimeter wavelength radar. The primary cause of the enhancement is a rapid increase in the dielectric constant of falling hydrometeors at the top of melting layer followed by an increase in the fall velocity of the melting hydrometeors towards the end of melting process (Fabry and Zawadzki 1995).

In radar QPE, melting layer has been considered a source of errors in the ground level precipitation estimation. The effect of melting particles on EM wave propagation, especially on the signal attenuation, is substantial for cm and mm wave-length radars (C-, X- and K-band). The advancement in dual-polarimetric capabilities of weather radars provide new tools to understand and quantify the effects of melting layer in the EM wave propagation. ML has complex physical phenomenon involving the coupling of particle melting with the dynamical and thermodynamical processes. We still do not fully understand the physics of ML. ML properties are affected by ambient environment such as relative humidity (Willis and Heymsfield 1989), snow microphysics above the ML such as aggregation and riming (Fabry and

Zawadzki 1995; Zawadzki et al. 2005). The thickness of ML depends on the partical size (brightband intensity), particle fall velocity (density), precipitation rate (intensity) and snow-microphysics like riming and aggregation (Fabry and Zawadzki 1995; Wolfensberger et al. 2016).

The RadAlp experiment, uses the valley based radar systems to scan the vertical structure of precipitation above Grenoble. QVP from PPI 25° elevation scan of XPORT and the vertical pointing MRR radar provide information on the structure and characteristics of the ML in winter stratiform events. XPORT provides dual-polarimetric insight into the ML from below, and the MRR uses its Doppler capabilities to track the change in hydrometeor reflectivity and fall velocity. A ML identification algorithm based on inflection points of the enhancement or depreciation within the ML of different polarimetric XPORT observations has been developed. A similar algorithm for MRR has been developed as well. The radar observables are then linked to the microphysical processes within and above ML with an extensive literature review. Different characteristics defining the ML are recorded from the long-term observations.

3.2 Datasets and Methods

The XPORT radar started recording high-resolution volumetric scan data of the most significant rain events in 2016. Its operating protocol was made of 5 PPI scans at elevation angles of 3.5, 7.5, 15, 25 and 45°, during the period considered in the present study. It systematically records five radar parameters at the radial resolution of 30 m and angular resolution of 0.5°. The recorded parameters are: horizontal reflectivity (Z_h), vertical reflectivity (Z_v), differential reflectivity (Z_{dr}), cross-polar correlation coefficient (ρ_{hv}) and cumulative differential phase (Φ_{dp}) (Bringi and Chandrasekar 2001). In this study, we consider 42 significant rain events between November 2016 and January 2018 with total rain accumulations greater than 5 mm at IGE weather station. Due to the presence of ground clutter and beam blockages for the three lowest elevation angles and technical difficulties in operating the radar at 45° for a considerable period of time, we will use hereinafter only the 25° elevation angle measurements, which have a 6-min revisit time, the PPI itself lasting about 1 min. From the measurements of the recorded parameters, we produced quasi-vertical profiles (QVPs) by averaging measurements over 360° azimuth and then projecting the results to the vertical (Ryzhkov et al. 2016). The ML identification algorithm, to be described below, performed poorly in case of large spatial variability of the 25° elevation angle measurements, notably when a rainy system was entering or leaving the valley. To limit the impact of such poor identifications on the ML statistical analyses, we used PPI scans of ρ_{hv} to determine visually time steps with homogeneous precipitation in the various sectors of the XPORT detection domain. This sorting resulted in a total of 980 XPORT vertical profiles, i.e. to about 98 hr of measurements. Monthly distribution of these vertical profiles is shown in Table 3.1. Note that the summer events are under-represented in this sample due to their convective nature, leading to strong spatial variability and subsequently poor identifications with the ML detection algorithm.

TABLE 3.1: Monthly distribution of ML profiles

month	**# of profiles**	**alt peak ρ_{hv}**
January	185	1564
February	6	1486
March	112	1303
April	119	1470
May	75	1902
September	41	2290
October	11	2715
November	224	1957
December	207	1584

The MRR allows the continuous acquisition of the vertical profiles of Doppler Spectra of apparent fall velocities of the hydrometeors with a radial resolution of 100 m and a temporal resolution of 1 min. We applied the algorithm developed by Maahn and Kollias (Maahn and Kollias 2012) which takes the unprocessed MRR data and apply an unfolding routine (called MK12 hereinafter) to reduce the error in Doppler spectra and fall velocity, especially in the solid phase precipitation, with respect to the original algorithm by the MRR manufacturer (METEK). The MK12 pre-processing routine results in full Doppler spectra of apparent vertical velocities of falling hydrometeors over a velocity range of 0-12 m/s and with vertical resolution of 100 m from which we deduced the vertical profiles of the average velocity (W) and standard deviation (SW, for spectral width). Note that the MRR radar was deployed in other field campaigns in summer, so MRR data is actually available for only 27 out of 42 precipitation events being studied.

3.3 Automated Melting Layer Detection Algorithm

For its importance in micro-physical processes leading to precipitation phase change and for coping with the associated artefacts (bright band, attenuation) that affect radar QPE, the characterization of the ML has received a long-standing interest in radar meteorology (Stewart et al. 1984; Fabry and Zawadzki 1995) and radar hydrology (Andrieu and Creutin 1995; Hardaker et al. 1995) communities.

Polarimetry offers unprecedented means for observing distinct ML radar signatures (Fabry and Zawadzki 1995; Brandes and Ikeda 2004): increase in reflectivity (Z_h, Z_v), differential reflectivity (Z_{dr}) and differential propagation phase (Φ_{dp}), decrease in cross-correlation coefficient (ρ_{hv}) within the ML. Vertical profiles of Doppler velocity spectra also bring valuable information on the hydrometeor falling velocities in stratiform precipitation (Zawadzki et al. 2005; Baldini and Gorgucci 2006). A number of automated ML detection algorithms have been proposed to deal with radar data collected in various configurations: vertically pointing measurements (Rico-Ramirez and Cluckie 2007), range-height indicators (Wolfensberger et al. 2016), PPIs at low-elevation angles (Hardaker et al. 1995; Giangrande et al. 2008), the latter being obviously the most unfavourable (small incidence angles on vertical layers, beam broadening effects) but also the common situation for QPE from the operational weather radars. In our context, we work with polarimetric QVPs (Ryzhkov et al. 2016) derived from the 25°-PPI XPORT radar measurements and with the vertical profiles of Doppler spectra derived from the MRR data. We hope attenuation and non-uniform beam filling to be of limited importance for such high-elevation angle measurements in predominantly stratiform precipitation with low intensity.

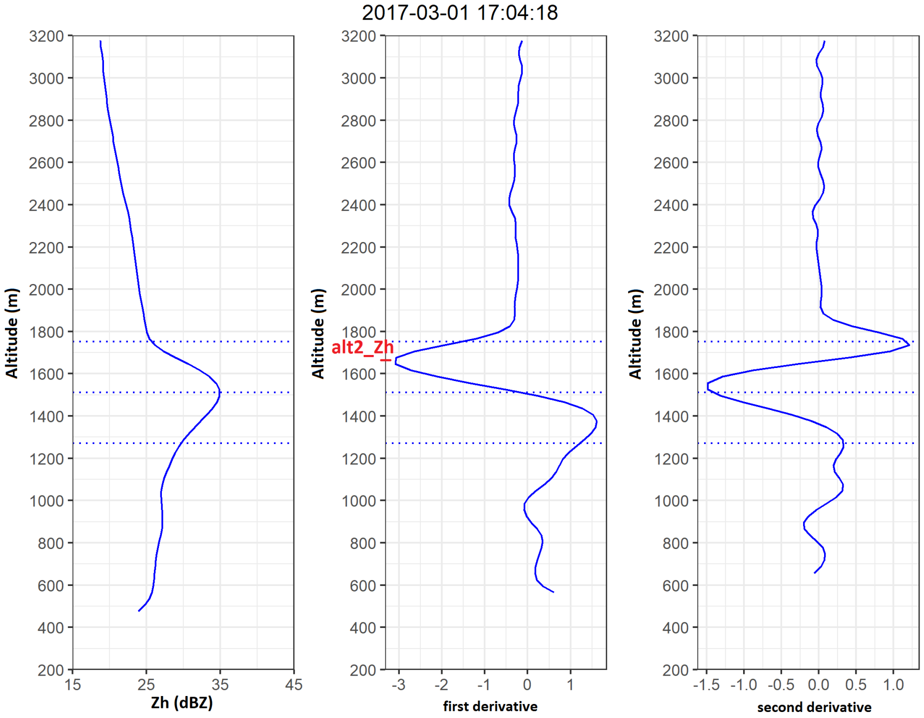

FIGURE 3.1: Example of automatic detection for a QVP of reflectivity in the horizontal polarization. The quasi-vertical profiles of Z_h, its 1st derivative and 2nd derivative are shown in left, middle and right subfigures respectively. The dotted lines show the estimated altitudes of “bright-band” top, peak and bottom.

Hereinafter, we denote upper and lower breakpoints of a given ML signature in QVP as “top" and "bottom" (“bot” in short), distinguishing the value and altitude coordinates of the point, e.g. Z_h top altitude, Z_h top value. Maxima/minima of the QVP is denoted as "peak" (e.g. Z_h peak altitude, Z_h peak value). For the sake of conciseness, a number of pseudo-variables are used in Tables and Figures; their description is given in Appendix A.1.

The identification algorithm for Z_h works as:

a. Compute quasi-vertical profile of Z_h, and its first and second derivatives.

b. Find the altitude with minimum first derivative of Z_h –> *alt2_Zh*

c. Search for altitude and value of Z_h peak (maxima with first derivative close to zero) up to 500m below alt2_Zh –> Z_h *peak altitude* and Z_h *peak value*

d. Search for Z_h *top altitude* and Z_h *top value* as max(second derivative of Z_h) up to 300 m above alt2_Zh

e. Search for Z_h *bot altitude* and Z_h *bot value* as max(second derivative of Z_h) up to 500 m below alt2_Zh

The same algorithm works for Z_v as well. Similarly for Z_{dr}, we search for Z_{dr} peak values and altitudes up to 800 m below alt2_Zh as max(Z_{dr}) with first derivative close to zero. We look for top and bottom of enhancement in Z_{dr} profile up to 500 m above and below Z_{dr}.alt.peak, as max(second derivative of Z_{dr}). In case of ρ_{hv}, we search for ρ_{hv} peak up to 800 m below alt2_Zh as min(ρ_{hv}) with first derivative close to zero. Then we search for ρ_{hv} top altitude as the first altitude with ρ_{hv} < max(ρ_{hv}) - 0.02 above Z_h peak. The ρ_{hv} bot altitude is determined by symmetry. Using a single reference altitude, alt2_Zh, for identification of ML in all the radar observables (Z_h, Z_v, Z_{dr}, ρ_{hv}) helps to reduce the errors in identification due to noise in different profiles in a given timestep, provided that the bright band in Z_h is well observed. The time series of alt2_Zh is also used to limit the allowed jumps in reference altitudes in between two successive timesteps. Furthermore, in vertical profile of MRR derived average fall velocity (W), we look for "W top" (and "W bot") as the maxima (and the minima) of second derivative of vertical profile of W, 500 m above and below ρ_{hv} peak altitude.

3.4 Microphysics of the ML and the vertical profiles of radar observables

In this section, we aim to perform a detailed analysis of ML with the help of QVPs of Z_h, Z_v, Z_{dr}, ρ_{hv} and vertical profile of W, their relationship with each other, definition of melting layer boundaries and associated micro-physical processes. The QVPs of Φ_{dp} are not considered here since they were found to be too noisy and hardly exploitable for a large majority of the considered events, as they have generally low precipitation intensities. The analysis of a single timestep (e.g. 2017-03-01 17:04:18 in Fig. 3.2) provides detailed insights into the vertical structure of rainfall and microphysical processes associated with the melting layer, especially the hydrometeors' evolution with time and/or height. A stratiform rain event with 9 mm of cumulative rainfall spread over 11 hours window is discussed here. At the given timestep, rainfall intensity and temperature at MTO station were 2 $mm\ h^{-1}$ and 7.8 °C respectively. Top of the brightband can be observed at 1770 m ASL, a bit below the 0°C isotherm at 1790 m estimated by the Météo-France AROME NWP model. The quasi vertical profiles of dual-polarimetric and vertical profiles of Doppler observations from XPORT (left) and MRR (right) radars are displayed in Fig. 3.2. Vertical profiles of XPORT are normalized between [0-1] to show the vertical profiles of Z_h, Z_{dr} and ρ_{hv} in a single plot.

$$Z_h, Z_v\text{: [15, 45] dBZ - -> [0, 1]}$$

$$Z_{dr}\text{: [-3, 3] dB - -> [0, 1]}$$
$$\rho_{hv}\text{: [0.65, 1] - -> [0, 1]}$$

As falling ice particles move from $-5°$ to $0°C$, they grow by aggregation, resulting in larger particles and in a reduction in the number of smaller particles (Heymsfield et al. 2002), this might be an explanation for the gradual decrease (upward) in reflectivity above the ML in Fig. 3.1 (left). When they pass through the $0°C$ isotherm, they receive latent heat of fusion from the atmosphere. Ice particles start to melt and become wet. The latent heat required cools the air, leading to a quasi-$0°C$ temperature layer. They continue to descend, encounter warmer air and melt completely, eventually collapsing to rain drops much smaller than original icy hydrometeors of same mass and higher fall velocities.

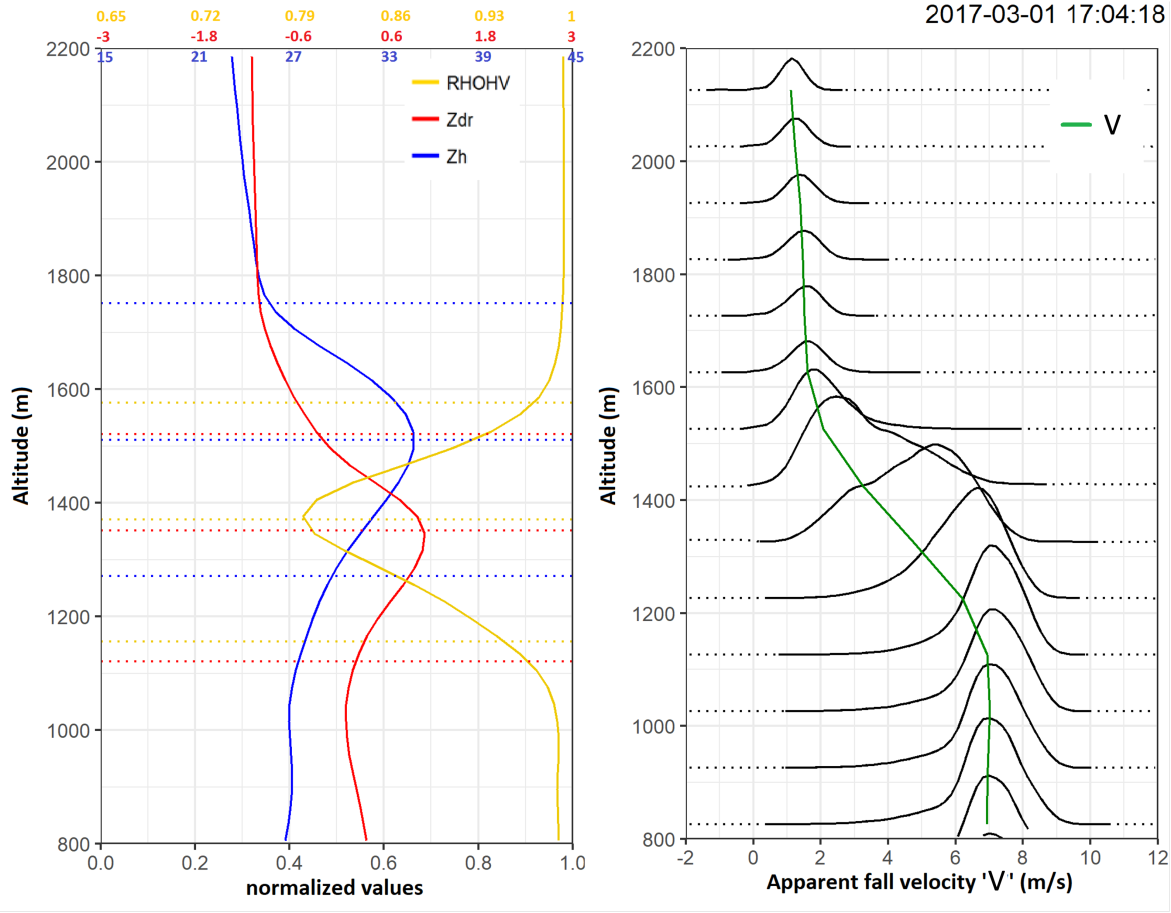

FIGURE 3.2: Representative vertical profiles. Normalized quasi-vertical profiles of XPORT observables (Z_h: *blue*, Z_{dr}: *red*, ρ_{hv}: *gold*) from PPI scan at 25° elevation angle, along with the ML identifications (dotted lines) are shown in the left. Vertically pointing K-band MRR produced Doppler spectra and average (V: *green*) of hydrometeors' apparent falling velocities are shown in the right. For the ease of reading, the unscaled and color-coded values of Z_h, Z_{dr} and ρ_{hv}, for normalized values of 0, 0.2, 0.4, 0.6, 0.8 and 1, are displayed on the top of the graph.

Textbooks (Pruppacher and Klett 2010) and articles based on in-situ observations (Knight 1979; Matsuo and Sasyo 1981; Fujiyoshi 1986), wind-tunnelling experiments (Mitra et al. 1990) and modelling studies (Russchenberg and Ligthart 1996; Leinonen and Lerber 2018) on snowflake melting processes establish that the melting of individual hydrometeor (a snowflake or an aggregate) occurs in several stages in an atmospheric column, that we may summarize as follows:

- In the first stage, melting starts at the tips of ice branches on the entire periphery, but mainly at the bottom of the snowflake.
- In the second stage, aerodynamic drag helps the meltwater to flow and surface tension draws meltwater preferentially into concave regions, e.g. from periphery to the linkages of the snow crystals comprising of aggregates, minimizing the capillary forces and surface tension effects. The hydrometeor is not covered by meltwater in this stage, as the main ice-frame is still intact and the icy hydrometeor has ragged surface.
- As these enclaves fill up and the edges erode due to melting, in the third stage, liquid water flows out of the filled concave regions, merges with other nearby liquid bodies, and melt water seeps into branches inside the snowflakes breaking the ice lattices. Surface tension stabilizes the hydrometeor into new equilibrium shapes and consequently the crystal mesh changes from one with many small and sharp protrusions to one with a few smoother and larger protrusions.
- Towards the end of melting process, in the fourth stage, the weak connections of ice separating drops/ liquid water bodies become sufficiently thin to fracture under aerodynamic forces or simply melt away relatively quickly. The particle assumes a spherical shape, initially around an ice core and eventually forming a water drop. Through the melting process, hydrometeors undergo change in shape and ice/ water content leading to smaller particles with higher mass density, which results in increase of fall velocities as they also experience less air resistance.

Melting of a distribution of hydrometeors in a stratiform rainfall produces distinct signatures of radar observables on ground-based Doppler and polarimetric radars (Fig. 3.2). Z_h and Z_v are sensitive to the phase (liquid, solid), concentration and size distribution of hydrometeors. Z_{dr} is a proxy for their shape anisotropy and variation of particle orientation. ρ_{hv} is a measure of coherence of the observations made in the horizontal and vertical polarisations, and as such, a good indicator of precipitation homogeneity within the resolution volume. One may note that the polarization planes are slanted by the elevation angle, at least the horizontal one.

- With aggregation as the dominant process, from 1000 m above the ML, there is an increase in radar **reflectivity (Z_h, Z_v)** of 6 to 7 dBZ, as observed in Figs 3.1 and 3.2, with little dependence on precipitation intensity, consistent with (Fabry and Zawadzki 1995). Small snowflakes melt faster than the big ones, causing some particles to fall faster than others and thus increasing probability of aggregation and coalescence. In an atmospheric column with steady precipitation, assuming stationarity, this leads to an increase in the particle size (in case of aggregation) or an increase in number density (if no aggregation) at a layer lower than the initial level (assuming larger hydrometeors are denser and falling faster initially). This leads to steady increase in Z_h below initial 0°C isotherm. When most big particles are at end of 3^{rd} stage of melting, i.e. with thin shell of meltwater with ice-core, they essentially have size of the ice-particle and di-electric constant of water. We would like to remind that the dielectric constant of water is 5 times that of ice, but Zh and Zv are computed with $|K_w|^2$ for all layers. These few large highly reflective particles, resembling big raindrops to a radar, explain the maximum of the reflectivity profile; around 10 dBZ bigger than the value at ML top for the example of Figs 3.1 and 3.2. The bright band peak is said to occur at a level where the particles have attained the high scattering property of water drops but have not yet attained their velocity (Atlas et al. 1953). As these big particles start to melt and gain higher falling velocities, the number concentration at the given altitude of the atmospheric column decreases and the size of the dominant particles starts to decrease. This causes a gradual decrease in reflectivity in the lower portion of ML (below the altitude of Z_h peak); reflectivity remains more or less constant below the ML. It might change with evaporation (decrease) and orographic enhancement (increase).

- **Differential reflectivity (Z_{dr})** is positive for particles whose major axes aligns close to horizontal, zero for spherical particles / particles with random distribution of orientation, and negative for vertically oriented particles. Big rain drops tend to flatten and orient themselves with major axes close to horizontal. Pristine ice crystals have small axis ratio (horizontal to vertical) and high bulk density, and fall with their major axes close to horizontal i.e. high Z_{dr}. Aggregates have large axis ratio, low bulk density and low dielectric constant resulting in "effectively isotropic" shape, so low Z_{dr}($\sim$ 0.5 dBZ) (Herzegh and Jameson 1992; Brandes and Ikeda 2004). The vertical profile of Z_{dr} is slightly different from Z_h. Z_{dr} increases as well during melting, but the maximum develops at lower altitude than Z_h. A peak with positive value of Z_{dr} below Z_h peak indicates an oblate mean shape at that height, and the small values above and upper part of ML indicates isotropic mean shape while individual ice particles can be very irregular (Russchenberg and Ligthart 1996). As the particles smoothen due to faster melting of protrusions, Z_{dr} decreases on the upper part of melting layer, and just before the ice-structure crumbles in 4^{th} stage of melting Z_{dr} peaks rapidly, to 1 dB during this event. This suggests maximum anisotropy of hydrometeors occurs at lower altitude than maximum size. Surface tension during 4^{th} stage of melting (following collaspe of ice-structure) acts much quicker compared to other melting processes. As hydrometeors assume more spherical shape, Z_{dr} decreases quickly i.e. the quasi-vertical profile of Z_{dr} enhancement is non-symmetric. This decrease in Z_{dr} might also be a result of break-up of large melted aggregates (Kumjian 2013). Rain drops take more oblate shape, as they reach terminal velocity. It is noteworthy to remind that the elevation angle of 25° is used in this study, Z_{dr} measurements within the ML might be more pronounced at lower scanning angle.

- **Co-polar cross correlation coefficient** (ρ_{hv}) is sensitive to changes in shape, size, orientation and thermodynamic phase of hydrometeors between successive pulses. It might be sensitive to elevation angles of PPI scan in mixed-phased regions (Vivekanandan et al. 1993). Vertical profile of ρ_{hv} shows relatively high values ($\sim$ 0.99) above (in snow) and below (in rain) the ML with a sharp decrease in the lower part of ML. Some ML detection algorithms (like (Giangrande et al. 2008)) use $\rho_{hv} < 0.97$ as a threshold criterion for mixed phase of precipitation. Decorrelation occurs if the two orthogonal backscattered waves do not vary in unison, i.e. with the change in net effective backscattering properties at horizontal and vertical polarization in the resolution volume. The decrease in correlation is pronounced for wet, large and irregular hydrometeors (Zrnić et al. 1994), likely a consequence of a greater variety of shapes and axis ratios associated with partly melted particles and introduction of raindrops (Brandes and Ikeda 2004). ρ_{hv} minima occurs below the Z_h maxima and slightly above the Z_{dr} maxima (Fig. 3.2), where some large particles are asymmetric with ice-frame still intact while some have already crumbled under surface tension to become more spherical.

- Vertically pointing MRR provides vertical profile of hydrometeor's apparent **fall velocity spectra *(S(v))***. The Doppler spectrum $S(v)$ is the power-weighted distribution of radial velocities within the resolution volume, i.e. $S(v)$ represents the power returned to the radar by scatterers with radial velocity between v and $v + \Delta v$, as shown in equation 1.29. The average radial velocity (V) is the first moment of the normalized Doppler spectrum, and spectral width is the square root of normalized second moment. Spectral width is a measure of dispersion of velocities within the resolution volume. Unlike other radar observables, average fall velocity has a monotonously decreasing vertical profile (with increase in elevation) within the ML. Above ML, snow has average fall velocity of 1-2 m/s; presence of crystalline ice, super cooled water and air updrafts/downdrafts can affect the average fall velocity of snow. Towards the end of 3^{rd} stage of melting, hydrometeors smoothen causing decrease in aerodynamic drag and slight increase in fall velocity. During the 4^{th} stage of melting, as hydrometeor melt fraction increases, its density increases and it assumes more spherical shape (size decreases), which also aids to decrease aerodynamic drag and to increase fall velocity. As the largest hydrometeors melt completely and become spherical rain drops, the average fall velocity reaches a maximum. As the raindrops continue to fall, they might assume oblate shape resulting in a slight decrease of the fall velocity to reach the terminal velocity of 6-8 m/s. At low rainfall intensities raindrops are small and remain mostly spherical and this decrease might be negligible, like in Fig. 3.2. Some ML detection algorithms (like (Klaassen 1988)) use the altitude of maximum average velocity as the bottom of ML. At the altitude of Z_h peak, the average fall velocity is still close to fall velocity of snow. The Doppler velocity spectra is narrow above and below ML, centered at terminal velocity of snow and rain respectively. Within the melting layer, the spectral width broadens gradually with decrease in ρ_{hv}, reaches maximum value at altitude with minimum ρ_{hv}, and it contracts again with increase of ρ_{hv}.

3.5 Results

Here, we study the statistical properties of the melting layer based on the available dataset of 42 rain events. We will seek to understand the dependence of ML parameters on altitude of the $0°C$ isotherm, intensity of rainfall at ground and density of snow. Being a standard hypothesis of 1D ML models (Hardaker et al. 1995), 1 to 1 correspondence of snowflake above ML to raindrop below ML is a question of interest. The added value of Doppler and dual-polarimetric measurements with respect to reflectivity measurements for the analysis of melting layer is also a subject of interest in this study.

3.5.1 ML boundaries and vertical organization of the ML

Let us first consider the altitudinal dimension of ML characteristic points. Our experience with the ML detection algorithm indicates that ρ_{hv} peak is the most consistently identified signature, and we expect it to be in between altitudes of Z_h peak and Z_{dr} peak. Figure 3.3 shows the probability distribution functions (pdf) of different distances between radar signatures, i.e. top, peak and bottom of Z_h, Z_{dr} and ρ_{hv}, with respect to the ρ_{hv} peak altitude, computed over the entire dataset of 980 profiles; a number of statistics (mean, standard deviation and quantiles of these distributions) are listed in Table 3.2.

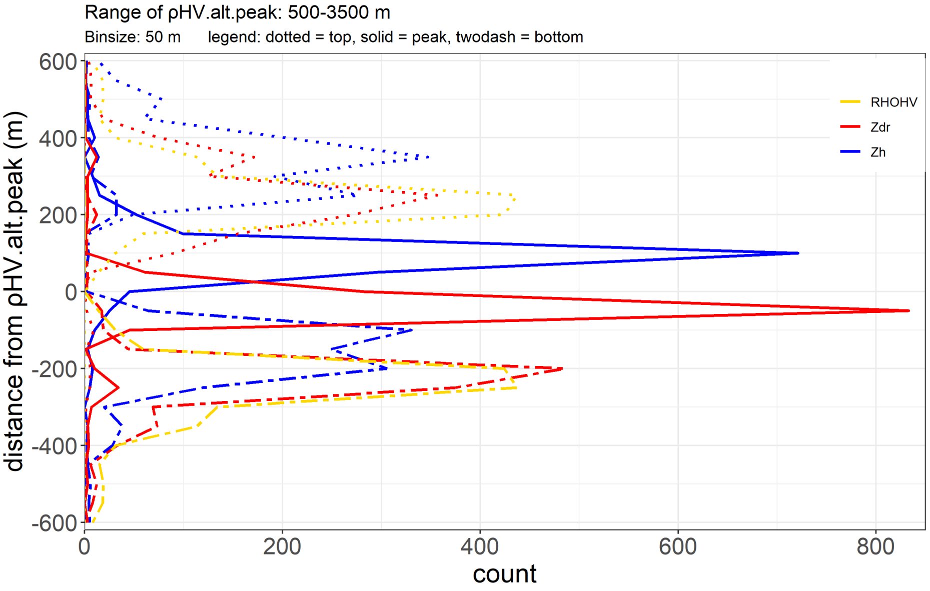

FIGURE 3.3: Pdfs of distances (binned with width of 50 m) of different radar signatures in ML with respect to ρ_{hv} peak altitude

We note that the pdfs of Z_h and Z_{dr} peak altitudes are quite narrow. The mean distance between ρ_{hv} peak and Z_{dr} peak is around 30 m, while the average distance between ρ_{hv} peak and Z_h peak is around 90 m. The distributions of the altitudes of the top and bottom are flatter compared to that of the peaks. The vertical profile of ρ_{hv} in ML is symmetric, by construction, with top and bottom at 225 m from the peak value. Z_h top and ρ_{hv} bottom are the altitudes furthest from ρ_{hv} peak. Study of ML microphysics in section 3.4 shows that Z_h is the first radar observation to change significantly when the particles are still in early stages of melting. So like Fabry and Zawadzki (1995) we assume that Z_h top coincides with 0°C isotherm. We also observe that ρ_{hv} bottom and max(W) occur at similar altitudes in Fig. 3.2, both of which signify the end of melting process. So, in this study we will refer Z_h*.alt.top* as **ML top** and ρ_{hv}.alt.bot as **ML bottom**. Hence, ***ML width*** = Z_h*.alt.top* - ρ_{hv}*.alt.bot*.

In our observation (Table 3.2), the mean ML width is 609 m; Q10 and Q90 of ML width are 450 m and 780 m respectively.

TABLE 3.2: Statistics of ML altitudes in terms of mean, standard deviation and quantiles

	units	mean	Std.Dev	Q10	Q25	Q50	Q75	Q90
Z_h.alt.top	[m]	2041	450	1411	1621	2071	2311	2671
Z_h.alt.t2p	[m]	265	80	180	210	240	300	360
Z_h.alt.p2b	[m]	268	81	180	210	240	300	360
Z_{dr}.alt.t2p	[m]	274	87	180	210	270	330	390
Z_{dr}.alt.p2b	[m]	208	57	150	180	180	240	270
ρ_{hv}.alt.t2p	[m]	254	76	180	210	240	270	330
ρ_{hv}.alt.p2b	[m]	254	76	180	210	240	270	330
Z_h.alt.peak - ρ_{hv}.alt.peak	[m]	90.2	66.1	30	60	90	120	150
ρ_{hv}.alt.peak - Z_{dr}.alt.peak	[m]	30	48	0	30	30	30	60
ML width	[m]	609	162	450	510	600	690	780

3.5.2 Statistics of ML characteristic values

Table 3.3 presents the statistics of the reflectivity and polarimetric values and Fig. 3.4 displays normalized pdfs of some of these variables. As a first guess, we considered the Marshal-Palmer relationship ($R = (Z_h\ bot\ /\ 200)^{1/1.6}$ with Z_h bot in $mm^6\ m^{-3}$) as an estimate of rainrate (R in $mm\ h^{-1}$) below the ML. Vsnow and Vrain are hydrometeors' apparent mean fall velocity in snow (60 m above ML top) and rain (100 m below ML bottom) respectively.

TABLE 3.3: Statistics of ML characteristic values

(see Appendix A.1 for the definitions of pseudo-variables)

	units	mean	Std.Dev	Q10	Q25	Q50	Q75	Q90
Z_h.val.bot	[dBZ]	24.19	4.64	18.07	20.85	24.59	27.38	29.89
Z_h.val.t2p	[dBZ]	8.97	1.80	6.70	7.87	9.13	10.19	11.15
Z_h.val.p2b	[dBZ]	6.37	1.69	4.14	5.49	6.56	7.38	8.13
Z_{dr}.val.peak	[dB]	0.63	0.61	-0.08	0.2	0.57	0.99	1.49
Z_{dr}.val.t2p	[dB]	1.24	0.41	0.82	0.99	1.18	1.4	1.8
Z_{dr}.val.p2b	[dB]	1.51	0.52	0.96	1.15	1.4	1.8	2.25
ρ_{hv}.val.peak	[-]	0.85	0.05	0.79	0.83	0.87	0.89	0.9
Rainrate	[mm/hr]	1.45	1.04	0.48	0.72	1.24	1.85	2.66
Vsnow	[m/s]	1.6	0.75	0.85	1.28	1.56	1.91	2.37
Vrain	[m/s]	5.92	1.2	4.46	5.24	6.01	6.73	7.23

Table 3.3 shows that the events considered in this study have a rather limited range of rainrate values, 0.48 $mm\ h^{-1}$ at 10% quantile, 2.66 $mm\ h^{-1}$ at 90% quantile and a maxima of 8.47 $mm\ h^{-1}$. This is mostly due to the difficulties in identifying ML during convective events, often associated with high rainfall rates, as they have high horizontal variability. Figure 3.4 shows that the variables of interest are generally monomodal with limited skewness. This is why various pdf quantiles are listed in Table 3.3. Both the altitude and value statistics (Tables 3.2 and 3.3) are in overall agreement with similar X-band radar observations (Wolfensberger et al. 2016) of ML made at Davos and Ardeche, except the mean ML width which is wider in our observations, possibly a result of different estimation technique between two studies.

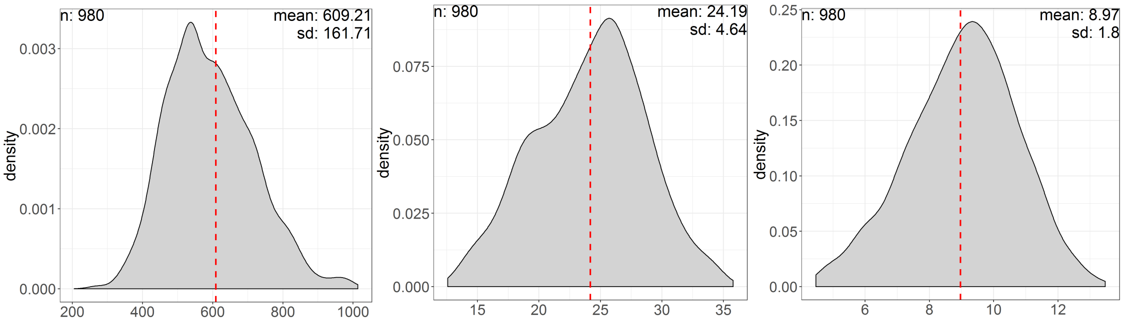

(A) ML width [m] (B) Z_h.val.bot [dBZ] (C) Z_h.val.t2p [dBZ]

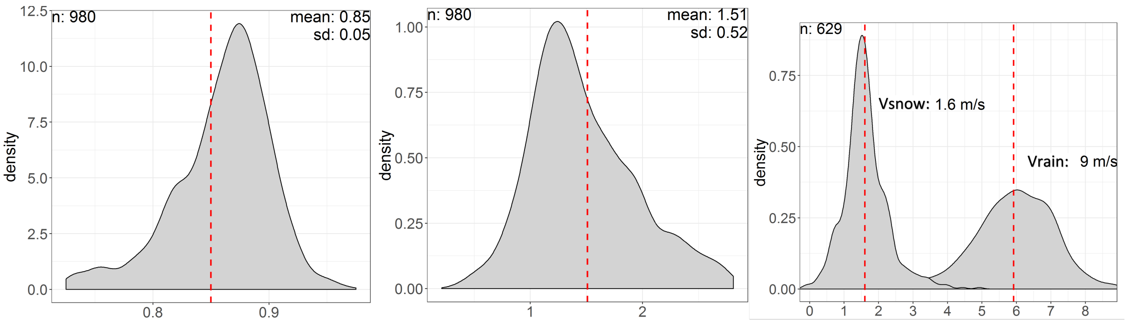

(D) ρ_{hv}.val.peak (E) Z_{dr}.val.p2b [dB] (F) Mean Fall velocities [m/s]

FIGURE 3.4: Pdf plots of some ML characteristic values; dotted red lines indicated the mean value. Limits of the plots are set at *mean* ± *2.5 * standard deviation*

The correlation matrix of the ML descriptors is shown in Fig. 3.5. Due to the limited skewness of their individual distributions and the likely non-linear relationships between pairs of them, we have computed the Spearman's rank correlation coefficient, more relevant for monotonic non-linear relationships than the classical Pearson's linear correlation coefficient. Z_h top, Z_h bot, Z_h peak and R show high correlation with each other. The correlation coefficient of 1 between Z bot and R results simply from the power-law transformation (deterministic and monotonic) applied. This high level of correlation is to be expected as the size and concentration of icy hydrometeors above ML are the common factors controlling these variables. Interestingly, the ρ_{hv} peak value correlates also significantly with Z_h top, Z_h bot, Z_h peak and R. We note that it correlates more with Z_h peak than with Z_h top or Z_h bot. This confirms that Z_h peak is more sensitive to (presence of) large particles than to the number concentration. In addition, we note that the Z_{dr} peak value is significantly correlated with ρ_{hv} peak value (which is also sensitive to particle orientation) and to a lesser extent to the reflectivity and rainrate descriptors. ML width correlates more with the reflectivity variables than with the polarimetric ones. Vsnow is essentially uncorrelated to all the other variables while Vrain is more correlated with the reflectivity and rainrate variables than with the polarimetric ones.

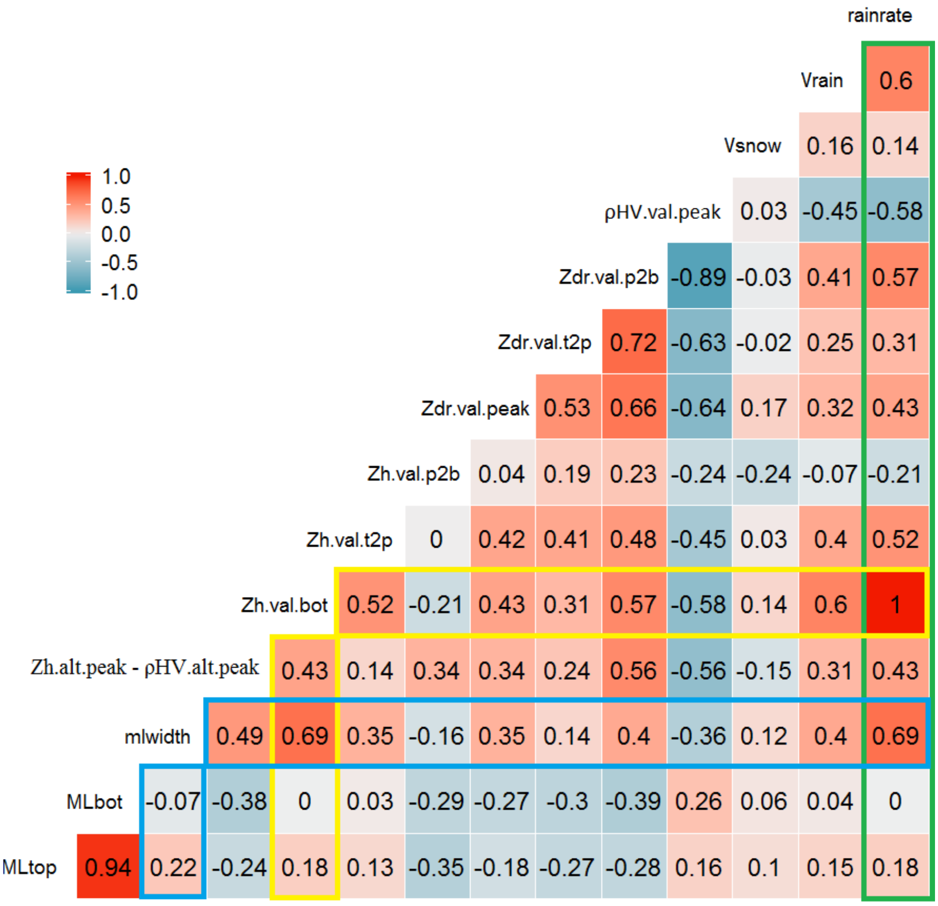

	MLbot	mlwidth	Zh.alt.peak - ρHV.alt.peak	Zh.val.bot	Zh.val.t2p	Zh.val.p2b	Zdr.val.peak	Zdr.val.t2p	Zdr.val.p2b	ρHV.val.peak	Vsnow	Vrain	rainrate
Vrain													0.6
Vsnow												0.16	0.14
ρHV.val.peak											0.03	-0.45	-0.58
Zdr.val.p2b										-0.89	-0.03	0.41	0.57
Zdr.val.t2p									0.72	-0.63	-0.02	0.25	0.31
Zdr.val.peak								0.53	0.66	-0.64	0.17	0.32	0.43
Zh.val.p2b							0.04	0.19	0.23	-0.24	-0.24	-0.07	-0.21
Zh.val.t2p						0	0.42	0.41	0.48	-0.45	0.03	0.4	0.52
Zh.val.bot					0.52	-0.21	0.43	0.31	0.57	-0.58	0.14	0.6	1
Zh.alt.peak - ρHV.alt.peak				0.43	0.14	0.34	0.34	0.24	0.56	-0.56	-0.15	0.31	0.43
mlwidth			0.49	0.69	0.35	-0.16	0.35	0.14	0.4	-0.36	0.12	0.4	0.69
MLbot		-0.07	-0.38	0	0.03	-0.29	-0.27	-0.3	-0.39	0.26	0.06	0.04	0
MLtop	0.94	0.22	-0.24	0.18	0.13	-0.35	-0.18	-0.27	-0.28	0.16	0.1	0.15	0.18

FIGURE 3.5: Spearman's Correlation Coefficient

3.5.3 Evolution of ML descriptors with rainfall intensity

During the events under study, rainfall in Grenoble valley has a slightly right skewed distribution with mean at 1.45 $mm\ h^{-1}$ and standard deviation of 1.04 $mm\ h^{-1}$. As noted previously Z_h top, Z_h bot and Z_h peak show high correlation with each other. Inspired by Fig 10 of (Fabry and Zawadzki 1995) we examine the relationships between Z_h bot and three descriptors of the reflectivity profile: Bright Band (BB) width (altitude difference between Z_h top and Z_h bot), Z_h top and Z_h peak in Fig. 3.6. As observed in (Fabry and Zawadzki 1995) the BB width increases slowly till the Z_h bot of 21 dBZ, beyond which the increase is rapid. Till 21 dBZ (Table 3.4), Z_h.alt.p2b is bigger than Z_h.alt.t2p, after which the former increases faster than the latter. Our explanation is as follows: at higher rainfall intensities there is higher probability of irregular shapes and aggregation above ML, resulting in particles with big concavities. When the ice particles start to melt, it takes longer to fill these concavities before a thin shell of liquid water can form around the biggest particles (Z_h peak), followed by longer melting period *(stage 4)* for larger particles.

Another observation in Fig. 3.6 and Table 3.4 is the increase in Z_h.val.t2p and decrease in Z_h.val.p2b with increase in reflectivity below the ML. It can be attributed to increase in particle size with increase in rainfall; another possible contribution is from microwave attenuation at higher rainfall intensities as raw data is used in this study i.e. without attenuation correction. Most models for vertical profiles of equivalent reflectivity (using $|Kw|^2$ of liquid phase for whole profile), assume that one snow particle results in one rain drop; this assumption seems to be refuted above 21 dBZ as well.

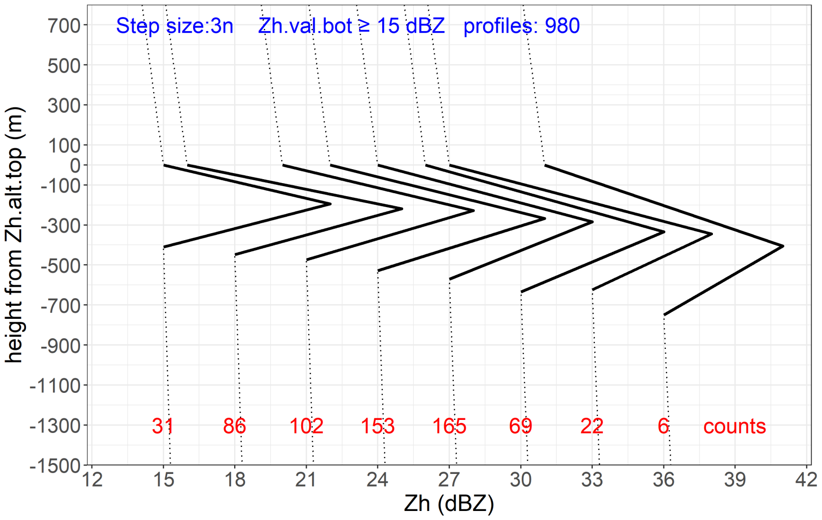

FIGURE 3.6: Intensity effect on the "Bright Band": Mean values of Z_h top, Z_h peak and Z_h bot calculated for vertical profiles at Z_h bot classes of 3n dBZ. Heights of each profiles are normalized by Z_h.alt.top.

TABLE 3.4: Summary of intensity effect

(see Appendix A.1 for the definitions of pseudo-variables)

Z_h val.top [dBZ]	Z_h val.t2p [dBZ]	Z_h val.p2b [dBZ]	BB width [m]	Z_h alt.t2p [m]	Z_h alt.p2b [m]
15	7	7	410	194	216
18	9	7	448	219	229
21	8	7	474	228	246
24	9	7	528	267	261
27	9	6	570	284	286
30	10	6	634	334	300
33	11	5	623	345	278
36	10	5	750	405	345

As further illustrations of the correlation matrix results in Fig. 3.5 for polarimetric and Doppler variables, the evolution of ρ_{hv} peak value, the differential reflectivity enhancement on top of the profile (Z_{dr}.val.t2p) and the Doppler mean velocity in rain (Vrain) as a function of R is displayed in Fig. 3.7. The evolution of the ML width, a priori slightly different from the BB width, is displayed as well as a function of R. Rainrates are divided into 7 classes, and mean intensities of each class are the X-labels. In each class, the distribution of the considered variable is presented in the form of box plots. As expected, the relationships are essentially non-linear. We underline that the upper two rainrate classes have low number of values, thus diminishing the significance of the trends observed there. Let us recall that with increase in intensity we expect increase in concentration, size, coalescence and increased diversity in shape/orientation of icy hydrometeors above the ML. With increase in number concentration and size of hydrometeors, we expect wider ML (Fig. 3.7d) as more latent heat is required to melt large number of ice particles. Bigger particles size also means higher fall velocity (Fig. 3.7c) and longer melting time, both of which resulting in the ML widening. Terminal velocity of rain drops depends on size, shape and mass of raindrops, and the density of air. At low rain intensity (drizzle), particles are smaller, resulting in lower terminal velocity. Correlation matrix [Fig. 3.5] as well shows considerably high correlation of both fall velocity and ML width with rainrate. With increase in diversity of shape, size and orientation of icy hydrometeors, we expect increase in Z_{dr}.val.t2p within ML with increase in rainfall intensity. In Fig. 3.7b we can observe that the Z_{dr} enhancement almost doubles (from 1.1 dB to 1.9 dB) as rainfall intensity increases from 0.6 to 5.2 $mm\ h^{-1}$. Finally, increase in diversity in shape, size, orientation, fall speed of melting particles within the pulse volume results in significant decrease of ρ_{hv} peak value as rainrate increases (Fig. 3.7a). At low rain intensity, ρ_{hv} peak value is quite high around 0.88 for rain-rate of 0.6 $mm\ h^{-1}$; it drops to 0.78 around rainfall intensity of 4.5 $mm\ h^{-1}$. A larger dataset would be necessary to determine if the non-monotonic trends visible for ρ_{hv} peak value and ML width for the highest rainrates are significant.

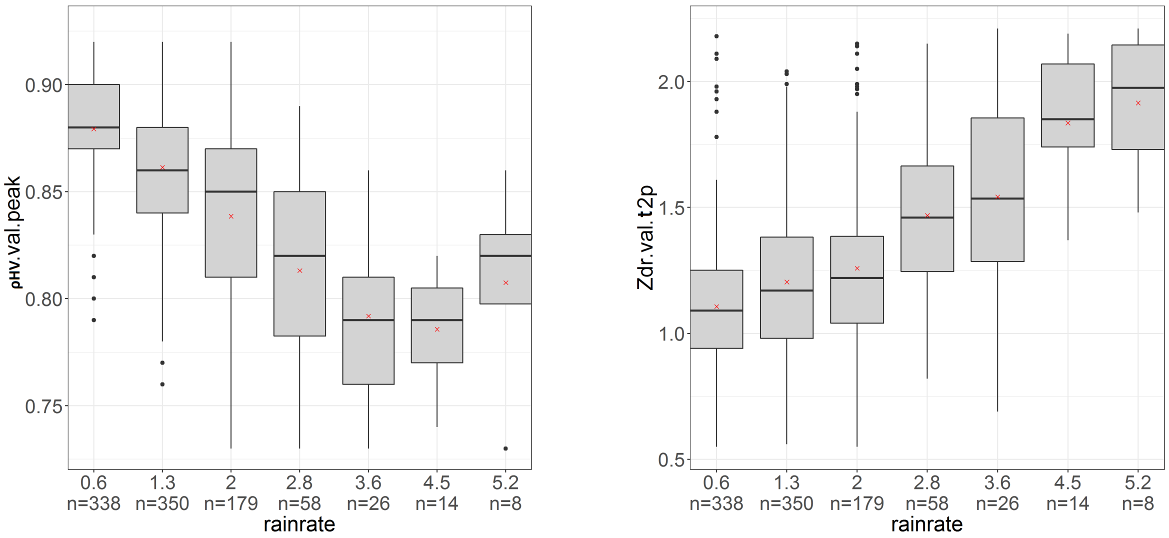

(A) ρ_{hv}.val.peak vs rainfall intensity $[mm\ h^{-1}]$

(B) Z_{dr}.val.t2p $[dBZ]$ vs rainfall intensity $[mm\ h^{-1}]$

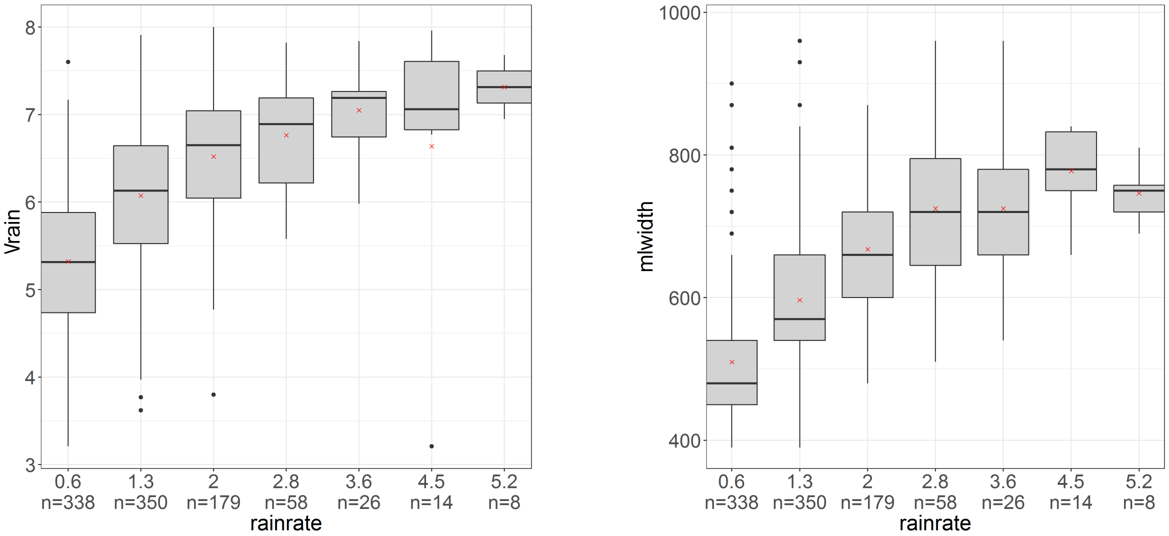

(C) Vrain $[m\,s^{-1}]$ vs rainfall intensity $[mm\ h^{-1}]$

(D) ML width $[m]$ vs rainfall intensity $[mm\ h^{-1}]$

FIGURE 3.7: Box-plots of different ML descriptors as a function of the rainrate. For each rainrate class, upper and lower hinges corresponds to 25 and 75 percentiles respectively; black line inside the box is the median and red cross is the y-mean. The number of observations in each interval is shown below corresponding x-label.

3.5.4 Evolution of ML characteristic values as a function of both rainrate and altitude of the $0°C$ isotherm

In this sub-section, we detail the correlation structure of the ML descriptors as a function of the rainrate, considered as the most natural variable for describing the intensity of the phenomenon of interest (precipitation), and the ML top altitude, as a proxy for the $0°C$ isotherm altitude.

Selection of physical explanatory variables helps to associate different ML radar signatures to different physical processes occurring in the ML. $0°C$ altitude and rainfall intensity at ground are the two most trivial and easy to investigate explanatory variables. Temperature profile is another possible explanatory variable for rates of melting process, most probably associated with width of ρ_{hv} decrease and vertical distance between Z_h peak value and ρ_{hv} peak value. Hydrometeors types (distribution and shape) are related to Z_{dr} peak value and ρ_{hv} peak value. Hydrometeor density can be another explanatory variable associated with Vsnow and the reflectivity enhancement on top of the profile (Z_h.val.t2p). In this sub-section, we limit ourselves to study the relationship of some of the ML descriptors with the rainrate and the $0°C$ isotherm altitude, using R and ML top derived from the radar dataset available as proxies. Investigations of other explanatory variables could be possible and desirable, e.g. with high-resolution NWP model outputs; this will be the subject of future research.

Using partial correlation coefficients in Fig. 3.5, we computed the total correlation coefficients $r_{1.23}$ (Appendix A.1.1) of different ML characteristic values as explained variables (index 1) as a function of the two explanatory variables (ML top and R). The most interesting results are displayed in Table 3.5. First we note that ML top is poorly correlated with R in correlation matrix 3.5 ($r_{23} = 0.18$). This is desirable, as the addition of second explanatory variable promises new information, potentially adding value in the explanation of variable of interest with respect to the first explanatory variable. The added value can be quantified by comparing the total correlation coefficient $r_{1.23}$ with the absolute value of highest partial correlation coefficient r_{12} or r_{13}. We found that there is actually little or no added-value with the second variable most of the time, e.g. for Z_h.val.t2p in Table 3.5, but also for Z_h top value, Vsnow and Vrain. However, there is a significant improvement on ρ_{hv} and Z_{dr} observations, i.e. +6 points improvement in explanation of ρ_{hv} peak and +12 points improvement in explanation of Z_{dr} enhancement at the bottom of the profile (Z_{dr}.val.p2b), +11 points improvement in explanation of the altitude difference between the ρ_{hv} peak and the Z_{dr} peak values. As visible in Table 3.5 and eq A.1.1, such gains in correlation are significant when r_{12} and r_{13} are of opposite sign, r_{23} being positive. The physical interpretation of such statistics is not trivial, but they do draw our attention towards the complex interplay of melting processes on polarimetric radar observables.

TABLE 3.5: Spearman's multiple regression with two explanatory variables: var 1 is the variable of interest, var2 and var3 are explanatory variables, ML top and R, respectively. 'r' is the Spearman's correlation coefficient between variables represented by subscripts

var1	**var2**	**var3**	**r12**	**r13**	**r23**	**r1.23**
Z_h.val.t2p	ML top	R	0.13	0.52	0.18	0.52
ρ_{hv} peak	ML top	R	0.16	-0.58	0.18	0.64
Z_{dr}.val.p2b	ML top	R	-0.28	0.57	0.18	0.69
Z_h.alt.peak - $\rho_{hv}.alt.peak$	ML top	R	-0.24	0.43	0.18	0.54

3.5.5 Density Effect on bright band

The study (Zawadzki et al. 2005) suggests that, for comparable precipitation rates, snow density affects the brightband intensity i.e. high density hydrometeors result in lower reflectivity peak due higher falling velocities and smaller particle sizes. Faster falling hydrometeors lead to lower number concentration which results in decrease of reflectivity. Larger icy hydrometeors, when covered with thin layer of water towards the end of second stage of melting (section 3.4), appear as large particles with high dielectric constant to a radar, effectively produces strong reflectivity signature. Conversely, smaller particles lead to smaller reflectivity peak. The co-existence of supercooled cloud water with snow above ML, leading to riming and change in snow densities. For stratiform precipitation with a melting layer, the authors propose high density hydrometeors above ML can result in smaller BB enhancement. Faster falling hydrometeors lead to lower number concentration and a decrease in reflectivity.

In order to check if this effect is visible in our dataset, in Figure 3.8 we examine the effect of snow density on BB enhancement. As most of the events under study are stratiform events with max rainfall intensity of 8.47 $mm\, h^{-1}$, we do not have significant number of observations at the last interval i.e. mean(Vsnow) > 2.3 $m\, s^{-1}$ as seen in Fig. 3.8. For a small class of reflectivity values below ML, [25 - 27 dBZ], we observe a decrease in BB enhancement of 1 dBZ with the increase in snow velocity / density.

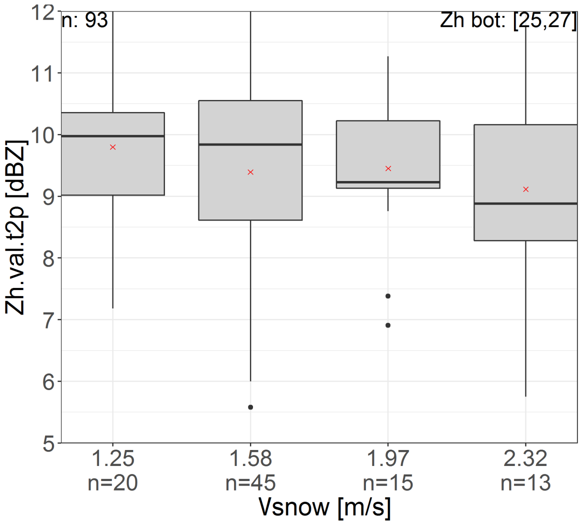

FIGURE 3.8: Density effect: BB enhancement vs W_{snow} for comparable precipitation rates. Left plot shows the density effect for Z_h bot in the [25-27 dBZ] range. X-labels show the mean value of fall velocity in the given interval and number of observations below that. Red crosses show the mean value of BB enhancement in each box.

3.5.6 Information Content of the ML dataset

In order to investigate more deeply the information content of the ML dataset available, we have implemented a number of statistical techniques ranging from Principal Component Analysis (PCA) to more complex clustering techniques, e.g. Kohonen's self-organizing maps. Herein we simply present results from the PCA technique. We remind that PCA is a statistical procedure that uses an orthogonal transformation to convert a set of observations of possibly correlated variables into a set of values of linearly uncorrelated variables called principal components (PCs). To perform PCA analysis we assume the variables to have quasi-normal PDFs, which is not fully satisfied in this dataset as seen in Fig. 3.4. By ordering the principal components, it is possible to reduce the dimensionality of the dataset if first few PCs retain most of the variance present in all of the original dataset. Here, we have selected 18 variables (x-labels of Fig. 3.9b), assumed to be representative of the total variance present in vertical profiles of Z_h, Z_{dr}, ρ_{hv} and W within the ML. Figure 3.9a shows that the first two PCs only explain about 50% of the total variance and that we need at least 9 PCs to explain 90% of the dataset variance. Lack of dominance of a few PCs is an indication that the dataset is quite rich and that polarimetric and Doppler variables bring significant information with respect to reflectivity data.

This is also evidenced with a further analysis of the contribution of each variable in the explanation of the total variance of the dataset. For this purpose, we simply computed the square of the total correlation coefficient (explained variance) of each variable with all the (independent) PCs. Figure 3.9b shows that the top 5 variables (when ordered) explain 20-24% of the total variance of the system and that the polarimetric variables (Z_{dr} and ρ_{hv}) rank high. We expected Doppler information (mean fall velocities) to rank high as well, but this is not the case, especially for Vsnow. Maybe some other Doppler-derived variables, e.g. the velocity gradient within the ML, should have been considered with a higher explanatory power.

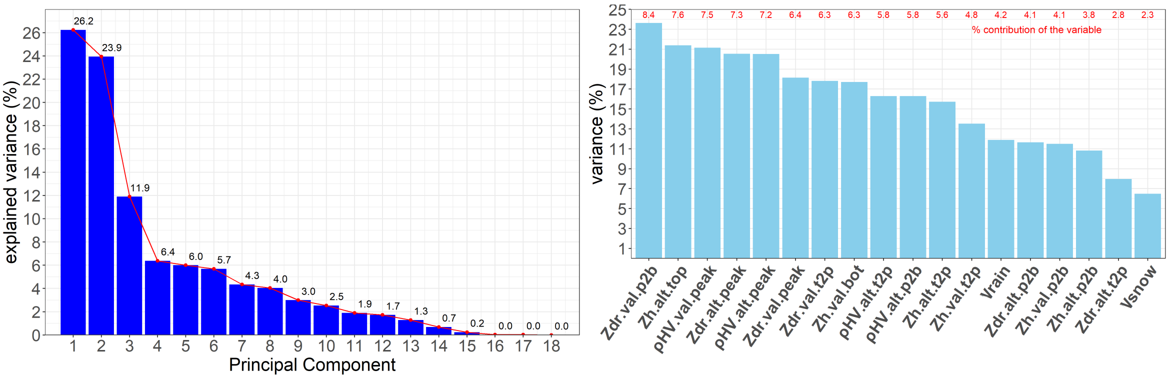

(A) Total Variance: PCs Contribution

(B) Total Variance: Variable Contribution

FIGURE 3.9: Principle Component Analysis: Explanation of total variance of the dataset

3.6 Discussion and Conclusions

The study presented here is an exploratory analysis within a broader project aimed at improving rain and snow quantitative estimation over high-mountain terrains, i.e. the study site is a large alpine valley in the French Alps. We studied the vertical variability of precipitation in the presence of melting layer through quasi-vertical profiles of polarimetric variables (Z_h, Z_v, Z_{dr} and ρ_{hv}) and vertical profiles of Doppler spectra with high resolution (30 m in radial for the XPORT radar; 100 m for the MRR radar). We have selected an elevation angle of 25° for establishing the polarimetric QVPs of the XPORT radar. By choosing such a relatively low elevation angle, we were able to capture interesting radar signatures of the heterogeneity of hydrometeors between their horizontal and vertical dimensions (Ryzhkov et al. 2016). On the other hand, for such an elevation angle, the horizontal variability of precipitation certainly influences the radar measurements. This was mitigated in our statistical analysis by discarding QVPs with high spatial variability related for instance to the precipitation system entering or leaving the valley or to highly convective situations. We used for this purpose a visual inspection of the ρ_{hv} PPI raster plots.

It is well established that the melting processes in the atmosphere give rise to enhancements in measurable radar parameters, which are precipitation and frequency dependent (Vivekanandan et al. 1993). Efforts to understand the effects of melting particles on electromagnetic waves and consequent uncertainties in the surface-rainfall estimation have resulted in several melting layer detection algorithms and definitions of ML boundaries, each with their advantages and limitations. We have built a ML detection algorithm that detects the top, peak and the bottom of the enhancements in vertical profiles of Z_h, Z_v, Z_{dr} and ρ_{hv}, and records the concurrent altitudes and values. We focused on stratiform events where ML occurs at rather low altitudes, e.g. within/below the Météo-France MOUC radar elevation. After an intensive review of the literature, we summarized the melting processes of an individual hydrometeor within the melting layer into four distinct stages. Then, we attributed different stages of the melting of the distribution of hydrometeors to the enhancements of the vertical profiles of radar observations. We observed that Z_h peak occurs at higher altitude compared to ρ_{hv} peak while the Z_{dr} peak occurs lower; this observation is consistent with the melting processes of the largest particles, which have a major influence on the peak values. Falling icy hydrometeors start to melt when they cross the 0 $°C$ isotherm. In radar only observation, Z_h top is the closest indicator of the 0 $°C$ isotherm altitude. So, we consider the altitude of Z_h top to be the ML top. At the end of the melting process, as the largest particles melt completely; they assume the smallest possible volume due to surface tension and they attain maximum velocity. We observe that the altitude of max(W) from MRR corresponds well with the altitude of ρ_{hv} bottom. We have considered the altitude of ρ_{hv} bottom to be ML bottom. The subsequent statistical analysis of different ML descriptors provides results consistent with observations made in similar climatological context. It also demonstrates that the polarimetric information brings a strong added-value about the characterization of the ML processes with respect to reflectivity measurements alone.

Although robust in its current form, the ML detection algorithm can be improved: in particular, we observed that ρ_{hv} peak is the most consistently identified parameter and we may consider this peak altitude as a reference to limit the altitude search ranges for each variable, as well as to initiate the algorithm and control the consistency of identifications from one time step to the next. Another area for improvement concerns the characterization and filtering of the variability of the quasi-vertical profiles associated with the horizontal variability of precipitation, e.g. when a precipitation system is entering or leaving the detection domain or in case of convective precipitation. This could be achieved with sectoral identifications based on detection of the horizontal precipitation intermittency. Although the impact of attenuation at X-band on radar observations is thought to be limited due to the short distances, high-elevation angles and the limited rainrate range considered in the present study, the pre-processing of radar observations for attenuation is certainly desirable prior to the ML identification algorithm implementation.

Chapter 4

PIA estimation using MRT

4.1 Introduction

Reliable QPE remains a challenge in the mountainous region. A well maintained and well calibrated network of raingauges provides the most direct measurements of precipitation intensities and accumulations in the liquid phase. It is much more problematic for solid and melting precipitation. In orographically complex terrain, the distribution of the raingauges is scarce while the precipitation often has high spatial and temporal variability both in intensity and thermodynamic phase. Wind introduces further uncertainties in gauge measurements, especially in the solid precipitation (Kochendorfer et al. 2017). Although the rain-gauge measurements are assumed as the ground-truth, they only offer the partial sampling of the rain-field. Weather radar are able to provide a high resolution measurements both in space and time.

Operational weather radar networks are designed for long-range coverage through heavy precipitation without substantial attenuation losses; conventionally they operate at C- or S- band wavelengths with range of typically 200 km in Europe. The radar QPE in mountainous regions suffers from beam blockage, ground clutter and harsh operating conditions. It is limited by beam blockage when the radars are too close to a mountain range and by the sampling resolution volume size when the radars are long way away. This impedes the ability of these systems to identify and detect rapidly changing fine-scale weather dynamics in the mountainous regions. Arrays of shorter wavelength dual polarimetric X-band radars provide promising solutions to these limitations and are successfully employed to fill gaps in the radar networks (McLaughlin et al. 2009; Van de Beek et al. 2010; Lengfeld et al. 2014). Higher frequency ($\sim$ 10 GHz at X- compared to $\sim$ 3 GHz at S- and $\sim$ 6 GHz at C-band) translates to smaller antenna and lower power i.e. lower cost and potentially mobile systems. Its is also less sensitive to ground clutter. Despite its advantages, the X-band radar suffers from significant power attenuation in heavy rain and in the melting layer of precipitation (Atlas and Banks 1951; Bringi et al. 1990; Delrieu et al. 2000; Willie et al. 2006) which needs to be corrected to obtain a reliable radar QPE.

The accurate estimation of precipitation at any range depends on the ability to correct radar return signal for attenuation. Hitschfeld and Bordan (1954) and Atlas and Ulbrich (1977) evidenced the attenuation problem early and Hitschfeld-Bordan proposed a straightforward solution. The Hitschfeld-Bordan method, however, is known to be unstable and very sensitive to radar calibration errors. Attenuated frequencies (X- and K-band) were generally abandoned in 1960s for meteorological applications. The launch of spaceborne and airborne radars 1980s renewed interest in higher frequencies due to the constraints in the antenna size on these platforms. A significant progress has been in radar software, signal processing and data analysis methods in last decades. Similarly, urban hydrology applications requiring short range high resolution observation further contributed in advancement of land based high frequency radars (Thorndahl et al. 2017).

Experiments and theoretical studies show that the path-integrated or path-averaged rain rates can be determined by the direct measurement of attenuation. Atlas and Ulbrich (1977) showed that the attenuation is linearly related to rainfall rate at 0.9 cm wavelength using the direct measurements of total attenuation. Meneghini et al. (1983) proposed the surface reference technique (SRT) for spaceborne radar configuration. The SRT uses the surface scattering properties to infer path integrated attenuation (PIA) through precipitation. It provides the estimate of PIA using the difference in surface returns in presence and absence of rain (Meneghini et al. 1983, 2000, 2021). Delrieu et al. (1997) applied similar techniques in the ground based attenuated radar systems (X-band) operating in the mountainous environment. The siting of the radar and scan strategies provided strong mountain returns at low elevation angles scans for PIA estimation, and the technique was named as "mountain reference technique" (MRT). Furthermore, the study of PIA constraints equation provided information on parametrization of radar data processing and the comparison of mountain return PIA to those calculated using the reflectivity profiles yielded a correction term compensating for the combined effects of radar calibration error and error on multiplicative coefficient of the specific attenuation vs reflectivity (A-Z) relation. The accuracy of PIA estimation using MRT is further discussed in Delrieu et al. (1999) and the use of MRT for radar self-calibration in hilly terrain are discussed in Serrar et al. (2000).

This chapter aims to build on these previous studies on the MRT and analyse long term stability of the mountain targets and estimated PIAs in the context of the RadAlp experiment.

4.2 Basic equations for PIA estimation using MRT

The measured rain reflectivity profile $Z_m(r)\,[mm^6\,m^{-3}]$ can be derived from the backscattered power profile $P(r)$ using the radar equation:

$$P(r) = \frac{C\,Z_m(r)}{r^2} \tag{4.1}$$

where, r is the range of observation, and C is the radar constant (Doviak and Zrnić 1993). The two common sources of error affecting the measured reflectivity are: (i) a radar miscalibration denoted by dC, and (ii) the effect of the attenuation by rainfall. Hence, the following relation can be written to relate the true reflectivity $Z(r)$ and the measured reflectivity:

$$Z_m(r) = Z(r)\,AF(r)\,dC \tag{4.2}$$

where, AF(r) is the attenuation factor at range r. For two way propagation, AF(r) is defined as the twice the integral of A between first stable gate range (r_0) and the range(r). Marzoug and Amayenc (1994) have defined it as:

$$AF(r) = AF(r_0)\,exp[-0.46\int_{r_0}^{r} A(s)\,ds] \tag{4.3}$$

where, A is the specific attenuation coefficient $(dB\,km^{-1})$ that depends on the wavelength, and size distribution and temperature of the raindrops, and $AF(r_0)$ is the on-site attenuation factor. Onsite attenuation is composed mainly of radome attenuation and blind range $(0, r_0)$ attenuation. Path integrated attenuation $PIA\ (dB)$ is the dB-transformed attenuation factor, i.e

$$PIA(r) = -10\,logAF(r) \tag{4.4}$$

Note that since $AF(r)$ ranges between 1 (no attenuation) and 0 (full attenuation), the PIA subsequently ranges between 0 (no attenuation) to $+\infty$ (full attenuation).

In spaceborne configuration, Meneghini et al. (1983) showed that the PIA can be calculated as the ratios of surface returns (i) at a given location in the presence and absence of rainfall, or (ii) at the same time within or outside the rain area. In the present context, the spatial variability of precipitation restricts us to the former solution. For a given mountain target at range (r_M), the ratios of the measured reflectivity in rain (Z_m^{rain}) and dry measured reflectivity (Z_m^{dry}) can be expressed using equation 4.2 as:

$$\frac{Z_m^{rain}(r_M)}{Z_m^{dry}(r_M)} = \frac{Z^{rain}(r_M)\,AF^{rain}(r_M)\,dC}{Z^{dry}(r_M)\,AF^{dry}(r_M)\,dC} \tag{4.5}$$

The radar calibration error dC is considered to be constant in time, i.e. transmitter-receiver unit is assumed to be stable within the precipitation event. Similar, the attenuation factor during the dry event is 1, and the real reflectivity from the mountain return targets are considered remain constant over time i.e. assume the only source of attenuation is the rain between the radar and the mountain target.

$$AF(r_M) = \frac{Z_m^{rain}(r_M)}{Z_m^{dry}(r_M)} \tag{4.6}$$

From 4.4 and 4.6, PIA[dB] for a mountain reference target at range r_M can be written as:

$$\begin{aligned} PIA(r_M) &= -10\, log \frac{Z_m^{rain}(r_M)}{Z_m^{dry}(r_M)} \\ PIA(r_M) &= 10\, log Z_m^{dry}(r_M) - 10\, log Z_m^{rain}(r_M) \end{aligned}$$

The reflectivity can be expressed in dB as $dBZ = 10\, logZ$. And, the PIA [dB] for a mountain target at range r_M can be written as:

$$PIA(r_M)[dB] = Z_m^{dry}(r_M)\ [dBZ] - Z_m^{rain}(r_M)\ [dBZ] \tag{4.7}$$

MRT gives a bulk estimation of on-site and along-path attenuation.

$$\begin{aligned} PIA(r_M)[dB] &= PIA(r_0) + PIA(r_0, r_M) \\ &= PIA_0 + PIA(r_0, r_M) \end{aligned} \tag{4.8}$$

where, PIA_0 is the on-site attenuation.

4.3 Mountain return targets

The estimation of the PIA using equation 4.7 needs a reference target for which the backscattering power can be measured in absence of precipitation i.e. dry periods. The echoes from the mountains surrounding a weather radar in the hilly terrain, provide stable and strong signal in the dry periods. In the RadAlp experiment, we define the mountain targets as the returns with reflectivity Z_m greater than 45 dB in long-term observation of X-band radars (for both XPORT and MOUC) in a given scan volume. The specific value was derived from the experience of the RadAlp team, with the help of digital terrain maps (DEM) and long-term observation of the radar returns. We are using the lowest elevation angle of the MOUC radar to get the strongest (otherwise undesired) signal from the mountains. As these mountain targets are embedded in a complex topology, the strong echo from a mountain target is often surrounded by less strong ground clutter where the radar observables are often not the reflection of hydrometeor characteristics. We define dry-weather echoes greater than 25 dBZ in the long-term observation to be ground clutter. Ground clutter, in a range profile with precipitation, is characterized by the sudden decrease in ρ_{hv} signal below 0.85 and significant oscillation in Ψ_{dp} signal. The choice of ρ_{hv} threshold is based on long-term observation of ML in Grenoble, as summarized in table 3.3. We observe that the dry periods are dominant in long-term observations.

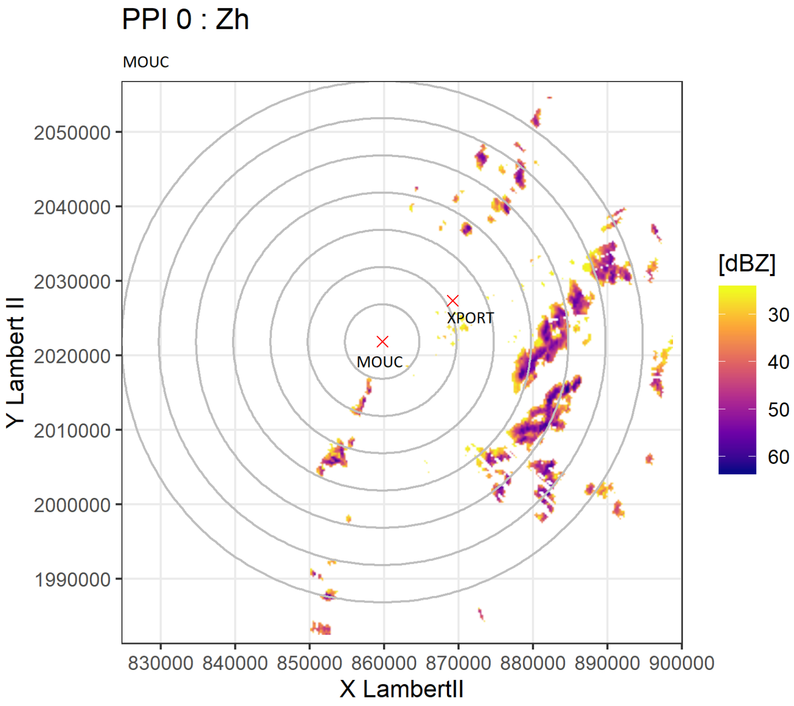

FIGURE 4.1: Mountain echoes seen in the long-term observation of 0° PPI scan of MOUC radar. Mountain targets ($Z_m \geq 45$) are most of the time surrounded by smaller ground clutter ($Z_m \geq 25$). MOUC radar sits in the center marked by a red cross. Concentric grey lines are placed at a 5 km radius expansion. IGE site containing XPORT and MRR radar sits around 11km from MOUC radar in the northeast, marked by another red cross. The raster is projected in the Extended Lambert II spatial coordinate system.

The distribution of these strong-permanent echoes at a radius of 40 km around MOUC radar, as seen in long-term observation of 0° PPI scans are shown in Fig 4.1. As the radar is placed on the top of a mountain, there is no significant issues of beam blockage from trees, buildings or towers. The plot is based on the mean Z_m map around MOUC radar obtained by aggregating all 87 days of data. Echoes from the Chartreuse mountains are in the northeast direction, Belledone mountains in east, Taillefer mountains in the southeast, and Vercors mountains' echoes are in the southwest. Mountain targets are defined as the compact groups of gates with dry-weather values greater than 45 dBZ. The mountain returns in successive radials are grouped together to form a target with significant surface area, which increases the overall stability of the PIA estimates.

Limits are introduced to the size of the targets, both in azimuth and gate, to reduce errors from variability in the precipitation field. Large continuous targets are broken into separate targets. The mountain returns are grouped into 20 targets, which hereinafter will be referred to as "mountain return targets" or simply "targets". In practice, the search of the mountain returns was limited to 30 km from MOUC radar, to minimize the effects of beam broadening. While most ground clutter (25 - 45 dBZ) surround the mountain target, some can be seen in between radar and the targets. For a given radial, the observations in the gates with the "in-between" ground clutter were set to NA during data processing.

The 25 dBZ threshold used to define ground clutter is equivalent to about 1 $mm\ h^{-1}$ of rain. The rain greater than 1 $mm\ h^{-1}$ will not have significant impact by ground clutter less than 25 dBZ due to the additivity of powers in Watt. Similarly, 45 dBZ, threshold of mountain target, is equivalent to 40 - 50 $mm\ h^{-1}$ of rain, and the rain less than that will not impact first the reflectivity of the mountain target, and the subsequent PIA estimation.

Figure 4.2 shows the spatial distribution of mountain targets with MOUC radar in its center. The mountain returns are grouped together (black border) with information about the mountain targets and surrounding ground clutter. The mountain targets are between 40° and 200° degree azimuth, at the range of 15 to 29 km from the MOUC radar site. The target area range from 1 km^2 to 3.8 km^2. Considering the average reflectivity of 87 days dataset, all the targets have reflectivity greater that 45 dBZ, ranging form 46.6 dBZ to 51 dBZ. Target 20 is the smallest and closest target, target 12 is the largest one, and target 1 is the furthest from MOUC radar. The characteristics of the targets are detailed in Table 4.1. The range $r_M(MRT)$ is the distance between radar and center of the target.

TABLE 4.1: Characteristics of mountain return targets

Target ID	# azimuth	# gates	azimuth mid(°)	range (km)	area (km^2)	Avg. Zh (dBZ)
1	5	13	40.25	28.6	2.00	47.44
2	6	11	43.25	24.5	1.45	49.27
3	4	11	76.25	27.0	1.60	47.34
4	5	18	78.25	26.3	2.55	47.52
5	4	11	82.25	23.7	1.40	48.66
6	6	15	84.75	22.1	1.78	48.75
7	7	27	87.75	21.9	3.18	48.68
8	5	26	90.75	22.6	3.16	48.28
9	7	28	94.25	20.9	3.15	48.67
10	7	31	98.75	19.9	3.33	48.37
11	7	18	102.25	19.1	1.85	48.13
12	9	26	106.75	23.9	3.35	50.95
13	9	25	111.25	23.9	3.22	48.82
14	10	29	116.25	24.3	3.80	50.08
15	7	24	121.25	22.4	2.90	47.54
16	5	12	124.25	22.9	1.48	48.21
17	8	21	127.75	27.9	3.15	49.05
18	5	9	137.25	24.9	1.21	47.42
19	6	14	140.25	25.0	1.88	48.13
20	5	11	199.75	15.5	0.92	46.64

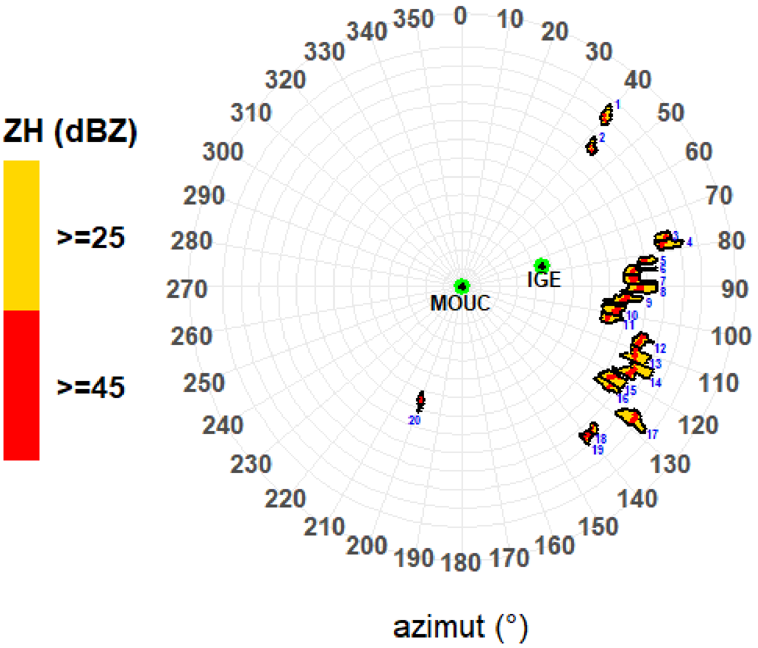

(A) Distribution of mountain return targets

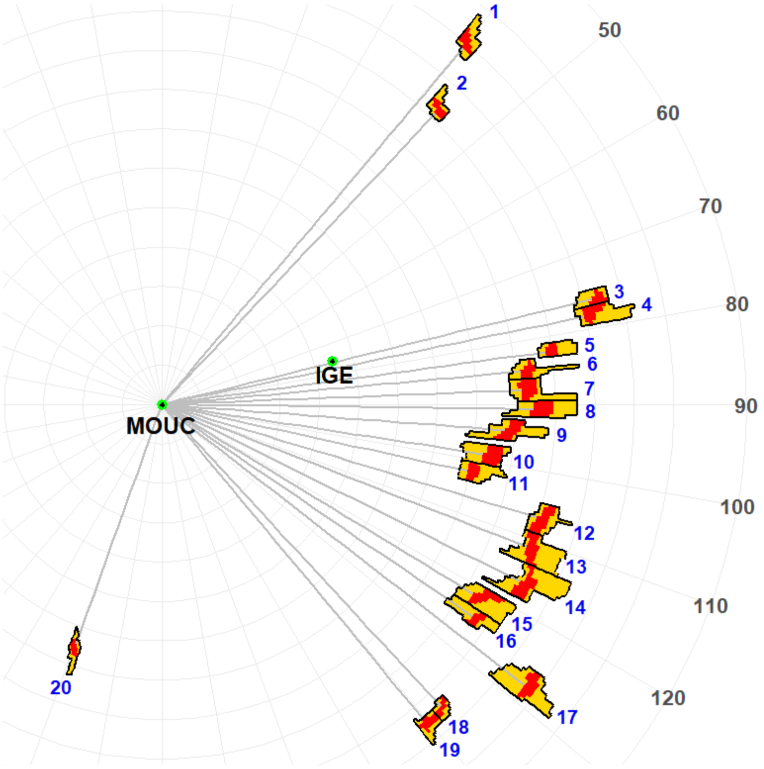

(B) Focus on 20 mountain return targets

FIGURE 4.2: Mountain return targets for 0° PPI scan of MOUC radar. In polar coordinates, radial lines are spaced at every 10° azimuth, and concentric lines are spaced at 10 gates (2.4 km). 0° azimuth is the geographic north. The mountain return targets are mapped in red, and the ground clutter surrounding them in gold. Target ids are annotated in blue. Top sub-plot shows the distribution of targets in 0° PPI scan of MOUC radar. The bottom sub-plot magnifies in the sector containing 20 targets. Targets 1 and 2 are located in the Chartreuse massif, 3-11 in the Belledone massif, 12-19 in Taillefer massif and 20 in the Vercors.

4.4 PIA Estimation

During precipitation, the hydrometeors between the radar and a mountain target attenuate the radar signal. Equation 4.7 shows that the dry weather signal from the mountain target can be utilized as a reference to calculate the total attenuation, also called path integrated attenuation. For a mountain target, PIA between the radar and the target can be formulated as the difference in reflectivities of mountain targets in presence (wet) and absence (dry) of precipitation.

$$PIA = Z_h^{dry} - Z_h^{rain}$$

where, the reflectivities are in dBZ and the PIA is in dB.

After defining the mountain targets, next step is to establish the dry-weather baseline reflectivity Z_m^{dry} for a given target. One possible method to estimate Z_m^{dry} is to utilize the long-term reflectivity averages for each target. It is however important to note that the strength of mountain return depends on factors like vegetation, snow cover, wetness of the rocks and also on the variations in the radar calibration. It is possible that the strength of mountain echoes can vary between different seasons and even during the event due to wetness or snow accumulation. As such, it is preferred that the Z_m^{dry} are recorded before and after each precipitation, i.e. in event scale. The reference Z_m^{dry} during precipitation is then estimated by interpolation between two dry weather periods. Finally, the difference in the measured returns (Z_m) and Z_m^{dry} gives the estimate of PIA.

The different steps of PIA estimation using MRT is demonstrated in Fig 4.3 for target 8 during 4-5 November 2017 event. First of all, to ensure the presence of significant dry periods, a time series corresponding to the apparent reflectivity of the mountain target for multiple days surrounding the events are taken from the MOUC observation, shown in blue in the figure. 3 days of data are taken in this example. As an indication of the presence/absence of precipitation, the mean measured reflectivity (attenuated) SZ between radar and the target is shown in grey. For example, if a target has 4 radials and 100 range gates between radar and the target, the measured reflectivity from all 400 gates are averaged.

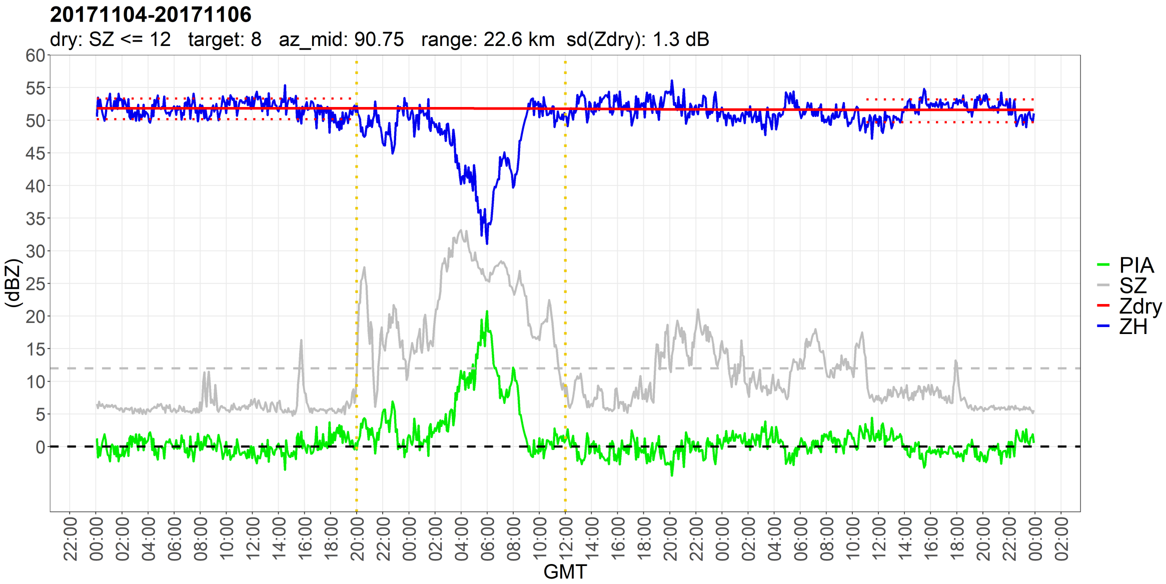

FIGURE 4.3: time series of PIA estimation: 4-5 November 2017 using MRT. Blue denotes the apparent reflectivity Z_m in the horizontal polarization of the mountain target, red line is the "baseline" of Z_m^{dry}. Grey line (SZ) is the path-averaged measured reflectivity between r_0 and r_M i.e. a proxy of rainfall and its intensity between the radar and the target. Green line is the PIA i.e the difference between red and blue lines. The vertical golden line marks precipitation event for which ML data is available. SZ indicates the presence of precipitation between radar and target, i.e. precipitation present when SZ is greater than threshold (12 dBZ) shown as dotted horizontal line.

Although based on the attenuated reflectivities, SZ provides an idea about the strength of precipitation between radar and the mountain target. We empirically use a threshold of $SZ \leq 12\ dBZ$ to define a dry period. It roughly translates to 0.2 mm/hr or rainfall intensity using the Marshall-Palmer relationship (Marshall and Palmer 1948). This threshold is shown as the dotted grey horizontal line in the figure. $Z_m^{dry}(t)$ is calculated for each significant dry period as mean of that period, red line in the figure. Standard deviation of Z_m^{dry} time series, 1.3 dB in this example, gives the stability of the dry echo of the mountain return target. The dotted red envelop around the Z_m^{dry} in dry segments is the $10^{th} - 90^{th}$ percentile range. For other targets and events, the standard deviation ranges, mostly, between 1.25 and 1.56 dB. In between two dry periods, Z_m^{dry} is estimated by inverse distance squared interpolation. Z_m^{wet} is simple the Z_m during the wet period, i.e. shown in blue. Difference of reflectivity during the dry and wet periods gives the PIA estimate, shown in green in the figure.

Another example of PIA estimation is shown for the 3-4 January 2018. Figure 4.4 shows the characteristics of the ML for the event, observed by XPORT radar. Solid blue and golden lines mark the altitude of ML top and bottom respectively. The horizontal dotted black line marks the altitude of MOUC radar i.e. the center of the

0° beam. In the beginning of the event, the MOUC radar is above the ML i.e in snow regime. Between 01h00 and 04h00 the elevation of ML raises significantly and the radar is mostly within the ML during this period. After 04:00, the ML continues to rise slowly and the center of the MOUC 0° elevation angle beam is the rain regime. The PIA estimation for target 10 of the corresponding event is shown in Fig 4.5, vertical dotted golden lines mark the event boundaries shown in the ML time series. Three clear dry periods used to estimate Z_m^{dry} are marked by the envelops of dotted red lines. In the snow regime, as expected, PIA is negligible. As the radar enters the ML the PIA increases gradually with a peak around 03:00 which is also when the ML width is maximum in relation the radar altitude i.e. radar is in the middle of ML. And, as the ML continues to raise the PIA decreases slowly. In rain regime, between 06:00 and 09:00, the PIA decreases slowly and is still significant.

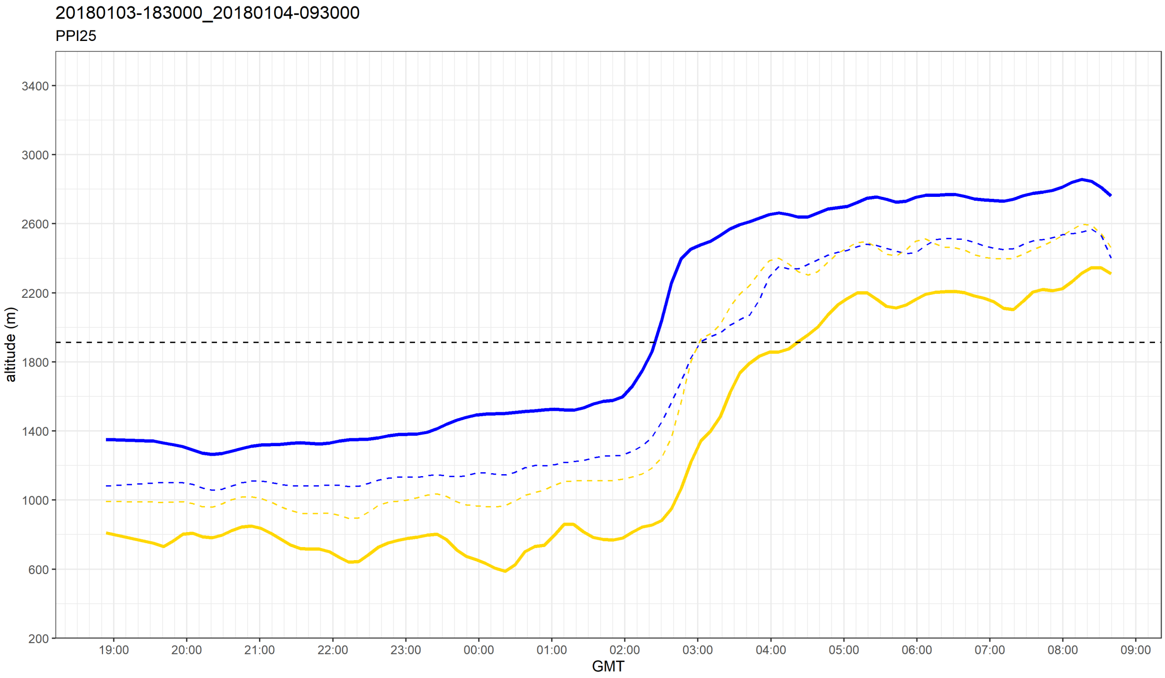

FIGURE 4.4: XPORT ML time series: 3-4 January 2018. ML characteristics of the event observed by XPORT radar. Regular golden and blue lines show ML bottom and top respectively. Dotted gold and blue line show altitudes of ρ_{hv} peak and Z_m peak respectively. Dotted black line is the center of the 0° beam in a PPI scan, i.e. altitude of MOUC radar. ML layer is below MOUC radar in the beginning of the event, between 01h00 and 05h00 the ML raises to altitude above MOUC radar. The center of the radar beam is within the ML between 02h20 and 04h30.

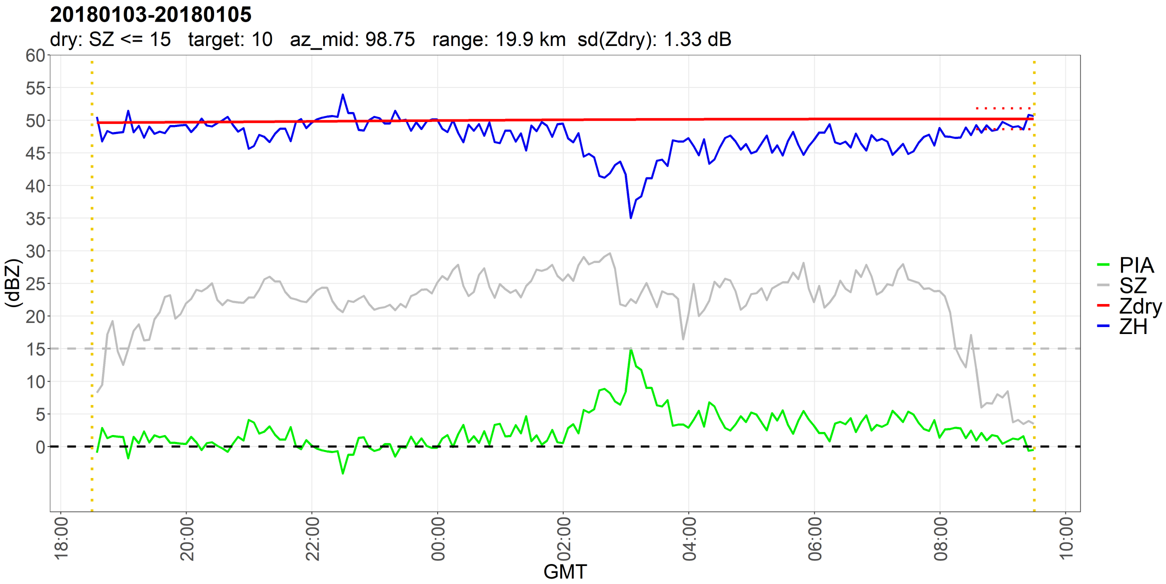

FIGURE 4.5: Another example of PIA estimation: 3-4 January 2018, a rather difficult case. Description similar to Fig 4.3.

The ML identification for 1 May 2020 precipitation event is shown in Fig 4.6. The characteristics of the ML has been determined with the MRR data, the XPORT radar not being operational at this date. During this event the center of 0° PPI beam is shown to be at/just above ML top. The radar beam widens with range, as most of the targets are between 20-30 km away from the radar, so at r_M, the beam (450-670 m vertical extent) is partially in the ML. Figure 4.7 shows time series for the the PIA estimation using the Z_m time series for 1-2 May 2020 for target 15. First observation in Fig 4.7 is that there are 3 precipitation events with presence of ML within this 2 days window. This is a complex weather window with different wet periods where the beginning and end of the dry/wet periods is difficult to separate. There is a significant period of dry weather between second (EV2) and third (EV3) precipitation events, and acts as a baseline of dry weather returns for all three events. Attempts to estimate PIA at event scale could have resulted in systematic underestimation of PIA. Another rather baffling observation is the unusually high PIAs for a radar in snow regime, especially between events EV1 and EV2 despite having a period of low gate averaged reflectivity (SZ). One possible explanation is the beam with integration in the vertical and the contamination by the ML, i.e. although the center of the beam is the snow regime (at least during 1^{st} event) closer to the radar, it gets contaminated by the upper part of ML (located just below the beam center) as the beam broadens further away from the radar.

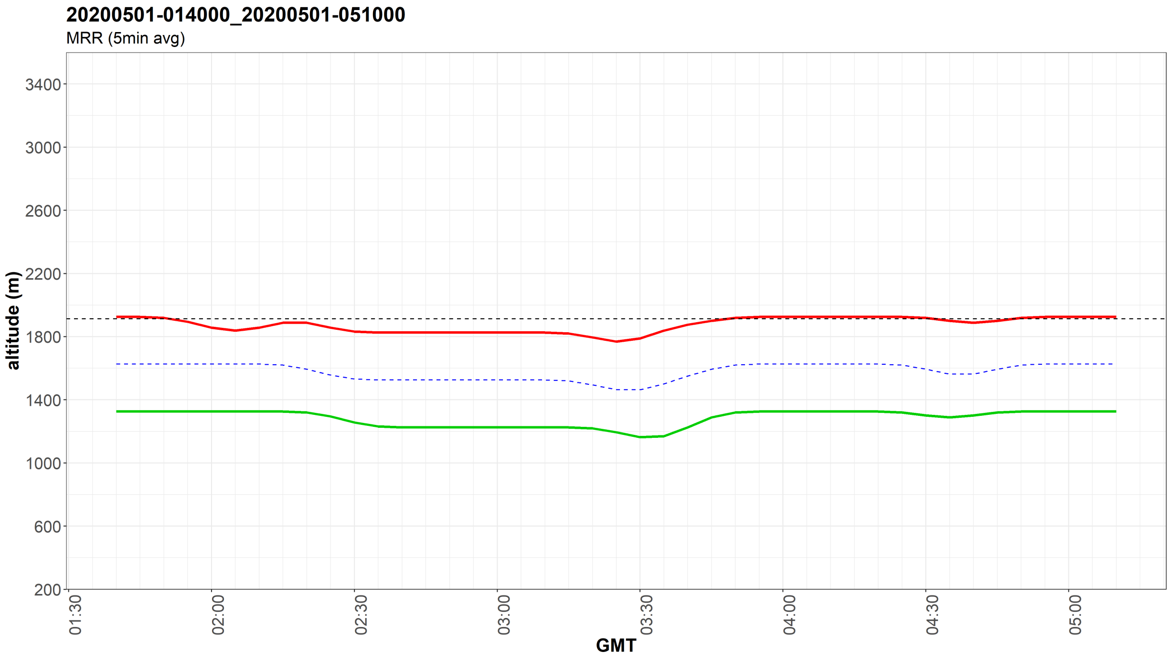

FIGURE 4.6: MRR ML time series: 1 May 2020. ML characteristics of the event observed by MRR radar. Solid red and green lines show ML top and bottom respectively. Dotted blue line shows altitude of the reflectivity peak. Dotted black line is the center of the 0° beam in a PPI scan, i.e. altitude of MOUC radar. Throughout the event, the MOUC radar is in close proximity of ML top.

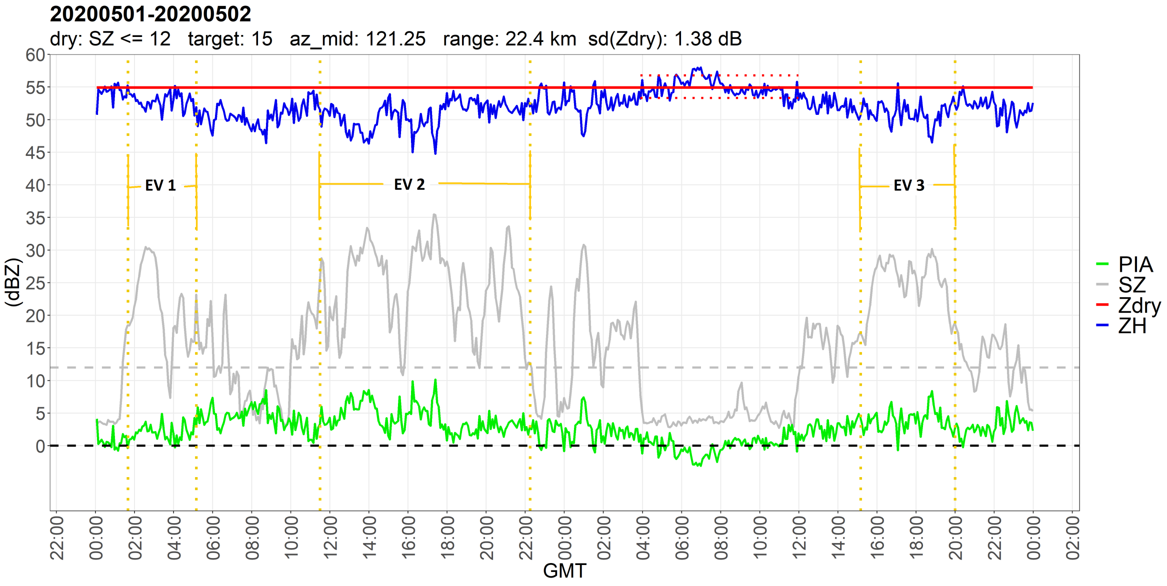

FIGURE 4.7: PIA estimation: 1-4 May 2020. 3 ML events corresponding to 3 different wet periods are recorded by MRR radar in 2 days span, marked as EV1, EV2 and EV3. Description similar to Fig 4.3.

4.5 Conclusions

Mountain Reference Technique (MRT) provides a unique opportunity to have a direct measurement of path integrated attenuation (PIA) using the stand alone radar observations. In our implementation of the MRT, we have identified two main error sources.

1. Time stability of the mountain returns
   The instability may be due to (i) possible changes in the radar calibration, (ii) modification of the mountain surface properties at long term (vegetation changes) and shorter term (wetting of the surfaces, accumulation of snow or melting snow on the ground). To cope with this problem we have implemented a dry-weather baseline estimation technique based on estimation of dry periods before, within and after each precipitation events. Dry weather reference at each timestep of the wet period is obtained by inverse distance squared interpolation of means of surrounding dry weather periods. The stability PIA is depicted by the stability of Z_m^{dry} estimation. The probability density function (pdf) of Z_m^{dry}, in particular the standard deviation $SD(Z_h^{dry})$, can be used to determine the sensitivity of the PIA estimated using MRT, in other words the minimum detectable PIA. For most events and targets the SD of Z_m^{dry} ranges between 1.25 and 1.56 dBZ. Setting PIA = 0 for $Z_{dry} - Z_h \leq 0$ is a good idea, similarly considering a minimal detectable PIA threshold of 1 dB is also reasonable. The stability of PIA estimation, improves with increase in target size (area), and the presence of significant dry weather spells before and after the precipitation event, resulting in smaller $SD(Z_h^{dry})$.

2. Beam width integration in the vertical
   For MOUC radar with a 3-dB beamwidth of 1.28°, at 0° elevation angle, the vertical extent of the beam is 223, 445 and 670 m at 10, 20 and 30 km respectively. Most mountain targets are at distance of 20 to 30 km from the radar. An example was shown with significant PIA when 0° elevation beam center was just above the ML top, i.e. in snow regime, due to attenuation in the upper part of the ML.

Delrieu et al. (1999), identified a third error source in case of the heavy rain falling over the target itself, i.e. when the precipitation intensities exceed the dry weather mountain returns. With the 45 dBZ threshold and stratiform events of interest, this error source should not be significant in our study. It is also important to remind that the MRT derived PIA estimate aggregates along path attenuation and on-site attenuation, the latter being essentially associated with water films over the radome. More about the statistics of the obtained PIAs to come in chapter 6.

Chapter 5

Differential phase shift and its regularization

5.1 Introduction

The phase shift of electromagnetic (EM) wave depends on the dielectric constant of the propagation medium. The dielectric constant of water is almost 80 times higher than that of air, i.e. the wave propagates slower. EM wave travelling through precipitation acquires larger phase shift compared to the wave travelling same distance through air. If the hydrometeor is non-spherical, like oblate rain drops which are larger in horizontal dimension, H-polarization wave encounters more liquid medium and slows relative to the V-polarization wave (Kumjian 2013). The resulting difference in phase shift between H and V polarization is known as the differential propagation phase shift (Φ_{dp}). As such, it provides information on the anisotropy of the hydrometeors along the beam path.

In a monostatic radar, the transmitter and receiver are co-located. The measured differential phase shift is the cumulative difference in 2-way attenuation for horizontal and vertical polarization in a pulse volume. The measured total differential phase shift (Ψ_{dp}) is composed of backscattering and forward-scattering (or propagation) components. A conceptual model of the measured differential phase shift (Ψ_{dp}) can be expressed as

$$\Psi_{dp}(r_0, r) = 2\int_{r_0}^{r} K_{dp}(s)ds + \delta_{hv}(r) = \Phi_{dp}(r) + \delta_{hv}(r) \tag{5.1}$$

where K_{dp} [$^\circ\ km^{-1}$] is the specific differential phase shift on propagation, $\Phi_{dp}(r_0, r)$ [$^\circ$] is the total propagation phase shift between the radar and target, and $\delta_{hv}(r)$ [$^\circ$] represents the local backscattering phase shift.

The propagation phase shift Φ_{dp} is cumulative along the path i.e. for two-way propagation in monostatic radars. It is dependent on the number concentration of hydrometeors and tends to increase with particle size. It is not affected by attenuation, partial beam blockage, or radar miscalibration, and is not biased by noise (Kumjian 2013). The one-way specific phase shift K_{dp} $[^{\circ}\, km^{-1}]$ is the half derivative of Φ_{dp}.

The backscatter differential phase is caused by backscattering from hydrometeors within the radar resolution volume. It becomes significant when nonspherical hydrometeors are large enough relative to the radar wavelength such that the scattering is in the Mie regime. In the melting layer of stratiform precipitation δ_{hv} manifests as non-monotonical radial profile ("bumps") of Ψ_{dp} (Trömel et al. 2013). δ_{hv} is not cumulative but is a local parameter, most evident when the scatterers are in Mie regime, and is independent of the length of the beam path within the melting layer. With the increase in elevation angles, forward propagation component Φ_{dp} , a result of anisotropy of the medium, reduces significantly, providing clean δ_{hv} (Trömel et al. 2014), mostly arising from the change in scattering regime by larger particles.

The algorithm to estimate Φ_{dp} from the measured Ψ_{dp}, often very noisy, is discussed in detail in section 5.2. In section 5.3, Φ_{dp} regularization algorithm is implemented to the Ψ_{dp} data corresponding to the MRT PIAs from chapter 4. Our experience of using the algorithm and its robustness is summarized in section 5.4.

5.2 Φ_{dp} regularization algorithm

The range profiles of measured/total differential phase shift (Ψ_{dp}) are significantly noisy in precipitation of low intensities, and even more so in the melting layer. An iterative approach based on two binding envelopes and maximum allowed jumps in Φ_{dp} between successive gates is developed here. This approach efficiently exploits the cumulative nature of range profile of Φ_{dp}. Figure 5.1 displays the organigram of the Φ_{dp} regularization algorithm developed in this study. The main steps of algorithm are discussed in detail, with the help of range profiles of Z_h, ρ_{hv} and Φ_{dp} in Fig 5.2 for a given timestep when the center of 0° beam is within ML for target 7. The Φ_{dp} regulation algorithm is illustrated in the bottom subplot. Colored lines of the sub-plot correspond to different stages of regularization process and are listed below after the discussion of the corresponding step.

The measured Ψ_{dp} contains the initial system differential phase offset ($\Phi_{dp}0$), its correction is the first step in the regularization algorithm. It is dependent on the configuration of the radar system, accumulation of hydrometeors on the radome and climate conditions at the radar site i.e first few gates. For MOUC radar, the $\Phi_{dp}0$ in dry-weather conditions oscillates around 300°. As most of the measurements are done in and around melting layer in this study, the value of $\Phi_{dp}0$ can vary significantly in time depending in the phase and intensity of the precipitation at the radar site.

Box 1: For a beam/azimuth, $\Phi_{dp}0$ is calculated as the mean of Φ_{dp} in first 5 consecutive gates with precipitation. The hydro-meteorological echos typically have $\rho_{hv} \geq 0.85$, a threshold to define these gates. For the azimuths related to a specified target, only the profiles following a criteria on inter-percentile range, between 90^{th} and 10^{th} are selected, in order to discard the outliers and maintain spatial stability in $\Phi_{dp}0$ values. In heavy rain, the Ψ_{dp} profile exhibit high values and might be folded as big negative values. So, it is necessary to have an unfolding algorithm in place.

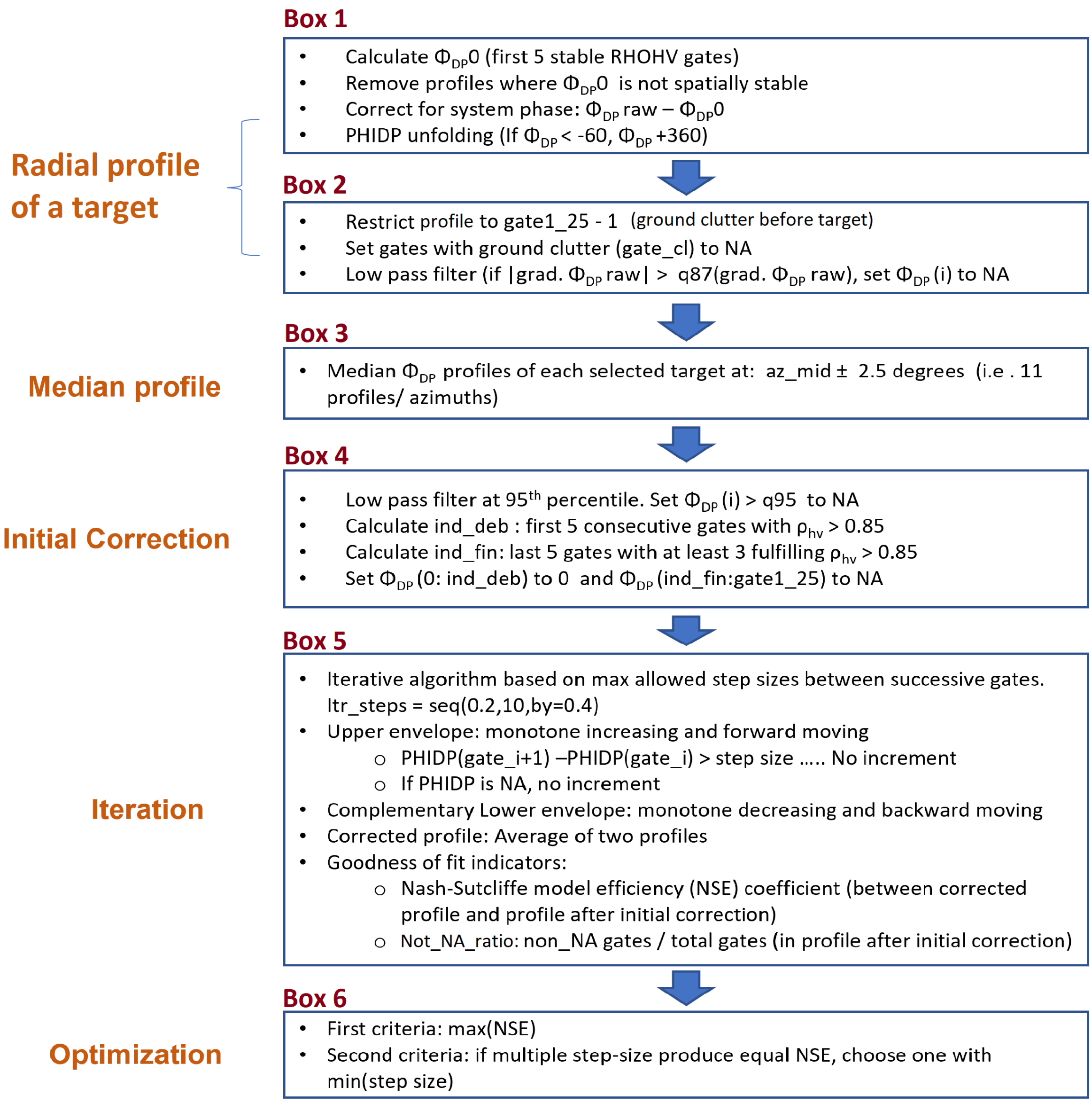

Box 1

- Calculate $\Phi_{DP}0$ (first 5 stable RHOHV gates)
- Remove profiles where $\Phi_{DP}0$ is not spatially stable
- Correct for system phase: Φ_{DP} raw – $\Phi_{DP}0$
- PHIDP unfolding (If $\Phi_{DP} < -60$, $\Phi_{DP} + 360$)

Box 2

- Restrict profile to gate1_25 - 1 (ground clutter before target)
- Set gates with ground clutter (gate_cl) to NA
- Low pass filter (if |grad. Φ_{DP} raw| > q87(grad. Φ_{DP} raw), set Φ_{DP}(i) to NA

Box 3

- Median Φ_{DP} profiles of each selected target at: az_mid ± 2.5 degrees (i.e . 11 profiles/ azimuths)

Box 4

- Low pass filter at 95th percentile. Set Φ_{DP}(i) > q95 to NA
- Calculate ind_deb : first 5 consecutive gates with $\rho_{hv} > 0.85$
- Calculate ind_fin: last 5 gates with at least 3 fulfilling $\rho_{hv} > 0.85$
- Set Φ_{DP}(0: ind_deb) to 0 and Φ_{DP}(ind_fin:gate1_25) to NA

Box 5

- Iterative algorithm based on max allowed step sizes between successive gates. Itr_steps = seq(0.2,10,by=0.4)
- Upper envelope: monotone increasing and forward moving
    - PHIDP(gate_i+1) –PHIDP(gate_i) > step size ….. No increment
    - If PHIDP is NA, no increment
- Complementary Lower envelope: monotone decreasing and backward moving
- Corrected profile: Average of two profiles
- Goodness of fit indicators:
    - Nash-Sutcliffe model efficiency (NSE) coefficient (between corrected profile and profile after initial correction)
    - Not_NA_ratio: non_NA gates / total gates (in profile after initial correction)

Box 6

- First criteria: max(NSE)
- Second criteria: if multiple step-size produce equal NSE, choose one with min(step size)

FIGURE 5.1: Organigramme of Φ_{dp} regularization algorithm. The measured differential phase-shift (Ψ_{dp}) is simply referred to as Φ_{dp} raw for simplicity.

Box 2: Ψ_{dp} profile oscillates significantly at the gates with ground clutter, and exhibits very low co-polar correlation coefficients ($\rho_{hv} < 0.85$). The choice of ρ_{hv} cutoff at 0.85 is based on the statistical analysis of the rain and ML in Grenoble (Tab 3.3 and Khanal et al. (2019)). For high elevation angles, Giangrande et al. (2008) suggest a ρ_{hv} threshold of 0.9 to minimize the contamination from non hydro-meteorological scatterers. In order to avoid the noise from ground clutter, Ψ_{dp} values are set to "NA" at the gates with ground clutter and range of Φ_{dp} correction limited to first gate of the target with $Z > 25\,dBZ$ ($gate1\_25$). Hubbert and Bringi (1995) proposed a repetitive low pass filter with cutoff at 1.5 standard deviation (SD) of the mean in their Φ_{dp} processing algorithm. Here, a single low pass filter is applied in the gradient of the profiles with the cutoff at 87^{th} percentile of the mean, which would be 1.5*SD in a normal distribution according to the empirical rule. This steps makes sure very large oscillations originating from ground clutter are discarded. At the same time large change in values due to backscattering differential phase shift (δ_{hv}) are discarded as well.

Box 3: After these adjustments, a median profile is calculated for each target. Trömel et al. (2013) recommend sectoral median of Φ_{dp} profiles in-order to have a stable signal. Here, sectors of 5° are taken for each target. 2.5° sector are taken on each side from the azimuth at the center of the target i.e $az_{mid} \pm 2.5°$, this amounts to 11 radial profiles for each target. Rest of the regularization processing is performed on this median profile. The raw median profile displayed in grey in the third subplot of Fig 5.2.

Box 4: The "raw" median profile is subjected to some initial processing before applying the iterative algorithm. Like in individual radials, a low pass filter is applied to the median profile, but with cutoff at 95^{th} percentile i.e approximately 2*SD in a normal distribution. The profile after this initial processing routine is shown in black in the third subplot of Fig 5.2. First 5 successive gates with $\rho_{hv} \geq 0.85$ indicates the start of gates with precipitation. Similarly last 5 successive gates that contain at least 3 gates with $\rho_{hv} \geq 0.85$ indicates the end of precipitating gates. Some targets have isolated ground clutter just before 'gate1_25' and taking 3 out of 5 stable gates helps to capture Φ_{dp} changes between them and the target, i.e. prevents the under-estimation of Φ_{dp} to some extent. In further regularization Φ_{dp} are allowed to change only between these gates with precipitation.

Box 5: The median profiles are subjected to a iterative algorithm that controls the maximum allowed jumps on the successive gates in backward and forward directions. The iterations are done at maximum allowed step-sizes between 0.2 - 10 degree per gate at the interval of 0.4 degree. In a forward envelope, envelope starts at $\Phi_{dp} = 0$ at gate 0. When the increase in Φ_{dp} values in the next gate are within the allowed range, the envelop takes new increased value, else it remains the same. This formulation is based on the cumulative i.e monotone increasing nature of the Φ_{dp} profile. A complementary backward monotone decreasing envelope is calculated starting from the last gate with precipitation. As there is no fixed initial value in the backward envelope (like 0 in forward envelope) it is estimated as 25^{th} percentile of Ψ_{dp} in last 4 gates with precipitation. Finally the 'corrected' Φ_{dp} profile is calculated as the average between the forward and backward envelopes in the each gate. As forward and backward envelopes are respectively monotone increasing and decreasing, monotone increasing nature of the corrected profile is preserved. For each iteration Nash-Sutcliffe model efficiency (NSE) coefficient between green and black profiles in Fig 5.2 is calculated. Not_NA_ratio (ratio of gates with black and grey values) is also recorded; it provides percentage of gates in Ψ_{dp} profiles populated with physical values.

Box 6: In the end, the final and Not NA ratio values are stored as the goodness of fit indicators for a given Φ_{dp} profile (chapter 6). NSE is the goodness of fit indicator for the considered jump allowed between the successive gates, and Not_NA_ratio provides the goodness of raw data.

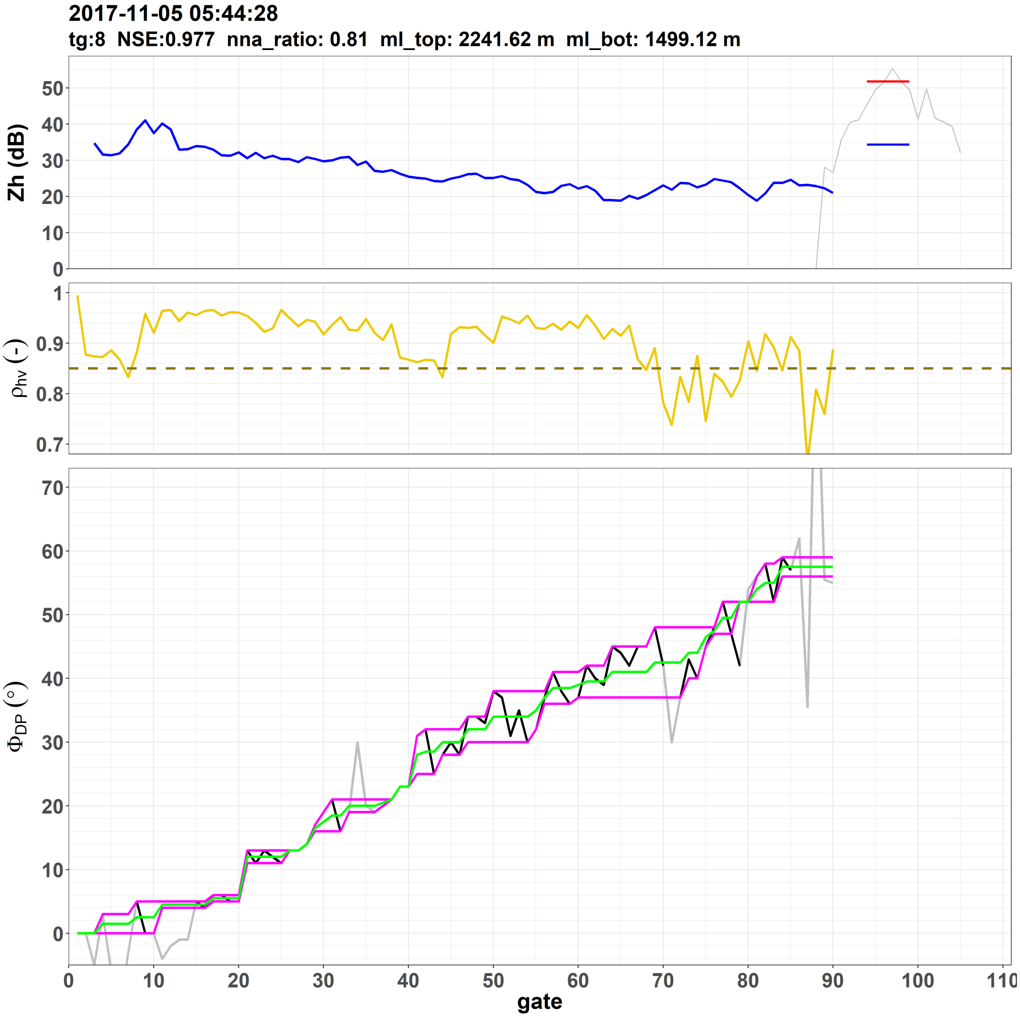

FIGURE 5.2: Working principle of Φ_{dp} regularization algorithm. Range profiles of Z_h (top), ρ_{hv} (mid) and Φ_{dp} (bottom) at PPI-O° of MOUC are shown here at the specific timestep when the center of 0° beam is within ML for target 8. In the bottom graph, grey line is the raw Phidp, corrected for $\Phi_{dp}0$ profile. The Φ_{dp} regulation algorithm is shown in the bottom subplot. Raw Φ_{dp} is shown in grey. After initial correction black profile is obtained. An average of forward moving monotone increasing upper envelop (upper violet) and backward moving monotone decreasing lower envelope (lower violet), provides the regulated Φ_{dp} profile (green). Nash-Sutfliffe efficiency (NSE) coefficient between green and black profiles are calculated, similarly ratio of gates with black to all (grey) values (nna_ratio, i.e. not NA ratio) is recorded.

If the regularized Φ_{dp} matches the pre-processed median Ψ_{dp} profile perfectly with an estimation error variance equal to zero, the resulting NSE coefficient is 1. $NSE = 0$ indicates that the model has the same predictive skill as the mean of the raw profile in terms of the sum of the squared error. When a modelled profile has an estimation error variance significantly larger than the variance of the observed profile, the NSE becomes negative, i.e observed mean is a better predictor than modelled one. Values of the NSE nearer to 1, suggest a model with more predictive skill. In profiles with many of NAs in the pre-processed median Ψ_{dp} or regulated Φ_{dp}

profile, the NSE criteria is not a sufficient criteria, as the comparisons are made only in the gates with both data. Not_NA_ratio makes sure that enough gates are populated within a given range profile, and provides additional criterion to improve upon the results provided by NSE coefficients.

The optimal step-size is selected by maximizing the NSE coefficient and then minimizing the step size, if two iterations produce the same NSE. The choice of algorithm based on maximum allowed step size between consecutive gates exploits monotone increasing nature of the range profile of Φ_{dp}. The forward moving monotone increasing upper envelop (upper violet) and backward moving monotone decreasing lower envelope (lower violet), provides the regulated Φ_{dp} profile (green) in the third subplot of Fig 5.2.

5.3 Implementation

Some examples of the application of Φ_{dp} regulation algorithm are discussed in this section. We again go back to the 3- 4 January 2018 event shown in Fig 4.4, where the radar is in the above ML (in snow) in the beginning of the event between 18h00 and 01h00; Fig 5.3 shows the example of the regularization at 21:40 during this period. The ML raises quickly between 01:00 and 05:00 on 4^{th} Jan; between 02:20 and 04:30 the radar is within the ML; Fig 5.4 shows an example of the Φ_{dp} regularization at 02:50 during this period. And towards the end of the event ML is above the radar, i.e. beam center is in rain; Fig 5.5 shows an example of regularization at 07:20 during this period.

The snow regime, Fig 5.3, displays relatively low PIA and ρ_{hv} is mostly greater than 0.97. The raw profiles of Φ_{dp}, shown in grey, are not very noisy. This results often in high NSE coefficient and high Not_NA_ratio, which signifies that the Φ_{dp} regulation algorithm performs well in this region. There are two probable cases in the snow regime when the raw profiles might fluctuate significantly. First such case can be the region of aggregation, where the scatterers tend to be in the Mie scattering regime, and this region is known to produce significant backscattering phase shift (Trömel et al. 2013). Another case with considerable fluctuations is when the radar is close to the ML top. As beam broadens further away from the radar, it might be contaminated by the upper part of ML, despite the beam center located in the snow regime.

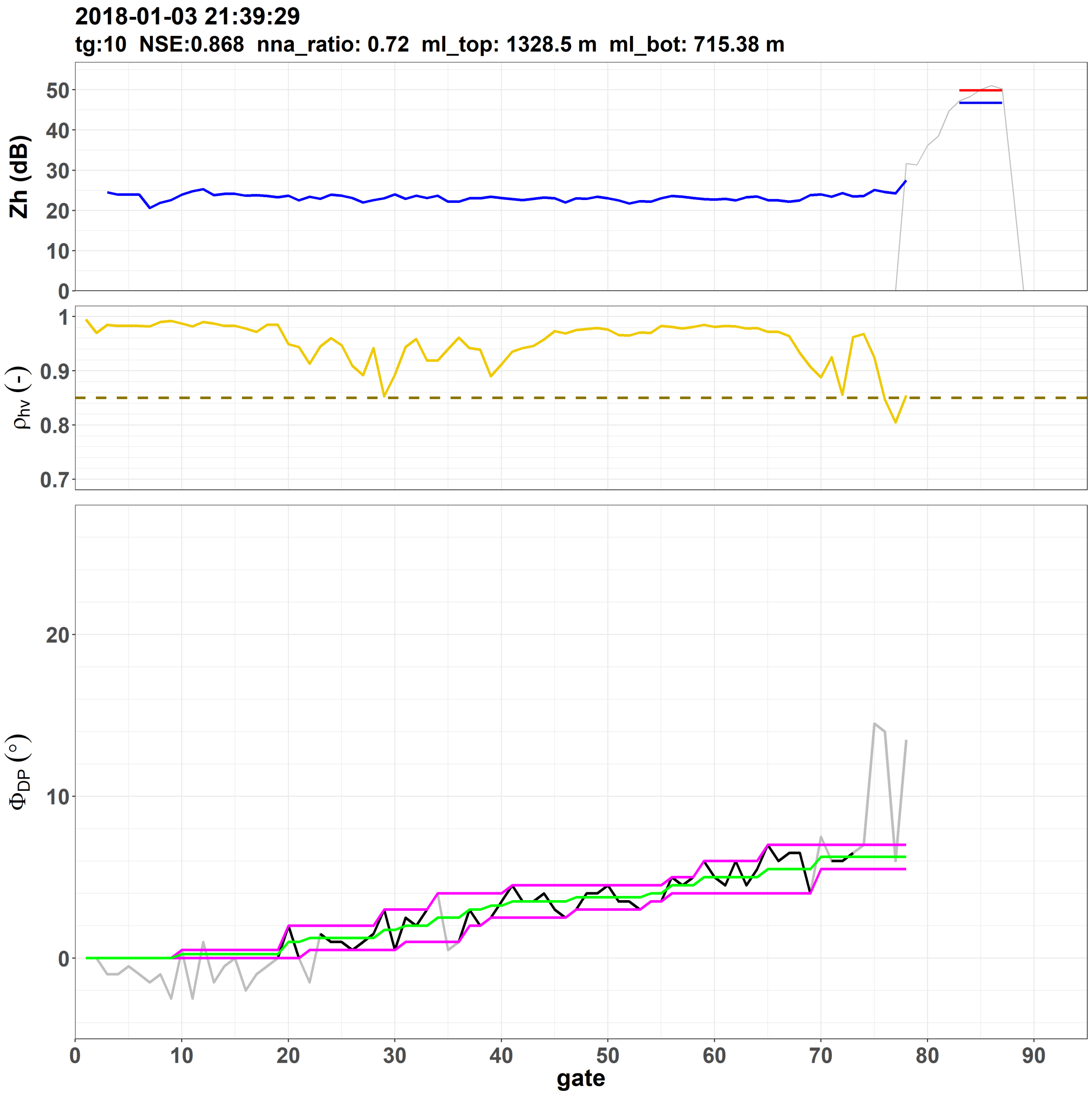

FIGURE 5.3: Φ_{dp} regularization: 3 January 2018, 21:40, target 10, snow, MOUC radar, 0° elevation angle. Top sub-plot shows the range profile of Z_h in blue; dry-weather echo of target 8 in grey where red and blue segments show the dry and wet returns for the current time-step. Middle sub-plot shows the range profile of ρ_{hv} with dotted horizontal at 0.85 used to identify non-meteorological returns. Bottom sub-plot shows the Φ_{dp} regularization process; raw profiles in grey, pre-processed profile in black, envelopes in violet and the regularized profile in green.

The ML "regime", Fig 5.4, displays relatively high PIA, high Φ_{dp} and lower ρ_{hv}, compared to (rain and) snow regime. The ρ_{hv} value in this regime is usually between 0.95 and 0.85. In the given example, the raw profile of Φ_{dp} is not very noisy, but in the regions of low ρ_{hv} and low Z_h it fluctuates significantly; same is true when the radar is located close to the ML boundaries. Within ML, the Φ_{dp} regularization, often has relatively lower NSE coefficient and lower Not NA ratios. As the elevation angle of the measurement is 0°, the propagation effect is dominant in the range profiles, and the backscatter effects are localized surges in raw profile (Ψ_{dp} profile, in grey) and filtered by the consecutive low pass and maximum allowed step-size filters. As long as these effects do not outlast the range of regularization, limited by the presence of mountain targets, the remaining local surges are removed by forcing the corrected profile to be monotone increasing.

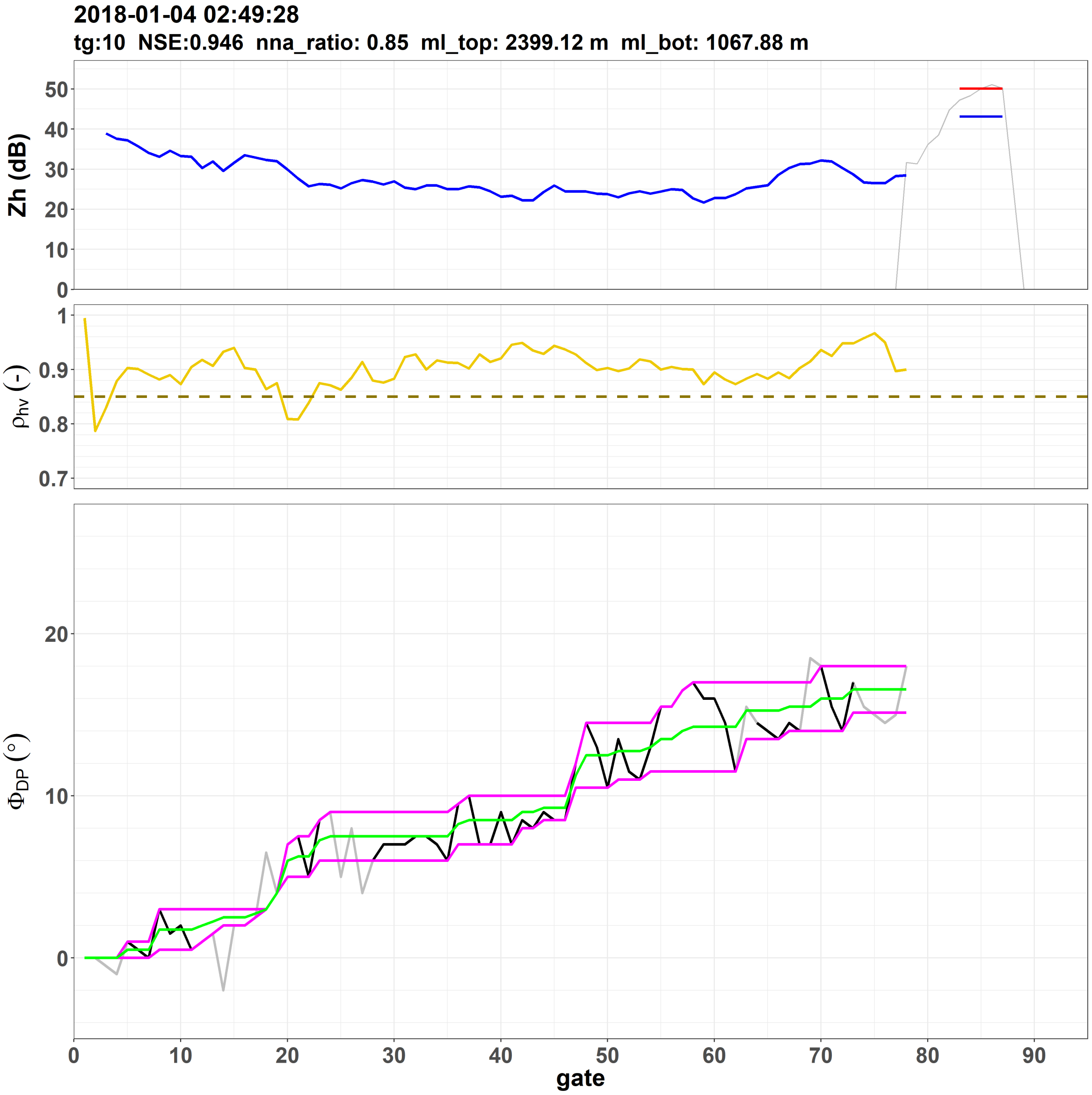

FIGURE 5.4: Φ_{dp} regularization: 3 January 2018, 02:50, target 10, ML, MOUC, 0° elevation angle. Same description as in Fig 5.3

The rain regime, Fig 5.5, displays PIA and ρ_{hv} larger than snow but lower than ML, and Φ_{dp} smaller than in ML. In rain, ρ_{hv} is often between 0.99 and 0.95. The Φ_{dp} profile can be very noisy in low rainfall intensities. Similarly, the profiles close to the ML bottom can be quite noisy as well due to non-uniform beam filling (NUBF).

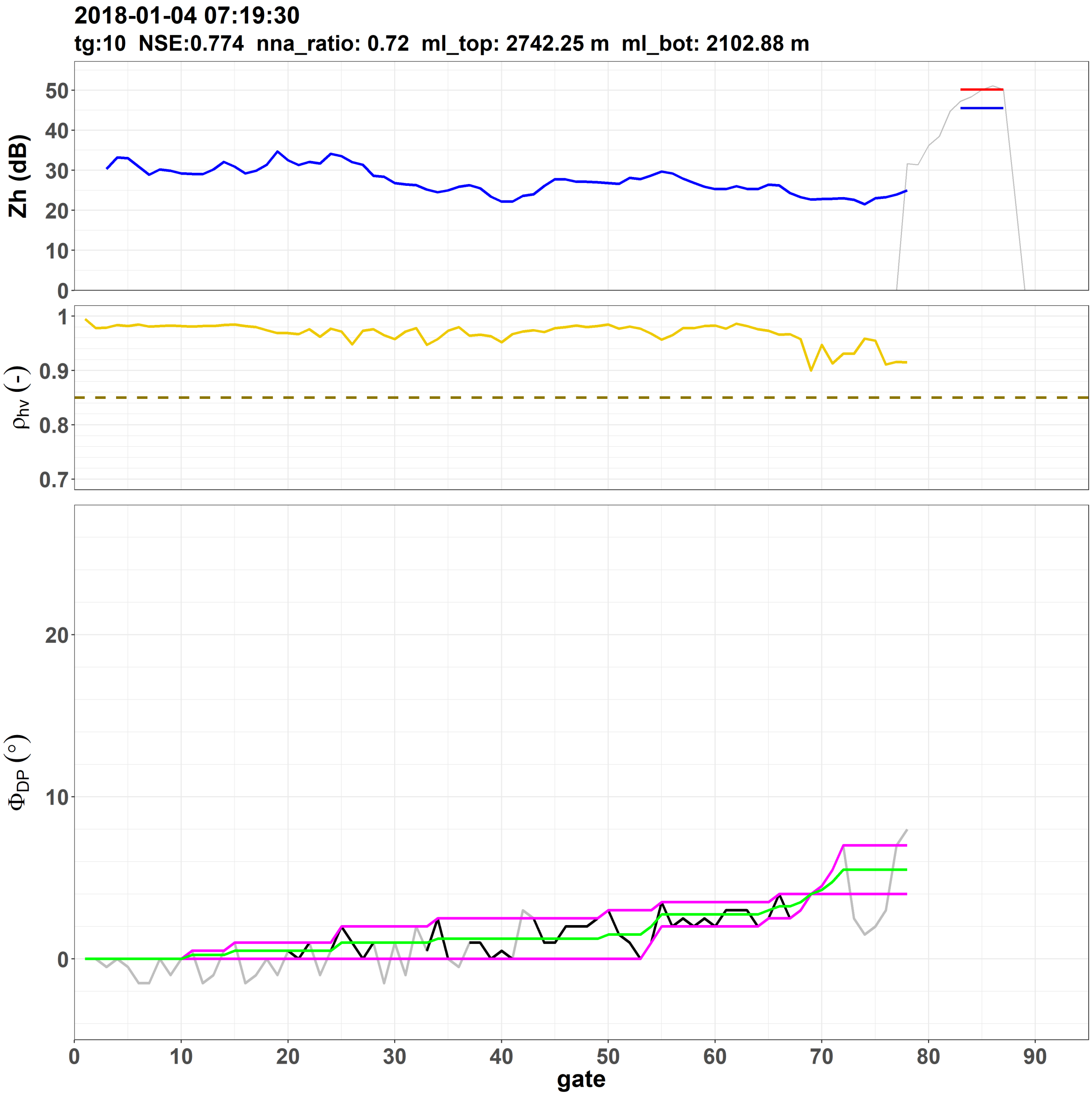

FIGURE 5.5: Φ_{dp} regularization: 3 January 2018, 07:20, target 10, rain, MOUC, 0° elevation angle. Description same as in Fig 5.3.

The examples of Φ_{dp} regularization shown above, in snow, ML and rain for 3 January 2018, all display stable Φ_{dp} range profiles without much noise. However, due to the low precipitation intensities, location of radar close to ML boundaries and presence of ground clutter, the Φ_{dp} range profiles are often noisy. One such example is shown in Fig 5.6. In this example, the radar measurements are in the upper part of ML, just below the ML top. The range profile of Ψ_{dp} is very noisy compared to the previous profiles. The ρ_{hv} profile regularly dips below 0.85. This is not a reliable profile and need to be rejected. The NSE coefficient is 0.253 and the Not_NA_ratio is 0.57, significantly lower compared to the previous examples. NSE and Not_NA_ratio provide a quantitative measure of goodness of fit of regularization and noise level in raw profile respectively. Based on observation of many regularized profiles, used, profiles with NSE < 0.5 or Not NA ratio < 0.4 are subject to caution hereinafter.

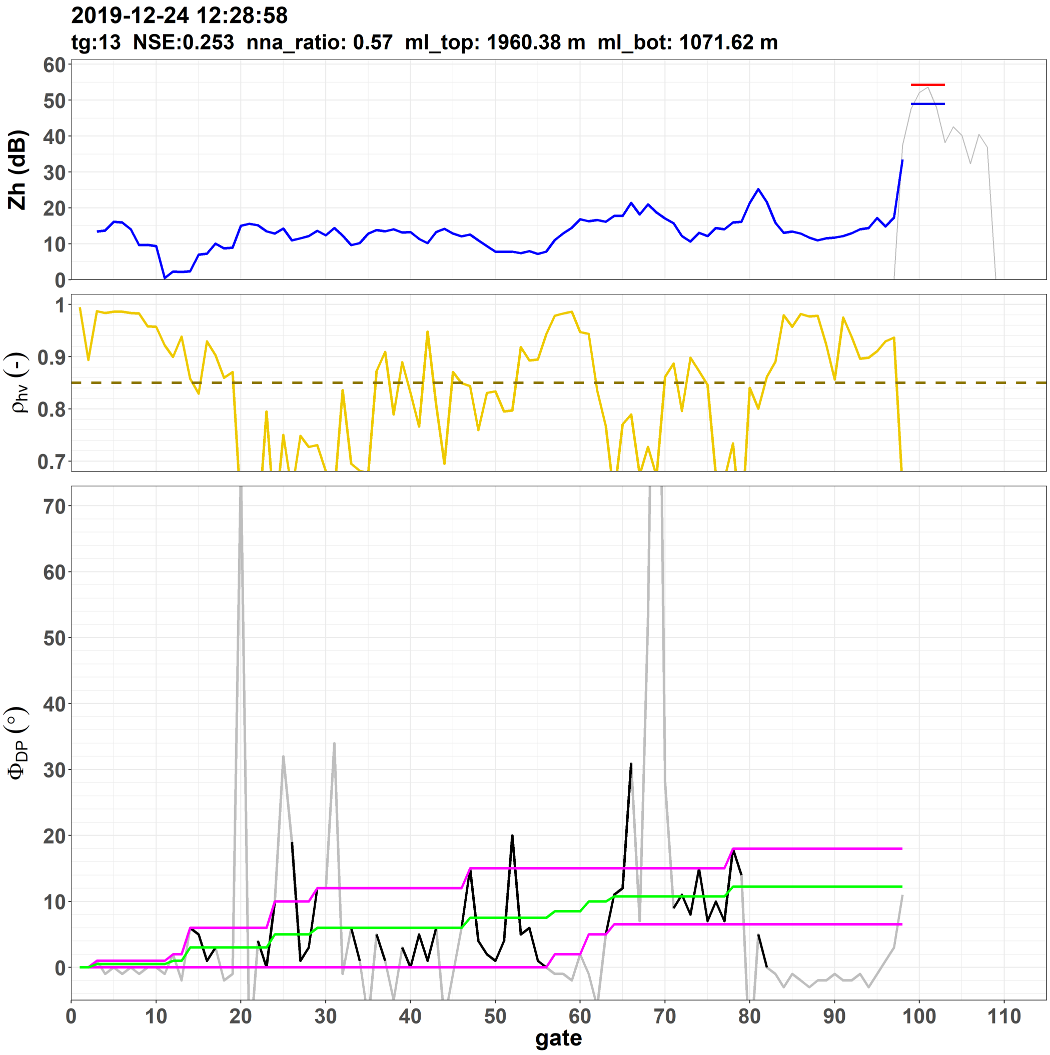

FIGURE 5.6: Φ_{dp} regularization: 24 December 2019, target 13. Description same as in Fig 5.3.

A similar strategy of Φ_{dp} regularization can be applied to the quasi-vertical profiles (QVPs), (Ryzhkov et al. 2016) of Φ_{dp} observed by the valley-based XPORT radar at high elevation angles, an example is shown in Fig 5.7. QVPs are produced by aggregating the observation at a given elevation angle of all the azimuths and projecting them to the vertical axis. Scans at high elevation angles are preferred to produce QVPs.

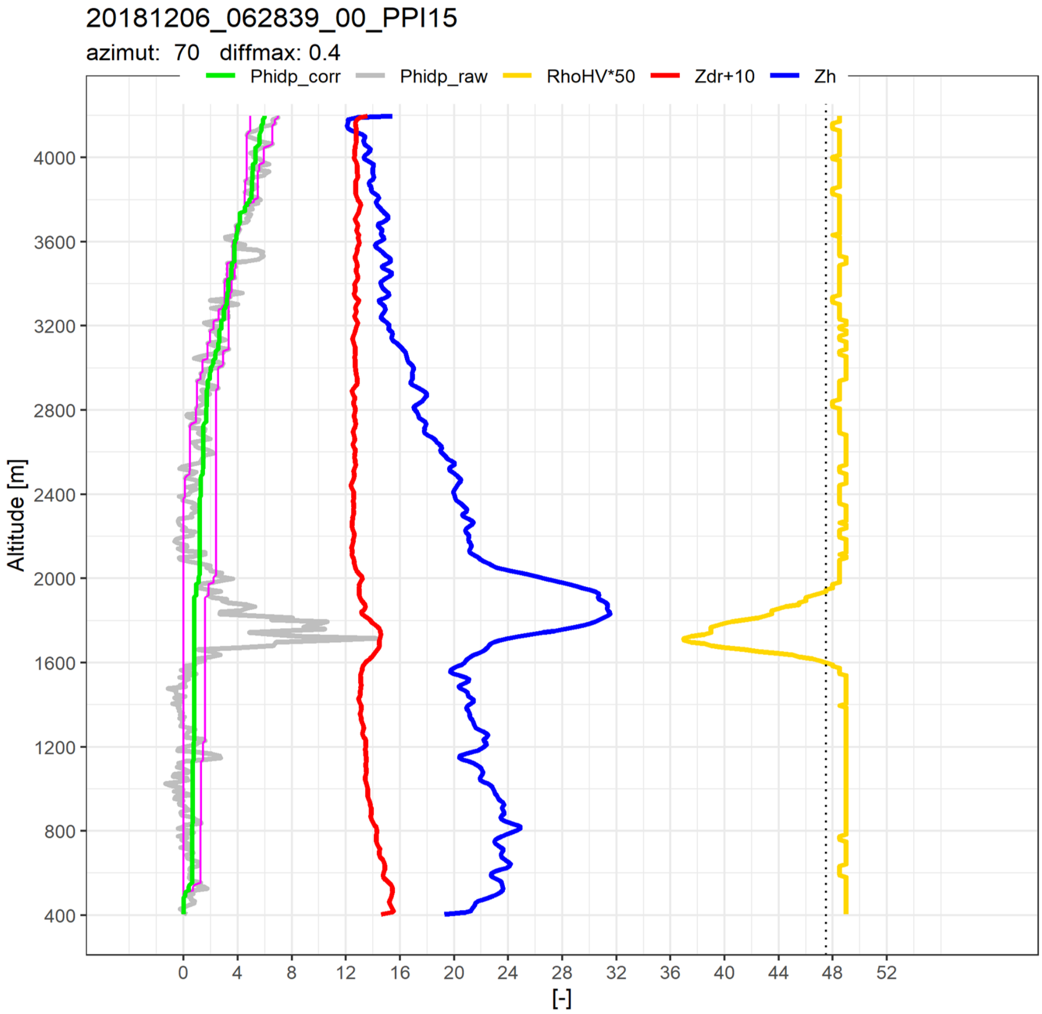

FIGURE 5.7: Φ_{dp} regulation for quasi vertical profile of XPORT observation. QVP from 15° elevation angle XPORT observables are shown; $Z_{dr} + 10$ in red, Z_h in blue, $\rho_{hv} * 50$ in gold, measured Ψ_{dp} in grey. The backward and forward envelopes are shown in violet. The regularized Φ_{dp} is shown in green. ML is present between 1600m and 2200m asl. Within the lower part of the ML, a "bump" can be observed in the Ψ_{dp} profile, which is attributed to backscatter phase shift.

In this example, PPI scans of XPORT at 15° elevation angles are used. All the observables of XPORT are shown in the figure. The presence of ML is shown by sudden changes in vertical profiles of horizontal reflectivity Z_h, differential reflectivity Z_{dr} and correlation coefficient ρ_{hv}. ML top is defined as the upper inflection point of Z_h profile and ML bottom is defined as the lower inflection point of ρ_{hv} profile (chapter 3). The Ψ_{dp} profile, in grey, is generally monotone increasing along the range, but in the ML altitudes, there is a large bump. This localized increase is attributed to the backscatter phase shift (δ_{hv}) (Trömel et al. 2013). The forward and backward envelopes in the Φ_{dp} regularization algorithm, in violet, efficiently separate this backscattering component from the propagation component, i.e Φ_{dp}, in green. The increase in Φ_{dp} above 2800 m altitude is most probably the result of

Mie scatters produced by aggregation of ice crystals. Collision and break-up most probably describe the reduction of Φ_{dp} below 2800m. Above the ML there is not much change in the regularized Φ_{dp} profile suggesting negligible attenuation for such high elevation angle and close-range measurements. This supports the hypothesis of negligible attenuation made in chapter 3.

5.4 Conclusions

The Φ_{dp} regularization algorithm performs satisfactorily well (from visual verification of many profiles) when the radar and the pulse volume is clearly in rain or snow regime. The noise in the profile increases significantly in presence of ground clutter, which is identified as Z_h > 25 dBZ in dry-weather observation and sudden decrease in ρ_{HV} profile. These non-meteorological targets often have high dry weather reflectivity (>25 dB) and low ρ_{HV} (<0.85). Also the local backscattering components (δ_{hv}) of the phase shift can add noise in the Ψ_{dp} profiles especially within and around ML. At low elevation angles, like 0° PPI scan, the backscattering component is not always evident like in high elevation angle, where it manifests itself as "bumps" in the range profile. It is however a local effect, use of low pass filters combined with the limits in maximum step-sizes between consecutive gate are able to remove the local surges or dips in the Ψ_{dp} range profiles. The NSE and Not NA ratio criteria provide the quantitative measurement of the goodness of fit of regularization and the raw profiles respectively. A threshold of NSE $\geq$ 0.5 and not NA ratio $\geq$ 0.4 is used in the following chapters to define well regularized Φ_{dp} profiles; the profiles not meeting either of the criteria are subject to caution. Two instances that can introduce significant errors in the regulated profiles are:
i) estimation of $\Phi_{dp}(r_0)$: The measurements from the first few gates are not reliable, and also the on-site meteorological conditions can introduce significant offset in the range-cumulative Φ_{dp} measurements.
ii) estimation of starting Φ_{dp} for the backward envelope.
We reiterate that, in order to stabilize the Φ_{dp} signal, the Φ_{dp} profiles at azimuthal segment of 5°, i.e. az_mid ± 2.5 degree from the azimuthal center of each target. Furthermore, in order to stabilize the $\Phi_{dp}(r_0)$ estimates, the real-time $\Phi_{dp}(r_0)$ of all the targets are compared to ensure that the azimuthal variation is within expected limits.

Chapter 6

PIA - Φ_{dp} relationship in the melting layer

6.1 Introduction

The relationship between specific attenuation (A) and specific differential phase (K_{dp}) is expressed as a power model:

$$A = a_{AK}\, K_{dp}^{b_{AK}} \tag{6.1}$$

In rain, Bringi et al. (1990), Matrosov et al. (1999) and Testud et al. (2000) have shown the $A - K_{dp}$ relationship to be quasilinear i.e. $b_{AK} \approx 1$, based on drop-size distributions (DSD) derived from disdrometer measurements and calculations based on the scattering properties of individual drops at X-band. With such hypothesis, we get $A = a_{AK}\, K_{dp}$ and the PIA at a given range r could be related to the Φ_{dp} profile as

$$PIA(r) = a_{AK}\, \Phi_{dp}(r) \tag{6.2}$$

The PIA and Φ_{dp} estimates in Chapter 4 and 5 allows us to study the PIA-Φ_{dp} relationship within the ML under the linearity hypothesis. As different microphysical processes are dominant in different phases of melting it is further interesting to investigate how the relationship evolves in different stages of melting.

6.2 Dataset

The 0° elevation PPI scan from the mountain-top MOUC radar is the primary source of data used to estimate $PIA(r_M)$ and regulate $\Phi(r_0, r_M)$. The characteristics of the melting layer is provided by XPORT and MRR radars operated in the valley. 78 days of MOUC data between 18 November 2016 and 11 December 2021 are available. It corresponds to 43 precipitation events for which the melting layer occurs close to the altitude of 0° elevation beam center of MOUC radar (1913 m asl). ML information on 29 of these events are provided by XPORT and 14 by MRR. The summary of all the events is shown in Table B.1. The temporal resolution of MOUC data is 5 minutes. For each time steps $PIA(r_M)$ and $\Phi(r_0, r_M)$ are available in the direction of (up to) 20 mountain targets described in Table 4.1.

6.3 PIA vs Φ_{dp}

To put things in perspective, we first look into the general evolution of $PIA(r_M)$ and $\Phi_{dp}(r_M)$ for an event with ML close to MOUC radar altitude. Figure 6.1 visualizes the time series of PIA and total Φ_{dp} from MOUC radar and ML identification time series from XPORT radar, during an event on 4-5 November 2017. The time series of the XPORT observation in the bottom plot shows the location of the ML, according to the ML identification procedure described in Chapter 3, with respect to the MOUC radar at 1913 m. The ML top is defined by the upper inflection point of Z_h and the ML bottom by the lower inflection point of ρ_{hv} (Chapter 3 and (Khanal et al. 2019)). At the beginning of the event the MOUC radar is below the ML i.e. in rain regime. As the event progresses the ML descends slowly, around 03:00 GMT the MOUC radar i.e. the center of 0° PPI beam is within the melting layer. Towards the end of the event, around 09:00 GMT the melting layer descends further and the MOUC radar is above the ML i.e. in the snow regime. The top subplot shows the time evolution of a mountain return (echo) and the corresponding PIA estimation at range r_M during this event. When the center of the 0° PPI beam is in rain regime, PIA is relatively small; it increases significantly (up to 15 dB over 20 km for target 10 in Fig 6.1) when the beam center is within the ML and decreases to 0 in the snow regime. The attenuation in the snow regime is negligible and could be an estimate of dry period echo when data in dry periods is not available. The middle sub-plot shows the corresponding $\Phi_{dp}(r_M)$ signature at the gates close to the mountain target, also observed using the MOUC radar. The $\Phi_{dp}(r_M)$ time series closely follows the pattern of $PIA(r_M)$ and shows a significant increase within the ML.

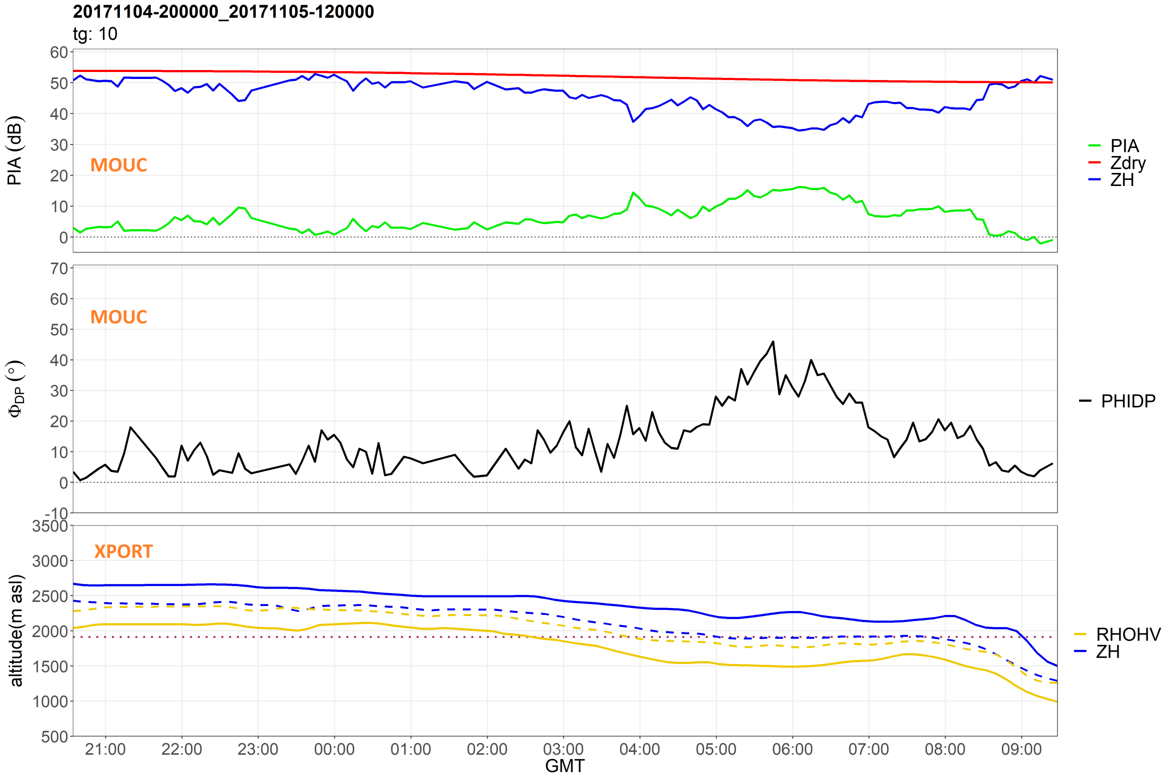

FIGURE 6.1: PIA, Φ_{dp} and ML time series: 4-5 November 2017, target 10, range 20 km. Top subplot shows the application of MRT for PIA (green) estimation as a difference of dry-weather returns Z_h^{dry} (red) and wet-weather returns Z_h (blue). Middle subplot shows the time series of regularized Φ_{dp} at range r_M of target 10. The bottom subplot shows the characteristic altitudes of the melting layer provided by XPORT observation: ML top (continuous blue line) as a altitude of Z_h top and ML bottom (continuous gold line) as altitude of ρ_{hv} bottom. Horizontal dotted maroon line at 1913 m asl shows the altitude of center of 0° elevation MOUC beam.

The $PIA(r_M)$ - $\Phi_{dp}(r_M)$ pairs for all available timesteps (corresponding to the 43 precipitation events) and all targets are plotted in Figure 6.2. Chapter 4 mentioned $PIA = 0$ as a reasonable assumption for cases with $Z_h^{dry} - Z_h < 0$, similarly Chapter 5 listed NSE and Not_NA_ratio as a goodness test for Phi_{dp} regularization. As such considering $PIA \geq 0$, $NSE \geq 0$ and $Not\_NA\_ratio \geq 0$ includes all reasonable PIA and Phi_{dp} estimates. The PIA vs Φ_{dp} scatterplot of all observations within the ML shows no clear relationship between two variables. The 0-forced linear fit has a slope (a_{AK}) of 0.27, but with very large spread and low R^2 of 0.46. Although the slope of the 0-forced fit is closer to the DSD observed slope in rain, the scatter neither converges towards the expected rain value ($a_{AK} \approx 0.3$) nor towards an expected ML value ($a_{AK} \approx 0.5$) (Delrieu et al. 2020). It is most probably due to the fact that hydrometeors' characteristics vary significantly at different stages of melting. In addition, the ML limits and widths vary significantly for different events.

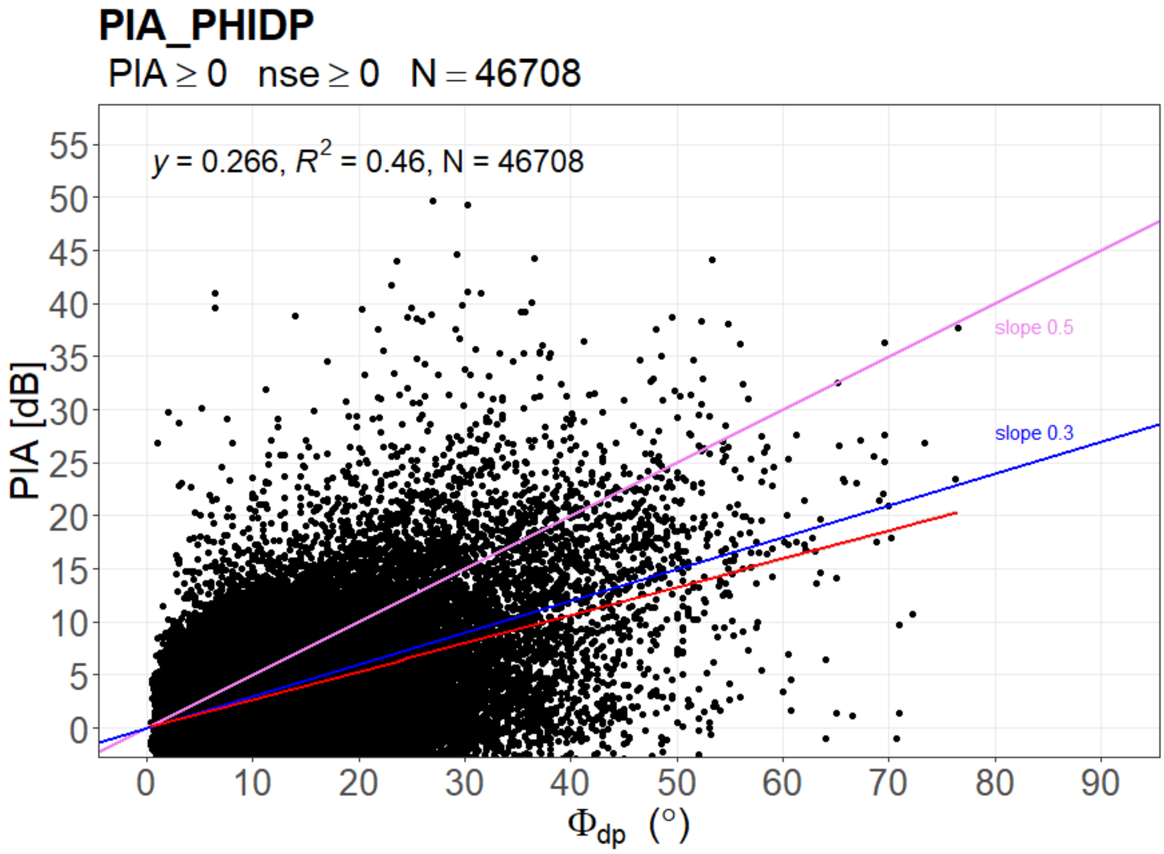

FIGURE 6.2: $PIA(r_M)$ vs $\Phi_{dp}(r_M)$ scatterplot for all the events and targets together. The violet line with slope of 0.5 corresponds to the expected a_{AK} value in the melting layer (Delrieu et al. 2020). The blue line with slope of 0.3 corresponds to the estimated a_{AK} value in rain. Red line is the 0-forced linear fit, and the summary of the fit is annotated towards the top of the plot.

In order to compare the PIA - Φ_{dp} pairs in the different parts of the ML and to account for the variations of the ML thickness we define a scaled altitude as $scaled\_alt = (alt.MOUC - alt.mlbot)/ml.width$. The idea is to refer, for each time step, the altitude of the 0° PPI beam center of MOUC radar in relation to the ML bottom, and normalize it by ML width. During these events the ML width has mean of 676m and standard deviation of 164 m. The scaled altitude value of 0 means that the beam center is at ML bottom altitude, and 1 means that it is at ML top altitude.

Scaled altitudes greater than 1 means that the MOUC radar i.e. beam center is located in snow region and values smaller than 0 signify it is in the rain region. The scaled altitudes are grouped at class of 0.1 i.e. the group 0.5 contains the values between 0.45 and 0.55. As such, each altitude class represents different stages of the melting process and is comparable for different events. In the later sections, scaled altitudes ≥ 1 are referred to as the snow region, $1 <$ altitudes <0.5 are be referred to as the upper melting layer, $0.5 <$ altitudes <0 are referred to as the lower melting layer and altitudes < 0 as the rain region.

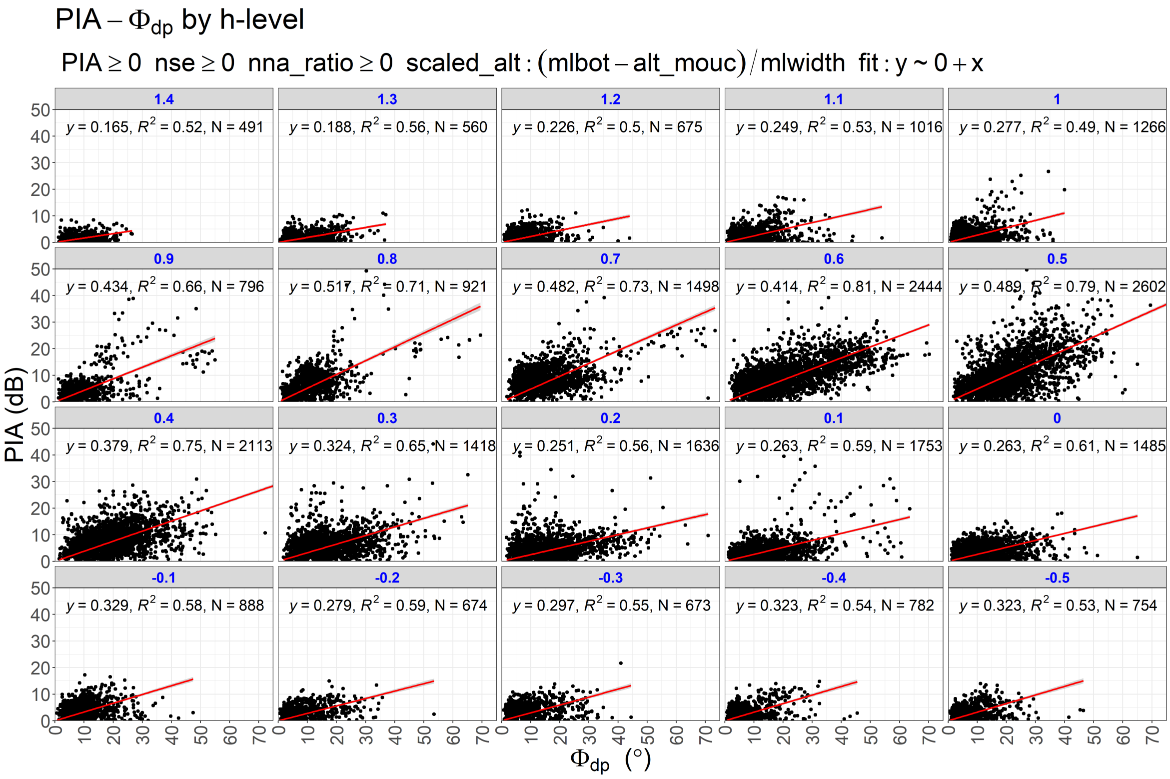

FIGURE 6.3: PIA vs Φ_{dp} 0-forced linear fits for all altitude class, full dataset. 0 corresponds to ML bottom and 1 corresponds to ML top. Every subplot: corresponds to a scaled-altitude highlighted in blue on the top; fits a 0-forced linear fit between PIA - Phi_{dp} pairs, fitted as the red line and summary of slope, R^2 and number of observations are annotated on the top within the graph. The subplots in the 1st row show the relationship in snow, 2nd row in upper ML, 3rd row in lower ML and 4th row in the rain.

Figure 6.3 shows the division of the PIA-Φ_{dp} pairs to different scaled altitudes. Almost all available observations are utilized here i.e. (PIA ≥ 0, NSE ≥ 0 and Not NA ratio ≥ 0). Looking at the slopes of the simplest correlation model (0-forced linear relationship, i.e. a_{AK} is estimated as the ratio of the means of the PIA and Φ_{dp} values), one can note that the slope is comprised between 0.16 and 0.28 in snow, it is significantly higher in the upper ML (0.43-0.51) and reduced in the lower ML (0.25-0.38). It is between 0.28 and 0.32, the expected range of values, in the rain region.

The evolution of the number of pairs in each class indicates that a greater number of observations are available within the ML, as the result of the selection of the events. The R^2 coefficients are relatively low in the snow and rain regions (less than 0.6); they consistently exceed 0.7 in the upper part of the ML (classes 0.4-0.8). Some of the scatterplots exhibit quite a large number of outliers with too low Φ_{dp} with respect to the PIA values (e.g. scaled altitude class 0.9) while some others present high Φ_{dp} values for very low PIA, especially in the rain, snow and lower ML regions (e.g. classes -0.3, 0.1 and 1.1). In order to mitigate the errors in the PIA estimation due to the dry-weather variability of the mountain targets in one hand, and the impact of the Ψ_{dp} measurement noise on the regularization of the Φ_{dp} profiles on the other hand. We consider a more stringent filtration criteria with $PIA_M \geq 1$ dB, NSE $\geq$ 0.5 and Not NA ratio ≥ 0.4. The standard deviation of the dry-weather mountain returns is between 1 and 1.5 dB (Chapter 4), leading to the minimum detectable PIA of about 1 dB considered here. The specific values of 0.5 for NSE and 0.4 for not NA ratio were taken after visual inspection of the Φ_{dp} regularization of numerous profiles similar to Fig 5.2 (Chapter 5).

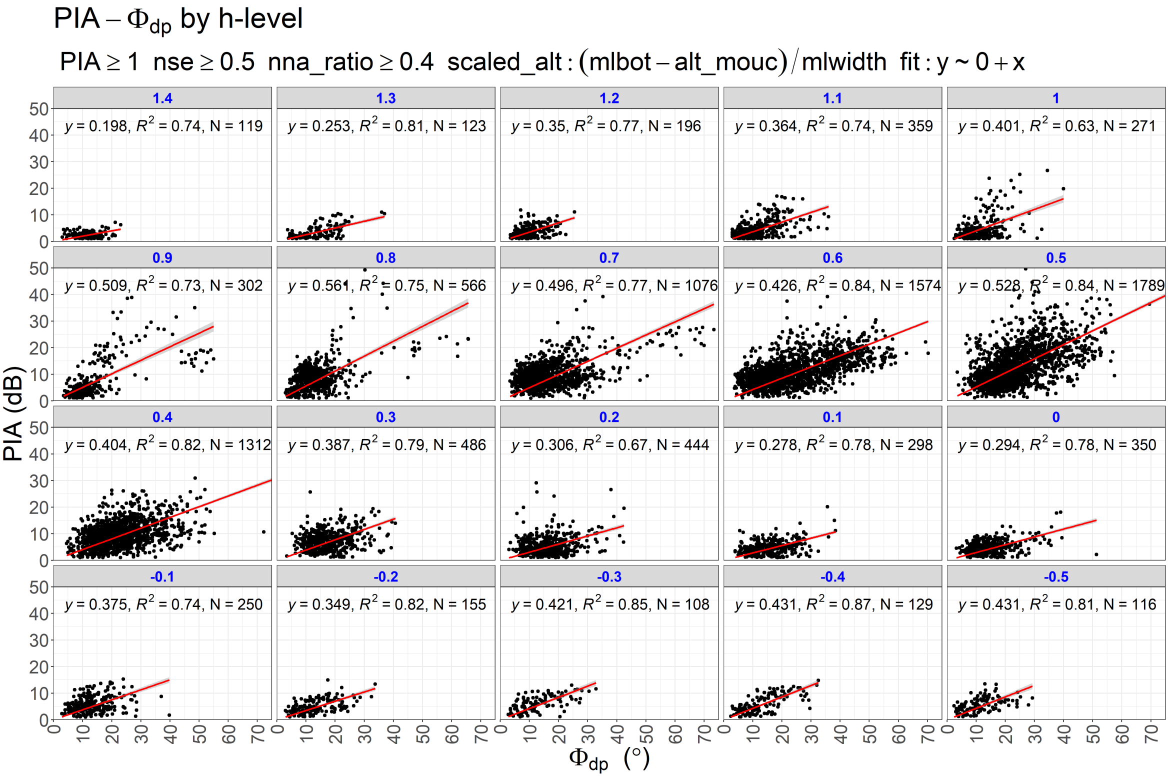

FIGURE 6.4: PIA vs Φ_{dp} 0-forced linear after filtration criteria, $PIA \geq 1$ dB, $NSE \geq 0.5$, $Not\_NA\_ratio \geq 0.4$. Description similar to Fig 6.3

The application of the more stringent filtration criteria produces Fig. 6.4. The noticeable differences are (i) an important decrease in the number of PIA-PHIdp pairs with variable rejection percentages in the snow region (71%), in the ML (31%) and in the rain region (79%), (ii) the successful removal of part of the outliers (especially those corresponding to high Φ_{dp} values for very low PIA values), and the general improvement of the R^2 criteria which become almost systematically greater than 0.7, and for most of the classes close to or better than 0.8. It is important to mention that the rejection is essentially based on the Φ_{dp} criteria and not on the PIA_m threshold of 1 dB compared to 0. Before looking at the evolution of a_{AK} as a function of the scaled altitude for the two sets of filtration criteria, we discuss in the following the distributions of the PIA and Φ_{dp} in the different scaled altitude classes and the shapes of the vertical profiles as well.

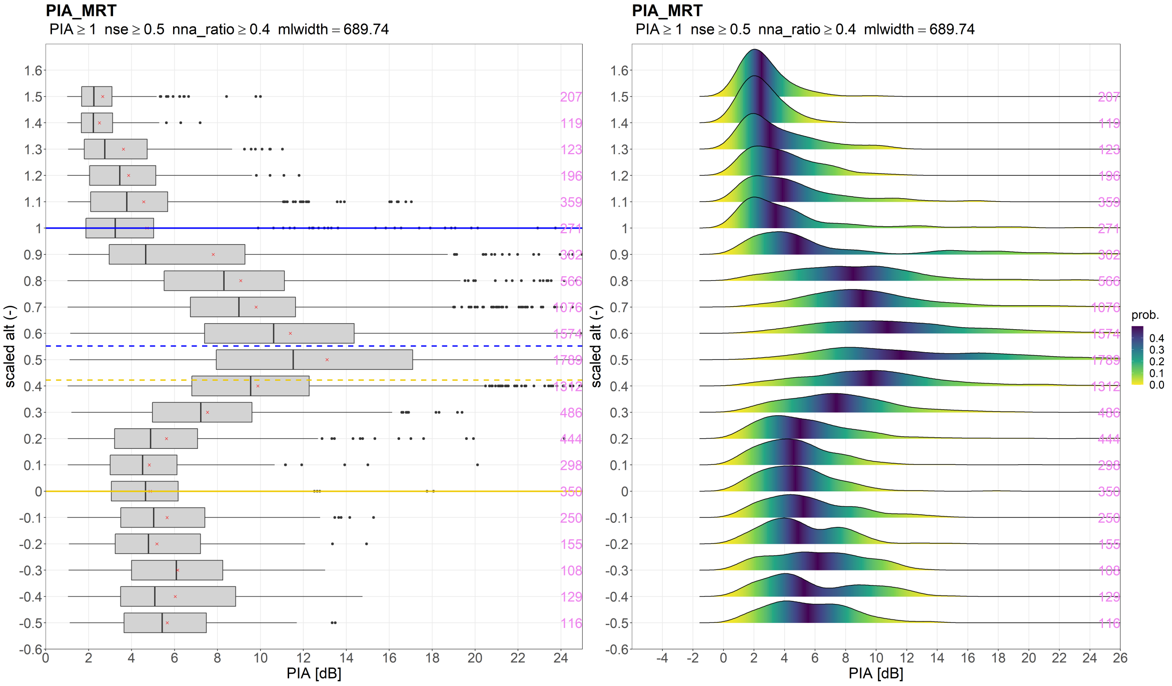

FIGURE 6.5: PIA at different scaled altitudes. Boxplots on the left and density plots on the right. In scaled altitudes 0 and 1 mark the ML top and ML bottom respectively. Dotted horizontal blue line is the average altitude of Z_h peak and the dotted horizontal gold line is the average altitude of ρ_{hv} peak.

Vertical profiles of PIA in Fig 6.5 show the boxplots and density plots of MRT estimated PIAs for each scaled altitude class for the most stringent filtration criteria. There is a clear signature of the ML in such vertical profiles:

- The PIA in snow region (scaled altitude levels ≥ 1) is the smallest with relatively narrow and unimodal distributions. While we expect the PIA to be close to 0 in snow region, it averages around 2 - 4 dB with maximum values as high as 10-12 dB for scaled altitudes classes greater or equal to 1.2. The maximum PIA value is even 17 dB in class 1.1.

- In the rain region, we observe mean PIA values of around 5-6 dB, maximum values up to 15 dB and distributions more spread out than in snow, sometimes bimodal.
- There is a significant increase in the PIA within the melting layer, with a peak at scaled altitude class 0.5 close to the altitude of reflectivity peak (scaled altitude of 0.55), as determined from below by the XPORT and MRR radars. The mean ρ_{hv} peak, determined with the XPORT radar data only, is slightly above the PIA peak at a scaled altitude of 0.42. Towards the center of the ML (classes 0.5, 0.6) the density plots show very spread out distributions with low amplitude and high mean values. The evolution of the means are quasi-linear between classes 0.5-0.8 in the upper ML and between classes 0.2-0.5 in the lower ML, with marked discontinuities with the mean values in the snow and rain regions.

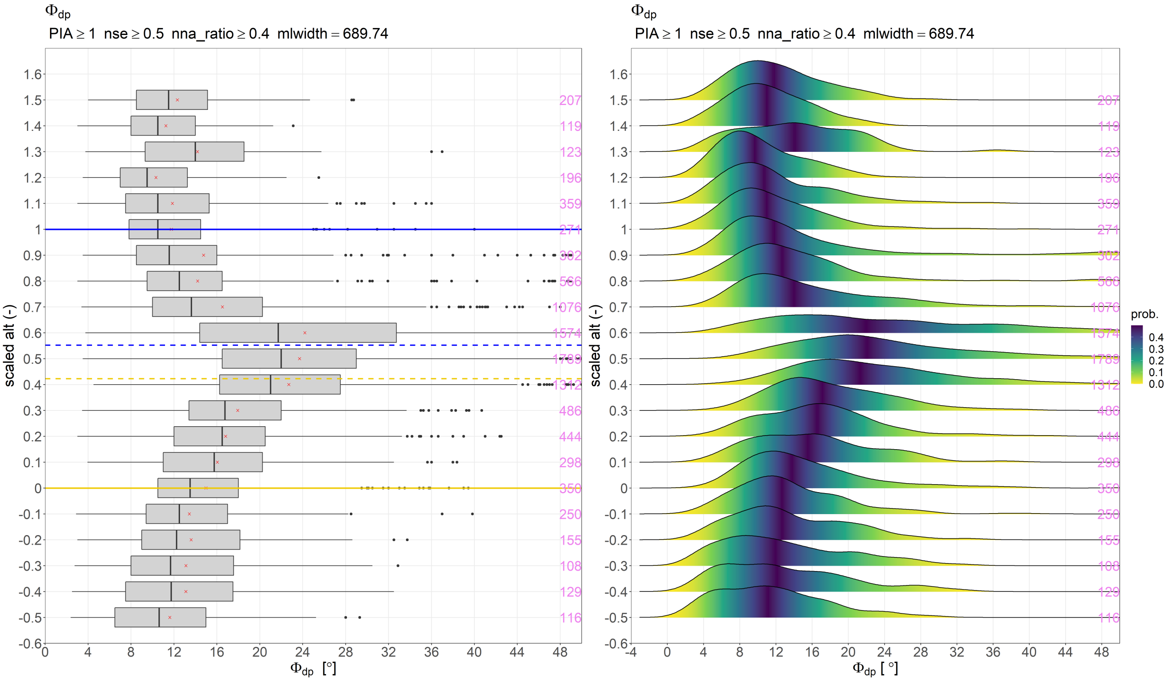

FIGURE 6.6: Φ_{dp} at different scaled altitudes. Boxplot on the left and density plots on the right. Scaled altitudes, 0 and 1 mark the ML bottom and ML top, respectively. Dotted horizontal blue line is the average scaled altitude of Z_h peak and the dotted horizontal gold line is the average scaled altitude of ρ_{hv} peak derived from the valley-based radars.

Figure 6.6 shows the vertical profiles of boxplots and density plots of Φ_{dp}. There is also a clear signature in the ML, but it is different from that of the PIA data. The boxplots vary at different stages of melting and peak just above the altitude of Zh peak at the scaled altitude class 0.6 with a mean value of 25°. There is a significant decrease between scaled altitude classes 0.6 and 0.7 while, in the upward direction, the profile decreases progressively with no marked discontinuity at the top of the ML. Mean values of about 12° are observed in the snow region. Small increase in the average Φ_{dp} at scaled altitude of 1.3 might be an indication of presence of large aggregates i.e. Mie scattering regime, unless due to statistical fluctuations. In the downward direction, one can note that the mean values of classes 0.4 and 0.5 remain close to the peak value of class 0.6. Then there is a break of about 5° between the means of classes 0.4 and 0.3. The evolution is gradual, quasi linear, in the rest of the lower ML and in the rain region. Again there is no marked discontinuity at the bottom of the ML and mean values of about 12° are observed in the rain region, like in snow. The spread of the distributions is particularly large for classes 0.4-0.6 while it is reduced and comparable in the snow and rain regions, eventually with bimodal distributions.

For both variables, the spread of the distributions is in part associated with the fact the targets are distributed over a range of distances (between 20 and 30 km). The sampling may play a role as well by putting together data from a limited number of precipitation events with contrasted intensities. However, the different signatures are likely associated with different physical processes, e.g. hydrometeor size and phase are probably dominant factors for the PIA, while shape may be more important for Φ_{dp}. To be more specific, we can propose the following explanations. The Φ_{dp} profile responds to the changes in the aspect ratios of the melting hydrometeors. In the upper part of the melting layer, it changes gradually as the melt water slowly fills the aggregates inside out while the ice lattice keeps intact supporting the structure, till between the Z_h and ρ_{hv} peaks where the ice lattice breaks and surface tension dominates causing a quick change in the structure of hydrometeor, leading consequently to a quick increase in Φ_{dp} value. The melting process causes a gradual increase in PIA in the upper part of ML as PIA responds to the change in size and water phase at the surface of hydrometeors. As such, the PIA reacts a bit slower than Φ_{dp} in the upper part of the ML. In the lower part of ML, PIA decreases relatively quickly as the hydrometeor is both getting smaller due to surface tension and becoming more and more oblate due to air drag, whereas the change in aspect ratio is quite gradual only affected by the buoyancy. As such, higher values of the ratio of the means (as a proxy for the prefactor of the linear A-K_{dp} relationship) are expected in the upper part of ML and a slightly smaller value just above the altitude of Z_h peak.

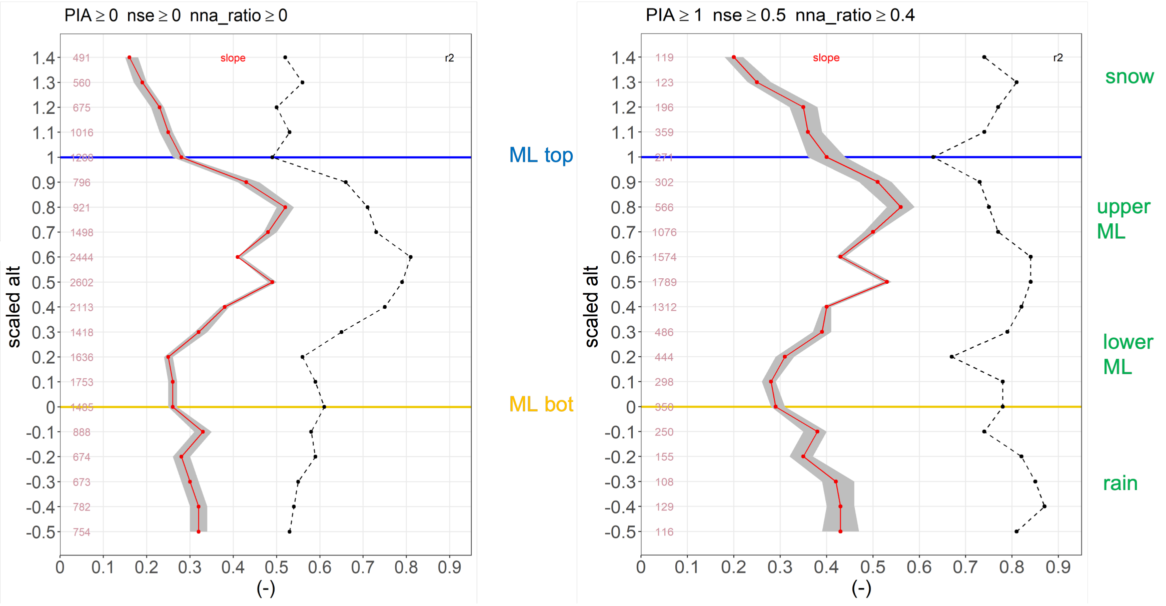

FIGURE 6.7: Summary of PIA vs Φ_{dp} 0-forced linear fits for 2 sets of rejection criteria,(left) $PIA \geq 0$, $NSE \geq 0$, $Not\_NA\_ratio \geq 0$, (right) $PIA \geq 1$, $NSE \geq 0.5$, $Not\_NA\_ratio \geq 0.4$. The corresponding scatterplots are shown in 6.4. Red line shows the slope (a_{AK}) of linear-fits with confidence interval of the slope in grey. The dotted black line shows the R^2 criterion of the 0-forced linear fits. Number of observations for each altitude class are annotated in the left. Horizontal blue line marks ML top and horizontal gold line marks ML bottom.

Figure 6.7 displays the vertical profiles of the slopes of the 0-forced linear fits presented in Figs 6.3 and 6.4 as estimations of the prefactor of a supposedly linear A-K_{dp} relationship at different scaled altitudes below, within and above the ML. The left graph based on a majority of PIA-PHIdp pairs is close to what one would expect for the a_{AK} coefficient both in the upper and lower parts of the ML, and in the rain region as well. The values seem a bit high in the snow region owing to the low values of specific attenuation in snow. As already said in the comments of Fig. 6.3, the R^2 statistics are however rather poor for all the altitude classes except in the central and upper ML. Introducing a more stringent filtration criteria (right graph) has a very positive impact on the R^2 statistics for all altitude classes but a detrimental one on the overall shape of the profile, again with respect to one's expectations for an a_{AK} estimation. The confidence interval of the slope displayed in Fig. 6.7 depends both on the correlation between the considered variables and on the number of pairs. As such, its variations at the different altitude classes between the two graphs modulates to some extent the gain in the R^2 criterion by the reduction of number of pairs introduced by the more stringent rejection criteria. Based qualitatively on these confidence intervals, one may see that in spite of the R^2 gain, the confidence on the slopes has decreased in some parts of the profiles, especially in the rain and snow regions, and in the upper part of the upper ML as well (altitude classes 0.8-1.0). Within the melting layer, the shape of the profiles is essentially preserved with slight increases, especially for classes 0.8-1.0. From the right figure, the value at the bottom of the ML is 0.3 and the maximum is observed for class 0.8 (0.54), slightly greater than the value for class 0.5 (reflectivity and ρ_{hv} peaks). Contrary to the expectations, the values above the ML decrease even more slowly than on the left figure and they depart significantly from the 0.3 value (up to 0.44) in the rain region.

Figure 6.8 plots all the $PIA - \Phi_{dp}$ pairs for all $scaled\ altitudes > 1$ i.e. snow regime (left) and $scaled\ altitudes < 0$ i.e. rain regime (right), after applying the filtration criteria. This shows the $a_{AK} \approx 0.25$ in snow and $a_{AK} \approx 0.39$ in rain, with R^2 of 0.65 and 0.77 respectively. The values in both rain and snow are quite larger expected.

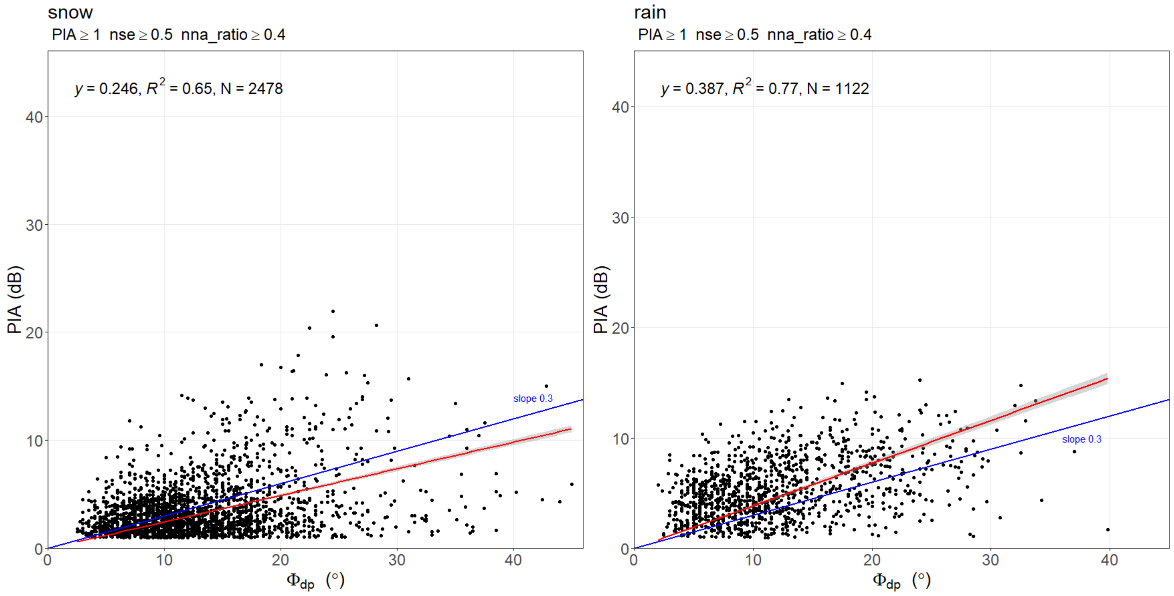

FIGURE 6.8: PIA - Φ_{dp} relationship in snow and rain, $PIA \geq 1$, $NSE \geq 0.5$, $Not\_NA\_ratio \geq 0.4$. PIA - Φ_{dp} pairs for $scaled\_altitude > 1$ corresponding to snow regime plotted on the left, and $scaled\_altitude < 1$ corresponding to rain regime plotted on the right. 0-forced linear fit is shown in red and its summary are annotated on the the top. Blue ab-line shows corresponds to slope of 0.3

It is important to note that the Φ_{dp} in the upper part of melting layer changes gradually as the melt-water slowly fills the aggregates inside-out while the ice-lattice keeps intact supporting the structure, till just above the Z_h peak where the ice-lattice breaks and surface tension dominates causing a quick change the structure of hydrometeor and consequently a quick increase in Φ_{dp} value. The Φ_{dp} profile respond to the changes in the aspect ratios of the melting hydrometeors. This process causes a gradual increase in PIA in the upper part of ML as PIA responds to the change in size, phase and intensity of dominant hydrometeors. As such, the PIA reacts a bit slower than Φ_{dp} in the upper part of the ML. In the lower part of ML, PIA decreases relatively quickly as the hydrometeor is both getting smaller due to surface tension and becoming more and more oblate due to air buoyancy, where as the change in aspect ratio is quite gradual only affected by the buoyancy. As such, higher values of the prefactor (a_{AK}) are expected in the upper part of ML and a slightly smaller value just above the altitude of Z_h peak (in the upper ML).

6.4 Discussion

The goal of this section is to analyze the usability of the slope of PIA-Φ_{dp} relationship in Fig 6.7 as a prefactor (a_{AK}) of $A - K_{dp}$ relationship in equation 6.1, assuming a linear relationship ($\beta \approx 1$). This relationship has been investigated well in the rain using disdrometer data and scattering models. Bringi and Chandrasekar 2001 found a_{AK} to be 0.233, Park et al. (2005) found the a_{AK} to vary between 0.195 and 0.335, Schneebeli and Berne (2012) found it to vary between 0.205 to 0.245 and Yu et al. (2018) suggest the value 0.276 at X-band.

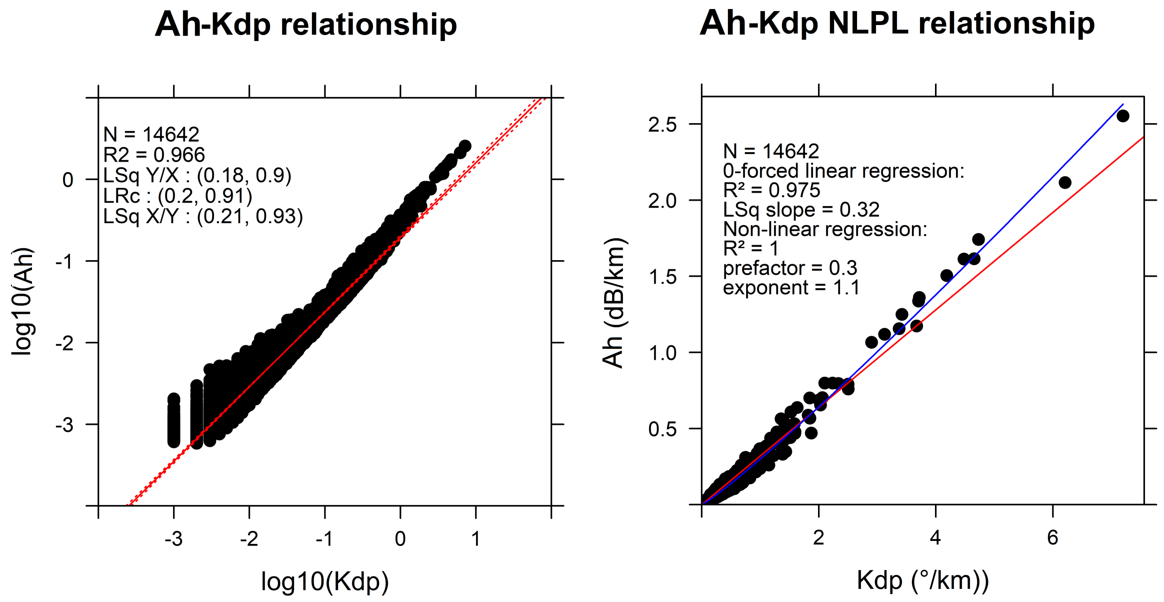

FIGURE 6.9: Disdrometer derived A_h vs K_{dp} in rain

The derivation of $A - K_{dp}$ relationship using disdrometer data at the IGE site (200 m asl) are shown in Fig 6.9 (Delrieu et al. 2022). Scattering model from the CANTMAT version 1.2 software developed by V.N. Bringi and C. Tang was used to calculate the A and K_{dp} from DSD. In left subplot, least square rectangle fit on log-log scale gives a prefactor of 0.2 and a exponent of 0.91. In the right subplot, a 0-forced linear fit (red) on natural values gives the slope of 0.32 with the $R^2 = 0.98$, whereas a non-linear power-law fit gives a prefactor of 0.3 and an exponent of 1.1. The linear approximation looks to be a sufficient approximation for low A and low K_{dp} scenarios i.e. low to medium precipitation intensities, but the linear approximation does not hold well at higher intensities. Along with the drop size and shape characteristics, the choice of regression model introduces variability in the estimation of coefficients as well.

In the rain regime of Fig 6.7, estimated a_{AK} varies between 0.29 and 0.42 with an increasing trend further away form the ML bottom. This trend is a bit counterintuitive as the coefficient is expected to be more or less stable, or even slightly lower as the oblateness of raindrops increases below the ML bottom until the drops reach a terminal velocity. Also, these values are slightly higher than the DSD modeled and widely accepted estimations in the literature. These discrepancies may be attributed to on-site attenuation, non-uniform beam filling and precipitation variability along the path between radar and mountain targets.

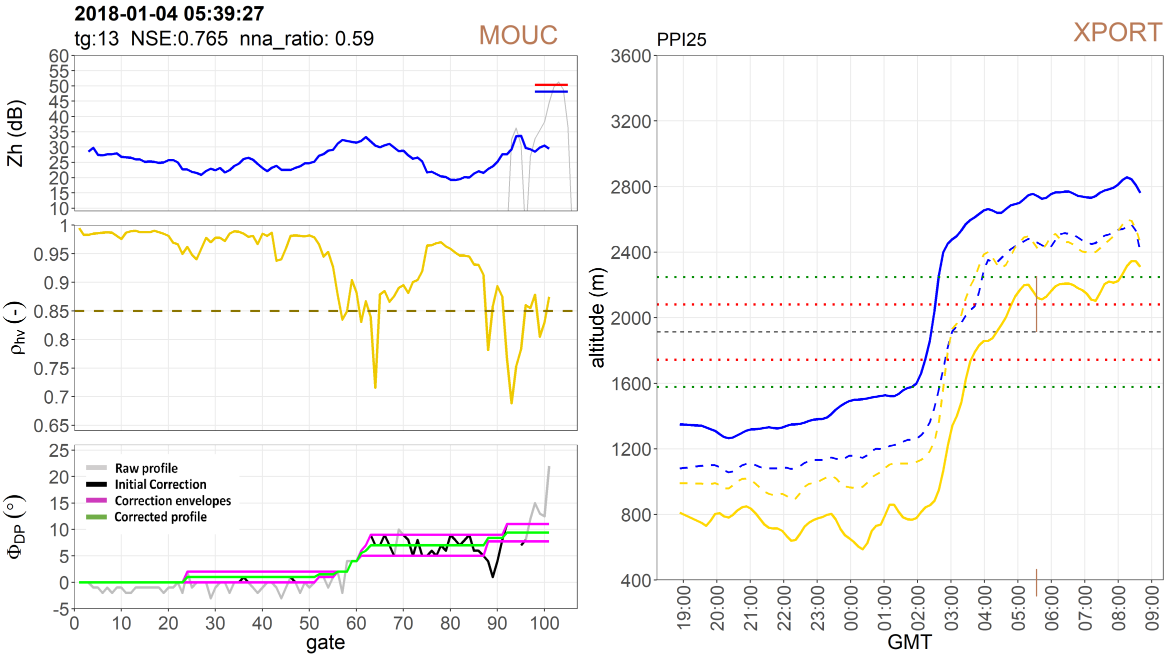

FIGURE 6.10: Non-uniform beam filling effect, 01 January 2018, target 13. Top left sub-plot shows the range profile of Z_h in blue; dry-weather echo of target 13 in grey where red and blue segments show the dry and wet returns at 05:40 GMT. Middle left sub-plot shows the range profile of ρ_{hv} with dotted horizontal at 0.85 used to identify non-meteorological returns. Bottom left sub-plot shows the Φ_{dp} regularization process; raw profiles in grey, pre-processed profile in black, envelopes in violet and the regularized profile in green. The right plot shows the ML characteristics of the 3-4 January 2018 event as observed by XPORT radar: ML top in continuous blue line, ML bottom in continuous gold line, altitude of Z_h peak in dotted blue, altitude of ρ_{hv} peak in dotted gold. Horizontal dotted black line marks the altitude of MOUC 0° beam center, dotted red and green lines show vertical extent of broadened MOUC 0° beam at 15 and 30 km respectively. Left plots corresponds to MOUC 0° elevation PPI observation and right plot corresponds to QVP of XPORT 25° elevation PPI observation

An example of beam broadening and subsequent NUBF on 4 January 2018 is shown in Fig 6.10. In the direction of target 13 at 05:40 GMT, MOUC 0° elevation beam center is theoretically in the rain regime; beyond 15 km range, the top part of the beam extends to the lower part of ML (right subplot). In the range plots of radar observables (in left), up to 16 km (gate 60) $\rho_{hv} > 0.95$ shows the presence of liquid rain with $Z_h \sim 25$ dBZ and very low Φ_{dp}. At 16 km, as the beam is partially in ML, ρ_{hv} decreases and Φ_{dp} increases significantly suggesting a non-uniform beam filling with liquid and melting hydrometeors. The sudden decrease of ρ_{hv} below 0.85 at gate 64 and beyond gate 85 is attributed to ground clutter. Another important observation is that ground clutter (beyond gate 85) surrounding the mountain target limits the range of Φ_{dp} regularization i.e. there is a discrepancy in the range at which PIA_m and Φ_{dp} are estimated for a given target, another possible source of error in $PIA - \Phi_{dp}$ relationship.

On-site attenuation can be differentiated into wet radome attenuation and blind-range attenuation related to precipitation at first few gates i.e. between radar and range r_0, where the radar observation is not reliable (Delrieu et al. 1997). PIA estimation using the MRT contains the on-site attenuation and needs to be removed. Frasier et al. (2013) studied the on-site attenuation at X-band in rain in the Alps. Radome attenuation can be significant in medium - heavy rain and the melting layer. They used two X-band radars, one with radome and another without, with the assumption of uniform dielectric radome and uniform layer of water coating to estimate the wet radome attenuation when it rains at the radar site. Their result, in dotted line, shows the 1-way radome attenuation [dB] as a function of rainrate $[mm\,hr^{-1}]$, presented in Fig 6.11. It shows that for low rainrates on-site attenuation is very small.

Adapting a power fit law to their result gives the following two-way radome attenuation correction formulation:

$$PIA_r = 0.0126\, Z_0^{1.6} \tag{6.3}$$

where Z_0 is the average reflectivity (dBZ) in first few usable gates around radar. This is in fact an implicit equation with

$$PIA_r = 0.0126\,(Z_0 + PIA_r)^(1.6) \tag{6.4}$$

hence Zo is affected by radome attenuation as well. In practice, we define a range of Z_0 to compensate for implicit PIA_r in Latin hypercube sampling of GSA (Delrieu et al. 2022).

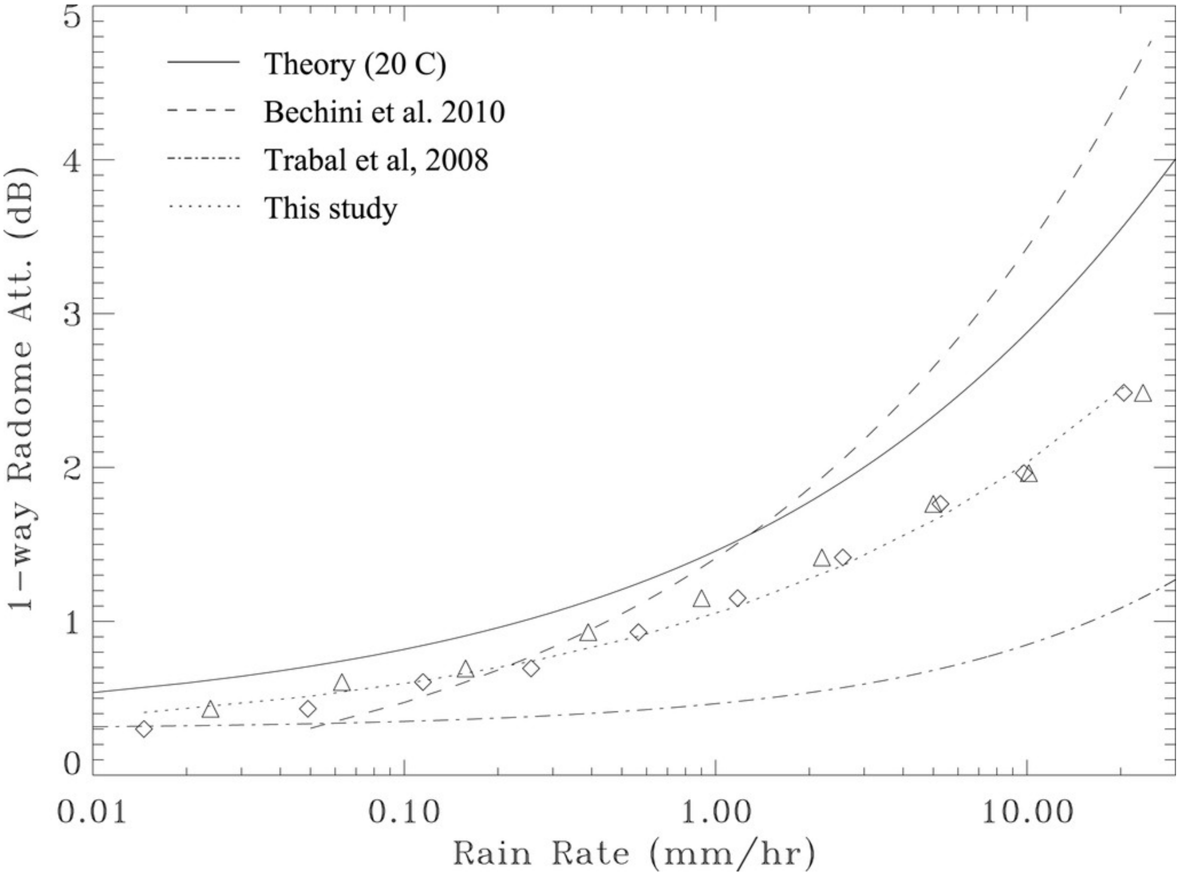

FIGURE 6.11: Radome attenuation estimation in rain at X-band: Fig 6 of Frasier et al. (2013). One-way radome attenuation as a function of rainrate R, using Marshall–Palmer (diamonds) or WSR-88D (triangles) Z–R relationships. The dotted line is the result of their study. Other results from the literature are as indicated.

Similarly, the on-site attenuation because of precipitation in blind range [0,r_0] can be estimated using ZPHI technique on the first few measurable gates (Testud et al. 2000; Reinoso-Rondinel et al. 2018). Delrieu et al. (2022) propose a parameter estimation procedure which estimates Z_0 using general sensitivity analysis framework. It is important to note that these methods of on-site attenuation are adapted for the rain regime, and equivalent correction are not available for the melting layer and the snow region. Investigation of the on-site attenuation estimations within the melting layer is beyond the scope of this study.

6.5 Conclusion

In this study, we evaluated the relationship between PIA and Φ_{dp} estimates in the melting layer of precipitation using X-band radars. Mountain reference technique is used to estimate the PIA. A method to regulate the range profile of Φ_{dp} is developed and presented in the method section. The algorithm iterates on the maximum allowed increase of monotone Φ_{dp} profile between each range gates. The optimum step-size produces the maximum Nash-Sutcliffe model efficiency coefficient (NSE). The PIA and Φ_{dp} are estimated from the 0° elevation PPI scans of mountain-top X-band MOUC radar. The valley based X-band XPORT radars identifies the position of the melting layer using 25° elevation PPI scans. As such, the position of MOUC 0° beam relative to the ML bottom is known. Hence vertical profiles of PIA, Φ_{dp} and relationship is studied at different stages of melting. It is shown that a single linear depiction of PIA - Φ_{dp} relationship throughout the melting layer is not sufficient. Depending on the stage of melting the prefactor (a_{AK}) in equation 6.1 varies within the melting layer. The upper part of ML has relatively high values of a_{AK} compared to the lower ML. Within the ML estimated a_{AK} varies between 0.26 to 0.54.

The range profiles of measured differential phase are quite noisy in the vicinity of the ML and this limits the size of usable observation. Large proportions of the available data had to be discarded using rejection criteria to improve the correlation between PIA - Φ_{dp} pairs. The on-site attenuation, both due to wet-radome and blind-range precipitation, may be significant when the radar site is within heavy-medium rain in the melting layer. While simplified methods to correct for on-site attenuation in rain are available, no such schemes are available for the melting layer. Similarly, the presence of ground clutter in the vicinity of mountain targets tends to decrease the range of Φ_{dp} and result in under-estimation the Φ_{dp}; it is unavoidable due to complexity of the terrain. The non-uniform beam filling due to beam broadening and vertical variation of precipitation phase causes perturbation PIA and the range profile of Φ_{dp} towards the top and bottom of the melting layer. More work needs to be done in terms of on-site attenuation and NUBF within the melting layer. The linearity hypothesis of PIA - Φ_{dp} relationship at each scaled altitude need to be investigated using a generalized sensitivity analysis (GSA) approach discussed in Chapter 7.

Chapter 7

Attenuation correction and Quantitative Precipitation Estimation

7.1 Introduction

The application of X-band radars has been recommended to capture the fine-scale dynamics required for QPE in mountainous terrain and urban hydrology (Delrieu et al. 1997; McLaughlin et al. 2009; Lengfeld et al. 2014). At X-band, while the high resolution observation is a strength, attenuation is the major limitation (Hitschfeld and Bordan 1954). The measured reflectivity needs to be corrected for attenuation before QPE applications. The development of polarimetric techniques (Bringi and Chandrasekar 2001; Ryzhkov et al. 2005) promises robust attenuation correction procedures (Testud et al. 2000; Matrosov et al. 2002, 2005; Koffi et al. 2014; Ryzhkov et al. 2014) that still need to be inproved in the high mountain context due to precipitation phase changes (snow, melting precipitation, rain) and topography.

The classical radar QPE is based on estimation of rainfall intensities $R[mm\,h^{-1}]$ in each range bin derived from the radar reflectivity $Z[dBZ]$ using a emperical nonlinear R-Z relationship, $R = aZ^b$, where a and b are two parameters to be determined. The well known Marshall-Palmer relationship $Z = 200R^{1.6}$ (Marshall and Palmer 1948) is often used as a standard reference before optimizing the parameters for a specific location and precipitation types. The relationship between the radar observables, reflectivity $Z[dBZ]$, specific attenuation $A[dB\,km^{-1}]$, and variable of interest in QPE, rainfall intensity $R[mm\,h^{-1}]$ are assumed to be of power type. The relationships will be referred to as R-Z, A-Z and R-A relationships in short.

$$R = a_{RZ}Z^{b_{RZ}} \tag{7.1}$$

$$A = a_{AZ}Z^{b_{AZ}} \tag{7.2}$$

$$R = a_{RA}A^{b_{RA}} \tag{7.3}$$

We are also interested in the A-K_{dp} relationship with

$$A = a_{AK}\, K_{dp}^{bAK} \tag{7.4}$$

The order used for the parameters is meaningful since the specific attenuation profile is derived from the measured reflectivity profile, while the rainrate profile can be derived in a second step either from the specific attenuation profile or from the corrected reflectivity profile. We will use the R-A relationship to generate rainrate profiles from the specific attenuation profiles.

Delrieu et al. (2022) developed a procedure for estimating these parameters using a generalized sensitivity analysis (GSA) of attenuation formulations in convective rainfall for X-band MOUC radar, discussed in detail in section 7.3. The physical model of the GSA is formulated in section 7.3.1. Four AZ algorithms constrained or not by $PIA(r_m)$, and one polarimetric algorithm based on the Φ_{dp} profile between radar and a mountain target were developed. The parameter structure and the inherent mathematical ambiguity of the system of equations make it necessary to organize the optimization procedure in a nested way. The core of the procedure (sections 7.3.2 - 7.3.4) consists of (i) exploring with classical sampling techniques the space of the parameters allowed to be variable from one target to the other and from one time step to the next, (ii) computing a cost function (CF) quantifying the proximity of the simulated profiles and (iii) selecting parameters sets for which a given CF threshold is exceeded. This core is activated for series of values of parameters supposed to be fixed, e.g. the radar calibration error for a given event. The GSA is performed for a set of three convective events, discussed in section 7.2, using the 0°-elevation PPI measurements of the MOUC radar. It allows estimation of critical parameters for radar QPE using radar data alone for the given event in section 7.3.2. In addition to the radar calibration error, this includes time series of radome attenuation and estimations of the coefficients of the power-law models relating the specific attenuation and the reflectivity (AZ algorithm) on the one hand and the specific attenuation and the specific differential phase shift (A-K_{dp} relationship) on the other hand.

Section 7.4 utilizes the parameter sets estimated and optimized using GSA to obtain the specific attenuation profiles. DSD derived rainrate - specific attenuation (R-A) relationship is then used to obtain range profiles of rainrate in the direction of mountain targets (directions with PIA_M). The next sections compare the rainrate profiles with raingauge accumulations in order to validate the GSA approach of attenuation correction and subsequent QPE. The raingauge accumulations are matched with the nearest available radar QPE in section 7.5. Overall performance of 5 QPE algorithms, the validity of optimized parameters, relevence of R-A relationship and performance of radar QPE at different stations are analyzed in the result section (7.6). We finally conclude our experience of using GSA based QPE estimation in section 7.7.

7.2 Dataset

In this study we consider 3 convective events in July and August 2017. For all these events the minimum altitude of ML bottom, detected using QVPs from 25°-elevation angle PPI measurements as described in Chapter 3, are well above the altitude of MOUC radar (1920 m asl). The characteristics of the events are shown in Table 7.1.

TABLE 7.1: Some characteristics of 3 convective events considered in this study

Date	**Beginning (UTC)**	**End (UTC)**	**Min. altitude of ML bottom (m asl)**	**Total rain amount at IGE (mm)**	**Max. rainrate in 10 min at IGE** ($mm\,h^{-1}$)
21^{st} July 2017	15:00	19:00	3000	35.2	42.0
8^{th} August 2017	08:30	15:00	3700	27.9	48.0
31^{st} August 2017	07:30	10:30	3200	19.5	15.5

The two primary sources of rainfall data are: (i) radar QPE from MOUC and (ii) ground observation using raingauges. The radar QPE is obtained from 0°-elevation PPI measurements of the X-band MOUC radar. The spatial resolution of the radar data is 240m (radial) and the temporal resolution is 5 minutes. 22 mountain targets are identified at 0°-elevation PPI scan of MOUC radar. There are 10 raingauge stations in the "inner" domain, in the azimuths close to and in-between the mountain targets. These raingauges are distributed between 30° to 150° azimuths and 6.8 km to 32.6 km distances wrt the MOUC radar. These raingauge stations are located at altitudes between 220m asl and 2000m asl. The time resolution of the raingauges ranges from 1 minute to 15 minutes. Figure 7.1 shows the relative position of different instruments and mountain targets wrt MOUC radar (at the center). Two additional mountain targets are considered in this chapter, 22 targets here compared to 20 in Chapter 4, by extending the range of detection to 40 km (from previous 30 km) to include all available raingauges in RadAlp setup.

Additionally, a $PARSIVEL2$ disdrometer is installed at IGE site. The raw DSD measurements have a time resolution of 1 minute. They are binned into 32 diameter classed with increasing sizes from 0.125 mm upto 6mm. Data for 337 rainy days between April 2017 and March 2020 are available. Scattering Model from the CANTMAT software version 1.20 from Colorado State University uses the T-matrix formulation to compute the radar observables (eg Z_h, Z_{dr}, ρ_{hv}, $A[dB\,km^{-1}]$ and K_{dp}), tuned to match the properties of X-band MOUC radar at incidence angle of 0°. The A-Z and A-K_{dp} relationships derived from DSD provides "initial" estimates of A-Z-K_{dp}-R prefactors and exponents.

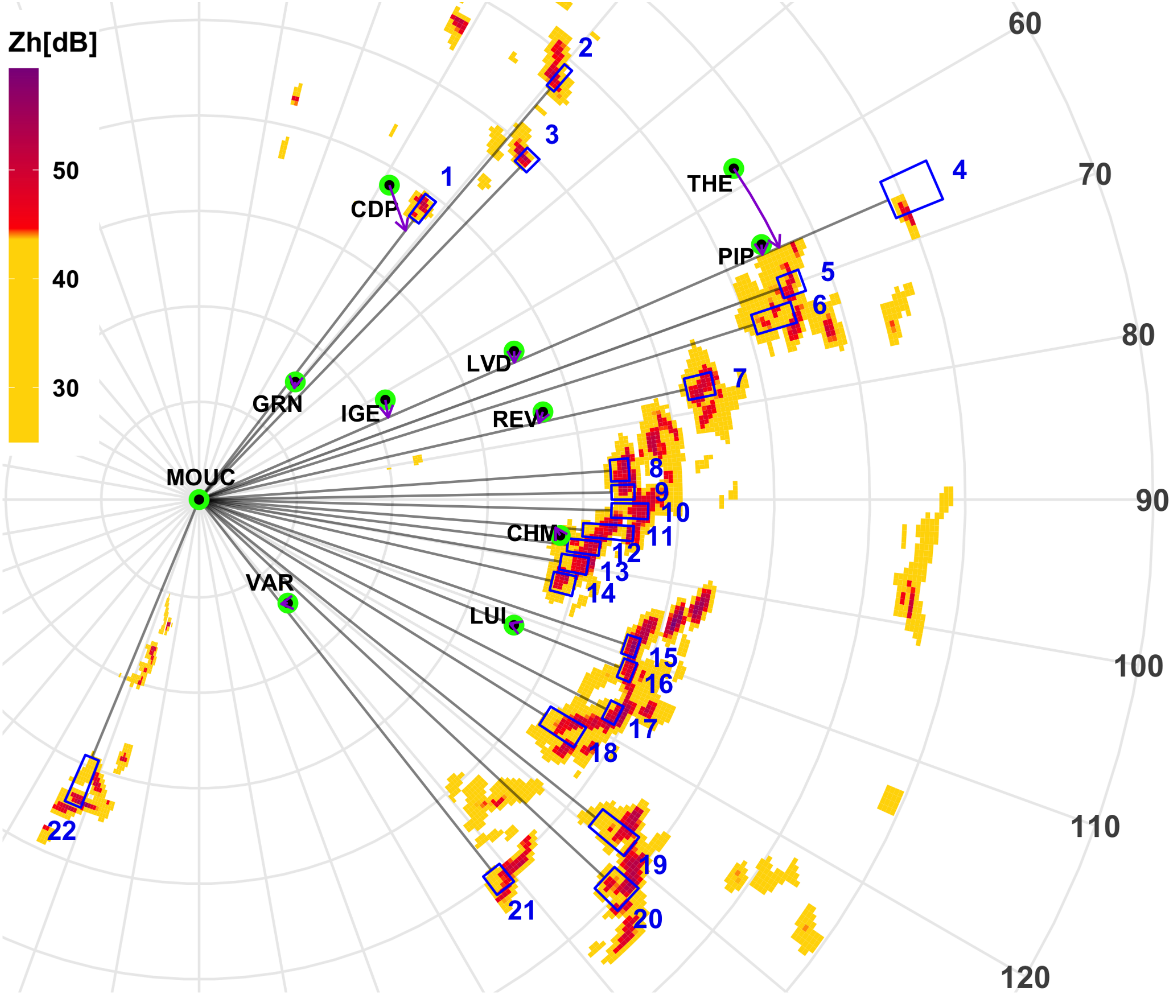

FIGURE 7.1: Relative position of mountain targets and raingauge stations wrt MOUC radar. The polar plot has MOUC radar in the center, concentric rings denoting every 5 km range and radial lines at every 10° azimuth. Long term observation of dry mountain echoes shows ground clutter with $Z_h \geq 25\,dB$ in gold and mountains with $Z_h \geq 45\,dB$ in red. The 22 mountain targets are shown demarcated by blue boxes accompanying numbers shows target id. Radial lines from center to targets shows the center of 0° PPI beam, where $R\,(mm\,h^{-1})$ profile is estimated. Green and black dots shows the location of 10 raingauge stations, with station ID nearby. The purple arrow shows location of radar grid matched with the corresponding raingauge station.

7.3 Physical Model, Sensitivity Analysis and Parameter Optimization

7.3.1 Physical Model

A-Z formulations

The A-Z algorithms shown in this section rely on two basic equations. The first one is the analytical solution of equation 4.3 assuming the power-law model 7.2 perfectly represents the A-Z relationship. By taking the derivative of $AF^{b_{AZ}}(r_0, r)$ with respect to r, we obtain:

$$d\left(AF^{b_{AZ}}\left(r_0, r\right)\right)/dr = AF^{b_{AZ}}\left(r_0, r\right)\left(-0.46\, a_{AZ}\, b_{AZ}\, Z(r)^{b_{AZ}}\right) \tag{7.5}$$

Substituting the true reflectivity from equation 7.12 and integration between r_0 and r yields:

$$AF^{b_{AZ}}\left(r_0, r\right) = 1 - 0.46\, a_{AZ}\, b_{AZ}\, SZ\left(r_0, r\right) / \left(AF\left(r_0\right) dC\right)^{b_{AZ}} \tag{7.6}$$

with

$$SZ\left(r_0, r\right) = \int_{r_0}^{r} Z_m(s)^{b_{AZ}} ds.$$

The second equation is obtained by integrating equation 7.5 upto r_m and by introducing attenuation factor estimate available at this range, yielding:

$$\left(AF\left(r_m\right)/AF\left(r_0\right)\right)^{b_{AZ}} + 0.46\, a_{AZ}\, b_{AZ}\, SZ\left(r_0, r_m\right) / \left(AF\left(r_0\right) dC\right)^{b_{AZ}} = 1 \tag{7.7}$$

Under the assumption of homogeneous precipitation type, the a_{AZ} and b_{AZ} are constant along the propagation path. We introduce four AZ algorithm formulations; each formulation filters out one of the four parameters $AF(r_m)$, dC, a_{AZ} and $AF(r_0)$. The corresponding AZ relationships will be referred to as $AZhb$, AZC, $AZ\alpha$ and $AZ0$ respectively. The first formulation $AZhb$ does not take reference PIA_m at r_m into account and is obtained solely based on 1^{st} equation (7.6). For the rest, parameter to be expressed is derived from 2^{nd} equation (7.7), then substituted in the 1^{st} equation (7.6). The final forms of corrected reflectivity profiles are listed below, refer to Delrieu et al. (2022) for details.

$$Z_{AZhb}(r) = \frac{Z_m(r)}{\{(AF(r_0)\, dC)^{b_{AC}} - 0.46\, a_{AZ}\, b_{AZ}\, SZ(r_0, r)\}^{1/b_{AZ}}} \tag{7.8}$$

$$Z_{AZC}(r) = \frac{Z_m(r)[AF(r_0)^{b_{AZ}} - AF(r_m)]^{b_{AZ}}]^{1/b_{AZ}}}{\{0.46\, a_{AZ}\, b_{AZ}[AF(r_0)^{b_{AZ}}\, SZ(r, r_m) + AF(r_m)^{b_{AZ}}\, SZ(r_0, r)]\}^{1/b_{AZ}}} \tag{7.9}$$

$$Z_{AZ\alpha}(r) = \frac{Z_m(r)\, SZ(r_0, r_m)^{1/b_{AZ}}}{\{dC\, [AF(r_0)^{b_{AZ}}\, SZ(r, r_m) + AF(r_m)^{b_{AZ}}\, SZ(r_0, r)]\}^{1/b_{AZ}}} \tag{7.10}$$

$$Z_{AZ0}(r) = \frac{Z_m(r)}{\{0.46\, a_{AZ}\, b_{AZ}\, SZ(r, r_m) + (AF(r_m)dC)^{b_{AZ}}\}^{1/b_{AZ}}} \tag{7.11}$$

The equivalent specific attenuation profiles are obtained by using the A-Z relationship. PIA profiles can then be estimated by integrating the A(r) profiles between range r_0 and r.

Assuming measured reflectivity is affected by both attenuation and radar calibration error (dC), one can write:

$$Z_m(r) = Z(r)AF(r)dC \tag{7.12}$$

where Z is the true reflectivity, AF is the attenuation factor and dC is the radar calibration error. AF ranges between 0 and 1. 0 means total attenuation and 1 means no-attenuation. dC depends on the equipment configuration and can be considered constant for an event.

In addition to the running range r, let us consider the range r_0 corresponding to the blind range of the radar system, eventually extended to the range where the reflectivity measurements start to be free of spurious detection due e.g. to side lobes. The attenuation factor $AF(r)$ is expressed as the product of two terms:

$$AF(r) = AF(r_0)\, AF(r_0, r) \tag{7.13}$$

where, $AF(r_0)$ is the on-site attenuation. The on-site attenuation can be attributed primarily to the formation of the water film on the radome, combined with along-path attenuation between radar site and range r_0. $AF(ro, r)$ is the attenuation factor due to precipitaion occuring between range r_0 and r.

As a classical formulation (Marzoug and Amayenc 1994), the two-way attenuation factor can be expressed as a function of specific attenuation A[$dB\, km^{-1}$]:

$$AF(r) = AF(r_0)\, exp(-0.46 \int_{r_0}^{r} A(S)ds) \tag{7.14}$$

Let us now consider another particular range, denoted r_m, where estimates of the attenuation factor may be available. We use the following notation:

$$AF_m(r_m) = AF(r_m)\, dAF(r_m) \tag{7.15}$$

where $AF(r_m)$ is the true attenuation factor at range r_m and the term $dAF(r_m)$ represents a multiplicative error term. Such direct estimates of the attenuation factor can be obtained in mountainous regions from the mountain reference technique (Chapter 4). The mountain reference technique makes it possible to directly measure PIA in the directions with the mountain target.

The notion of path-integrated attenuation (PIA), in units of dB, can be recalled from equation 4.4

$$PIA(r) = -10\, log_{10}(AF(r))$$

Polarimetric formulation

It was shown in Chapter 5 that it is possible to derive the PIA range profile using radar polarimetry, from the profile of the total differential phase shift on propagation $\Phi_{dp}[^\circ]$. The Φ_{dp} profile is not affected by attenuation and radar calibration error. From equation 5.1, $\Phi_{dp}(r)$ can be formulated as:

$$\Phi_{dp}(r_0, r) = 2 \int_{r_0}^{r} K_{dp}(s) ds \tag{7.16}$$

where K_{dp} is the specific differential phase shift on propagation $[^\circ km^{-1}]$. Assuming a power-law relationship between the specific attenuation and the specific differential phase shift on propagation with:

$$A = a_{AK} K_{dp}^{b_{AK}} \tag{7.17}$$

and combining equations 4.4, 7.16 and 7.17 gives:

$$PIA_{\Phi_{dp}}(r) = PIA_0 + 2\, a_{AK} \int_{r_0}^{r} K_{dp}^{b_{AK}}(s) ds \tag{7.18}$$

where PIA_0 is the on-site attenuation

This polarimetry-derived PIA can be related to the PIA profiles obtained by integrating the specific attenuation profile obtained from solving the attenuation-reflectivity (A-Z) algorithms.

A 5th formulation is obtained from the polarimetric PIA equation7.18:

$$PIA_{\Phi_{dp}}(r) = PIA_0 + 2\,a_{AK} \int_{r_0}^{r} K_{dp}^{b_{AK}}(s)ds$$

The $AZhb$ formulation is equivalent to the solution proposed early by Hitschfeld and Bordan (1954), hence the name $AZhb$. It can be termed as the "forward algorithm" as only measured reflectivites between r_0 and r are used for correction at range r. The negative sign in the denominator means the solution is unstable at large SZ cumulative terms, i.e. high rainrates. It is also known to be highly sensitive to calibration error, to inadequate values of AZ relationship coefficients and to on-site attenuation. The $AZ0$ algorithm has the simplest mathematical expressions among the three algorithms using PIA constraints. It looks like a "backward algorithm" since the reflectivity and the specific attenuation estimated at range r depends only on the measured reflectivities between range r and r_m, while AZC and $AZ\alpha$ algorithms make use of the entire measured reflectivity profile between range r_0 and r_m.

The prefactors and exponents of the Z-A-K_{dp}-R relationships (i.e. a_{AZ}, b_{AZ}, a_{AK} and b_{AK}) are mutually dependent as they are determined by the shape, density and size of hydrometeors and their electromagnetic properties, driven by their solid vs liquid composition and temperature. They might vary significantly from one precipitation type to another. Here, we consider a homogeneous precipitation type (convective rainfall). Because of the mathematical form of the equations and the likely mutual dependence of the exponents and prefactors if the power-law models, we will assume the exponents of the A-Z and the A-K_{dp} relationships to be constant for all considered events while the prefactors are allowed to vary for each single target and timestep. This assumption holds in rain, so we started with a similar assumption in the melting layer.

The parameters dC, PIA_0 and PIA_m are mutually independent, and a priori independent of the coefficients of the Z-A-K_{dp}-R power-law models. The radar calibration error is considered to be constant for a given precipitation event. The PIA_0 has two components, radome attenuation and attenuation due to rain in $[0, r_0]$ range which depends on on-site precipitation conditions. Following the findings of Frasier et al. (2013), the measured reflectivity in radar vicinity Z_0 is used as an index for the presence of on-site attenuation. It allows defining a search range for PIA_0 (refer to Delrieu et al. (2022) for details). The PIA_m is estimated using the MRT (Delrieu et al. 1999). The PIA_m contains onsite attenuation, so it is necessary to correct PIA_m for PIA_0 before QPE applications.

In the physical model consisting of A-K and A-Z formulations, we have 7 parameters/unknowns that define QPE of a polarimetric radar. These are: a_{AZ} and b_{AZ} from A-Z relationship, a_{AK} and b_{AK} from the A-K relationship, radar calibration error dC, on-site attenuation PIA_0 and reference attenuation $PIA(r_m)$ at range r_m.

7.3.2 Parameter Estimation

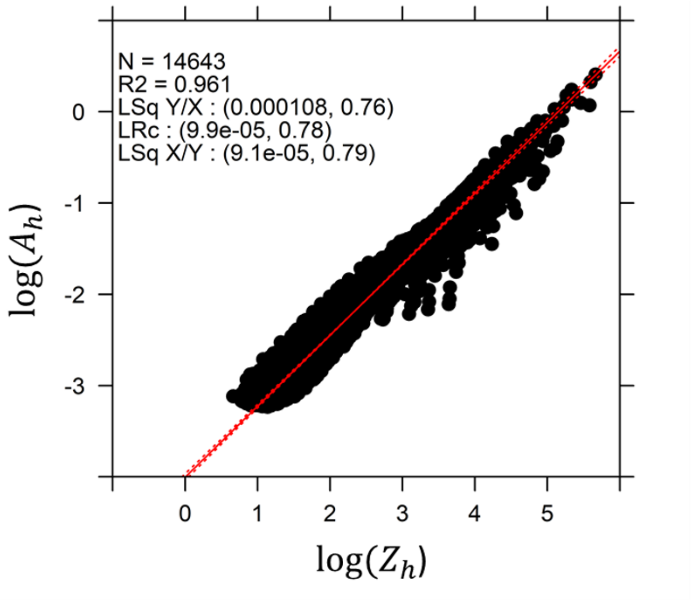

FIGURE 7.2: $A - Z$ relationship based on DSD-derived power law models using log_{10} transformation of both variables. N refers to the number of points, R^2 gives the square of the correlation coefficient of the logarithmic regression. The prefactors and exponents of the resulting least square regressions of A vs Z (Lsq Y/X) and vice versa (Lsq X/Y); and the least rectangle regression (LRc), which considers the two variables on an equal footing, are shown

For the simulations the fixed parameters i.e. exponents of the A-Z-K_{dp} i.e. b_{AZ} and b_{AK} are obtained from the DSD simulations of radar variables. For the prefactors i.e. a_{AZ} and a_{AK} Latin hyper cube sampling is utilized, central values values and ranges of variation are again based on the DSD simulations. Figure 7.2 shows the relationship log(A_h) vs log(Z_h) relationship utilizing the full dataset i.e. 337 days. The scatterplot has high R^2 fit of 0.961, and shows no curvature, i.e. it is good fit for the power-law like model. Although the statistics from the log-log fit gives higher importance to the data in the mid-section, the model provides a good fit for the highest values which relate to the convective events. The least-rectangle fit provides $b_{AZ} = 0.78$ for the exponent and $a_{AZ} = 1.0\,10^{-4}$ as the central value for LHS sampling of the prefactor. It also suggests a possible range of variation of [-5,5 dB] for the DSD-derived values. We however limit this range to [-3, 3 dB] on the basis that the resolution volume of the radar is much larger and the assumption that the prefactor is constant throughout the reflectivity profile (i.e. homogeneous precipitation type).

Figure 7.3 shows the scatter-plots of the A-K_{dp} relationship. The left sub-plot once again considers the log-log transformed A-K_{dp} relationship. However it can be seen that there is a slight curvature and the higher values are not fitted well. The right sub-plot shows two different fitting techniques, 0-forced linear fit in the red and a non-linear fit in the blue. The linear fit performs well for low and medium values with R^2 of 0.975, but underestimates A at the highest K_{dp}s. The non-linear power-law model (NLPL, equation 6.1) fit in blue performs better. NLPL fit in the A-K_{dp} relationship provides the exponent $b_{AK} = 1.1$ and central value of prefactor $a_{AK} = 0.3$ for LHS sampling.

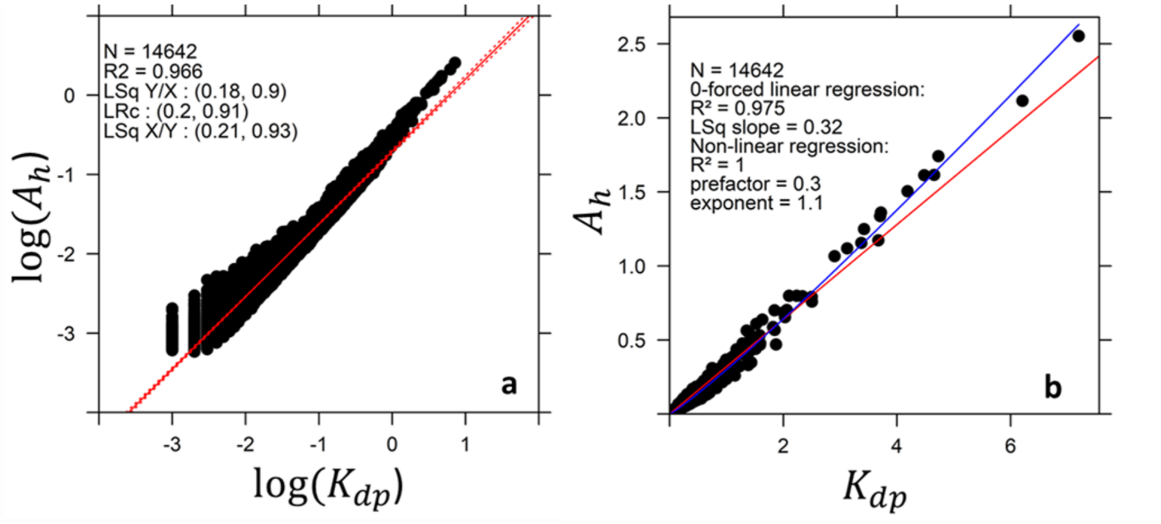

FIGURE 7.3: $A - K_{dp}$ relationship from DSD-derived power law models (a) using a classical logarithmic of base 10 transformation of the two variables (similar to Fig. 7.2) and (b) using natural values of the two variables. The red line in panel (b) is the zero-forced linear regression with a slope equal to 0.32, and the blue curve is the non-linear fit of a power law model with a prefactor of 0.30 and an exponent of 1.1.

7.3.3 Sensitivity analysis

The interdependence of Z-A-K_{dp}-R parameters lead the optimization procedure to be organized in a nested way. For a series of convective events, the exponents of the A-Z, A-K_{dp} relationships, i.e. b_{AZ} and b_{AK}, are considered to be constant. For each event radar calibration error dC is considered to be constant. A simulation is performed for each combination of b_{AZ} [0.78], b_{AK} [0.9, 1.2] by 0.1 and dC [-2, 2] by 0.4. The simulation core is implemented for each mountain target and each time step.

- The $Z_m(r)$ and $\Phi_{dp}(r)$ profiles between radar and the mountain target are preprocessed. Z_0 calculated as product of 1/dC and mean reflectivity of 1st 4 gates (1 km).
- Latin Hypercube sampling (LHS) technique is used to generate N parameter sets (with N=200) filling uniformly the parameter space composed of four parameters: a_{AZ}, a_{AK}, $AF(r_0)$ and dAF_m (multiplicative error on MRT attenuation factor). Central values, intervals of variations of the parameters used in the simulations are listed in appendix Table C.1.
- After discarding nonphysical parameter sets (leading to $PIA_0 > PIA_m$), the five algorithms are implemented for all remaining sets. A cost function (CF) is evaluated in order to measure the convergence of the five simulated profiles for each set of parameters.

$$\begin{aligned} CF = mean(&NSE(Z_{AZhb}(r), Z_{AZC}(r)),\\ &NSE(Z_{AZC}(r), Z_{AZ\alpha}(r)),\\ &NSE(Z_{AZC}(r), Z_{AZ0}(r)),\\ &NSE(Z_{AZ\alpha}(r), Z_{AZ0}(r)),\\ &NSE(PIA_{AZC}(r), PIA_{\Phi_{dp}}(r)),\\ &NSE(PIA_{AZ0}(r), PIA_{\Phi_{dp}}(r))) \end{aligned} \tag{7.19}$$

where NSE is the Nash-Sutcliffe model efficiency coefficient between two profiles. $NSE = 1$ denotes the perfect agreement between two profiles. $CF_i \geq 0.8$ is the thresold to consider a given set of parameter to be "optimal". The number of optimal parameter sets (NOPS) is computed for each target and timestep and summed up for all targets and the timesteps of an event or group of events. Maximizing the numbers of optimal parameter sets (NOPS), accumulated for all the targets, timesteps and events, yields a measure of the overall quality of a given simulation involving a given set of parameters (fixed and randomly drawn from LHS sampling).

7.3.4 Parameter Optimization

The sensitivity analysis provides the basis for the optimization of the prefactors of the $A-Z$ and $A-K_{dp}$ relationships, PIA_0 values for a series of dC values (constant for a given event), and optimal dC for any given event. The exponents of the $A-Z$ and $A-K_{dp}$ relationships are considered to be constant for the convective events considered in the study. PIA derived from the MRT can provide a series of these exponents for different precipitation types.

As described in Table 7.1, 3 convective events within a span of a month are included in this event. For these events, Fig. 7.4 shows the estimation of optimal dC by maximizing NOPSs, with fixed parameters $b_{AZ} = 0.8$ and $b_{AK} = 1.1$. It gives the results as a function of $dZ = -dC$, dZ represents the dBZ value to be added to the measured Zm to cope with calibration error. The optimal dC values for given events, represented as dC^* hereinafter, are estimated as 0.4 dBZ for 21^{st} July 2017, -1.2 dBZ for 8^{th} August 2017 and -0.4 for 31^{st} August 2017. The combined result for 3 events indicates no calibration error of the measured reflectivities.

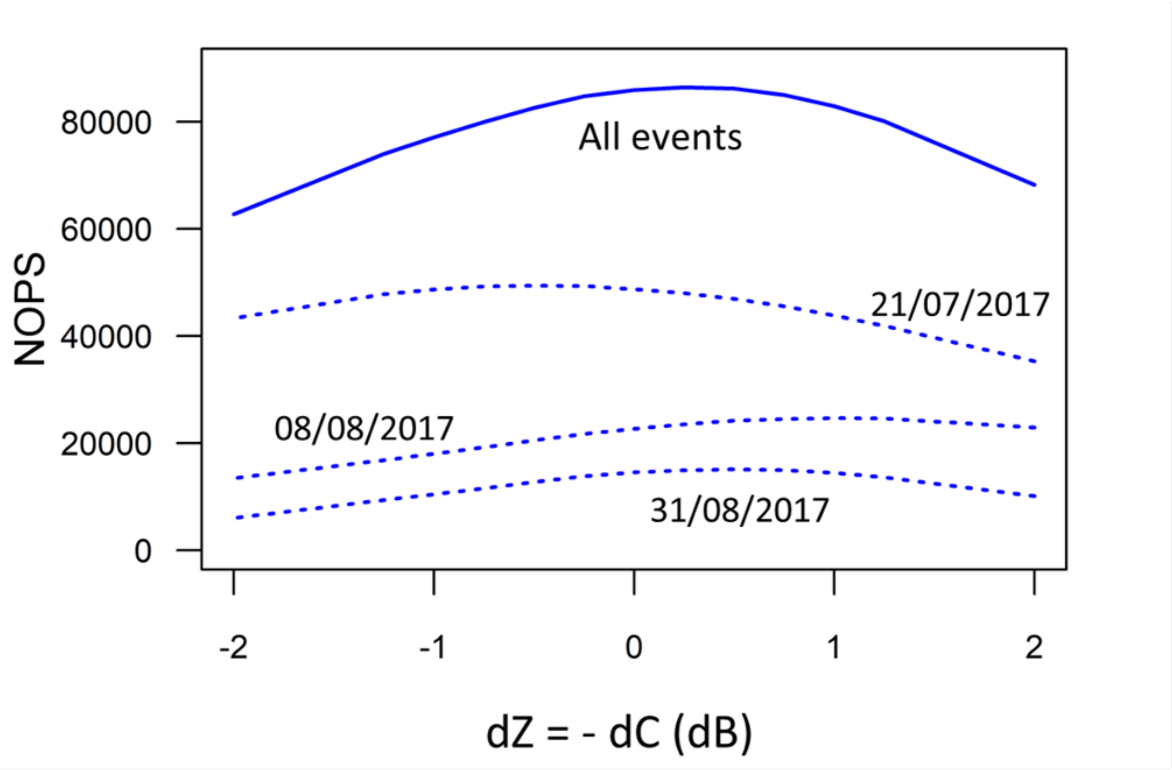

FIGURE 7.4: Evolution of the total number of optimal parameter sets (NOPS) as a function of the radar calibration error for three convective events separately (dotted blue curves) and all together (solid blue curve). The fixed parameters for these simulations are $b_{AZ} = 0.8$ and $b_{AK} = 1.1$.

For the 21^{st} July 2017 event, with $dC^* = 0.4$, Fig. 7.5 presents the time series of quantiles of the distributions of the input variables and the estimated optimal parameters obtained for the best simulation by maximizing the cost function 7.19. The PIA and Φ_{dp} plots indicate that the storm was intense between 15h30 and 17h00 GMT, with medians of 20 dB and 60° respectively. As a result of spatial distribution of the targets and corresponding precipitation variability, the interquartile ranges of

PIA and Φ_{dp} are quite large. The time evolution of the precipitation intensity is represented in the NOPS time series, most probably corresponding to higher counts of range profiles with $PIA_m \geq 1\,dB$ threshold and stable signal corresponding to significant precipitation intensities. The time series of the prefactors a_{AZ} and a_K show a stable median value close to the central values ($a_{AZ} = 1.0\,10^{-4}$ and $a_{AK} = 0.3$) of LHS sampling, and the limits of LHS sampling encompass the variability of the estimated prefactors. This reassures the relevance of DSD-derived relationships deduced from the microphysical measurements and scattering models to simulate radar observations of the convective storms. The interquartile range of a_{AZ} is significantly larger than of a_K. This suggests that the mathematical ambiguity of AZ algorithm alone is much larger and the introduction of the A-K_{dp} relationship improves the attenuation correction significantly (Delrieu et al. 2022). The sampling strategy making use of Z_0 is considered for PIA_0. The close range reflectivity measurements are affected by radome attenuation. This may explain the significant increase in estimated PIA_0 at 17h00 compared to 16h30 and 17h30. It is important to note that there is also a significant increase of PIA_m and $\Phi_{dp}(r_m)$ at this instance.

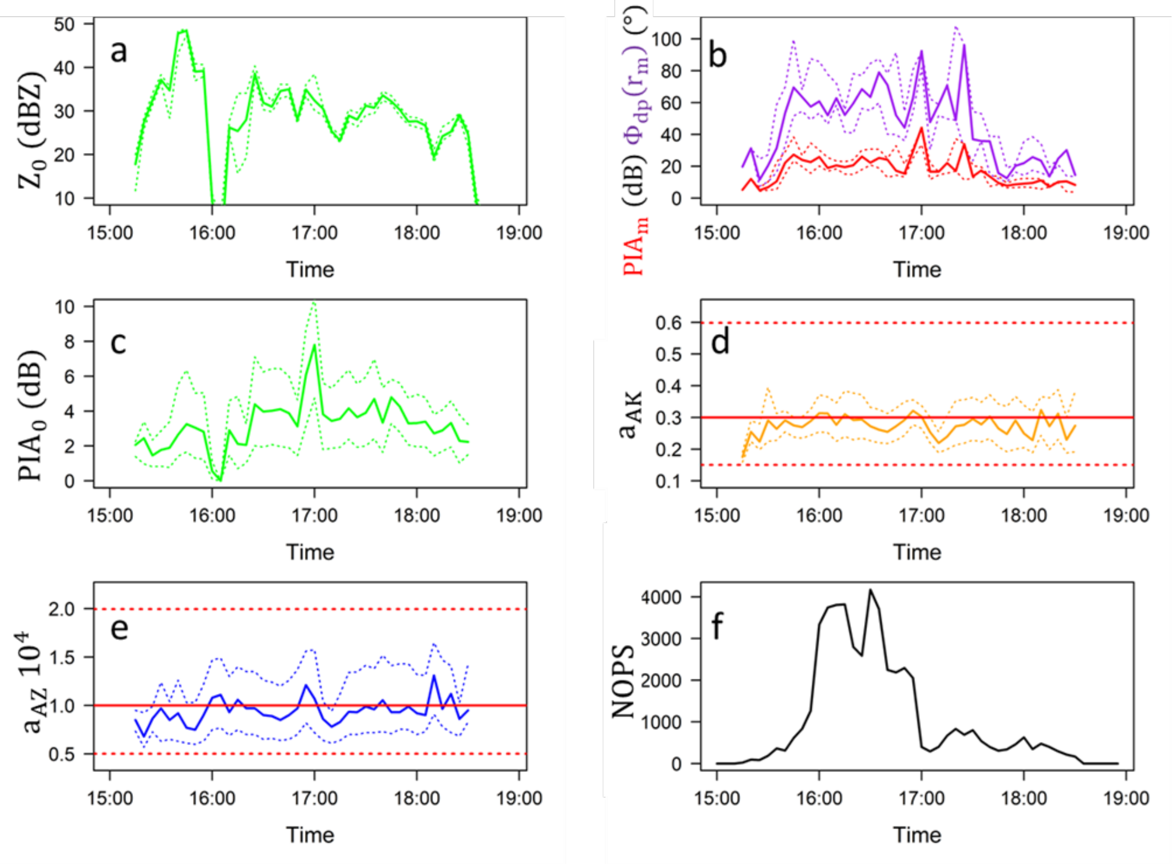

FIGURE 7.5: time series of the input variables and optimal parameters for the best simulation obtained for the 21 July 2017 convective event. The optimal set of fixed parameters for this event is $dC^* = 0.4$ dB, $b_{AZ} = 0.8$ and $b_{AK} = 1.1$. For each of the three considered input variables (a) Z_0; (b) PIA_m (red) and $\Phi_{dp}(r_m)$ (purple), the median (continuous line) and the 25 and 75% quantiles (dotted lines) of their distributions are displayed over the 22 mountain targets. Similar representation is shown for the LHS optimal parameters (c) PIA_0; (d) a_{AZ}; (e) a_{AZ}, except that the distributions are established over all optimal parameters of all targets. In (d) and (e), the dotted horizontal lines materialize the lower and upper limits consider in the LHS of the considered parameter. The time series of the number of optimal parameter sets cumulated over all the 22 targets (NOPS) is displayed in (f).

7.4 Radar QPE implementation

The application of 5 attenuation correction algorithms provides range profiles of corrected reflectivity, specific attenuation and PIA in the direction of mountain targets for each timestep for a given parameter set.

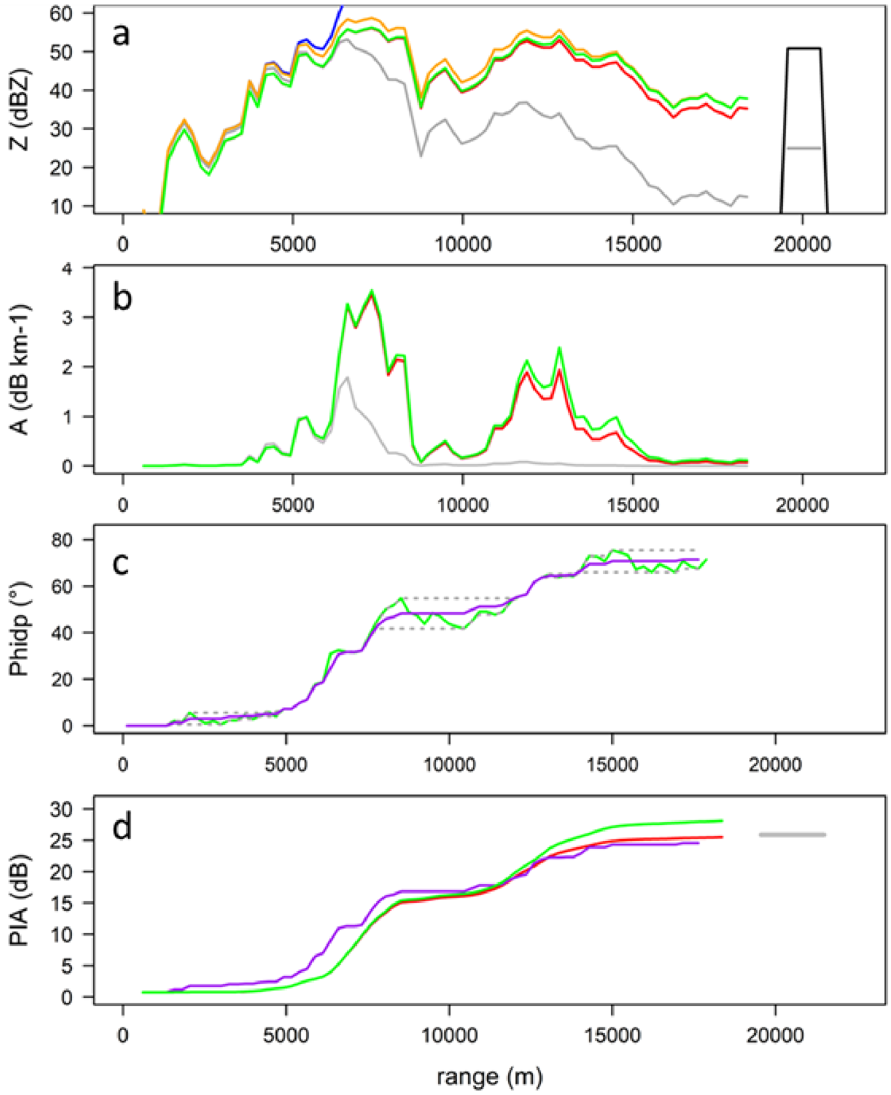

FIGURE 7.6: Implementation of the five algorithms (blue: $AZhb$; red: AZC; orange: $AZ\alpha$; green: $AZ0$; purple: $PIA_{\Phi_{dp}}$) for mountain target "13" (7.1) during the 21 July 2017 convective event at 16h00 GMT using a near-optimal parameter set (Figs 7.4 and 7.5). The results are displayed in terms of profiles of (a) reflectivity, (b) specific attenuation, (c) differential phase shift on propagation and (d) path-integrated attenuation. The grey profile in (a) is the measured reflectivity (Z_m) profile; at 20 km range horizontal black and grey lines show dry-weather and measured reflectivities, respectively. The resulting measured PIA value of 25.2 dB is reported in grey in (d). The grey profile in (b) is derived from the Z_m. The green line in (c) is the raw Φ_{dp} profile and the grey dotted curves are the envelope curves used in the regularization procedure and corrected Φ_{dp} is shown in purple.

Figure 7.6 shows an example of attenuation correction using the 5 algorithms and corresponding range profiles on 21^{st} July 2017 at 16h00 GMT towards the direction of target 13 using a near optimal parameter set form the generalized sensitivity analysis. The near optimal parameter set leads to a cost function (CF) value over passing the CF threshold, but not the best one obtained for this target and time step so that we can visualize some difference between the solutions of the various algorithms. Located at a range of 20 km in the Belledone mountain, it has $Z_{dry} = 50.9$ dB, $PIA_{MRT} = 25.9$ dB, $\Phi_{dp}(r_0, r_m) = 71.5°$ and $Z_0 = 9.5$ dB. The fixed parameter set utilized in this event are $b_{AZ} = 0.8$, $b_{AK} = 1.1$ and $dC^* = -0.4$. The overlapping of the corrected reflectivity profiles from different formulations means the result corresponds to the near-optimal parameter set. The set of LHS parameters for this specific target/time step is $PIA_0^* = 0.46$ dB, $a_{AZ}^* = 1.0\,10^{-4}$, $a_{AK}^* = 0.34$ and $dAF_m^* = 0.99$. The figure corresponds to the simulation with $CF = 0.925$, while the best OPS is 0.981, and NOPS = 55. Although not the best solution, this example displays some differences between different the solutions of different algorithms while still showing convergence. For this parameter set, the solution of AZ_{hb} shows inherent instability and diverges from rest of the solutions at 7 km range. This is consistent with the previous explanations of instability of HB solution at higher precipitation intensities. This algorithm is not considered in the formulation of CF (eqn 7.19). For high PIA_M values, remaining 3 AZ algorithms give similar results. We note that the optimal parameterizations lead to the convergence of the AZC and $AZ0$ algorithms near the radar and to the convergence of the $AZ\alpha$ and $AZ0$ algorithms at the other end of the profile. In the specific attenuation profiles, $AZ\alpha$ and AZC solutions are identical (in red) and slightly different at a long range from the $AZ0$ solution. The significant increments in the Φ_{dp} profile corresponds well with the bumps in A_h profiles. The raw Φ_{dp} profile is quite smooth without significant bumps, suggesting no significant backscattering differential phase (δ_{hv}) contamination (Trömel et al. 2013). The comparision of PIA estimation from 4 algorithms (without $AZhb$) show good overall consistency. PIA from the $AZ\alpha$ and AZC algorithms show very good consistency with the polarimetric derivation at longer range.

The radar QPE is based on the estimation of the rainfall intensities $R(mm\,h^{-1})$ in each range bin using the range profiles of attenuation corrected reflectivity $Z(dBZ)$ or specific attenuation $A(dB\,km^{-1})$, i.e. R-Z and R-A relationships. As proposed in equation 7.3 the R-A relationship is expressed as $R = a_{RA}A^{b_{RA}}$. The parameters a_{RA} and b_{RA} could be estimated and optimized using additional relationships and constraints in the core procedure of GSA approach. However, the main restriction of this method is the requirement of ground based measurements in the direction of each target as constraint. It is therefore beyond the scope of this study. Here, we will utilize the R-A relationship derived using DSD observations at IGE site to obtain a_{RA} and b_{RA}. We will then compare the radar QPE with the raingauge measurements and analyse the results.

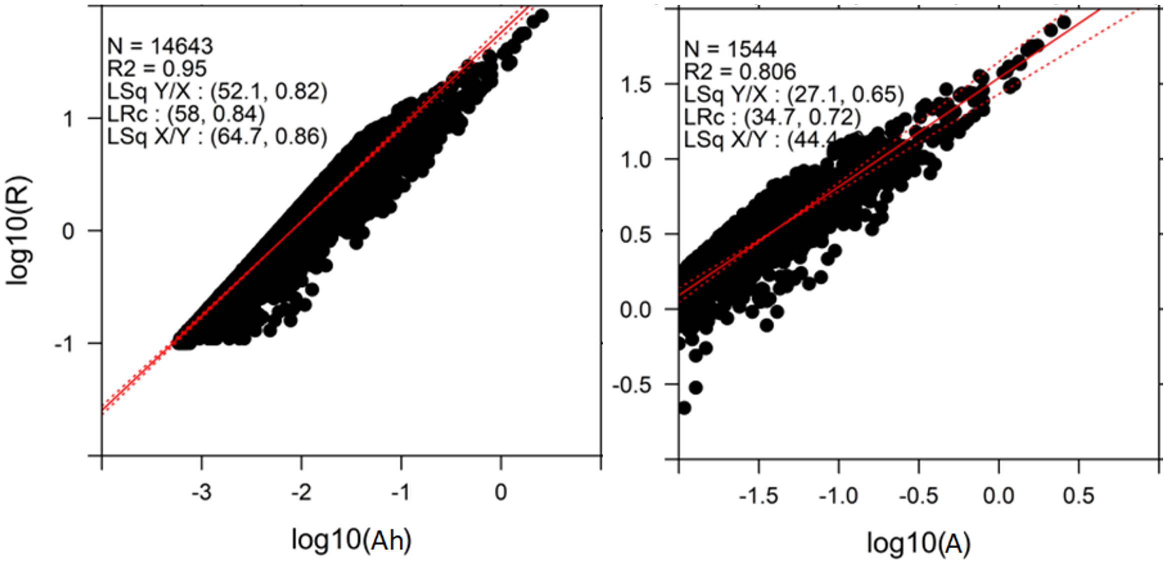

FIGURE 7.7: Fitting of DSD-derived power law models for rainfall intensity $R\,(mm\,h^{-1})$ as a function of the specific attenuation $A_h\,(dB\,km^{-1})$ using the log_{10} transformation of two variables. Annotations are similar to Fig. 7.2. The left subplot utilizes all available dataset and right subplot correspond to the convective events. A threshold of 0.01 $db\,km^{-1}$ is also introduced on the A values to mitigate the impact of low values on the regression.

Figure 7.7 gives the fittings of R-A relationships obtained using the log_{10} transformation of both variables. An event is considered convective if a 5-minutes rainrate of $10 mm\,h^{-1}$ is exceeded at given moment. The first observation is that both log-log scatterplots are distributed in rather linear fashion with high coefficient of determination ($R^2 \geq 0.8$). It suggests that the power-law type R-A relationship is well justified. In the all event fitting (left subplot), the fitting overestimates rainfall intensities at high specific attenuation observations, related to the convective events. This is addressed in convective only fitting (right subplot). As a result of large variation in precipitation intensities during convective events and smaller sample size, the R^2 of logarithmic regression decreases from left to right. As both variables are derived using same DSD and scattering model, both variables have same importance and reliability. As such, we rely on the least rectangle regression (LRc) to obtain the coefficients of R-A relationship. The coefficients of R-A relationship for all events are: $a_{RA} = 58$ and $b_{RA} = 0.84$. During the convective events the coefficients are: $a_{RA} = 34.7$ and $b_{RA} = 0.72$. There is slight difference in the coefficients between "all events" and "convective events" observation. We will study the dependence of QPE in R-A relationships in section 7.6.

In the next section we will analyse the overall performance of 5 algorithms and effects of different parameters on radar QPE, by comparing results with ground based raingauge observations. We perform 3 simulations with different parameter sets to obtain rainfall intensity profiles.

- **Sim001: No parameter optimization**
  This simulation uses the a priori information of the $A - Z - K_{dp} - R$ relationships one could get from the DSD. All the parameters for the A-Z and A-K_{dp} relationships are estimated from the DSD data, i.e. central values for LHS sampling for non-fixed parameters. In addition, on-site attenuation $PIA_0 = 0$ and dC is varied from -2 to 2 dB with stepsize of 0.4 (based on experience with the dataset). The R-A relationship derived from DSD observation of all available convective events (left sub-plot in Fig. 7.7).
  $a_{AZ} = 9.9\,10^{-5}, \;\; b_{AZ} = 0.78$
  $a_{AK} = 0.3, \;\; b_{AK} = 1.1$
  $a_{RA} = 58, \;\; b_{RA} = 0.84$

- **Sim002: Optimized parameters from GSA and all event R-A relationship**
  This simulation takes into account the optimal parameter sets. The calibration error dC varies from -2 to 2 dB. The fixed parameters are $b_{AZ} = 0.8$ and $b_{AK} = 1.1$. Each timestep has an optimal parameter set and PIA_0 similar to one shown in Fig. 7.5 for each target. The OPS leading to the best convergence is actually used for a given target and time step; since it was checked that the convergence takes place over a reduced range of A(r) profiles. The R-A relationship is derived from DSD observation of all events, similar to simulation 001.
  $a_{RA} = 58, \;\; b_{RA} = 0.84$

- **Sim003: Optimized parameters and convective R-A relationship**
  The optimization criteria and parameter set are similar to Sim002, it takes into account the parameter optimization procedure. The R-A relationship derived from the DSD observation of convective events (right sub-plot in Fig. 7.7).
  $a_{RA} = 35, \;\; b_{RA} = 0.72$ is considered owing to the poor fitting of high $R - A$ pairs in Fig. 7.7 left.

7.5 Radar- raingauge matching

The radar QPE procedure provides the range profiles of rainfall intensities $R\,(mm\,h^{-1})$ in the direction of 22 mountain targets as observed by 0° PPI observation using MOUC radar (1920 m asl). The first radar gate is centered at 120 m; the subsequent radar grids have spatial resolution of 0.5° (angular) and 240 m (radial). The time resolution of the radar observation is 5 minutes i.e there is one PPI scan made at the

0° elevation angle each 5 minute. In order to compare the radar QPE with raingauge measurements, we will consider that radar observation at every timestep is representative of average conditions in the last 5 minutes in the given resolution volume. There might be some missing values (NA) in range profiles of $R\ (mm\, h^{-1})$ due to the limitations of 5 algorithms, like grids close to mountain targets for $PIA_{\Phi_{dp}}(r)$ algorithm. The rain-rates R_{AZC}, $R_{AZ\alpha}$ and R_{AZ0} are available only when $PIA_M > 1$ dB (corresponding to the minimum detectable PIA using MRT). The missing $R_{\Phi_{dp}}$ rain-rates are replaced by $R_{AZ\alpha}$ whenever available, if not by R_{AZhb}. The AZ_{hb} algorithm is known to diverge at high PIAs, so we cap R_{AZhb} to the ceiling of $200 mm\ \ h^{-1}$. Another rainrate estimate R_{cor1} is obtained from basic algorithm with calibration correction, without attenuation correction and using the R-Z relationship.

The mountain targets are distributed from 30° to 210° azimuth wrt MOUC radar within the range of 40 km. This area is considered the "inner domain" for radar QPE. There are 10 raingauge stations in this inner domain out of which 8 stations recorded the precipitation during the 3 convective events. Figure 7.1 shows the spatial distribution of different mountain targets and raingauges in the inner domain of MOUC radar. Two main issues must be addressed before the radar QPE can be compared with the raingauge measurements, namely matching temporal resolution and spatial distribution. Figure 7.1 shows that in most cases the raingauges are not located directly in the direction of the mountain targets along the black radial lines. So, the raingauge stations need to be assigned the nearest radar grid where rainrate profile is available. It is done in 2 steps for each station: i) locate the mountain target with closest azimuth, ii) locate the radar grid with minimum distance from the station in this azimuth.

The details of radar - raingauge matching is given in Table 7.2. Each station is assigned a radar grid where rainfall estimate is available; azimuth: mid azimuth of associated target, gate: gate of station wrt target. In case of Col de Porte (CDP) station, it can be observed from the table as well the Fig. 7.1, that station is located within the mountains surrounded by mountain clutter and beyond the range (gate 80) where target 1 starts (gate 76). In this case, it was necessary to adjust the closest grid from gate 80 to gate 74 where rainfall estimate is available and free of ground clutter, at a horizontal distance of 2.37 km from the station. Similarly, there are not mountain targets in the immediate vicinity of Theys station (THE), and the nearest radar grid with rainfall estimates is 4.76 km horizontal distance away, and close to ground clutter.

TABLE 7.2: Details of radar - raingauge matching

station	**id**	**azimut**	**gate**	**range (km)**	**associated mountain target**	**mid azimuth of target**	**start gate of target**	**range of station wrt target (km)**	**gate of station wrt target**	**distance station to grid (km)**	**time resolution (min)**
MOUC	**MOUC**	0	0	0	**0**	**0**	0	0	**0**	0	5
COLDEPORTE	**CSP**	31.2	79.2	18.9	**1**	**37.5**	77	19	$80^* \to 74$	2.37	15
GREENER	**GNR**	39.3	32.2	7.6	**2**	**40.5**	118	7.6	**32**	0.16	1
IGE	**IGE**	61.8	45.1	10.7	**4**	**66.5**	164	10.7	**45**	0.88	10
THEYS	**THE**	58.2	136.2	32.6	**4**	**66.5**	164	32.9	**138**	4.76	6
GRE_LVD	**LDV**	64.8	75	17.9	**4**	**66.5**	164	17.9	**75**	0.53	6
PIPAY	**PIP**	65.6	133.7	32	**4**	**66.5**	164	32	**134**	0.50	6
REVEL	**REV**	75.7	76.4	18.2	**7**	**77.2**	109	18.2	**76**	0.48	6
CHAMROUSSE	**CHM**	95.7	78.2	18.6	**11**	**94.5**	84	18.6	**78**	0.39	6
LUITEL	**LUI**	111.7	72.9	17.4	**16**	**111.8**	99	17.4	**73**	0.03	15
VARCES	**VAR**	139.4	28.8	6.8	**21**	**141.8**	103	6.8	**29**	0.29	6

The second issue is related to the different time-resolution of different measurement stations (Table 7.2). The GREENER station has the finest resolution of 1 minute, IGE has resolution of 10 minutes, Météo-France operated station have a resolution of 6 min, EDF-CEN operated stations have resolution of 15 minutes, and the MOUC performs 0° PPI scans every 5 minutes. While the radar measure is instantaneous, the raingauge time resolution refers to accumulate the rainfall during that time-period. To level the playing field, we assume the radar measurement to represents the average situation of the storm in last 5 minutes, i.e convert rainrate R($mm\ h^{-1}$) to accumulation R(mm in 5 min). Now the least common denominator of all the measurements is 30 minutes, i.e. we aggregate all the rainrates to 30 minutes resolution. It will be referred as 30 minutes scale rainfall hereinafter. Similarly, event scale aggregation is also performed for all 3 events.

7.6 Results

In this section, we compare the results of radar QPE with ground observation and study performance of the parameter estimation procedure. The main goals are: i) to analyse overall performance of 5 attenuation correction algorithms; ii) to understand the dependence and robustness of the algorithms wrt the parametrization and to test the relevance of DSD-derived A-R relationships.

7.6.1 Overall performance of 5 QPE algorithms

The rainfall estimated using different $A(r)$ profiles obtained from different algorithms are compared with the raingauge measurements. Rainfall estimates obtained form $AZhb$, AZC, $AZ\alpha$, $AZ0$ and $PIA_{\Phi_{dp}}$ algorithms will be denoted R_{AZhb}, R_{AZC},

$R_{AZ\alpha}$, R_{AZ0} and $R_{\Phi_{dp}}$ respectively, hereinafter. Rainfall estimated only using calibration correction and no attenuation correction will be referred to as R_{cor1}. AZC and $AZ\alpha$ have same formulation for A(r), hence give the same R estimates; only AZC will be discussed here. Similarly, rainfall measured at the station will be referred to as RG. Rainfall estimates and measurements are aggregated at 30 minutes and event scale.

Event scale

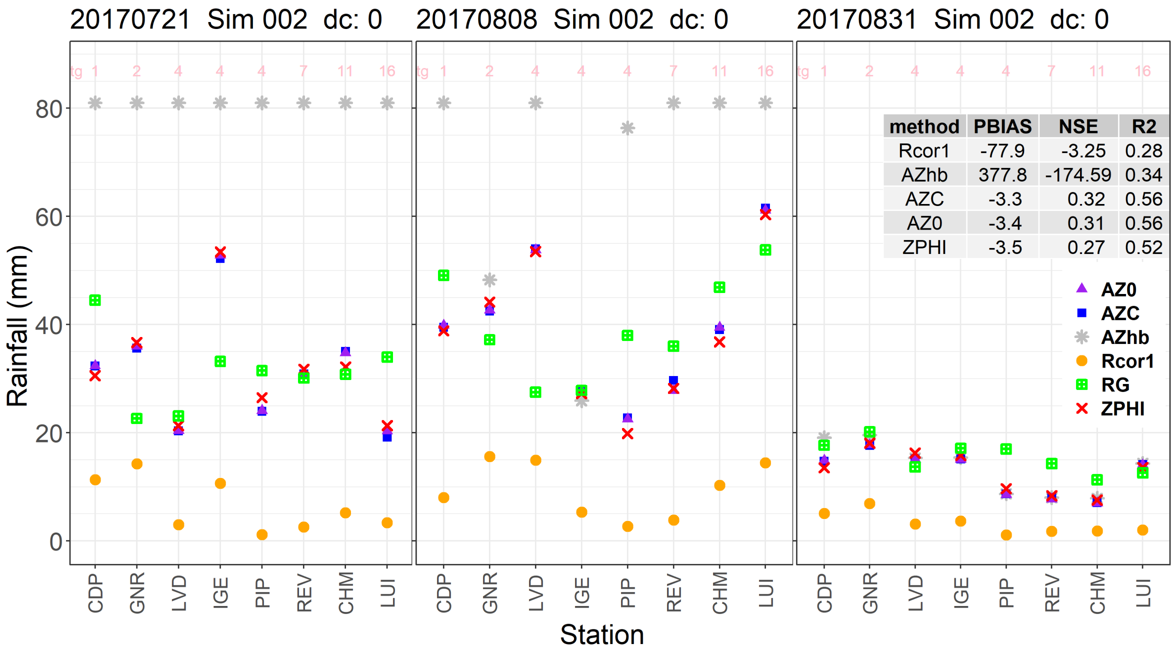

method	PBIAS	NSE	R2
Rcor1	-77.9	-3.25	0.28
AZhb	377.8	-174.59	0.34
AZC	-3.3	0.32	0.56
AZ0	-3.4	0.31	0.56
ZPHI	-3.5	0.27	0.52

FIGURE 7.8: Radar QPE vs raingauge station: rainfall accumulation by event, optimal parameters and global optimal $dC = 0$, Sim 002. Total accumulation (mm) at different stations during 20170721, 20170808 and 20170831 events are presented in left, middle and right subplots respectively. Estimates of 5 different algorithms are marked by different color and symbols. Numbers in grey at the top of plot annotate the mountain target matched with the station.

The characteristics of 3 convective events between 21st July 2021 and 31st August 2021 are detailed in Table 7.1. Figure 7.8 compares the rainfall accumulated at 8 stations whose measurements are available during these events and compares them to the radar QPE estimates at event scale for simulation 002 and global optimal dC = 0. Simulation 002 utilizes the optimal parameter set and dC is allowed to vary from -2 to 2 dB. We can observe that estimates of R_{cor1} are negative biases at every station and every event. Similarly, R_{AZhb} results are unreliable for the (high) PIAs observed during these events; accumulations greater than 80 mm are capped at 81 mm ceiling. R_{AZC} and R_{AZ0} provide similar results. The polarimetric estimate $R_{\Phi_{dp}}$ also matches closely with the R_{AZC} and R_{AZ0} estimates. The rainfall at Col de Porte

(CDP) and Pipay (PIP) stations are consistently underestimated even by R_{AZC}, R_{AZ0} and $R_{\Phi_{dp}}$ formulations. Both these stations are located in the mountainous and have significant ground clutter around them (see Fig. 7.1). At other stations, the latter 3 algorithms seem to underestimate rainfall high accumulations, and work well for low accumulations. Although this tendency is not very strong.

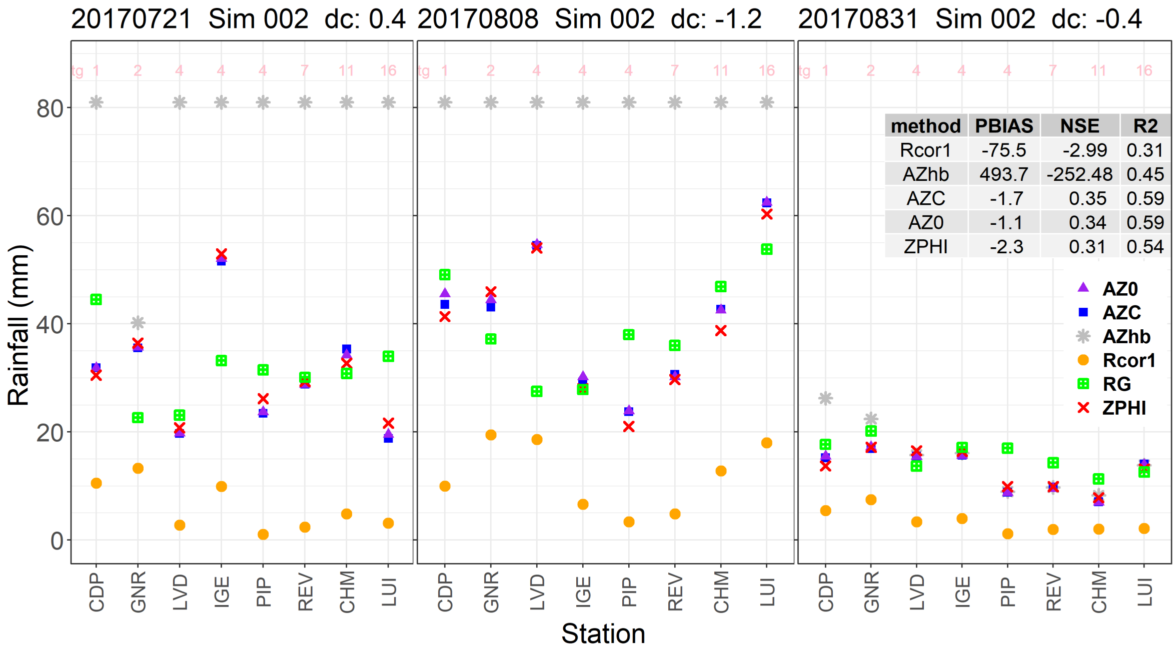

method	PBIAS	NSE	R2
Rcor1	-75.5	-2.99	0.31
AZhb	493.7	-252.48	0.45
AZC	-1.7	0.35	0.59
AZ0	-1.1	0.34	0.59
ZPHI	-2.3	0.31	0.54

FIGURE 7.9: Radar QPE vs raingauge station: rainfall accumulation by event, optimal parameters and event-wise optimal $dC = dC^*$, Sim 002. Similar explanation of the content to Fig. 7.8.

Figure 7.9 plots the QPE estimates accumulated at event scales for Sim002 and event optimal dC (dC^*). There is only a slight gain on all the criteria (pbias, R^2 and NSE) in radar QPEs of second event which has the largest difference in dC between Figs 7.8 and 7.9. Changing from global optimal dC to event optimal dC^*, does not show significant improvement in radar QPEs in event scale accumulation.

Radar - raingauge time series 30 min

Figure 7.10 shows the time series of 30 min rainfall accumulation for Sim002 and event optimal dC (dC^*). The three best performing algorithms and raingauge measurements are shown in the figure. The GREENER station is located in the valley (220 m asl) at around 7 km from MOUC radar. All radar QPE methods overestimate the precipitation by around 20% compared to the raingauge measurement. For specific timesteps with high rain amounts, the overestimation is very large e.g. up to 162% for 8 August 2017 at 11:15. The 30 min rainfall accumulation radar - raingauge scatterplots have many outliers and the difficulty to find valid explanations has led us to focus on the event scale rainfall accuulations for further analysis of the QPE results.

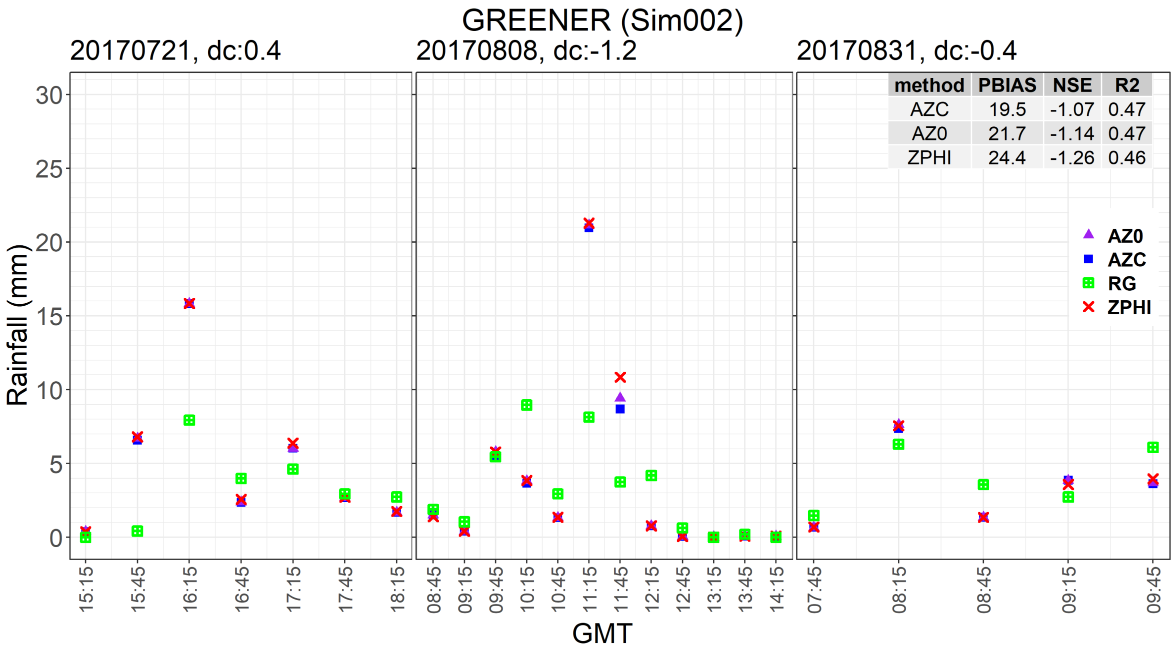

FIGURE 7.10: Radar QPE vs GREENER rain station measurements: time series of evolution of 30 minutes rainfall accumulation, Sim 002, event optimal $dC = dC^*$. 3 events shown in 3 subplots. Estimates of different algorithms marked in different colors. Rainfall (mm) in Y-axis is the rain accumulated in 30 minutes. Time steps in X-axis is the midpoint of 30 min collection interval.

Figures 7.11 and 7.12 show the time series of evolution of 30 minutes rainfall accumulation for the 3 events with Sim 002 at Pipay station for global optimal dC and event optimal dC^* respectively. The Pipay station is located in the mountains at around 33 km from the MOUC radar and surrounded by ground clutter. Radar QPE mostly underestimates the rainfall at Pipay station by around 35%. Similar under estimation is observed at another station Col de Porte, also located in the mountains (although not shown here). Comparison of summary statistics at Pipay for global (Fig. 7.11) and event optimal dC (Fig. 7.12)shows no significant difference; there is only a slight improvement in $R_{\Phi_{dp}}$ using dC^*. It suggests that the calibration error does not have significant impact on the QPE at lower precipitation intensities. The station in the valley does not show the similar trend. At GREENER there is some over-estimation in the periods with high precipitation intensity. Although just 26 km apart, the storms at two stations show quite different characteristics which is typical to convective systems. Like in the event scale accumulation, the R_{cor1} consistently underestimates the precipitation and R_{AZhb} is unreliable (not shown here). R_{AZC}, R_{AZ0} and $R_{\Phi_{dp}}$ perform the best and give similar QPE estimates. Pipay is one of the best performing stations, most probably due to less periods with high rainfall intensities.

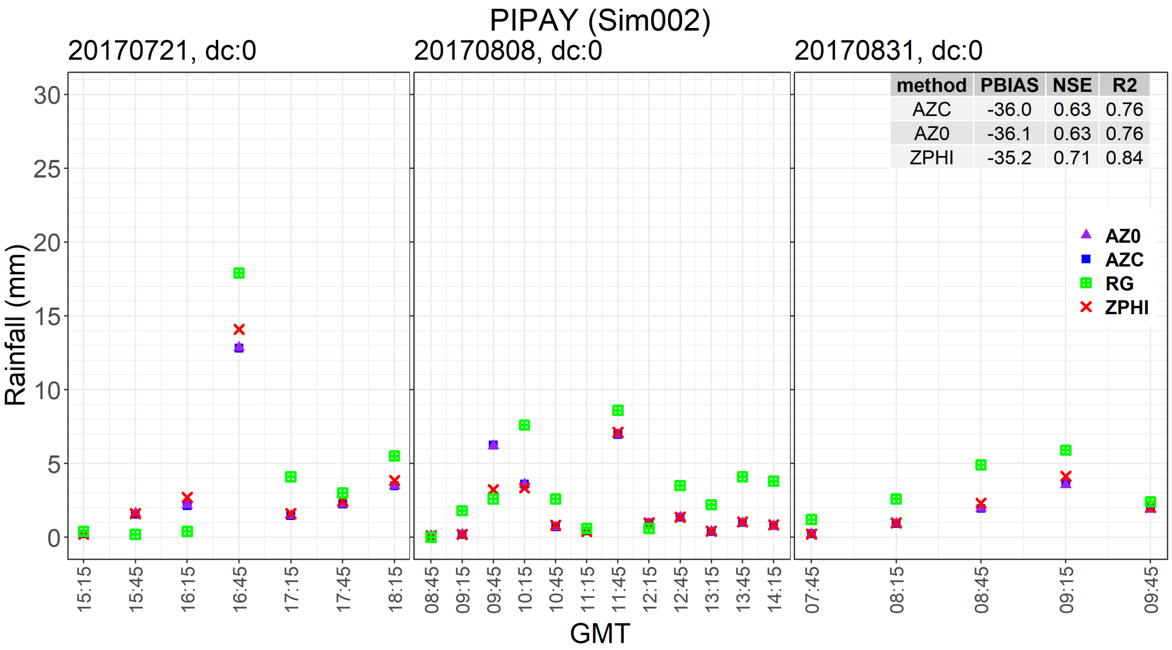

FIGURE 7.11: Radar QPE vs PIPAY rain station measurements: time series of evolution of 30 min rainfall accumulation, Sim 002, global optimal $dC = 0$. Explanations similar to GREENER station

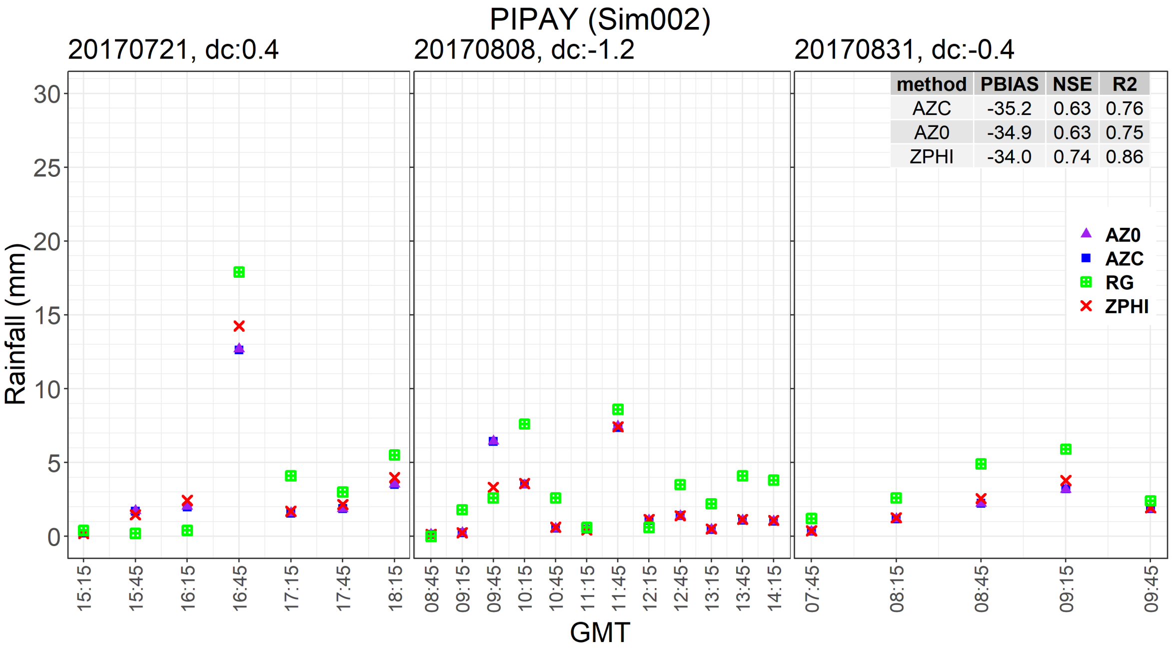

FIGURE 7.12: Radar QPE vs PIPAY rain station measurements: time series of evolution of 30 min rainfall accumulation, Sim 002, event optimal $dC = dC^*$. Explanations similar to GREENER station

7.6.2 Dependence on the parameterization and robustness of 5 QPE algorithms

Figure 7.13 shows the radar - raingauge rainfall accumulation at the event scale using the R_{cor1} formulation, which simply corrects for the calibration error and does not take attenuation into account. For all types of parameter sets, irrespective of parameter optimization and choice of R-A relationships, R_{cor1} systematically underestimates the rainfall accumulation. It suggests the presence of attenuation and the need to correct for attenuation before QPE applications.

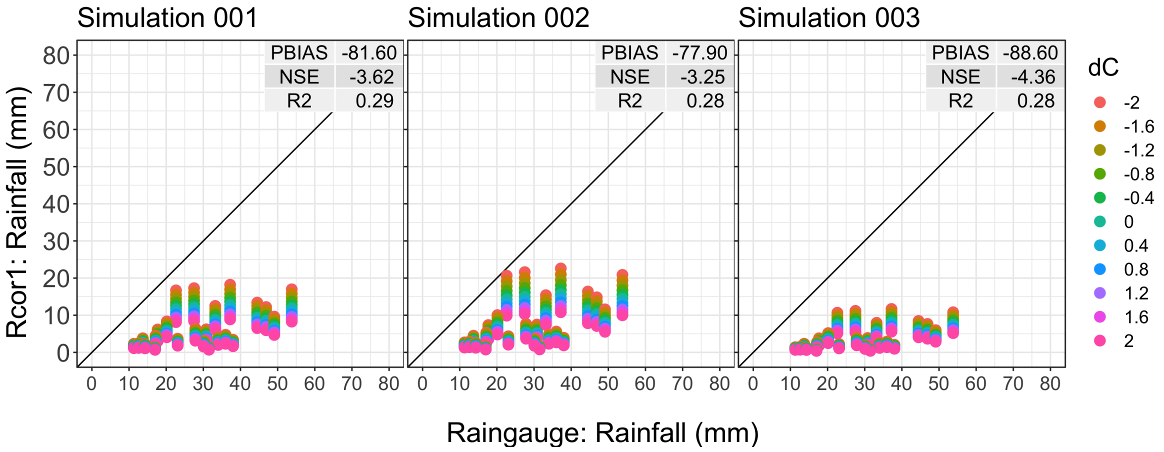

FIGURE 7.13: Radar - raingauge scatterplot: R_{cor1}, event scale accumulation, all stations, all events, all dC. GSA results for different dC shown in different colors. Grey line marks the 1:1 line. Sim 001, Sim 002 and Sim 003 are shown in left, middle and right sub-plots respectively. Summary statistics at $dC = 0$ for the corresponding simulation are shown on the top-right of each sub-plot.

As the AZC and $AZ\alpha$ produce identical specific attenuation profiles, i.e. same precipitation estimate, we focus on the performance of 4 algorithms (R_{AZhb}, R_{AZ0}, R_{AZC} and $R_{\Phi_{dp}}$). Figure 7.14 shows the radar - raingauge (R_G) scatterplot for R_{AZhb} method. Sim 001 and Sim 002 correspond to the all precipitation types R-A relationship (section 7.4, Fig. 7.7), Sim 003 makes use of convective R-A relationship. Sim 002 utilizes the optimal parameter set from GSA, Sim 001 only utilizes the DSD derived relationships. R_{AZhb} method is known to diverge dramatically for high PIAs as seen in Fig. 7.14, irrespective of the choice of parametrization and the dC values.

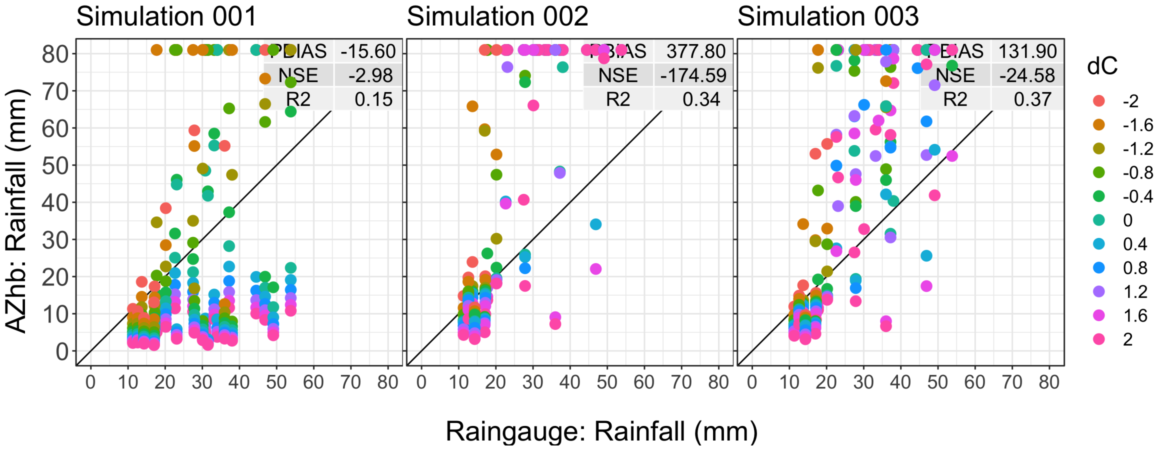

FIGURE 7.14: Radar - raingauge scatterplot: AZhb formulation, event scale accumulation, all stations, all events, all dC. Radar estimated rainfall accumulation is capped at 80 mm ceiling and accounted for in the criteria calculation. Description similar to Fig. 7.13

.

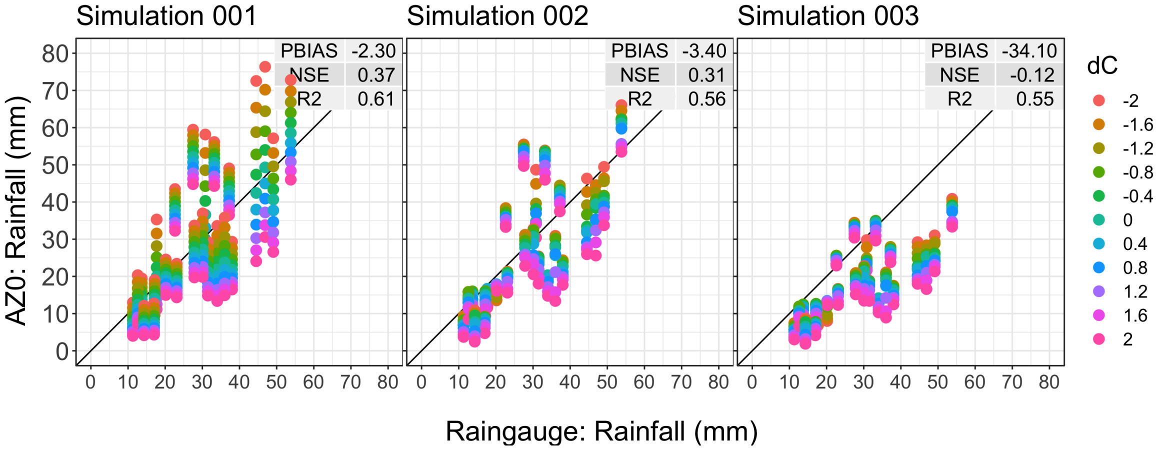

FIGURE 7.15: Radar - raingauge scatterplot: AZ0 formulation, event scale accumulation, all stations, all events, all dC. Similar description as Fig. 7.13.

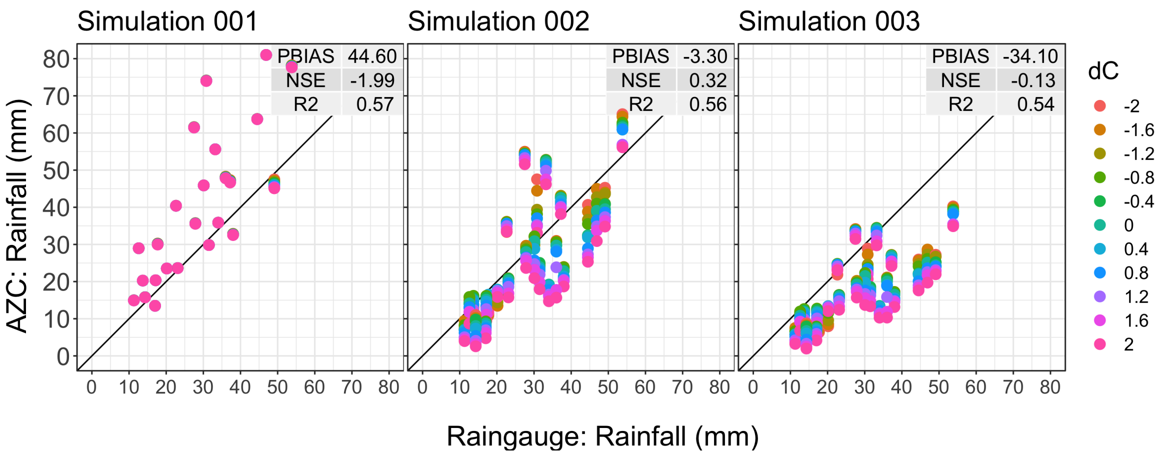

FIGURE 7.16: Radar - raingauge scatterplot: AZC formulation, event scale accumulation, all stations, all events, all dC. Description similar to Fig. 7.13.

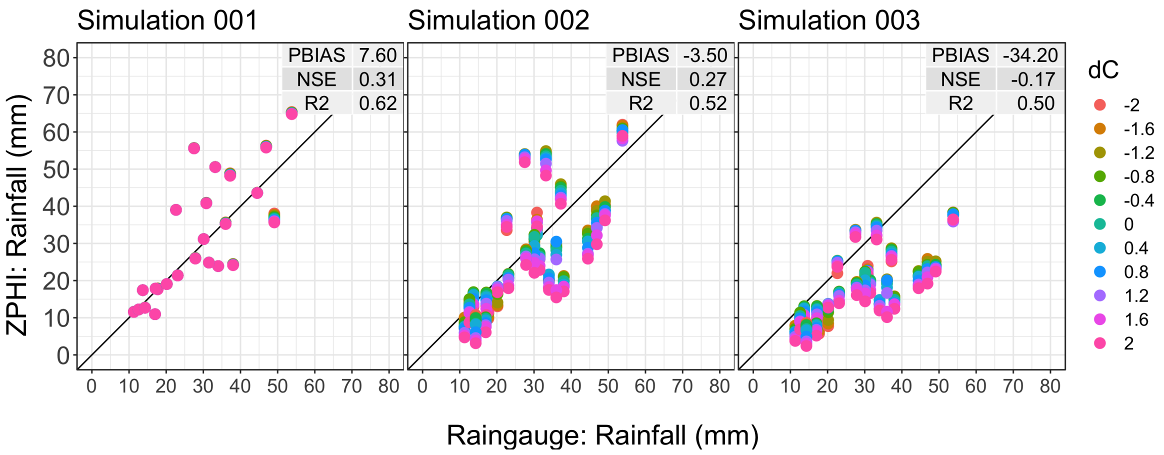

FIGURE 7.17: Radar - raingauge scatterplot: $PIA_{\Phi_{dp}}$ formulation, event scale accumulation, all stations, all events, all dC. Description similar to Fig. 7.13.

Figures 7.15, 7.16 and 7.17 show similar analysis for R_{AZ0}, R_{AZC} and $R_{\Phi_{dp}}$ formulations respectively. As the convergence of A(r) profiles are ensured, except for R_{AZhb} algorithm, the R_{AZC}, R_{AZ0} and $R_{\Phi_{dp}}$ estimates are very similar for Sim 002 and Sim 003. Sim 001 which does not take GSA into account shows that the R_{AZC} and polarimetric $R_{\Phi_{dp}}$ formulations do not depend on the calibration error. Ensuring the convergence of different methods for parameter optimization means there is some impact of dC in R_{AZC} and $R_{\Phi_{dp}}$ methods for Sim 002 and Sim 003. R_{AZ0} is most sensitive to calibration error, especially for Sim 001 parametrization, while some compensation occurs between the GSA parameters in Sim 002 and Sim 003. There is an overcorrection in Sim 001 of R_{AZC} algorithm, due to $PIA_0 = 0$ and independence from dC. It is not the case in Sim 001 of $R_{\Phi_{dp}}$, also independent of dC but with $PIA_0 \neq 0$. This suggests that the on-site attenuation and radar calibration error are dependent on each other. As the summary statistics shown in the figures correspond to dC = 0, in terms of R^2 statistics Simulation 001, which does not use optimal parameter set, performs slightly better than Simulation 002 and Simulation 003. Simulation 001 also shows that the $R_{\Phi_{dp}}$ algorithm performs best in terms of NSE statistics and R_{AZ0} is the best in terms of R^2 statistics. It is clear that R_{AZ0}, R_{AZC} and $R_{\Phi_{dp}}$ perform much better than R_{AZhb} algorithm, and only these 3 methods will be used for further analysis.

7.6.3 Relevance of DSD derived A-R relationship

We have 3 different simulations with 2 different DSD-derived A-R relationships for convective events. Sim 002 utilizes the R-A relationship based on all events, while Sim 003 utilizes the R-A relationship based on convective events. Figures 7.15, 7.16 and 7.17 all show that QPE based on convective RA relationship (Sim 003) consistently underestimates the rainfall estimates by around 35% while the bias is much less with the all-events R-A relationship. The result is a bit surprising but it shows the limitation of the validity of implementing the DSD-based $Z - A - K_{dp} - R$ relationships at the radar resolution scale. It suggests the need to parametrize the coefficients of R-A relationships by including rainrate data in GSA.

7.6.4 Calibration error dC estimation

Delrieu et al. (2022) estimated optimal dC based on GSA approach for the physical model (described in section 7.3.1) during 3 events in discussion here. They estimated the global optimal dC to be 0; but the event optimal dC values were estimated as 0.4, -1.2 and -0.4 dBZ for the 20170721, 20170808 and 20170831 events respectively. It is interesting to see if the radar - raingauge summary statistics confirm or not the GSA results, based on the NOPS, about the optimal dC. The radar calibration error dC is considered to be constant for an event or group of close events. Figure 7.18 attempts to find a global (all 3 events together) optimal dC using event scale accumulation of R_{AZ0}, R_{AZC} and $R_{\Phi_{dp}}$ in Sim 002. Due to parameter compensation provided by GSA for dC in [-1.2,0.4], the dCs have quite low NSE, with a plateau of 0.3 for dC between [-1.2,0.4]. It is interesting to observe that NSE decreases for $dC > 0$ i.e. when Z_m decreases.

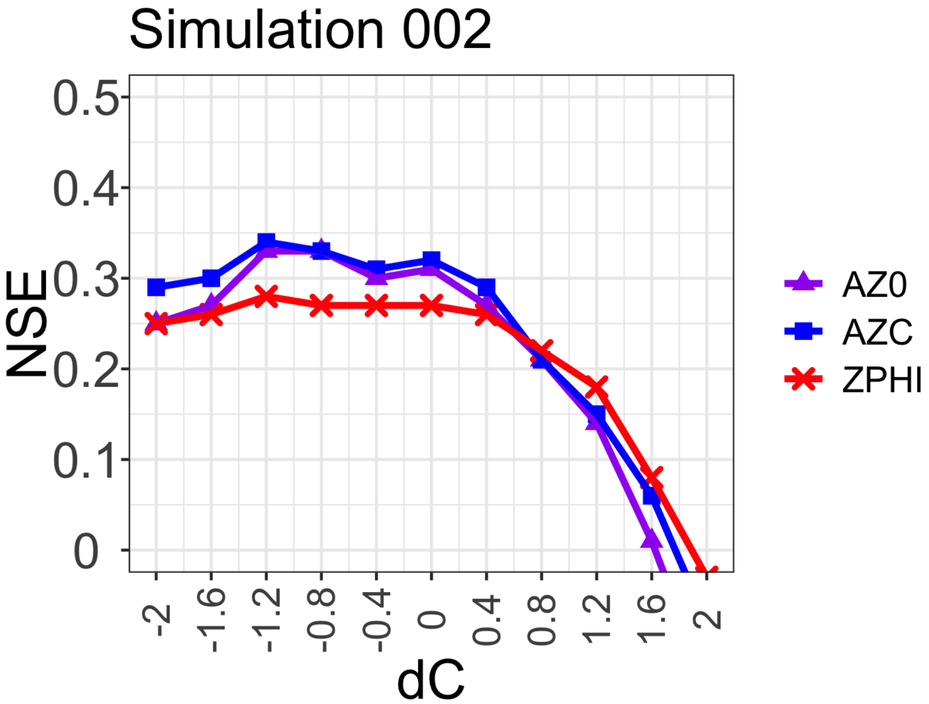

FIGURE 7.18: NSE of radar QPE vs raingauge measurement regression fitting at event scale accumulation as a function of calibration error dC for Simulation 002. Three QPE estimation methods are considered: R_{AZ0} (purple), R_{AZC} (blue) and $R_{\Phi_{dp}}$ (red).

In conclusion, the search for optimal dC (both global and event wise) is hardly feasible here due to consideration of 3 short rain events and poor relationship between radar and raingauge measurements at the 30 min timescale, illustrated in Figs 7.10 - 7.12 and section 7.6.5.

7.6.5 Performance of radar QPE at different stations

Figures 7.8 and 7.9 show the performance of the radar QPE formulations at different station for event scale accumulation. Radar QPE overestimates rainfall at valley based stations (GREENER, IGE), whereas underestimates rainfall on the mountain based stations (CDP, PIP, CHM). At low rainfall intensity event(31 August 2018) radar QPE at most stations fare better than in high intensity event(08 August 2017). Pipay (PIP) station is surrounded by ground clutter, radar QPE in this station is significantly underestimated. Similarly, Col de Porte (CDP) station is also surrounded by ground clutter and is relatively further from nearest available radar pixel.

In complement to the comparison of the radar - raingauge estimates at the event scale Fig. 7.19 shows the overall performance of radar QPE formulations at the 30 min scale at 3 different stations (CDP, IGE and PIP) for Sim 002 with event optimal dC^*. In all 3 stations, R_{AZC} and $R_{\Phi_{dp}}$ provide the best estimates of precipitation at 30 min accumulation interval, based on large R^2 and small bias. There are clearly some outliers that are difficult to understand. Among 3 stations, PIPAY performs the best with R^2 of 0.89 for $R_{\Phi_{dp}}$, while Col de Porte performs the worst (R^2 of 0.17 for $R_{\Phi_{dp}}$).

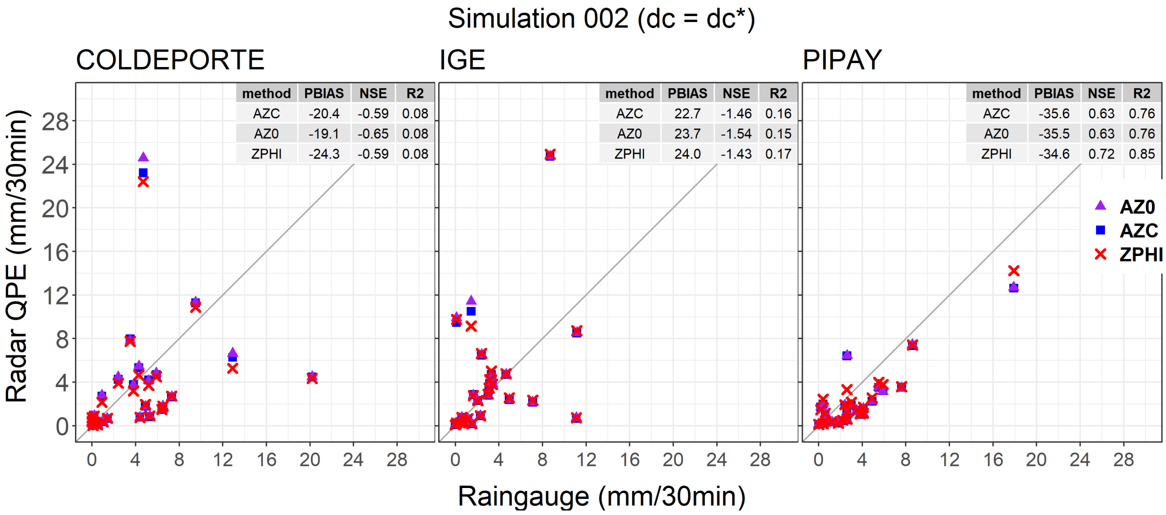

COLDEPORTE

method	PBIAS	NSE	R2
AZC	-20.4	-0.59	0.08
AZ0	-19.1	-0.65	0.08
ZPHI	-24.3	-0.59	0.08

IGE

method	PBIAS	NSE	R2
AZC	22.7	-1.46	0.16
AZ0	23.7	-1.54	0.15
ZPHI	24.0	-1.43	0.17

PIPAY

method	PBIAS	NSE	R2
AZC	-35.6	0.63	0.76
AZ0	-35.5	0.63	0.76
ZPHI	-34.6	0.72	0.85

FIGURE 7.19: Performance at different stations: Radar - raingauge scatter-plots for Sim 002, event optimal dC^*, 30 minutes accumulation of rainfall, all events. Different radar QPE algorithm products are colour coded and shown in the legend. 3 stations are presented: Col de Porte (left), IGE (mid) and Pipay(right). Summary statistics of errors are presented as annotation table on top of each subplot. 1:1 grey line represents the perfect estimate.

Table 7.3 summarises the performances of $R_{\Phi_{dp}}$ and R_{AZC} based on bias, R^2 and NSE wrt raingauge measurements at all the stations. The statistics is for estimates using simulation 003, with event optimal dC^* and 30 minutes accumulation. Once again, among all the stations, QPE estimation is the best at Pipay station, and the worst at Col de Port and IGE stations. There is a clear trend of positive bias in radar QPE at the stations in the valley (LDV, GREENER, IGE) and negative bias at the stations in the mountains (CHAMROUSSE, COLDEPORTE, LUITEL, PIPAY, REVEL). In the mountains due to ground clutter from smaller mountains close to the targets, radar observation might not be available in immediate vicinity of the stations, eg. at COLDEPORTE. Similarly, within a horizontal distance of 2 km the precipitation dynamic might be completely different. A similar summary for the global optimal dC is presented in Table C.2.

TABLE 7.3: Performance of radar QPE at different stations.
Sim 002, 30 min accumulation, event optimal dC

station	AZ0			AZC			ZPHI		
	PBIAS%	R^2	NSE	PBIAS%	R^2	NSE	PBIAS%	R^2	NSE
COLDEPORTE	-16.5	0.08	-0.67	-18.5	0.08	-0.58	-23.1	0.08	-0.54
GREENER	21.7	0.47	-1.14	19.5	0.47	-1.07	24.4	0.46	-1.26
GRE_LVD	39.9	0.23	-1.15	39.6	0.23	-1.11	42.1	0.26	-1.12
IGE	25.2	0.15	-1.59	23.5	0.15	-1.49	24.6	0.17	-1.43
PIPAY	-34.9	0.75	0.63	-35.2	0.76	0.63	-34.0	0.86	0.74
REVEL	-14.8	0.46	0.06	-13.8	0.46	0.05	-14.2	0.49	0.09
CHAMROUSSE	-5.9	0.49	0.17	-4.4	0.48	0.08	-10.9	0.51	0.29
LUITEL	-4.5	0.22	-0.30	-5.2	0.21	-0.31	-5.2	0.23	-0.32

7.7 Discussion and Conclusion

While value of high resolution X-band radars is significant for mountain and urban hydrology, severe attenuation limits their use in QPE. Robust attenuation correction is difficult unless the estimates of total attenuation are available at a distance from the radar. The mountainous regions are specially data scarce and lack complementary observation systems. Under the framework of RadAlp experiment, Delrieu et al. (2022) proposed a more or less 'stand alone' attenuation correction framework for X-band radar during convective events (i.e. without the influence of the melting layer) operating in mountainous terrain. The formulations of the physical models is based on attenuation-reflectivity (A-Z) algorithms constrained, or not, by estimated PIAs, and polarimetric total differential phase Φ_{dp}. A general sensitivity analysis approach is used for parameter estimation required in radar QPE, like the coefficients of A-Z and $A - K_{dp}$ relationships. This chapter briefly discussed the main components of the said physical model, important results of the sensitivity analysis for parameter estimation, and parameter optimization. We discussed some interesting results of optimal radar calibration errors and prefactors of A-Z, $A - K_{dp}$ relationships during 3 convective events. Using the same 3 convective events we performed a validation exercise of estimated parameters using DSD-derived R-A relationships and estimated A(r) profiles. The rainrates were estimated in the direction of mountain targets, where PIA constaints are available, and compared measurements of the nearby raingauge stations.

From Radar - raingauge comparisions at the event scale, we found that R_{cor1} underestimates precipitation accumulation i.e. there is an absolute need to correct for attenuation. R_{AZhb} i.e. the algorithm unconstrained by PIA_M is dramatically unstable and useless for attenuation correction of convective rain at x-band. With the optimized parameters (Sim 002), R_{AZC}, R_{AZ0} and $R_{\Phi_{dp}}$ provide similar results with moderate sensitivity to the dc^* value in the [-1.2,0.4 dB] range. This may be related to the internal compensation of the parameters optimization in the GSA.

Suprisingly the convective R-A relationship derived from DSD measurements leads to more biased radar - raingauge estimates than all rain types R-A relationship, a possible indication of scaling effects between the DSD and radar measurements. Similarly, the radar measurements are made at 1900 m asl while the disdrometer estimation of the some parameters are made at ground level (200 m asl). DSD measurements at the ground level might not be representative of the precipitation observed by the radar due to the possibilities of collision-coalescence (growth) or evaporation (decrease) in between. Several limitations of the study are related to (i) the observation of numerous outliers at the 30-min time scale possibility related to the radar - raingauge spatial matching, the presence of clutter, and inherent large variability of convective precipitation; (ii) the small number of events considered impacting the robustness of the statistics.

Chapter 8

Conclusion and Perspective

8.1 Conclusion

The goal of this study was to continue improving the precipitation estimation in complex terrain (high mountains) using weather radars. The RadAlp experiment has unique setup of 2 dual-polarimetric X-band radar systems (MOUC: on top of Mount Moucherotte, and XPORT: in Grenoble valley) with an altitude gradient of 1700 m and a distance of 11 km. They are complemented by another K-band vertically pointing micro rain radar and disdrometer in the valley; and a network of 10 rain gauges around the valley. This setup essentially overcomes the radar positioning dilemma; able to capture both the fine-scale dynamics in convective systems using mountain-top radar and thermodynamic phase changes at low altitudes in winter stratiform systems using valley based radars. Attenuation is significant at X-band; especially in the melting layer, which is still poorly understood. We aimed to exploit the dual polarimetric capabilities of the radars, and capability to observe horizontal and vertical cross-sections of atmosphere above the valley to further our understanding of the micro-physical processes in the melting layer and to improve the radar QPE. Chapter 3 investigates the vertical extent of atmosphere in presence of melting layer using valley based radars. The permanent echoes of surrounding mountains are used in Chapter 4 to obtain the direct measures of path integrated attentions. A new algorithm is developed in Chapter 5 to regularize, often noisy differential phase shift signal which is immune to attenuation, radar miscalibration and partial beam blockage. Chapter 6, utilizes the ML characterization, PIA estimation and Φ_{dp} regularization from previous chapters to study the PIA - Φ_{dp} relationships within the ML. Chapter 7 explores the use of generalized sensitivity analysis based physical model of attenuation corrections for qualitative precipitation estimation during 3 convective events.

- The long-term observation of ML using the quasi vertical profiles of 25 deg elevation angle PPI scans of XPORT radar utilizing different polarimetric observations enabled us to study the micro-physical processes in the melting layer and their corresponding radar signatures. The Z_h, Z_{dr} and ρ_{hv} signals are enhanced in the melting layer, while the fall velocity (W) increases steadily. The Z_h peak altitude occurs at higher altitude, followed by ρ_{hv} and Z_{dr} largely influenced by the melting process of largest hydrometeors. Z_h first catches the start of melting process at ML top as large number of small ice particles start to melt as they cross the 0°C isotherm, while ρ_{hv} responds longest to the end of melting of largest hydrometeors towards the ML bottom. Z_h and ρ_{hv} are the best indicator of ML top and ML bottom in radar-only identification of ML. In MRR, maximum(W) corresponds well with the altitude of ρ_{hv} bottom. Long term ML characterization shows that polarimetric variables have strong added-value in describing the ML processes. Intensity of precipitation has the biggest (proportional) effect on the ML width. In average the ML over Grenoble has width of 609 m with standard deviation of 162 m.

- While a limitation due beam blockage, the mountains also provide a very stable and strong echo in dry weather. Precipitation between radar and mountain range attenuates the mountain returns. Mountain reference technique (MRT) utilizes this discrepancy between wet- and dry-weather mountain returns to measure the path integrated attenuation due to precipitation between radar and a mountain target. Typically grids with $Z_h \geq 45 dBZ$ in long-term observation are considered to be mountain targets. The stability of the targets is given by the standard deviation of the "dry" weather returns ranges. It ranges from 1.25 to 1.56 dBZ for MOUC 0° elevation angle PPI scans. It sets the minimum detectable PIA to 1 dB. Time stability of mountain returns, beam width integration in the vertical and heavy rainfall over the target itself are the main sources of error.

- The polarimetric observation differential phase shift (Φ_{dp}) is directly measurable and immune to attenuation, calibration error and partial beam blockage. In chapter 5, an iterative algorithm based on maximum-allowed step size between consecutive bins was developed to regularize the range profiles of Φ_{dp}. The algorithm works well in the rain and snow. Noise in the measured Ψ_{dp} profiles is significant at the ML boundaries, ground clutter and in presence of Mie-scatterers. At high elevation angle scans, in the melting layer, the backscatter differential phase manifests as a "bump" Φ_{dp} profiles. However, in low elevation scans, there is no significant "bumps" in Φ_{dp} profile. Two goodness of fit parameters, NSE (of the final profile) and Not NA ratio (of the pre-processed profile) allow us to quantify the quality of regularized profiles. Estimation of initial values, $\Phi_{dp}(r_0)$ for forward envelope and $\Phi_{dp}(r_m)$ for the backward envelope are the main sources of error.

- Investigation of PIA - Φ_{dp} relationship at different stages of melting layer yields the most important results of this study. The goal was to obtain a relationship similar to $A - K_{dp}$ relationship used for robust attenuation correction in the rain. In rain this relationship is almost linear with slope of 0.3. We were able to study similar relationship in the melting layer, by utilizing the PIA estimated using MRT and Φ_{dp} in the direction of the corresponding target, using the MOUC 0° elevation angle PPI scan, supported by ML identification from the valley based radars. We created normalized vertical profiles of PIA and Φ_{dp} by using a large dataset with ML at different altitudes close to MUOC 0° elevation beam center. The "vertical" profiles PIA and Φ_{dp} have clear ML signal. However unlike in rain, a single linear $PIA - \Phi_{dp}$ relationship is not able to define the relationship in the ML. At different stages of melting there are different linear $PIA - \Phi_{dp}$ relationships, with a maxima just above the Ml center. The slopes of these linear relationship ranges from 0.3 to 0.58 at different stages of melting. Vertical extent of radar beam and non-uniform beam filling were the main limitations of this study.

- A physical model with 5 different formulations that utilizes the PIA derived from the MRT and corresponding regulated Φ_{dp} profiles to estimate and optimize radar QPE parameters using generalized sensitivity analysis approach were used to correct for attenuation correction in rain during 3 events. The 0° elevation PPI scans of MOUC radar were used. The physical method delivers a 'stand-alone' radar only attenuation correction mechanism. 8 rain gauges were available during the events. The radar QPE overestimated the rainfall accumulation in the valleys while underestimated them in the mountains. The rain gauge stations surrounded by ground clutter had maximum bias. DSD derived $R - A$ relationships were used to estimate the rain rates. The performance of the radar QPE algorithm was sensitive to the choice of R-A relationship.

8.2 Future Perspective

- Investigation of PIA - Φ_{DP} relationship with a larger dataset to include more observations in the ML boundaries and in the snow and rain regime is necessary. Diversity in events and altitudes of the ML will allow investigating if the assumption of linearity of PIA - Φ_{DP} relationship at different 'scaled altitudes' is reasonable. It remains to be understood if this relationship evolves with the intensity and density effect. Also, the on-site attenuation was not corrected before the study of the PIA - Φ_{DP}, which might have a significant effect on the melting layer.

- GSA style radar QPE parameter estimation/optimization for the dataset utilized in Chapter 6, especially in presence of ML at MOUC 0° elevation angle PPI scans is the next big step. So far, we only considered a few convective cases for QPE application, we have a large dataset with ML (at MOUC altitude) that needs to be explored. We assumed linear PIA - Φ_{dp} relationship at different stages of melting in Chapter 6; optimized parameter set from GSA could look for non-linearity in the relationship, if any, at different stages of melting. Thus, evaluating if the assumption of linearity was reasonable.

- The RadAlp experiment has a unique setup of two X-band radars, one on the mountaintop and another in the valley. This is rarely the case in complex terrain, most operational radars are on mountaintops. A feasibility study on the use of cheaper and portable MRRs in the valleys for ML identification to complement the operational mountain-top radars is a topic of interest as well. Similarly, microwave links provide opportunistic sensing (free of cost) of attenuation at altitudes below the mountaintop radar. A comparison between XPORT, MRR, and microwave link-derived ML identification needs to be performed. This might open new possibilities in remote areas where the installation and maintenance of radar are not feasible. This can be especially beneficial to developing countries and remote communities.

- A machine learning approach to assimilate and correlate multi-platform observations (radar, DSD, micro-wave link, atmospheric sounding, and meteorological satellites) might provide new insights into the impact of melting-layer on the EM propagation effect at different frequencies. RadAlp experiment already has a very good instrument cluster to try innovative solutions. However, this kind of project requires significant computational infrastructures. European Space Agency (ESA) together with ECMWF and EUMETSAT is launching a project to build a digital twin of Earth's weather and climate with a new supercomputer. This kind of study in Grenoble could be a good use case for Destination Earth (DestinE) to build a digital twin of hydrometeorological processes in the mountainous area.

- Study of EM propagation effects in rain and ML with mountain targets in intersecting resolution volumes of XPORT and MOUC could provide more insights on on-site (especially radome) attenuation and impact of elevation angle on propagation effects (eg PIA - Φ_{dp}). As we will not be looking at the 'same' mountain target, correction for the difference in the resolution volume due to the difference in elevation angle and range needs to be taken into account before any such study.

A better understanding of the microphysical process in the ML and its impact on EM propagation would eventually allow us to build a physics-based "inverse" model to recreate vertical profiles of radar observables (including ML) just using mountaintop radar observations that provide reliable QPE at the ground level in mountainous terrain. Similarly, these inverse models could also be fed to the numerical weather prediction model (like AROME) to improve their performance in the mountainous region. If the numerical model can be significantly improved the QPE in mountainous terrain, it will open new avenues of hydrological risk estimation and early warning systems in remote communities.

Appendix A

Appendix: Melting Layer

A.1 Definition of Pseudo variables

Following are the definition of pseudo-variables used to characterize ML in the text, shown to represent the horizontal reflectivity (Zh) profile. Similar definitions are used for other variables wherever applicable.

Zh peak = Maximum value of Zh *[dBZ]*
Zh.alt.peak = Altitude of the Zh peak *[m]*
Zh.val.top = Zh value at top inflection point *[dBZ]*
Zh.alt.top = Altitude corresponding to Zh.val.top *[m]*
Zh.val.bot = Zh value at bottom inflection point *[dBZ]*
Zh.alt.bot = Altitude corresponding to Zh.val.bot *[m]*
Zh.val.t2p = | Zh.val.top - Zh.val.peak | *[dBZ]*; Reflectivity enhancement on top of the profile
Zh.alt.t2p = | Zh.alt.top - Zh.alt.peak | *[m]*
Zh.val.p2b = | Zh.val.peak - Zh.val.bot | *[dBZ]*; Reflectivity enhancement on bottom of the profile
Zh.alt.p2b = | Zh.alt.peak - Zh.val.bot | *[m]*

A.1.1 Correlation coefficient with 2 explanatory variables

The following formula was used to determine the total Spearman's correlation coefficient of an explained variable 1 with two explanatory variables 2 and 3, denoted $r_{1.23}$, as a function of the Spearman's partial correlation coefficients between pairs of them (r_{12}, r_{13}, r_{23}):

$$r^2_{1.23} = \frac{r^2_{12} + r^2_{13} - 2 * r_{12} * r_{13} * r_{23}}{1 - r^2_{23}} \tag{A.1}$$

Appendix B

Appendix: PIA vs Φ_{DP}

TABLE B.1: Summary of ML events used in this study

event	radar	length [hrs]	MLtop[m asl]	MLbot [m asl]	MOUC days
20161118-180000_20161119-060000	XPORT	12.00	2251.60	1629.89	20161118,20161119,20161120
20161122-070000_20161122-092000	XPORT	2.33	2600.54	1949.41	20161122,20161123,20161124,20161125,20161126
20161124-060000_20161124-080000	XPORT	2.00	2315.44	1652.38	20161122,20161123,20161124,20161125,20161126
20161125-070000_20161125-090000	XPORT	2.00	2084.22	1389.25	20161122,20161123,20161124,20161125,20161126
20170228-040000_20170228-060000	XPORT	2.00	1857.56	1236.31	20170228
20170301-170000_20170302-090000	XPORT	16.00	1783.83	1269.96	20170301,20170302,20170303
20170401-121000_20170401-190000	XPORT	6.83	1576.00	1131.52	20170401,20170402
20170425-190000_20170426-073000	XPORT	12.50	1893.40	1255.56	20170425,20170426,20170427
20170427-180000_20170428-073000	XPORT	13.50	830.15	401.49	20170425,20170426,20170427
20170506-080000_20170506-140000	XPORT	6.00	2389.20	1690.04	20170506,20170507
20171104-200000_20171105-120000	XPORT	16.00	2340.60	1740.40	20171104,20171105,20171106
20171111-153000_20171112-060000	XPORT	14.50	2141.31	1693.50	20171111,20171112,20171113
20171210-110000_20171210-230000	XPORT	12.00	2114.16	1480.69	20171210,20171211,20171212
20171211-090000_20171211-200000	XPORT	11.00	1877.48	1306.07	20171210,20171211,20171212
20171230-010000_20171230-200000	XPORT	19.00	1904.56	1277.49	20171230,20171231
20180103-183000_20180104-093000	XPORT	15.00	2012.54	1325.65	20180103,20180104,20180105
20180108-190000_20180108-230000	XPORT	4.00	1742.99	1139.23	20180108,20180109
20180120-110000_20180121-020000	XPORT	15.00	1940.13	1212.19	20180120,20180121,20180122,20180123
20180121-070000_20180121-140000	XPORT	7.00	1338.69	926.19	20180120,20180121,20180122,20180123
20180122-000000_20180122-100000	XPORT	10.00	2334.57	1641.59	20180120,20180121,20180122,20180123
20180122-160000_20180122-230000	XPORT	7.00	2021.20	1451.88	20180120,20180121,20180122,20180123
20180522-180000_20180522-220000	XPORT	4.00	2978.23	2149.82	20180522,20180523
20181027-090000_20181028-080000	XPORT	23.00	1634.84	1062.41	20181027,20181028,20181029,20181030
20181106-090000_20181106-150000	XPORT	6.00	2353.41	1779.66	20181106,20181107
20181121-060000_20181121-120000	XPORT	6.00	1880.37	989.93	20181121,20181122
20181206-063000_20181206-120000	XPORT	5.50	2187.41	1583.67	20181206,20181207
20181221-100000_20181222-082000	XPORT	22.33	2644.13	1844.89	20181221,20181222
20191220-100000_20191220-163000	XPORT	6.50	2044.64	1343.65	20191220,20191221
20191224-100000_20191224-150000	XPORT	5.00	2501.16	1807.88	20191224,20191225
20200117-112000_20200117-164000	MRR	5.33	1650.62	1046.00	20200117
20200302-125000_20200302-235000	MRR	11.00	1259.83	666.11	20200302,20200303,20200304,20200305
20200501-014000_20200501-051000	MRR	3.50	1877.16	1284.14	20200501,20200502
20200501-113000_20200501-221500	MRR	10.75	2519.31	1878.02	20200501,20200502
20200502-151000_20200502-200000	MRR	4.83	2762.33	2153.01	20200501,20200502
20200510-185000_20200511-013000	MRR	6.67	2965.90	2389.41	20200510,20200511
20200925-022000_20200925-030000	MRR	0.67	2381.56	1759.33	20200924,20200925,20200926
20200925-170000_20200926-040000	MRR	11.00	1479.05	895.92	20200924,20200925,20200926
20201002-215000_20201003-034000	MRR	5.83	2219.75	1609.33	20201002,20201003
20201023-162500_20201023-190500	MRR	2.67	2468.42	1824.86	20201023
20201026-013000_20201026-105000	MRR	9.33	1856.97	1230.42	20201026
20201115-194000_20201116-043500	MRR	8.92	2531.56	1909.33	20201115,20201116
20201204-090000_20201204-120000	MRR	3.00	1368.06	768.23	20201204
20201211-194000-20201211_233000	MRR	3.83	1590.13	951.00	20201211

Appendix C

Appendix:Radar QPE

TABLE C.1: Values and ranges of the variation of the attenuation model parameters in the sensitivity analysis

<table>
<tr><th colspan="4">Parameters fixed for a given simulation</th></tr>
<tr><th>Parameter</th><th colspan="3">Values</th></tr>
<tr><td>b_{AZ}</td><td colspan="3">0.78</td></tr>
<tr><td>b_{AK}</td><td colspan="3">1.10</td></tr>
<tr><td>dC</td><td colspan="3">[-2,2] with a step of 0.4 dB</td></tr>
<tr><th colspan="4">Parameters taken into account in the Latin Hypercubes Sampling for a given simulation</th></tr>
<tr><th>Parameter</th><th>Central value</th><th>Range of multiplicative coefficient of the central value (dB)</th><th>Lower and upper limit</th></tr>
<tr><td>a_{AZ}</td><td>$1.0\,10^{-4}$</td><td>[-3,3 dB]</td><td>$[0.5\,10^{-4}, 2.0\,10^{-4}]$</td></tr>
<tr><td>a_{AK}</td><td>0.3</td><td>[-3,3 dB]</td><td>[0.15, 0.6]</td></tr>
<tr><td>dAF_m</td><td>1.0</td><td>[-1,1 dB]</td><td>[0.79, 1.26]</td></tr>
<tr><td>$AF(r_0)$: sampling #1</td><td>0.316</td><td>[-5,5 dB]</td><td>$AF(r_0)$: [1.0, 0.1]
corresponding to
PIA_0: [0,10 dB]</td></tr>
<tr><td>$AF(r_0)$: sampling #2</td><td>$PIA_0^* = 0.0126\,Z_0^{1.6}$
PIA_0^* [dB]; Z_0 [dBZ]
$AF^*(r_0) = 10^{-PIA_0^*/10}$</td><td></td><td>Lower limits:
$PIA_0^L = 0$; $A(r_0)^L = 1$
Upper limits
$PIA_0^U = n\,PIA_0^*$
$A(r_0)^U = 10^{-PIA_0^U/10}$
with n=3, or n=10</td></tr>
</table>

TABLE C.2: Performance of radar QPE at different stations.
Sim003, 30 min accumulation, global optimal dC (dC=0)

station	**AZ0**			**AZC**			**ZPHI**		
	PBIAS%	R^2	**NSE**	**PBIAS%**	R^2	**NSE**	**PBIAS%**	R^2	**NSE**
COLDEPORTE	-21.7	0.08	-0.62	-22.2	0.08	-0.60	-25.5	0.07	-0.64
GREENER	20.5	0.47	-1.03	19.7	0.48	-1.00	23.7	0.47	-1.17
GRE_LVD	38.9	0.23	-1.10	39.3	0.23	-1.11	41.6	0.25	-1.13
IGE	22.3	0.16	-1.48	21.8	0.16	-1.44	23.5	0.17	-1.44
PIPAY	-36.1	0.76	0.63	-36.0	0.76	0.63	-35.2	0.84	0.71
REVEL	-17.7	0.51	0.13	-14.7	0.52	0.12	-15.0	0.57	0.19
CHAMROUSSE	-8.7	0.48	0.12	-8.7	0.46	0.06	-13.9	0.53	0.30
LUITEL	-4.8	0.21	-0.36	-5.5	0.20	-0.37	-5.1	0.22	-0.36

Bibliography

Anagnostou, Emmanouil N., Marios N. Anagnostou, Witold F. Krajewski, Anton Kruger, and Benjamin J. Miriovsky (Feb. 2004). "High-Resolution Rainfall Estimation from X-Band Polarimetric Radar Measurements". In: *Journal of Hydrometeorology* 5.1, pp. 110–128. ISSN: 1525-755X. DOI: 10.1175/1525-7541(2004)005<0110:HREFXP>2.0.CO;2. URL: http://journals.ametsoc.org/doi/abs/10.1175/1525-7541%282004%29005%3C0110%3AHREFXP%3E2.0.CO%3B2.

Andrieu, Hervé and Jean Dominique Creutin (Jan. 1995). "Identification of Vertical Profiles of Radar Reflectivity for Hydrological Applications Using an Inverse Method. Part II: Formulation". In: *Journal of Applied Meteorology* 34.1, pp. 240–259. ISSN: 0894-8763. DOI: 10.1175/1520-0450(1995)034<0240:IOVPOR>2.0.CO;2. URL: http://journals.ametsoc.org/doi/10.1175/1520-0450(1995)034%3C0240:IOVPOR%3E2.0.CO;2.

Atlas, David and Harold C. Banks (Oct. 1951). "The interpretation of microwave reflections from rainfall". In: *Journal of Meteorology* 8.5, pp. 271–282. ISSN: 0095-9634. DOI: 10.1175/1520-0469(1951)008<0271:TIOMRF>2.0.CO;2. URL: http://journals.ametsoc.org/doi/10.1175/1520-0469(1951)008%3C0271:TIOMRF%3E2.0.CO;2.

Atlas, David, Milton Kerker, and Walter Hitschfeld (Feb. 1953). "Scattering and attenuation by non-spherical atmospheric particles". In: *Journal of Atmospheric and Terrestrial Physics* 3.2, pp. 108–119. ISSN: 00219169. DOI: 10.1016/0021-9169(53)90093-2. URL: https://linkinghub.elsevier.com/retrieve/pii/0021916953900932.

Atlas, David and Carlton W. Ulbrich (Dec. 1977). "Path- and Area-Integrated Rainfall Measurement by Microwave Attenuation in the 1–3 cm Band". In: *Journal of Applied Meteorology* 16.12, pp. 1322–1331. ISSN: 0021-8952. DOI: 10.1175/1520-0450(1977)016<1322:PAAIRM>2.0.CO;2.

Baldini, Luca and Eugenio Gorgucci (June 2006). "Identification of the Melting Layer through Dual-Polarization Radar Measurements at Vertical Incidence". In: *Journal of Atmospheric and Oceanic Technology* 23.6, pp. 829–839. ISSN: 1520-0426. DOI: 10.1175/JTECH1884.1. URL: http://journals.ametsoc.org/doi/10.1175/JTECH1884.1.

Bartsotas, N. S., E. N. Anagnostou, E. I. Nikolopoulos, and G. Kallos (May 2018). "Investigating Satellite Precipitation Uncertainty Over Complex Terrain". In: *Journal of Geophysical Research: Atmospheres* 123.10, pp. 5346–5359. ISSN: 2169897X. DOI: 10.1029/2017JD027559. URL: http://doi.wiley.com/10.1029/2017JD027559.

Bellon, Aldo, Isztar Zawadzki, and Frédéric Fabry (May 1997). "Measurements of melting layer attenuation at X-band frequencies". In: *Radio Science* 32.3, pp. 943–955. ISSN: 00486604. DOI: 10.1029/97RS00492. URL: http://doi.wiley.com/10.1029/97RS00492.

Blanchet, Juliette, Jean-Dominique Creutin, and Antoine Blanc (Mar. 2021). "Retreating winter and strengthening autumn Mediterranean influence on extreme precipitation in the Southwestern Alps over the last 60 years". In: *Environmental Research Letters* 16.3. ISSN: 1748-9326. DOI: 10.1088/1748-9326/abb5cd.

Bouilloud, Ludovic, Guy Delrieu, Brice Boudevillain, M Borga, and F Zanon (July 2009). "Radar rainfall estimation for the post-event analysis of a Slovenian flash-flood case: application of the Mountain Reference Technique at C-band frequency". In: *Hydrology and Earth System Sciences* 13.7, pp. 1349–1360. ISSN: 1607-7938. DOI: 10.5194/hess-13-1349-2009. URL: http://www.hydrol-earth-syst-sci.net/13/1349/2009/.

Brandes, Edward A. and Kyoko Ikeda (Nov. 2004). "Freezing-Level Estimation with Polarimetric Radar". In: *Journal of Applied Meteorology* 43.11, pp. 1541–1553. ISSN: 0894-8763. DOI: 10.1175/JAM2155.1. URL: http://journals.ametsoc.org/doi/abs/10.1175/JAM2155.1.

Bringi, V. N., V. Chandrasekar, N. Balakrishnan, and D. S. Zrnić (Dec. 1990). "An Examination of Propagation Effects in Rainfall on Radar Measurements at Microwave Frequencies". In: *Journal of Atmospheric and Oceanic Technology* 7.6. ISSN: 0739-0572. DOI: 10.1175/1520-0426(1990)007<0829:AEOPEI>2.0.CO;2.

Bringi, V. N., V. Chandrasekar, J. Hubbert, E. Gorgucci, W. L. Randeu, and M. Schoenhuber (Jan. 2003). "Raindrop Size Distribution in Different Climatic Regimes from Disdrometer and Dual-Polarized Radar Analysis". In: *Journal of the Atmospheric Sciences* 60.2, pp. 354–365. ISSN: 0022-4928. DOI: 10.1175/1520-0469(2003)060<0354:RSDIDC>2.0.CO;2. URL: http://journals.ametsoc.org/doi/10.1175/1520-0469(2003)060%3C0354:RSDIDC%3E2.0.CO;2.

Bringi, V.N. and V. Chandrasekar (2001). *Polarimetric Doppler weather radar: principles and applications*. Cambridge University Press, p. 636. ISBN: 0521623847.

Claude, Aurélien, Alain Gautheron, Isabella Zin, Charles Obled, Christian Perret, and Arnaud Belleville (Oct. 2016). "Integrated representation of hydropower facilities in an operational flood warning system for a mountainous watershed". In: *E3S Web of Conferences* 7, p. 18012. ISSN: 2267-1242. DOI: 10.1051/e3sconf/

20160718012. URL: http://www.e3s-conferences.org/10.1051/e3sconf/20160718012.

De Jong, C ., P. Masure, and T. Barth (2008). "Challenges of alpine catchment management under changing climatic and anthropogenic pressures". In: *iEMSs Fourth Biennial Meeting: International Congress on Environmental Modelling and Software (iEMSs 2008)*, pp. 694–702. URL: http://www.iemss.org.

Delrieu, G., S. Caoudal, and J. D. Creutin (June 1997). "Feasibility of Using Mountain Return for the Correction of Ground-Based X-Band Weather Radar Data". In: *Journal of Atmospheric and Oceanic Technology* 14.3, pp. 368–385. ISSN: 0739-0572. DOI: 10.1175/1520-0426(1997)014<0368:FOUMRF>2.0.CO;2. URL: http://journals.ametsoc.org/doi/10.1175/1520-0426(1997)014%3C0368:FOUMRF%3E2.0.CO;2.

Delrieu, G., A. Kumar Khanal, N. Yu, F. Cazenave, B. Boudevillain, and N. Gaussiat (2020). "Preliminary investigation of the relationship between differential phase shift and path-integrated attenuation at the X band frequency in an Alpine environment". In: *Atmospheric Measurement Techniques* 13.7. ISSN: 18678548. DOI: 10.5194/amt-13-3731-2020.

Delrieu, Guy, Hervé Andrieu, and Jean Dominique Creutin (June 2000). "Quantification of Path-Integrated Attenuation for X- and C-Band Weather Radar Systems Operating in Mediterranean Heavy Rainfall". In: *Journal of Applied Meteorology* 39.6, pp. 840–850. ISSN: 0894-8763. DOI: 10.1175/1520-0450(2000)039<0840:QOPIAF>2.0.CO;2. URL: http://journals.ametsoc.org/doi/abs/10.1175/1520-0450%282000%29039%3C0840%3AQOPIAF%3E2.0.CO%3B2.

Delrieu, Guy, Jean Dominique Creutin, and Hervé Andrieu (Oct. 1995). "Simulation of Radar Mountain Returns Using a Digitized Terrain Model". In: *Journal of Atmospheric and Oceanic Technology* 12.5, pp. 1038–1049. ISSN: 0739-0572. DOI: 10.1175/1520-0426(1995)012<1038:SORMRU>2.0.CO;2.

Delrieu, Guy, Anil Kumar Khanal, Frédéric Cazenave, and Brice Boudevillain (June 2022). "Sensitivity analysis of attenuation in convective rainfall at X-band frequency using the mountain reference technique". In: *Atmospheric Measurement Techniques* 15.11, pp. 3297–3314. ISSN: 1867-8548. DOI: 10.5194/amt-15-3297-2022. URL: https://amt.copernicus.org/articles/15/3297/2022/.

Delrieu, Guy, Soumia Serrar, Elena Guardo, and Jean Dominique Creutin (Apr. 1999). "Rain Measurement in Hilly Terrain with X-Band Weather Radar Systems: Accuracy of Path-Integrated Attenuation Estimates Derived from Mountain Returns". In: *Journal of Atmospheric and Oceanic Technology* 16.4, pp. 405–416. ISSN: 0739-0572. DOI: 10.1175/1520-0426(1999)016<0405:RMIHTW>2.0.CO;2. URL: http:

//journals.ametsoc.org/doi/abs/10.1175/1520-0426%281999%29016%3C0405%3ARMIHTW%3E2.0.CO%3B2.

Delrieu, Guy, Annette Wijbrans, Brice Boudevillain, Dominique Faure, Laurent Bonnifait, and Pierre-Emmanuel Kirstetter (Sept. 2014). "Geostatistical radar–raingauge merging: A novel method for the quantification of rain estimation accuracy". In: *Advances in Water Resources* 71, pp. 110–124. ISSN: 03091708. DOI: 10.1016/j.advwatres.2014.06.005. URL: http://dx.doi.org/10.1016/j.advwatres.2014.06.005%20https://linkinghub.elsevier.com/retrieve/pii/S0309170814001146.

Dinku, Tufa, Pietro Ceccato, and Stephen J. Connor (Nov. 2011). "Challenges of satellite rainfall estimation over mountainous and arid parts of east Africa". In: *International Journal of Remote Sensing* 32.21, pp. 5965–5979. ISSN: 0143-1161. DOI: 10.1080/01431161.2010.499381. URL: https://www.tandfonline.com/doi/full/10.1080/01431161.2010.499381.

Diss, S., J. Testud, J. Lavabre, P. Ribstein, E. Moreau, and J. Parent du Chatelet (July 2009). "Ability of a dual polarized X-band radar to estimate rainfall". In: *Advances in Water Resources* 32.7, pp. 975–985. ISSN: 03091708. DOI: 10.1016/j.advwatres.2009.01.004. URL: https://linkinghub.elsevier.com/retrieve/pii/S0309170809000141.

Doviak, R.J., D.S. Zrnic, and D.S. Sirmans (1979). "Doppler weather radar". In: *Proceedings of the IEEE* 67.11, pp. 1522–1553. ISSN: 0018-9219. DOI: 10.1109/PROC.1979.11511.

Doviak, Richard J. and Dušan S. Zrnić (1993). *Doppler Radar and Weather Observations*. 2nd. Academic Press. ISBN: 9780122214226. DOI: 10.1016/C2009-0-22358-0.

Fabry, Frédéric (May 2015). *Radar Meteorology*. Cambridge University Press. ISBN: 9781107070462. DOI: 10.1017/CBO9781107707405.

Fabry, Frederic and Isztar Zawadzki (Apr. 1995). "Long-Term Radar Observations of the Melting Layer of Precipitation and Their Interpretation". In: *Journal of the Atmospheric Sciences* 52.7, pp. 838–851. ISSN: 0022-4928. DOI: 10.1175/1520-0469(1995)052<0838:LTROOT>2.0.CO;2. URL: http://journals.ametsoc.org/doi/abs/10.1175/1520-0469%281995%29052%3C0838%3ALTROOT%3E2.0.CO%3B2.

Foresti, Loris, Ioannis Vasileios Sideris, Luca Panziera, Daniele Nerini, and Urs Germann (Oct. 2018). "A 10-year radar-based analysis of orographic precipitation growth and decay patterns over the Swiss Alpine region". In: *Quarterly Journal of the Royal Meteorological Society* 144.716, pp. 2277–2301. ISSN: 00359009. DOI: 10.1002/qj.3364. URL: http://doi.wiley.com/10.1002/qj.3364.

Frasier, Stephen J., Fadela Kabeche, Jordi Figueras i Ventura, Hassan Al-Sakka, Pierre Tabary, Jeffrey Beck, and Olivier Bousquet (May 2013). "In-Place Estimation of

Wet Radome Attenuation at X Band". In: *Journal of Atmospheric and Oceanic Technology* 30.5, pp. 917–928. ISSN: 0739-0572. DOI: `10.1175/JTECH-D-12-00148.1`.

Fujiyoshi, Yasushi (Feb. 1986). "Melting Snowflakes". In: *Journal of the Atmospheric Sciences* 43.3, pp. 307–311. ISSN: 0022-4928. DOI: `10.1175/1520-0469(1986)043<0307:MS>2.0.CO;2`. URL: `http://journals.ametsoc.org/doi/abs/10.1175/1520-0469%281986%29043%3C0307%3AMS%3E2.0.CO%3B2`.

Germann, Urs, Marco Boscacci, Lorenzo Clementi, Marco Gabella, Alessandro Hering, Maurizio Sartori, Ioannis V. Sideris, and Bertrand Calpini (Jan. 2022). "Weather Radar in Complex Orography". In: *Remote Sensing* 14.3, p. 503. ISSN: 2072-4292. DOI: `10.3390/rs14030503`.

Germann, Urs, Gianmario Galli, Marco Boscacci, and Martin Bolliger (July 2006). "Radar precipitation measurement in a mountainous region". In: *Quarterly Journal of the Royal Meteorological Society* 132.618, pp. 1669–1692. ISSN: 00359009. DOI: `10.1256/qj.05.190`. URL: `http://doi.wiley.com/10.1256/qj.05.190`.

Giangrande, Scott E., John M. Krause, and Alexander V. Ryzhkov (May 2008). "Automatic Designation of the Melting Layer with a Polarimetric Prototype of the WSR-88D Radar". In: *Journal of Applied Meteorology and Climatology* 47.5. ISSN: 1558-8432. DOI: `10.1175/2007JAMC1634.1`.

Goger, Brigitta, Mathias W. Rotach, Alexander Gohm, Ivana Stiperski, and Oliver Fuhrer (July 2016). "Current challenges for numerical weather prediction in complex terrain: Topography representation and parameterizations". In: *2016 International Conference on High Performance Computing & Simulation (HPCS)*, pp. 890–894. ISBN: 978-1-5090-2088-1. DOI: `10.1109/HPCSim.2016.7568428`. URL: `http://ieeexplore.ieee.org/document/7568428/`.

Hardaker, P. J., A. R. Holt, and C. G. Collier (Apr. 1995). "A melting-layer model and its use in correcting for the bright band in single-polarization radar echoes". In: *Quarterly Journal of the Royal Meteorological Society* 121.523, pp. 495–525. ISSN: 00359009. DOI: `10.1002/qj.49712152303`. URL: `http://doi.wiley.com/10.1002/qj.49712152303`.

Herzegh, Paul H. and Arthur R. Jameson (Sept. 1992). "Observing Precipitation through Dual-Polarization Radar Measurements". In: *Bulletin of the American Meteorological Society* 73.9, pp. 1365–1374. ISSN: 0003-0007. DOI: `10.1175/1520-0477(1992)073<1365:OPTDPR>2.0.CO;2`. URL: `http://journals.ametsoc.org/doi/abs/10.1175/1520-0477%281992%29073%3C1365%3AOPTDPR%3E2.0.CO%3B2`.

Heymsfield, Andrew J., Aaron Bansemer, Paul R. Field, Stephen L. Durden, Jeffrey L. Stith, James E. Dye, William Hall, and Cedric A. Grainger (Dec. 2002). "Observations and Parameterizations of Particle Size Distributions in Deep Tropical Cirrus and Stratiform Precipitating Clouds: Results from In Situ Observations in TRMM

Field Campaigns". In: *Journal of the Atmospheric Sciences* 59.24, pp. 3457–3491. ISSN: 0022-4928. DOI: `10.1175/1520-0469(2002)059<3457:OAPOPS>2.0.CO;2`. URL: `http://journals.ametsoc.org/doi/abs/10.1175/1520-0469%282002%29059%3C3457%3AOAPOPS%3E2.0.CO%3B2`.

Hitschfeld, Walter and Jack Bordan (Feb. 1954). "Errors inherent in the radar measurement of rainfall at attenuating wavelengths". In: *Journal of Meteorology* 11.1, pp. 58–67. ISSN: 0095-9634. DOI: `10.1175/1520-0469(1954)011<0058:EIITRM>2.0.CO;2`.

Hong, Yang, Guoqiang Tang, Yingzhao Ma, Qi Huang, Zhongying Han, Ziyue Zeng, Yuan Yang, Cunguang Wang, and Xiaolin Guo (2019). "Remote Sensing Precipitation: Sensors, Retrievals, Validations, and Applications". In: pp. 107–128. DOI: `10.1007/978-3-662-48297-1{\_}4`. URL: `http://link.springer.com/10.1007/978-3-662-48297-1_4`.

Hubbert, J. and V. N. Bringi (June 1995). "An Iterative Filtering Technique for the Analysis of Copolar Differential Phase and Dual-Frequency Radar Measurements". In: *Journal of Atmospheric and Oceanic Technology* 12.3. ISSN: 0739-0572. DOI: `10.1175/1520-0426(1995)012<0643:AIFTFT>2.0.CO;2`.

Ives, J.D., B. Messerli, and E. Spiess (1997). "Mountains of the world: A global priority, in Mountains of the World: A Global Priority". In: ed. by B. Messerli and J.D. Ives. New York: Parthenon, pp. 1–16.

Jewell, Sharon A. and Nicolas Gaussiat (July 2015). "An assessment of kriging-based rain-gauge-radar merging techniques". In: *Quarterly Journal of the Royal Meteorological Society* 141.691, pp. 2300–2313. ISSN: 00359009. DOI: `10.1002/qj.2522`. URL: `http://doi.wiley.com/10.1002/qj.2522`.

Joss, Jürg and Robert Lee (Dec. 1995). "The Application of Radar & Gauge Comparisons to Operational Precipitation Profile Corrections". In: *Journal of Applied Meteorology* 34.12, pp. 2612–2630. ISSN: 0894-8763. DOI: `10.1175/1520-0450(1995)034<2612:TAORCT>2.0.CO;2`. URL: `http://journals.ametsoc.org/doi/abs/10.1175/1520-0450%281995%29034%3C2612%3ATAORCT%3E2.0.CO%3B2`.

Khanal, Anil Kumar, Guy Delrieu, Frédéric Cazenave, and Brice Boudevillain (Dec. 2019). "Radar Remote Sensing of Precipitation in High Mountains: Detection and Characterization of Melting Layer in the Grenoble Valley, French Alps". In: *Atmosphere* 10.12, p. 784. ISSN: 2073-4433. DOI: `10.3390/atmos10120784`. URL: `https://www.mdpi.com/2073-4433/10/12/784`.

Klaassen, Wim (Dec. 1988). "Radar Observations and Simulation of the Melting Layer of Precipitation". In: *Journal of the Atmospheric Sciences* 45.24, pp. 3741–3753. ISSN: 0022-4928. DOI: `10.1175/1520-0469(1988)045<3741:ROASOT>2.0.CO;2`.

URL: http://journals.ametsoc.org/doi/abs/10.1175/1520-0469%281988%29045%3C3741%3AROASOT%3E2.0.CO%3B2.

Knight, Charles A. (1979). *Observations of the Morphology of Melting Snow*. DOI: 10.1175/1520-0469(1979)036<1123:OOTMOM>2.0.CO;2. URL: http://journals.ametsoc.org/doi/abs/10.1175/1520-0469(1979)036%3C1123:OOTMOM%3E2.0.CO;2.

Kochendorfer, John et al. (Apr. 2017). "The quantification and correction of wind-induced precipitation measurement errors". In: *Hydrology and Earth System Sciences* 21.4, pp. 1973–1989. ISSN: 1607-7938. DOI: 10.5194/hess-21-1973-2017.

Koffi, A. K., M. Gosset, E. P. Zahiri, A. D. Ochou, M. Kacou, F. Cazenave, and P. Assamoi (2014). "Evaluation of X-band polarimetric radar estimation of rainfall and rain drop size distribution parameters in West Africa". In: *Atmospheric Research* 143, pp. 438–461. ISSN: 01698095. DOI: 10.1016/j.atmosres.2014.03.009.

Kumjian, Matthew (Nov. 2013). "Principles and applications of dual-polarization weather radar. Part I: Description of the polarimetric radar variables". In: *Journal of Operational Meteorology* 1.19, pp. 226–242. ISSN: 23256184. DOI: 10.15191/nwajom.2013.0119. URL: http://linkinghub.elsevier.com/retrieve/pii/0022510X89900257%20http://nwafiles.nwas.org/jom/articles/2013/2013-JOM19/2013-JOM19.pdf.

Leinonen, Jussi and Annakaisa von Lerber (Feb. 2018). "Snowflake Melting Simulation Using Smoothed Particle Hydrodynamics". In: *Journal of Geophysical Research: Atmospheres* 123.3, pp. 1811–1825. ISSN: 2169897X. DOI: 10.1002/2017JD027909. URL: http://doi.wiley.com/10.1002/2017JD027909.

Lengfeld, K., M. Clemens, H. Münster, and F. Ament (Dec. 2014). "Performance of high-resolution X-band weather radar networks – the PATTERN example". In: *Atmospheric Measurement Techniques* 7.12, pp. 4151–4166. ISSN: 1867-8548. DOI: 10.5194/amt-7-4151-2014.

Löffler-Mang, Martin, Michael Kunz, and Willi Schmid (Mar. 1999). "On the Performance of a Low-Cost K-Band Doppler Radar for Quantitative Rain Measurements". In: *Journal of Atmospheric and Oceanic Technology* 16.3, pp. 379–387. ISSN: 0739-0572. DOI: 10.1175/1520-0426(1999)016<0379:OTPOAL>2.0.CO;2. URL: http://journals.ametsoc.org/doi/abs/10.1175/1520-0426%281999%29016%3C0379%3AOTPOAL%3E2.0.CO%3B2.

Maahn, M. and P. Kollias (Nov. 2012). "Improved Micro Rain Radar snow measurements using Doppler spectra post-processing". In: *Atmospheric Measurement Techniques* 5.11, pp. 2661–2673. ISSN: 1867-8548. DOI: 10.5194/amt-5-2661-2012. URL: https://amt.copernicus.org/articles/5/2661/2012/.

Marshall, J. S. and W. Mc K. Palmer (Aug. 1948). “The distribution of raindrops with size”. In: *Journal of Meteorology* 5.4, pp. 165–166. ISSN: 0095-9634. DOI: 10.1175/1520-0469(1948)005<0165:TDORWS>2.0.CO;2. URL: http://journals.ametsoc.org/doi/abs/10.1175/1520-0469%281948%29005%3C0165%3ATDORWS%3E2.0.CO%3B2.

Marzoug, Mongi and Paul Amayenc (Dec. 1994). “A Class of Single- and Dual-Frequency Algorithms for Rain-Rate Profiling from a Spaceborne Radar. Pad I: Principle and Tests from Numerical Simulations”. In: *Journal of Atmospheric and Oceanic Technology* 11.6, pp. 1480–1506. ISSN: 0739-0572. DOI: 10.1175/1520-0426(1994)011<1480:ACOSAD>2.0.CO;2. URL: http://journals.ametsoc.org/doi/abs/10.1175/1520-0426%281994%29011%3C1480%3AACOSAD%3E2.0.CO%3B2.

Matrosov, Sergey Y., Kurt A. Clark, Brooks E. Martner, and Ali Tokay (2002). “X-Band Polarimetric Radar Measurements of Rainfall”. In: *Journal of Applied Meteorology* 41.9, pp. 941–952. ISSN: 0894-8763. DOI: 10.1175/1520-0450(2002)041<0941:xbprmo>2.0.co;2.

Matrosov, Sergey Y., David E. Kingsmill, Brooks E. Martner, and F. Martin Ralph (June 2005). “The Utility of X-Band Polarimetric Radar for Quantitative Estimates of Rainfall Parameters”. In: *Journal of Hydrometeorology* 6.3, pp. 248–262. ISSN: 1525-7541. DOI: 10.1175/JHM424.1. URL: https://journals.ametsoc.org/jhm/article/6/3/248/5347/The-Utility-of-XBand-Polarimetric-Radar-for.

Matrosov, Sergey Y., Robert A. Kropfli, Roger F. Reinking, and Brooks E. Martner (June 1999). “Prospects for Measuring Rainfall Using Propagation Differential Phase in X- and Ka- Radar Bands”. In: *Journal of Applied Meteorology* 38.6. ISSN: 0894-8763. DOI: 10.1175/1520-0450(1999)038<0766:PFMRUP>2.0.CO;2.

Matsuo, Takayo and Yoshio Sasyo (1981). “Melting of Snowflakes below Freezing Level in the Atmosphere”. In: *Journal of the Meteorological Society of Japan. Ser. II* 59.1, pp. 10–25. ISSN: 0026-1165. DOI: 10.2151/jmsj1965.59.1{_}10. URL: https://www.jstage.jst.go.jp/article/jmsj1965/59/1/59_1_10/_article.

McLaughlin, David et al. (Dec. 2009). “Short-Wavelength Technology and the Potential For Distributed Networks of Small Radar Systems”. In: *Bulletin of the American Meteorological Society* 90.12, pp. 1797–1818. ISSN: 0003-0007. DOI: 10.1175/2009BAMS2507.1.

Meneghini, Robert, Jerome Eckerman, and David Atlas (Jan. 1983). “Determination of Rain Rate from a Spaceborne Radar Using Measurements of Total Attenuation”. In: *IEEE Transactions on Geoscience and Remote Sensing* GE-21.1, pp. 34–43. ISSN: 0196-2892. DOI: 10.1109/TGRS.1983.350528.

Meneghini, Robert, Toshio Iguchi, Toshiaki Kozu, Liang Liao, Ken'ichi Okamoto, Jeffrey A. Jones, and John Kwiatkowski (Dec. 2000). "Use of the Surface Reference Technique for Path Attenuation Estimates from the TRMM Precipitation Radar". In: *Journal of Applied Meteorology* 39.12, pp. 2053–2070. ISSN: 0894-8763. DOI: 10.1175/1520-0450(2001)040<2053:UOTSRT>2.0.CO;2.

Meneghini, Robert, Hyokyung Kim, Liang Liao, John Kwiatkowski, and Toshio Iguchi (2021). "Path Attenuation Estimates for the GPM Dual-frequency Precipitation Radar (DPR)". In: *Journal of the Meteorological Society of Japan. Ser. II* 99.1, pp. 181–200. ISSN: 0026-1165. DOI: 10.2151/jmsj.2021-010. URL: https://www.jstage.jst.go.jp/article/jmsj/99/1/99_2021-010/_article.

Mishchenko, Michael I, Gorden Videen, Victor A. Babenkom, Nikolai G. Khlebtsov, and Thomas Wriedt (Sept. 2004). "T-matrix theory of electromagnetic scattering by partciles and its applications: a comprehensive reference database". In: *Journal of Quantitative Spectroscopy and Radiative Transfer* 88.1-3, pp. 357–406. ISSN: 00224073. DOI: 10.1016/j.jqsrt.2004.05.002.

Mitra, S. K., O. Vohl, M. Ahr, and H. R. Pruppacher (Mar. 1990). "A Wind Tunnel and Theoretical Study of the Melting Behavior of Atmospheric Ice Particles. IV: Experiment and Theory for Snow Flakes". In: *Journal of the Atmospheric Sciences* 47.5, pp. 584–591. ISSN: 0022-4928. DOI: 10.1175/1520-0469(1990)047<0584:AWTATS>2.0.CO;2. URL: http://journals.ametsoc.org/doi/abs/10.1175/1520-0469%281990%29047%3C0584%3AAWTATS%3E2.0.CO%3B2.

Mountain Partnership (2014). *Mountains as the water towers of the world: A call for action on the sustainable development goals (SDGs)*. Tech. rep. URL: http://www.fao.org/fileadmin/templates/mountain_partnership/doc/POLICY_BRIEFS/SDGs_and_mountains_water_EN.pdf.

Nguyen, Phu, Mohammed Ombadi, Soroosh Sorooshian, Kuolin Hsu, Amir AghaKouchak, Dan Braithwaite, Hamed Ashouri, and Andrea Rose Thorstensen (Nov. 2018). "The PERSIANN family of global satellite precipitation data: a review and evaluation of products". In: *Hydrology and Earth System Sciences* 22.11, pp. 5801–5816. ISSN: 1607-7938. DOI: 10.5194/hess-22-5801-2018. URL: https://hess.copernicus.org/articles/22/5801/2018/.

Park, S-G., V. N. Bringi, V. Chandrasekar, M. Maki, and K. Iwanami (Nov. 2005). "Correction of Radar Reflectivity and Differential Reflectivity for Rain Attenuation at X Band. Part I: Theoretical and Empirical Basis". In: *Journal of Atmospheric and Oceanic Technology* 22.11, pp. 1621–1632. ISSN: 1520-0426. DOI: 10.1175/JTECH1803.1.

Pruppacher, H R and J D Klett (2010). "Growth of Ice Particles by Accretion and Ice Particle Melting". In: *Microphysics of Clouds and Precipitation*. Dordrecht: Springer

Netherlands, pp. 659–699. ISBN: 978-0-306-48100-0. DOI: 10.1007/978-0-306-48100-0{_}16. URL: https://doi.org/10.1007/978-0-306-48100-0_16.

Reinoso-Rondinel, Ricardo, Christine Unal, and Herman Russchenberg (Mar. 2018). “Adaptive and high-resolution estimation of specific differential phase for polarimetric X-band weather radars”. In: *Journal of Atmospheric and Oceanic Technology* 35.3, pp. 555–573. ISSN: 15200426. DOI: 10.1175/JTECH-D-17-0105.1.

Rico-Ramirez, M. A. and I. D. Cluckie (Sept. 2007). “Bright-band detection from radar vertical reflectivity profiles”. In: *International Journal of Remote Sensing* 28.18, pp. 4013–4025. ISSN: 0143-1161. DOI: 10.1080/01431160601047797. URL: https://www.tandfonline.com/doi/full/10.1080/01431160601047797.

Rotunno, Richard and Robert A. Houze (Apr. 2007). “Lessons on orographic precipitation from the Mesoscale Alpine Programme”. In: *Quarterly Journal of the Royal Meteorological Society* 133.625, pp. 811–830. ISSN: 00359009. DOI: 10.1002/qj.67. URL: website:%20http://www.kemkes.go.id%20http://doi.wiley.com/10.1002/qj.67.

Russchenberg, H.W.J. and L.P. Ligthart (1996). “Backscattering by and propagation through the melting layer of precipitation: a new polarimetric model”. In: *IEEE Transactions on Geoscience and Remote Sensing* 34.1, pp. 3–14. ISSN: 01962892. DOI: 10.1109/36.481885. URL: http://ieeexplore.ieee.org/document/481885/.

Ryzhkov, Alexander V., Terry J. Schuur, Donald W. Burgess, Pamela L. Heinselman, Scott E. Giangrande, and Dusan S. Zrnic (June 2005). “The Joint Polarization Experiment: Polarimetric Rainfall Measurements and Hydrometeor Classification”. In: *Bulletin of the American Meteorological Society* 86.6, pp. 809–824. ISSN: 0003-0007. DOI: 10.1175/BAMS-86-6-809. URL: http://journals.ametsoc.org/doi/10.1175/BAMS-86-6-809.

Ryzhkov, Alexander, Malte Diederich, Pengfei Zhang, and Clemens Simmer (Mar. 2014). “Potential Utilization of Specific Attenuation for Rainfall Estimation, Mitigation of Partial Beam Blockage, and Radar Networking”. In: *Journal of Atmospheric and Oceanic Technology* 31.3, pp. 599–619. ISSN: 0739-0572. DOI: 10.1175/JTECH-D-13-00038.1. URL: https://journals.ametsoc.org/jtech/article/31/3/599/39281/Potential-Utilization-of-Specific-Attenuation-for.

Ryzhkov, Alexander, Pengfei Zhang, Heather Reeves, Matthew Kumjian, Timo Tschallener, Silke Trömel, and Clemens Simmer (Mar. 2016). “Quasi-Vertical Profiles—A New Way to Look at Polarimetric Radar Data”. In: *Journal of Atmospheric and Oceanic Technology* 33.3, pp. 551–562. ISSN: 0739-0572. DOI: 10.1175/JTECH-D-15-0020.1. URL: http://journals.ametsoc.org/doi/10.1175/JTECH-D-15-0020.1.

Ryzhkov, Alexander and Dusan Zrnic (June 1998). "Beamwidth Effects on the Differential Phase Measurements of Rain". In: *Journal of Atmospheric and Oceanic Technology* 15.3, pp. 624–634. ISSN: 0739-0572. DOI: `10.1175/1520-0426(1998)015<0624:BEOTDP>2.0.CO;2`.

Saltikoff, Elena et al. (June 2019). "OPERA the Radar Project". In: *Atmosphere* 10.6, p. 320. ISSN: 2073-4433. DOI: `10.3390/atmos10060320`.

Schneebeli, Marc and Alexis Berne (May 2012). "An Extended Kalman Filter Framework for Polarimetric X-Band Weather Radar Data Processing". In: *Journal of Atmospheric and Oceanic Technology* 29.5, pp. 711–730. ISSN: 0739-0572. DOI: `10.1175/JTECH-D-10-05053.1`. URL: `http://journals.ametsoc.org/doi/abs/10.1175/JTECH-D-10-05053.1`.

Serrar, Soumia, Guy Delrieu, Jean-dominique Creutin, and Remko Uijlenhoet (Jan. 2000). "Mountain reference technique: Use of mountain returns to calibrate weather radars operating at attenuating wavelengths". In: *Journal of Geophysical Research: Atmospheres* 105.D2, pp. 2281–2290. ISSN: 01480227. DOI: `10.1029/1999JD901025`. URL: `http://doi.wiley.com/10.1029/1999JD901025`.

Sideris, I. V., M. Gabella, R. Erdin, and U. Germann (Apr. 2014). "Real-time radar-rain-gauge merging using spatio-temporal co-kriging with external drift in the alpine terrain of Switzerland". In: *Quarterly Journal of the Royal Meteorological Society* 140.680, pp. 1097–1111. ISSN: 00359009. DOI: `10.1002/qj.2188`. URL: `http://doi.wiley.com/10.1002/qj.2188`.

Sodemann, Harald and Elias Zubler (2009). "Seasonal and inter-annual variability of the moisture sources for Alpine precipitation during 1995-2002". In: *International Journal of Climatology*. ISSN: 08998418. DOI: `10.1002/joc.1932`.

Sohoulande Djebou, Dagbegnon C. and Vijay P. Singh (Aug. 2016). "Impact of climate change on precipitation patterns: a comparative approach". In: *International Journal of Climatology* 36.10, pp. 3588–3606. ISSN: 08998418. DOI: `10.1002/joc.4578`. URL: `http://doi.wiley.com/10.1002/joc.4578`.

Stewart, Ronald E., John D. Marwitz, John C. Pace, and Richard E. Carbone (Nov. 1984). "Characteristics through the Melting Layer of Stratiform Clouds". In: *Journal of the Atmospheric Sciences* 41.22, pp. 3227–3237. ISSN: 0022-4928. DOI: `10.1175/1520-0469(1984)041<3227:CTTMLO>2.0.CO;2`. URL: `http://journals.ametsoc.org/doi/abs/10.1175/1520-0469%281984%29041%3C3227%3ACTTMLO%3E2.0.CO%3B2`.

Szyrmer, Wanda and Isztar Zawadzki (Oct. 1999). "Modeling of the Melting Layer. Part I: Dynamics and Microphysics". In: *Journal of the Atmospheric Sciences* 56.20, pp. 3573–3592. ISSN: 0022-4928. DOI: `10.1175/1520-0469(1999)056<3573:`

MOTMLP>2.0.CO;2. URL: http://journals.ametsoc.org/doi/abs/10.1175/1520-0469%281999%29056%3C3573%3AMOTMLP%3E2.0.CO%3B2.

Testud, Jacques, Erwan Le Bouar, Estelle Obligis, and Mustapha Ali-Mehenni (2000). "The rain profiling algorithm applied to polarimetric weather radar". In: *Journal of Atmospheric and Oceanic Technology* 17.3, pp. 332–356. ISSN: 07390572. DOI: 10.1175/1520-0426(2000)017<0332:TRPAAT>2.0.CO;2.

The Water Cycle (n.d.). URL: https://scied.ucar.edu/learning-zone/how-weather-works/water-cycle.

Thorndahl, Søren, Thomas Einfalt, Patrick Willems, Jesper Ellerbæk Nielsen, Marie-Claire ten Veldhuis, Karsten Arnbjerg-Nielsen, Michael R. Rasmussen, and Peter Molnar (Mar. 2017). "Weather radar rainfall data in urban hydrology". In: *Hydrology and Earth System Sciences* 21.3, pp. 1359–1380. ISSN: 1607-7938. DOI: 10.5194/hess-21-1359-2017.

Trenberth, Kevin E (June 2008). "The Impact of Climate Change and Variability on Heavy Precipitation, Floods, and Droughts". In: *Encyclopedia of Hydrological Sciences*. DOI: 10.1002/0470848944.hsa211. URL: http://doi.wiley.com/10.1002/0470848944.hsa211.

Trömel, Silke, Matthew R. Kumjian, Alexander V. Ryzhkov, Clemens Simmer, and Malte Diederich (Nov. 2013). "Backscatter differential phase-estimation and variability". In: *Journal of Applied Meteorology and Climatology* 52.11, pp. 2529–2548. ISSN: 15588424. DOI: 10.1175/JAMC-D-13-0124.1.

Trömel, Silke, Alexander V. Ryzhkov, Pengfei Zhang, and Clemens Simmer (2014). "Investigations of backscatter differential phase in the melting layer". In: *Journal of Applied Meteorology and Climatology* 53.10, pp. 2344–2359. ISSN: 15588432. DOI: 10.1175/JAMC-D-14-0050.1.

Van de Beek, C. Z., H. Leijnse, J. N. M. Stricker, R. Uijlenhoet, and H. W. J. Russchenberg (Feb. 2010). "Performance of high-resolution X-band radar for rainfall measurement in The Netherlands". In: *Hydrology and Earth System Sciences* 14.2, pp. 205–221. ISSN: 1607-7938. DOI: 10.5194/hess-14-205-2010.

Vivekanandan, J., R. Raghavan, and V.N. Bringi (1993). "Polarimetric radar modeling of mixtures of precipitation particles". In: *IEEE Transactions on Geoscience and Remote Sensing* 31.5, pp. 1017–1030. ISSN: 01962892. DOI: 10.1109/36.263772. URL: http://ieeexplore.ieee.org/document/263772/.

Viviroli, Daniel, Hans H. Dürr, Bruno Messerli, Michel Meybeck, and Rolf Weingartner (July 2007). "Mountains of the world, water towers for humanity: Typology, mapping, and global significance". In: *Water Resources Research* 43.7. ISSN: 00431397. DOI: 10.1029/2006WR005653. URL: http://doi.wiley.com/10.1029/2006WR005653.

Westrelin, S, P Mériaux, P Tabary, and Y Aubert (2012). "Hydrometeorological risks in Mediterranean mountainous areas RHYTMME Project 1 : Risk Management based on a Radar Network". In: *ERAD 2012 7th European Conference on Radar in Meteorology and Hydrology*. URL: `https://hal.archives-ouvertes.fr/hal-01511157`.

Wexler, R., R. J. Reed, and J Honig (Feb. 1954). "Atmospheric Cooling by Melting Snow". In: *Bulletin of the American Meteorological Society* 35, pp. 48–51. URL: `https://www.jstor.org/stable/26241996`.

Willie, Delbert, Wanyu Li, Yanting Wang, and V. Chadraseker (2006). "Attenuation statistics for X-band radar design". In: *International Geoscience and Remote Sensing Symposium (IGARSS)*, pp. 2647–2650. DOI: `10.1109/IGARSS.2006.683`.

Willis, Paul T. and Andrew J. Heymsfield (July 1989). "Structure of the Melting Layer in Mesoscale Convective System Stratiform Precipitation". In: *Journal of the Atmospheric Sciences* 46.13, pp. 2008–2025. ISSN: 0022-4928. DOI: `10.1175/1520-0469(1989)046<2008:SOTMLI>2.0.CO;2`. URL: `http://journals.ametsoc.org/doi/abs/10.1175/1520-0469%281989%29046%3C2008%3ASOTMLI%3E2.0.CO%3B2`.

Wolfensberger, Daniel, Danny Scipion, and Alexis Berne (Aug. 2016). "Detection and characterization of the melting layer based on polarimetric radar scans". In: *Quarterly Journal of the Royal Meteorological Society* 142, pp. 108–124. ISSN: 00359009. DOI: `10.1002/qj.2672`. URL: `http://doi.wiley.com/10.1002/qj.2672`.

Yu, Nan, Guy Delrieu, Brice Boudevillain, Pieter Hazenberg, and Remko Uijlenhoet (Jan. 2014). "Unified Formulation of Single- and Multimoment Normalizations of the Raindrop Size Distribution Based on the Gamma Probability Density Function". In: *Journal of Applied Meteorology and Climatology* 53.1, pp. 166–179. ISSN: 1558-8424. DOI: `10.1175/JAMC-D-12-0244.1`.

Yu, Nan, Nicolas Gaussiat, and Pierre Tabary (2018). "Polarimetric X-band weather radars for quantitative precipitation estimation in mountainous regions". In: *Quarterly Journal of the Royal Meteorological Society* 144.717, pp. 2603–2619. ISSN: 1477870X. DOI: `10.1002/qj.3366`.

Zawadzki, I., W. Szyrmer, C. Bell, and F. Fabry (Oct. 2005). "Modeling of the Melting Layer. Part III: The Density Effect". In: *Journal of the Atmospheric Sciences* 62.10, pp. 3705–3723. ISSN: 1520-0469. DOI: `10.1175/JAS3563.1`. URL: `https://journals.ametsoc.org/doi/10.1175/JAS3563.1`.

Zrnić, D. S., R. Raghavan, and V. Chandrasekar (Jan. 1994). "Observations of Copolar Correlation Coefficient through a Bright Band at Vertical Incidence". In: *Journal of Applied Meteorology* 33.1, pp. 45–52. ISSN: 0894-8763. DOI: `10.1175/1520-`

`0450(1994)033<0045:OOCCCT>2.0.CO;2`. URL: `http://journals.ametsoc.org/doi/abs/10.1175/1520-0450%281994%29033%3C0045%3AOOCCCT%3E2.0.CO%3B2`.